Universitat Autònoma de Barcelona

Hybrid photovoltaic-thermoelectric devices based on organic semiconductors

José Piers Jurado

Hybrid photovoltaic-thermoelectric devices based on organic semiconductors

Ph.D. Thesis of

José Piers Jurado

Supervisor: Dr. Mariano Campoy-Quiles

Tutor: Dr. Javier Rodríguez-Viejo

Universitat Autònoma de Barcelona
Facultat de Ciències
Departament de Física

ICMAB
INSTITUT DE CIÈNCIA DE MATERIALS DE BARCELONA
EXCELENCIA SEVERO OCHOA
CSIC
CONSEJO SUPERIOR DE INVESTIGACIONES CIENTÍFICAS

September 2021

Acknowledgements

This thesis would not have been possible without the continuous support and encouragement of many people including friends, family and coworkers. First and foremost, I would like to thank my supervisor, Dr. Mariano Campoy-Quiles, for providing an invaluable opportunity to be a part of a challenging, yet exciting PhD project. I am deeply grateful for his guidance, help, and most importantly patience throughout the past few years to help make my Ph.D. project a success.

I am extremely thankful to Dr. Agustín Mihi, Dr. Sebastián Reparaz, and Dr. Alejandro Goñi for taking the time to teach me new experimental techniques and the in-depth discussions. I especially want to thank Bernhard for always making time to help and resolve any problem I faced in the lab.

I would like to thank all of my officemates for being more than just officemates, especially Martí, Nerea, Juan, and Carles. Even the most frustrating days they provided me with support, laughs and food. I want to say thanks to Os for always being a good friend and showing me the ropes at ICMAB when I first arrived. I would like to thank Iván too for all his help with electronics and for also the many in-depth discussions about life in general.

I want to thank Pau for organizing trips outside of work and inviting me to try rock climbing and hiking. I want especially give my thanks to Rana and Fatma for the great memories inside and outside of ICMAB, and the countless Egyptian lunch/dinners we shared together. I'd like to thank Adrián for the lunch time soccer games we played.

I would also like to express my gratitude to all of my colleagues I had the pleasure to work with in Nanopto, including Isabel, Miquel, Jose, Laura, Mayte, Camilla, Valentia, Alex, Enrique, Cristiano Luis, Albert, Leonardo, Xabier, Marta, Jinui, Minghua, Ylli, and Kai.

Outside of my work colleagues, I'd like to especially thank the other la Caixa fellows, Jan, Milica and Ambrus, for support during the fellowship and for the great memories from the la Caixa networking events. I must also thank my closest friends, Chris, Shannon, Marce, Karim, Alex, Ahmed, Marco, and Zdravko, for the constant moral support throughout my Ph.D. Lastly, I would like to thank my family, both near and far, for their unconditional support provided before and during my Ph.D., making sure everything I needed along the way was there for me.

Fundación "la Caixa"

Horizon 2020
European Union funding
for Research & Innovation

The project that gave rise to these results received support through the INPhINIT Fellowship Grant for Doctoral Studies at Spanish Research Centers of Excellence from the "la Caixa" Foundation (ID **100010434**). The fellowship code is **LCF/BQ/DI17/11620035**.

The project has received funding from the European Union's Horizon 2020 research and innovation program under the Marie Skłodowska-Curie grant agreement No. **713673**.

Abstract

With the global energy demand growing every year and the need to mitigate the effects of climate change, low-cost and scalable technologies capable of harvesting energy from renewable sources are core to a future sustainable energy landscape. The largest renewable source, the Sun, provides us with an inexhaustible amount of energy in the form of light and infrared heat, leading to the development of numerous solar energy conversion technologies ranging from electricity generation to domestic water heating.

In this thesis, coupling organic thermoelectrics (TE) with organic solar cells (OSCs) is explored as an approach to solid-state solar harvesting. In the first part of the thesis, we demonstrate the ability of organic TE materials to absorb solar radiation and convert it into electricity via a two-step process. In a first step, solar radiation is converted into heat, so we characterized the materials as solar absorbers, using Fourier transform infrared (FTIR) spectroscopy to investigate their optical properties and infrared thermography to investigate their photothermal properties. In a second step, the heat is converted into electricity via the Seebeck effect. Typically, TE materials are investigated in the context of waste heat recovery, so we investigated secondary light effects on the TE parameters, namely electrical conductivity and Seebeck coefficient. Next, we explored geometrical device parameters, such as device leg length, and propose several planar geometries for solar organic thermoelectric generators (SOTEGs). SOTEGs based on planar geometries were the focus of this part, but we briefly compared planar geometries to vertical geometries. Finally, we fabricate and characterize a proof-of-concept device incorporating a concentrating mirror.

In the second part of the thesis, the work focuses on investigating three different device geometries to couple an OSC to a thermoelectric generator (TEG), drawing upon experimental data from FTIR spectroscopy and IR thermography. When a semi-transparent organic solar cell is used in a hybrid device, the thermoelectric generator can make use of the heat generated by the solar cell and light transmitted by the solar cell. We observed that the PCE of a commercial OSC improved with temperature.

Motivated by the enhancement in PCE with temperature observed in the second part, we investigated the effect of temperature on OSC device performance via light-intensity- and temperature-dependent J-V characteristics in the last part of the thesis. The workhorse system investigated is PBDB-T:ITIC because of its excellent thermal stability. A high-

throughput fabrication technique, blade coating, was used to produce active layers with a variable thickness. For this and three other material systems, we observed that temperature significantly enhanced short-circuit current density (J_{SC}), Fill Factor (*FF*), and power conversion efficiency (PCE). Combining drift-diffusion simulations (carried out by a collaborator) with temperature-dependent space-charge limited current (SCLC) measurements, temperature-dependent external quantum efficiency (EQE) measurements and scattering techniques, namely GIWAXS and GISAXS, we demonstrate that the reversible enhancement in device performance arises as a result of thermally-activated charge transport in the device.

List of Abbreviations

AM0	Air mass zero spectrum
BHJ	Bulk heterojunction
Bi_2Te_3	Bismuth telluride
CNTs	Carbon nanotubes
DMSO	Dimethyl sulfoxide
EH-IDTBR	5,5'-[[4,4,9,9-tetrakis(2-ethylhexyl)-4,9-dihydro-s-indaceno[1,2-b:5,6-b']dithiophene-2,7-diyl]bis(2,1,3-benzothiadiazole-7,4-diylmethylidyne)]bis[3-ethyl-2-thioxo-4-thiazolidinone]
EQE	External quantum efficiency
ETL	Electron transport layer
F_4TCNQ	2,3,5,6-Tetrafluoro-7,7,8,8-tetracyanoquino-dimethane
FEM	Finite element method
FF	Fill factor
FTIR	Fourier-transform infrared spectroscopy
HOMO	Highest occupied molecular orbital
HTL	Hole transport layer
IR	Infrarred
ITIC	3,9-Bis(2-methylene-(3-(1,1-dicyanomethylene)-indanone))-5,5,11,11-tetrakis(4-hexylphenyl)-dithieno[2,3-d:2',3'-d']-s-indaceno[1,2-b:5,6-b']-dithiophene)
ITIC-4F	3,9-Bis(2-methylene-(3-(1,1-dicyanomethylene)-indanone))-5,5,11,11-tetrakis(4-hexylphenyl)-dithieno[2,3-d:2',3'-d']-s-indaceno[1,2-b:5,6-b']-dithiophene)
ITO	Indium tin oxide
J_0	Reverse saturation current density
J_{ph}	Photocurrent density
J_{SC}	Short circuit current density
LUMO	Lowest unoccupied molecular orbital
MEH-PPV	Poly[2-methoxy-5-(2'-ethylhexyloxy)-1,4-phenylene vinylene]
n	Ideality factor
N2200	Poly{[N,N′-bis(2-octyldodecyl)-naphthalene-1,4,5,8-bis(dicarboximide)-2,6-diyl]-alt-5,5′-(2,2′-bithiophene)}
NFA	Non-fullerene acceptor
Ni-btt	Poly(nickel-benzene-1,2,4,5-tetrakis(thiolate)

Ni-diett	Poly(nickel-[2,2′-bi(1,3-dithiolylidene)]-4,4′,5,5′-tetrakis(thiolate))
Ni-ett	Poly(nickel-ethylenetetrathiolate)
OMCP	Organometallic coordination polymers
OSC	Organic solar cell
OTE	Organic thermoelectric
OTEG	Organic thermoelectric generator
P3HT	Poly(3-hexylthiophene)
PAL	Photoactive layer
PANI	Polyaniline
PBDB-T/PCE12	Poly[(2,6-(4,8-bis(5-(2-ethylhexyl)thiophen-2-yl)-benzo[1,2-b:4,5-b′]dithiophene))-alt-(5,5-(1′,3′-di-2-thienyl-5′,7′-bis(2-ethylhexyl)benzo[1′,2′-c:4′,5′-c′]dithiophene-4,8-dione)]
PBDB-T-2Cl	Poly[(2,6-(4,8-bis(5-(2-ethylhexyl-3-chloro)thiophen-2-yl)-benzo[1,2-b:4,5-b’]dithiophene))-alt-(5,5-(1’,3’-di-2-thienyl-5’,7’-bis(2-ethylhexyl)benzo[1’,2’-c:4’,5’-c’]dithiophene-4,8-dione)]
PBDBT-T-2F/PCE13	Poly[(2,6-(4,8-bis(5-(2-ethylhexyl-3-fluoro)thiophen-2-yl)-benzo[1,2-b:4,5-b’]dithiophene))-alt-(5,5-(1’,3’-di-2-thienyl-5’,7’-bis(2-ethylhexyl)benzo[1’,2’-c:4’,5’-c’]dithiophene-4,8-dione)]
PBTTT-C_{14}	Poly[2,5-bis(3-tetradecylthiophen-2-yl)thieno[3,2-b]thiophene]
$PC_{61}BM$	[6,6]-Phenyl-C61-butyric acid methyl ester
$PC_{71}BM$	[6,6]-Phenyl-C71-butyric acid methyl ester
PCE	Power conversion efficiency
PCE11	Poly[(5,6-difluoro-2,1,3-benzothiadiazol-4,7-diyl)-alt-(3,3‴-di(2-octyldodecyl)-2,2′;5′,2″;5″,2‴-quaterthiophen-5,5‴-diyl)]
PEDOT	Poly(3,4-ethylenedioxythiophene)
PEDOT:PSS	Poly(3,4-ethylenedioxythiophene):poly(styrenesulfonate)
PEI	Polyethylenimine
PET	Polyethylene terephthalate
PFO	Poly(9,9-dioctylfluorene)
PFBT	Poly(9,9-dioctylfluorene-alt-benzothiadiazole)
PLA	Polyactic acid
PTB7-th/PCE10	Poly[4,8-bis(5-(2-ethylhexyl)thiophen-2-yl)benzo[1,2-b;4,5-b′]dithiophene-2,6-diyl-alt-(4-(2-ethylhexyl)-3-fluorothieno[3,4-b]thiophene-)-2-carboxylate-2-6-diyl)]
PV	Photovoltaic
PVDF	Polyvinylidene fluoride

R_s	Series resistance
R_{sh}	Shunt resistance
S	Seebeck coefficient
SCLC	Space charge limited current
SDBS	Sodium dodecylbenzenesulfonate
SOTEG	Solar organic thermoelectric generator
STEG	Solar thermoelectric generator
TE	Thermoelectric
TEG	Thermoelectric generator
TQ1	Poly[[2,3-bis(3-octyloxyphenyl)-5,8-quinoxalinediyl]-2,5-thiophenediyl]
UV	Ultraviolet
VIS	Visible
V_{OC}	Open-circuit voltate
Y6	2,2'-((2Z,2'Z)-((12,13-bis(2-ethylhexyl)-3,9-diundecyl-12,13-dihydro-[1,2,5]thiadiazolo[3,4-e]thieno[2",3'':4',5']thieno[2',3':4,5]pyrrolo[3,2-g]thieno[2',3':4,5]thieno[3,2-b]indole-2,10-diyl)bis(methanylylidene))bis(5,6-difluoro-3-oxo-2,3-dihydro-1H-indene-2,1-diylidene))dimalononitrile
ZnO	Zinc Oxide
σ	Electrical conductivity
ZT	Device figure-of-merit
zT	Material figure-of-merit
κ	Thermal conductivity

Table of Contents

List of Figures

List of Tables

Chapter 1. Introduction

1.1. Motivation

Society in the 21st century has been faced with the challenge of transitioning from fossil fuels to renewable energy to mitigate the effects of climate change and to ensure future energy security. At the center of this transition to clean energy are active solar energy conversion technologies, including photovoltaics (PV). The state-of-the-art photovoltaics, such as those made from silicon, have reported laboratory efficiencies of 26.7% [1]. However, they require high temperatures and vacuum conditions, implying long energy payback times and modest energy investments on return, and thick active layers (hundreds of microns) compared to other thin-film PV technologies (less than 5 microns for inorganics and less than 0.5 microns for organics). The importance of PVs will undoubtedly continue to grow in the years to come, but PVs must continually become more sustainable and more efficient before the clean energy transition can be fully realized.

Cost-effective and efficient devices can be achieved through a materials approach or a device approach. In a materials approach, a common method is to try to replace the traditional inorganic semiconductors (such as silicon, CIGS, CdTe, etc.) with materials such as kesterites, perovskites, quantum dots, or organic semiconductors. In this thesis, organic semiconductors are the main type of material investigated, but the reader can refer to in-depth reviews on kesterites, perovskites, and quantum dots [2]–[5]. Organic semiconductors possess characteristics that may lead to portable devices that are tuneable, lightweight, flexible and cheap. Devices based on organic materials are foreseen to complement devices based on inorganic materials, particularly in niche applications such as semitransparent windows, agrivoltaics, portable electronics, etc. Currently, the highest reported efficiency for organic solar cells (OSCs) is over 19%, which lags significantly behind the efficiency of silicon-based photovoltaics (PV) [6]–[8]. Apart from the low efficiencies, two other obstacles faced by OSCs are poor stability and up-scaling. Continued focus on these three weak points along with research on the fundamental material properties of organic semiconductors can unlock the full potential of organic photovoltaics.

In a device approach, PV can be combined with other conversion technologies to harness more of the Sun's energy. In the field of PV, tandem devices are commonly used to enhance

overall device efficiency by combining individual subcells targeting different regions of the solar spectrum. Solar cells are largely only able to harvest visible sunlight, while solar infrared heat (about 50% of energy emitted by the Sun) goes unused and, in the case of inorganic semiconductors, is even detrimental to device performance. Coupling PV with a technology capable of harvesting solar heat could further enhance device efficiency.

A promising heat-to-electricity conversion technology are thermoelectric generators (TEGs), which make use of the Seebeck effect. Organic materials, in addition to being compatible with inexpensive, scalable processing methods, would enable flexible energy generation. Similarly to the field of OSCs, there have been many breakthroughs in organic thermoelectrics (OTEs) since the field's inception, yet OTEs face the same three key challenges: poor material performance, poor stability, and up-scaling. Despite these obstacles, organic semiconductors could be promising materials for solar organic TEGs (SOTEGs) because of their ability to absorb and directly convert sunlight and infrared heat into electricity.

The purpose of this work is to investigate how OTEs can be best used to harvest the Sun's energy and explore possible geometries for SOTEGs and hybrid PV-TE devices. The worked carried out in this thesis leverages the group's extensive experience on the characterization and fabrication of both OSCs and organic TEGs (OTEGs).

1.2. Organic Semiconductors

Organic semiconductors are a class of materials that are comprised mainly of carbon and hydrogen atoms, and in lesser quantities, also oxygen, nitrogen and sulfur atoms. The semiconducting nature of these materials arises from the covalently-bonded carbon atoms, which comprise the molecular backbone. In semiconducting materials, the planar backbone contains alternating single and double or triple carbon-carbon bonds, also referred to as conjugation. In order for the carbon atoms to be in their lowest energy state, they will form three sp^2 hybridized orbitals and one unhybridized p-orbital (Figure 1-1). These orbitals form two types of bonds: σ-bonds and a π-bond. The sp^2 hybridized orbitals form stronger σ-bonds because they are in-plane with the nuclei, allowing for direct overlap of the orbitals between the two nuclei. The unhybridized p-orbitals are out-of-plane with the nuclei and overlap partially to form a weaker π-bond. The electrons that reside in the π-bond are delocalized and can move along the conjugated backbone.

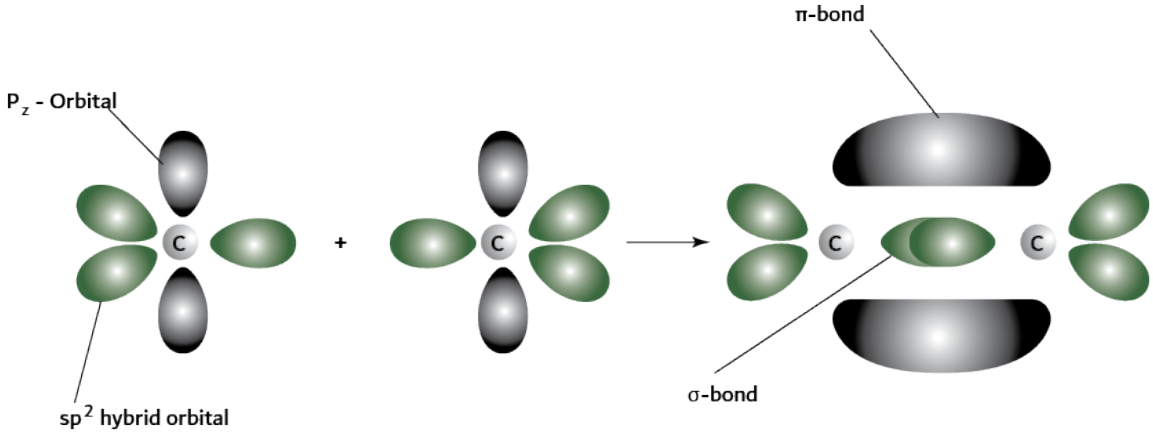

Figure 1.1. Scheme of covalent bonds between carbon atoms

When the two unhybridized p-orbitals combine to make the π-bond, they form a lower-energy bonding orbital (π) and a higher-energy anti-bonding orbital (π^*).

1.3. Solar Harvesting

Humanity as well as many forms of life on Earth owe our existence to the Sun, which allows plants to grow via photosynthesis and provides habitable conditions on Earth. Indirectly, the Sun's energy has been harvested through many products and phenomena derived from the Sun. The most common sources of energy, fossil fuels, are derivatives of Solar energy, as they are formed from the remains of dead animals and plants from millions of years ago. Wind energy also is a form of energy derived from the Sun, because the phenomena of wind comes as a result of the uneven heating of the Earth's surface and the Earth's rotation. Rain is another meteorological phenomenon caused by the Sun, which is necessary for hydroelectricity. Sunlight causes water to evaporate, and later this evaporated water is returned to dams and hydroelectric plants in the form of rain.

Today, a rapidly growing and increasingly important field of research is to harness the Sun's energy to directly generate electricity [9]–[11]. Sunlight in the ultraviolet and visible regions of the solar spectrum can be readily harvested by photovoltaics, a promising solar-to-electricity conversion technology that will be introduced in detail later on. For the infrared heat emitted by the sun, thermosolar energy technologies, such as solar thermoelectrics, can be used [12]–[15]. Solar thermoelectrics will be discussed in detail in chapter 3. In this section, the focus will be on the Sun's energy and the solar spectrum.

1.3.1. Solar Energy and the Solar Spectrum

The amount of energy available to Earth from the Sun dwarfs the amount of energy from nuclear and alternative renewable energy sources. According to Perez et. al., the Sun delivers 23,000 TW-year of energy per year, while the total recoverable reserves for coal and wind energy are 900 TW-year and 70-120 TW-year per year, respectively.

It has been estimated that the world consumed 14 TW-year of energy in 2018, according to data from the International Energy Agency [16]. This number is expected to increase significantly by 2050, with estimates topping 27TW-year per year by 2050 [17]. According to the International Energy Agency, solar energy accounted for only 0.4% of the energy consumed in 2018, while fossil fuels were the largest source of energy. As humanity becomes ever-more energy dependent, alternative sources of energy must be used to avoid depletion of the finite energy sources.

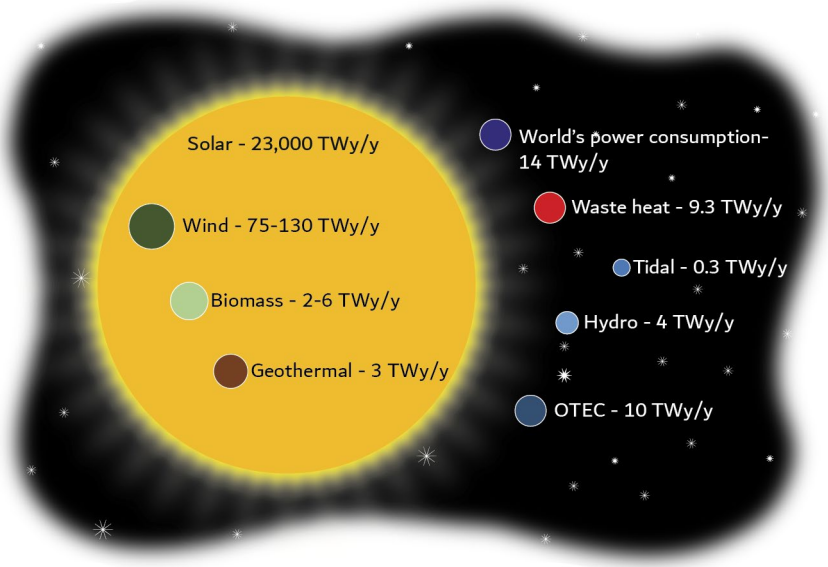

Figure 1-2. Estimate of energy reserves

The standard value of solar radiation outside the Earth's atmosphere is known as the air mass zero (AM 0) and has an integrated power density of 1,366 kW m^{-2}. Due to atmospheric absorption losses, the radiation at the Earth's surface is described by the air mass global standard (AM 1.5G) spectrum, which yields 1 kW m^{-2}. In reality, this value differs significantly across the globe due to the tilt of Earth's axis and differences in climatic conditions. The Sun emits energy across a broad region of the electromagnetic spectrum, but the three

relevant bands being the ultraviolet (UV), visible (VIS) and infrared (IR) domains (Figure 1-3). Solar radiation at the Earth's surface is comprised of 5% UV light (~280-400 nm), 43% VIS light (400-700 nm) and 52% IR radiation (700-3000 nm).

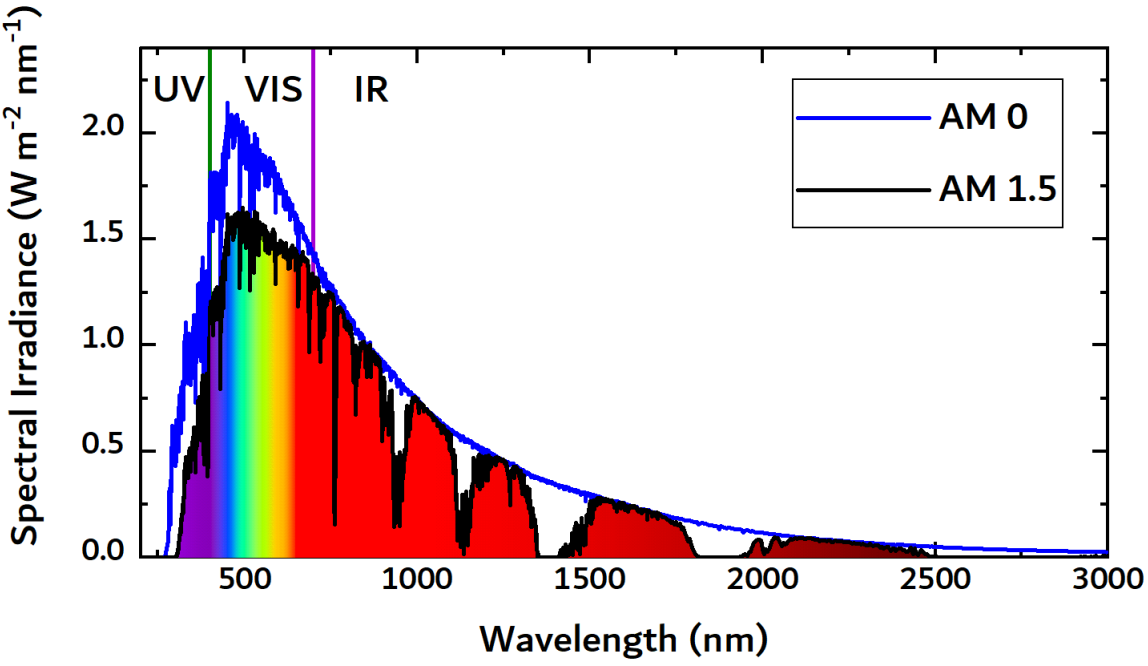

Figure 1-3. Spectral solar irradiance. The blue and black lines correspond to the AM 0 and AM 1.5G spectra, respectively

1.3.2. Solar Energy Conversion Technologies

At present, the two primary classes of solar energy conversion technologies are PV and solar thermal systems.

1.3.2.1. PV

PV devices directly convert sunlight into usable electricity. An incident photon with energy higher than the bandgap of the PV's active layer is absorbed, creating an electron-hole pair. The electron and hole are separated and collected at their respective electrodes to generate electricity. Ideally, a solar cell has both a small band gap to absorb more incident photons (a higher photocurrent density) as well as a high internal cell voltage. However, the band gap of a material is proportional to the cell's internal voltage. A PV material with a large bandgap is likely to have a high internal cell voltage, so a trade-off is therefore necessary. The optimal bandgap of a PV material is approximately 1.34 eV (~925 nm), leading to a

theoretical efficiency limit of 33.7% (Shockley-Queisser limit). Silicon has a bandgap of 1.12 eV and is the most common inorganic material used in commercial PV devices (such as the array of solar cells shown in Figure 1-4a). Commercial devices achieve efficiencies in the range of 18-22%. Laboratory device efficiencies over 25% for monocrystalline silicon cells and 20% for multicrystalline silicon cells have been reported [18].

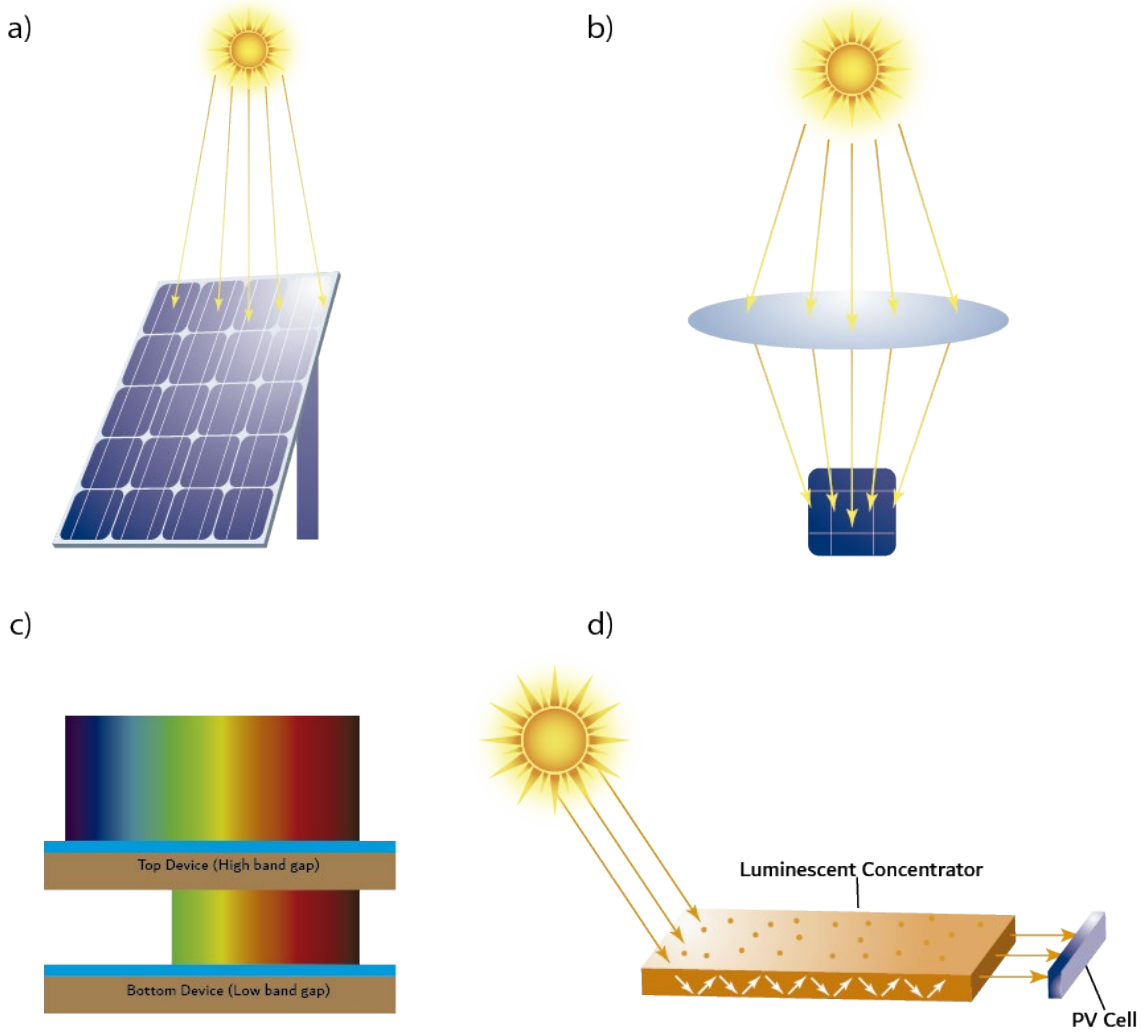

Figure 1-4. Solar energy conversion technologies: a) Array of solar cells; b) Example of a solar cell with concentrating optics; c) Tandem solar cell; d) Example of a luminescent concentrator with a solar cell

To overcome the output power limitation imposed by the Shockley-Queisser limit for single-junction solar cells, two approaches have been used: concentration and multijunction cells. In the first approach, sunlight is focused via mirrors or lenses onto the device causing the photocurrent to increase as a result of the higher photon flux and the cell's voltage to increase logarithmically (Figure 1-4b) [19]. It is important to note that only direct light can

be concentrated effectively, so the concentrators must track the Sun's position. Concentration can increase the working temperature of the cell, which is detrimental to efficiency for solar cells based on inorganic materials. A benefit to using concentration is that the size of the cell area can be reduced, thus cutting the costs associated with the cells in these systems.

Multijunction cells have emerged as another approach to achieve devices with higher power conversion efficiencies (PCE). In one type of multijunction cells, solar cells optimized for different parts of the solar spectrum are stacked atop each other to form a tandem cell (Figure 1-4c). Effectively, a tandem cell splits the solar spectrum in such a fashion that higher energy photons are absorbed by high bandgap solar cells at the front of the device and lower energy photons are absorbed by low bandgap solar cells at the back of the device. In principle, tandem cells can be comprised of an infinite number of subcells, however, from a cost point of view, the gain in PCE must outweigh the additional costs associated with fabrication of these complex devices. In the field of inorganics, much effort has been placed on fabricating tandem silicon/perovskite devices, with the highest reported PCE being 29.15% [20]. The highest PCEs reported for tandem organic solar cell are over 17% [21], [22]. Currently, multijunction solar cells made of III-V alloys have PCEs among the highest reported, with a 6-junction solar cell under 143 sun concentration exhibiting a PCE of 47.1% [23].

Apart from spectrum splitting, a different approach to solar harvesting are devices incorporating light manipulation elements. The mismatch between the energy of incident photons and the solar cell's bandgap is one of the largest loss mechanism in the energy conversion process, so manipulating incident sunlight may help boost PCE. Solar cells can manipulate light by incorporating luminescent concentrators, up- and down-converters, and thermal emitters. In one type of device, luminescent concentrators generally consist of an optically transparent polymeric matrix impregnated with luminophores (Figure 1-4d). Luminescent concentrators have a large face area filled with lumniphores used to capture Sunlight, either direct or diffuse, and these luminophores re-emit light at a lower wavelength close to the bandgap of the solar cell. The lumniphore emits light in random directions, but the light is guided to the solar cell through total internal reflection to the edge of the device, where a small-area solar cell can be placed. In this configuration, a large amount of Sunlight is effectively concentrated onto a small area, thus increasing the output power density compared to a solar cell without concentration.

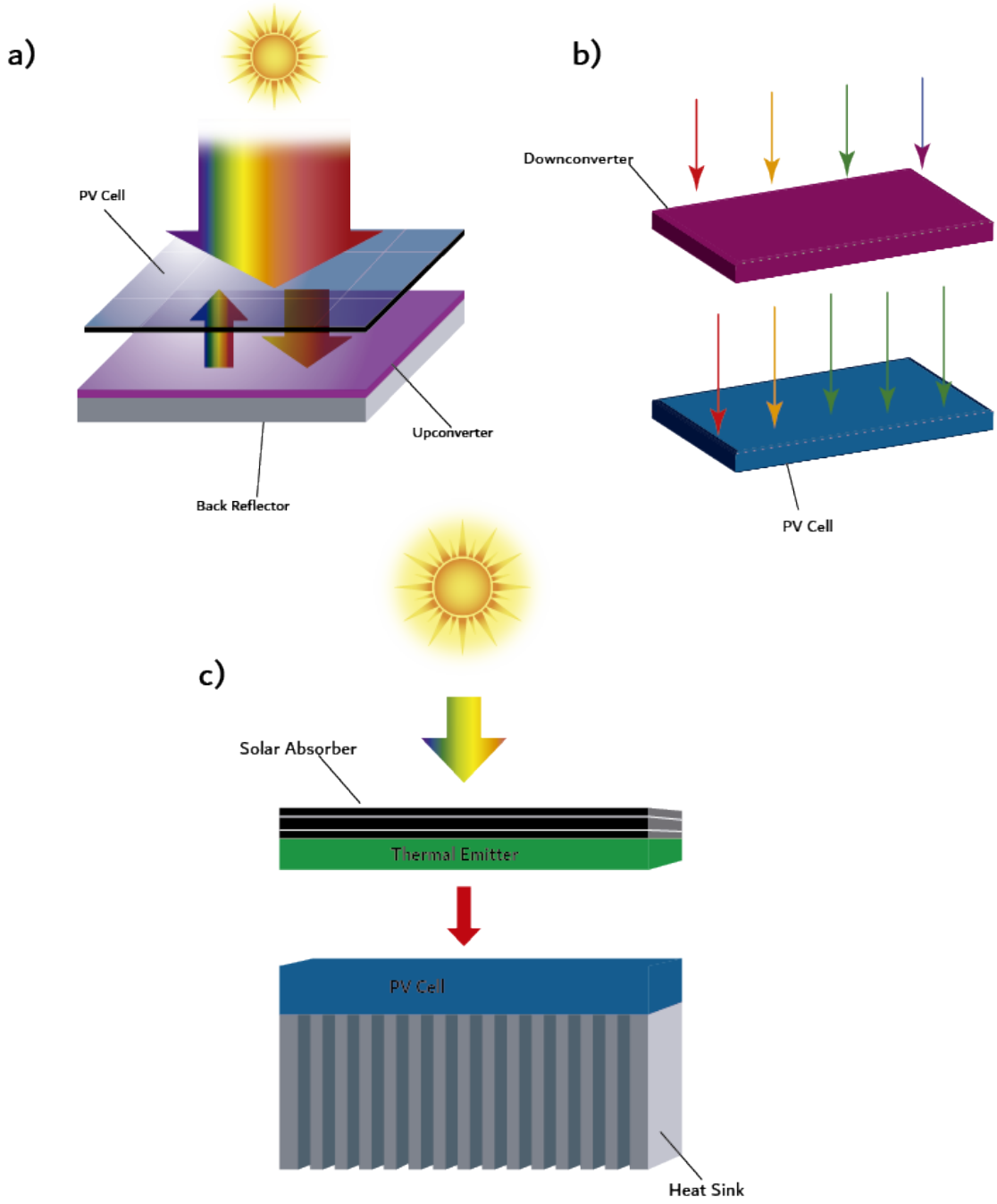

Figure 1-5. Solar cells with light managers: a) Schematic of a solar cell with an upconverter; b) Schematic of a downconverter with a solar cell; c) Schematic of a thermophotovoltaic device

Photon up-conversion is a process by which two low energy photons are combined into one high energy photon (Figure 1-5a). An up-converter with a bandgap similar to the solar cell is placed behind the solar cell to absorb photons with energy below the bandgap. Upon absorption of two or more of the sub-bandgap photons, an electron-hole pair is generated via a two-step process [24], [25]. The charge carriers are not collected, rather the electron-

hole pair recombines radiatively to emit a single higher-energy photon towards the solar cell. The energy of the emitted photon should be higher than the band gap of the solar cell's active layer. Conversely, photon down-conversion is a process by which one high energy photon (ideally with energy more than twice the bandgap of the solar cell) can be converted into two low energy photons (Figure 1-5b).

Thermophotovoltaic cells are another type of multijunction solar cell that incorporate a thermal emitter and sometimes, concentrating optics (Figure 1-5c). In this approach, the thermal emitter absorbs incident solar radiation and reemits thermal radiation with a narrow bandwidth towards the solar cell. Much effort has been focused on developing materials for the thermal emitter that have a selective emission spectrum, especially to suppress the emission of low-energy photons [26]. Thermophotovoltaic devices can also incorporate mirrors to recycle sub-bandgap photons. However, low bandgap cells are needed to maximize the output power density from the cell, which reduces the PCE of the device. The performance of low bandgap materials, especially organic materials, is hindered largely due to an increase in non-radiative recombination [27], [28].

1.3.2.2. Solar Thermal Systems

Solar thermal systems convert incident solar radiation into heat. Common to all of these systems is a selective absorber capable of absorbing both sunlight and infrared radiation, causing the temperature of the absorber to rise. The temperature rise will depend on its absorption and emission spectra, as well as system losses by conduction and convection. Concentration with mirrors or lenses can be used to further enhance the temperature of the absorber. Additionally, reasonably high temperatures can be readily achieved by limiting convection using vacuum insulation, for example.

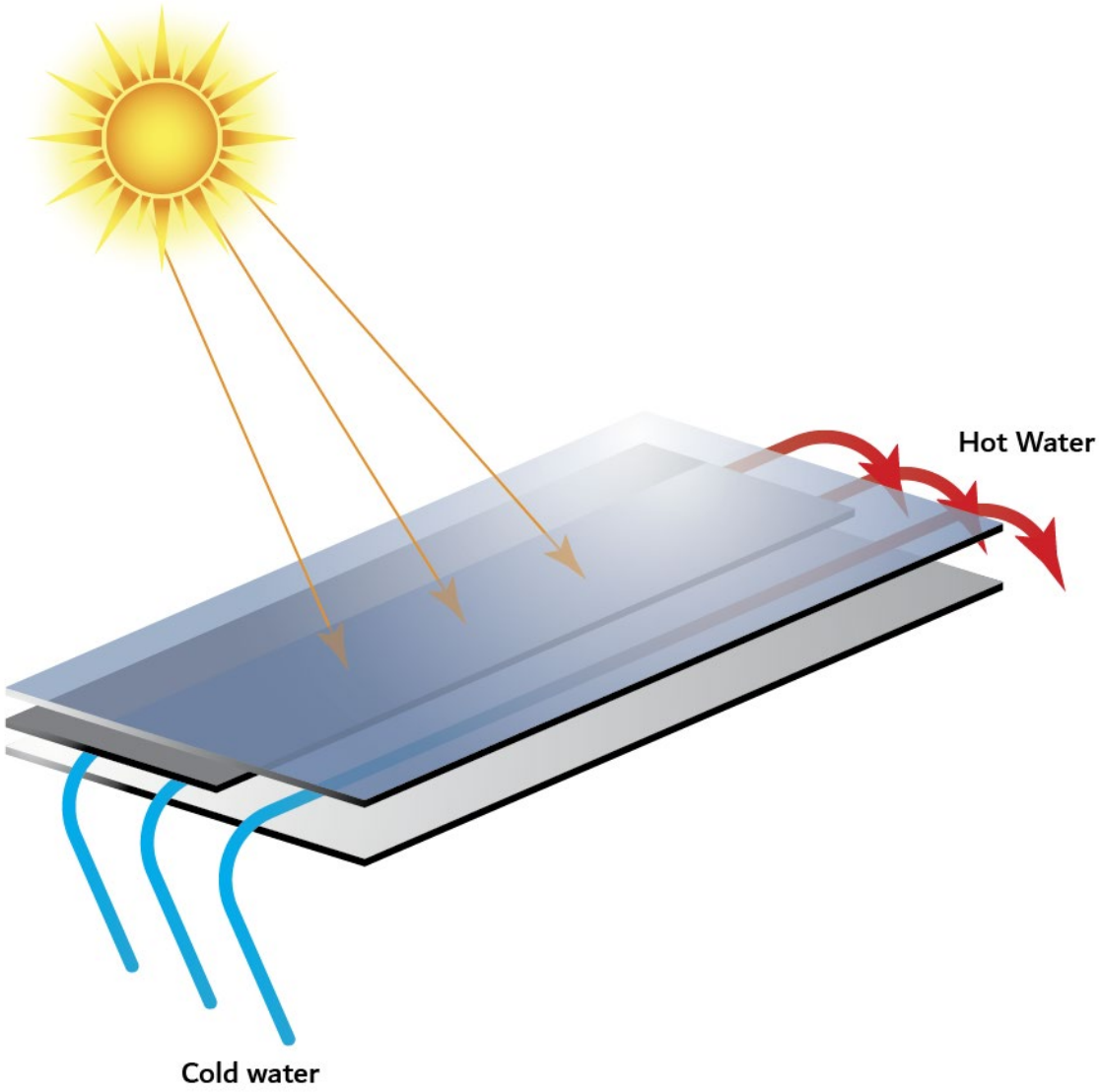

Figure 1-6. Flat plate solar thermal collector

The two most common applications for solar thermal systems are domestic water heating and electricity generation. Solar collectors for domestic water heating vary in complexity, but the design principle is the same. In the simplest device, a selective absorber, such as black paint, surrounds pipes through which a fluid flows, such as water. The absorber material absorbs the solar radiation, heating up the fluid passing through the pipes. In residential applications, flat plate collectors (Figure 1-6) and evacuated tube collectors are the most widely used systems.

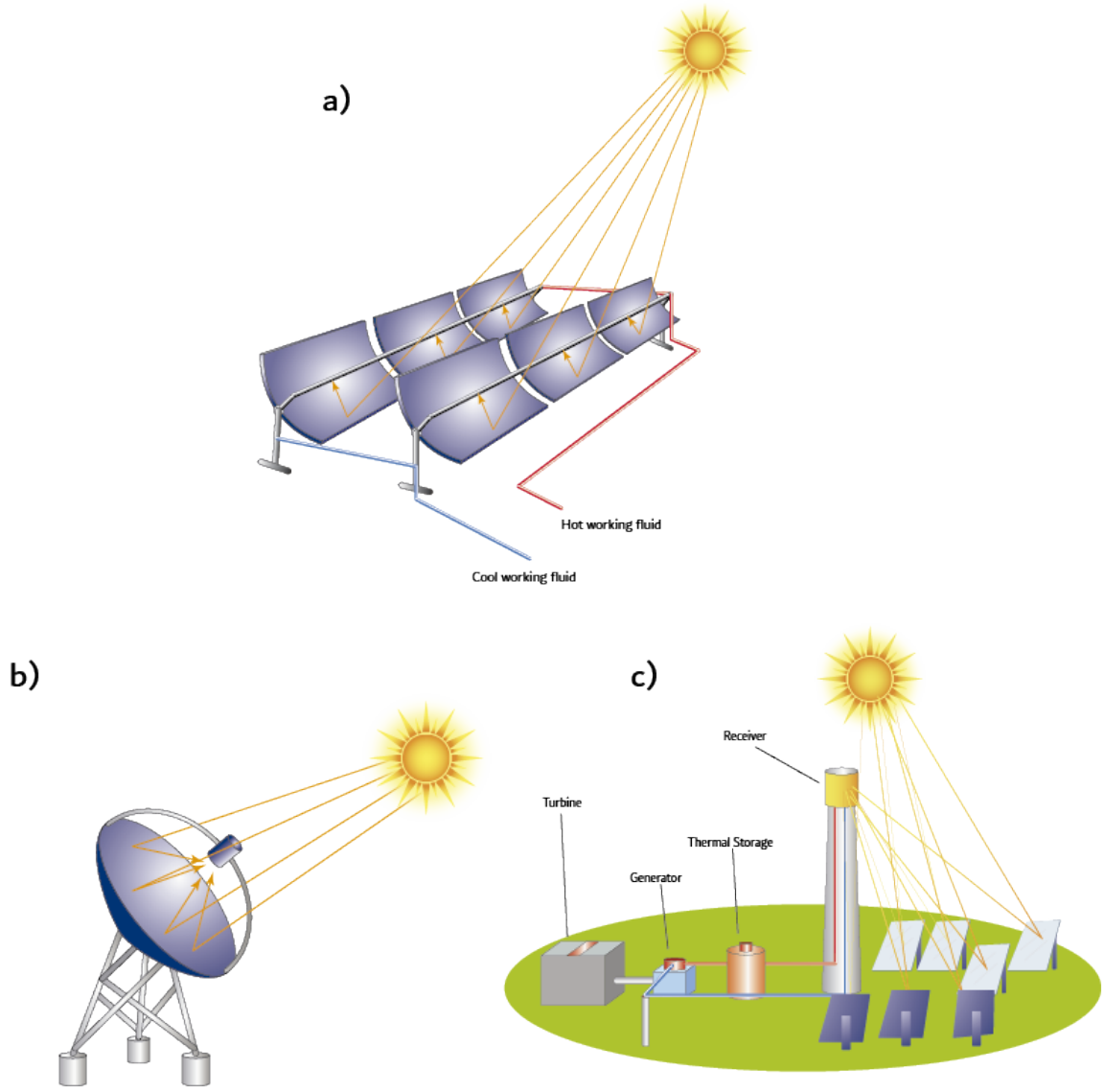

Figure 1-7. Solar thermal concentration systems: a) parabolic trough collector; b) parabolic dish with receiver; c) solar tower and example schematic of a concentrated solar power plant

For electricity generation, solar radiation is used to heat a heat transfer fluid, such as molten salt, which is pumped through heat exchangers to produce steam. The steam, in turn, drives a turbine, and the mechanical energy generated by the movement of the turbine is then converted into electricity via a generator. Heat energy is more efficiently converted to electricity at higher temperatures, so these systems are significantly more complex. They incorporate heliostats or concentrating optics to focus sunlight to achieve higher temperatures. Three types of solar thermal systems for electricity generation include parabolic troughs (Figure 1-7a), parabolic dishes (Figure 1-7b) and solar towers, such as those found in solar thermal plants (Figure 1-7c). Solar thermal power plants sometimes have a storage system for the heat transfer fluid, which is advantageous over other solar

conversion technologies. The storage system provides the plant with a degree of dispatchability, allowing excess energy to be stored until needed as sensible, latent, or chemical heat [29], [30].

1.4. Organic Solar cells

OSCs have emerged has a promising solar conversion technology, with reported efficiencies over 19% [6], [31]–[33]. The optical and electrical properties of organic materials can be readily tuned via modification of their chemical structure, unlike for their silicon counterparts. Additionally, OSCs are made from abundant materials and are solution processable. They can be deposited at low temperatures using high-throughput techniques, resulting in low-cost devices and devices with shorter energy payback times compared to silicon solar cells [34], [35]. Furthermore, OSCs can be flexible and lightweight because they incorporate thin layers [36]. The high absorption coefficients of organic materials allow for significant light absorption with thin films [37].

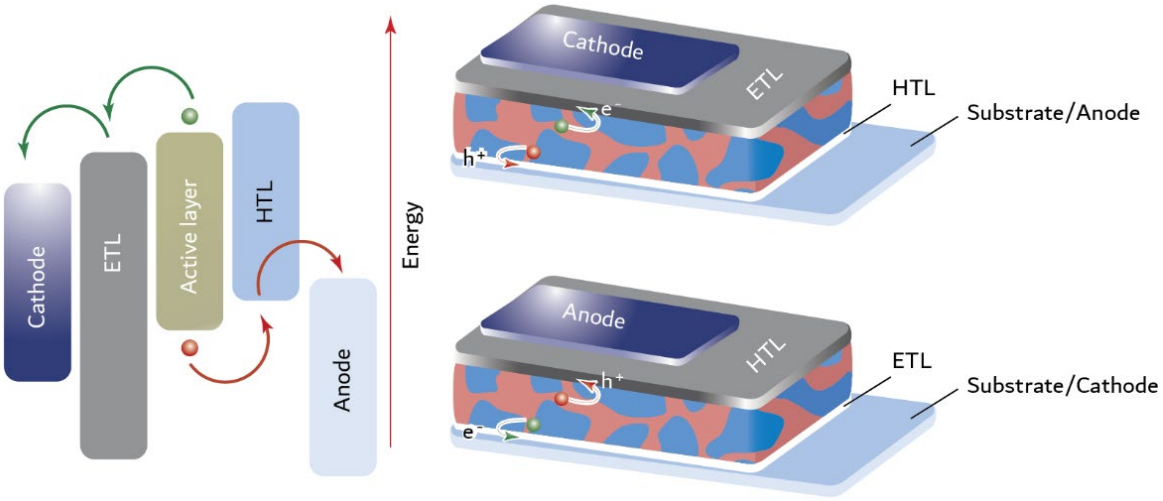

Figure 1-8. Left: Energy level diagram of the components in an organic solar cell. Right (top): device with a conventional geometry; Right (bottom): Device with an inverted geometry

An OSC is a multilayer stack of various thin films as seen in Figure 1-8 (right). The bulk heterojunction active layer consists of at least one electron donor and electron acceptor material and is sandwiched between the cathode and the anode. Donor materials used in OSCs are usually conjugated polymers, but recently some small molecule donors have shown efficiencies higher than 14% [38]. The electron acceptors have traditionally been fullerene derivatives, but much effort has been put into developing non-fullerene acceptor

materials to help improve OSC performance and stability [39]–[41]. To enhance contact selectivity, two interfacial layers, a hole transport layer (HTL) and an electron transport layer (ETL), are placed between the active layer and the two electrodes [42]. It is important to note that one of the electrodes must be transparent to allow light to penetrate into the active layer. The four fundamental steps in energy conversion in OSCs are described as follows: i) incident photon absorption and exciton formation, ii) exciton diffusion, transfer, and separation, iii) charge carrier transport, and iv) charge carrier extraction at the electrodes.

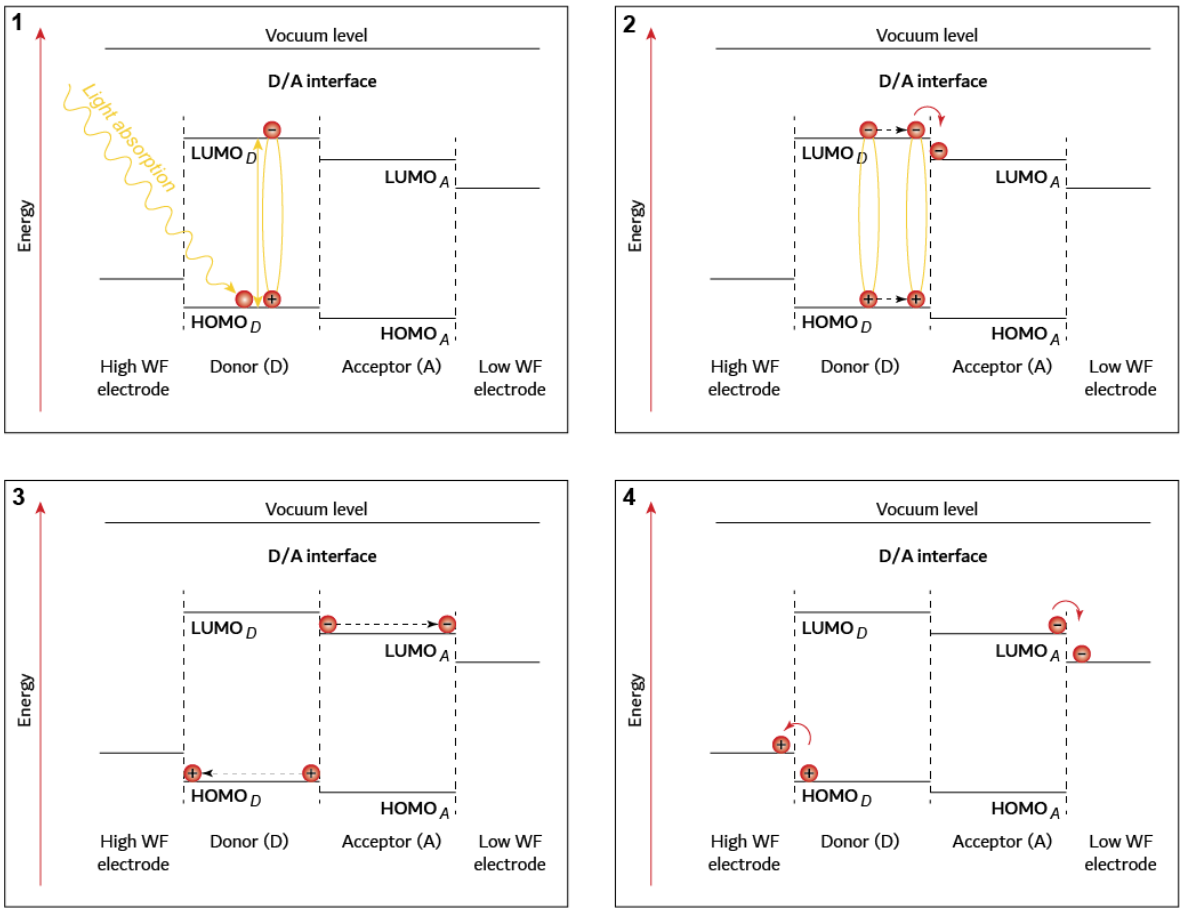

Figure 1-9. Working principles of an OSC. 1) Photon absorption and exciton formation; 2) exciton diffusion and separation; 3) charge carrier transport; 4) charge carrier extraction

1.4.1. Photon Absorption and Exciton Formation

In OSCs, the electron donor is usually the most strongly absorbing material, although state-of-the-art acceptor materials, namely non-fullerence acceptors (NFAs) also significantly contribute to light absorption. The amount of light absorbed depends on two key factors: the absorption coefficient of the donor(s) and acceptor(s) and film thickness.

The band gap of a material is given as the difference between the lowest unoccupied molecular orbital (LUMO) and the highest occupied molecular orbital (HOMO). An OSC can absorb light with energy equal to or greater than the band gap of the materials in the active layer. Unfortunately, the absorption bands of organic materials are much narrower than of inorganic materials, so only a small portion of the solar spectrum can be harvested. Designing materials with lower band gaps can be a strategy to harvest more sunlight.

Organic semiconductors possess high absorption coefficients, which allows for thin films to absorb a significant portion of incident sunlight. It is estimated that about 60% of incident sunlight can be absorbed within the first 100 nm of the active layer [43]. Silicon solar cells, in comparison, require thicknesses on the order of hundreds of micrometers to absorb light. While thicker layers generally enhance light absorption, they are in practice limited to ca. 100 nm due to the poor charge carrier mobilities in organic semiconductors.

Upon absorption, an electron is excited from the HOMO to the LUMO, leaving behind a positively-charged hole (Figure 1-9.1). Absorption mainly happens in the donor phase for fullerene-based OSCs, although, non-fullerene acceptors have been shown to absorb light efficiently [44], [45]. The excited electron and hole still exert Coulombic forces on each other and form an exciton.

1.4.2. Exciton Diffusion, Charge Transfer, and Separation

Because organic materials possess low dielectric constants, the Coulombic forces binding the hole and electron together in the exciton are large. In order to dissociate excitons into electrons and holes, the active layer in OSCs includes at least one donor and one acceptor. The energy offset in the LUMO levels of the donor and acceptor is larger than the Coulombic forces binding the charge carriers together, enabling exciton dissociation at the donor/acceptor interface. Alternatively, charge separation can happen via hole transfer between the HOMOs of the acceptor and donor if the energy offset of the HOMOs is sufficiently large [46].

The excitons must diffuse to the donor/acceptor interface for dissociation into free charges to occur. Excitons, due to their short lifetimes in conjugated polymers, have diffusion lengths less than 20 nm [47]. Therefore, it is critical to control the domain sizes of the donor and acceptor phases. Exciton generation must occur within the material’s diffusion lengths, or

the excitons will recombine. The process by which an exciton is formed is called geminate, or monomolecular, recombination [48], [49].

At the donor/acceptor interface, the energy level offset of the OSC can overcome the exciton binding force, resulting into two free charge carriers (Figure 1-9.2). The free electrons will move to the acceptor (the material with the deeper LUMO) and the holes will remain in the donor phase (the material with the shallower HOMO).

1.4.3. Charge Carrier Transport

After exciton dissociation, the free charge carriers must be transported to their respective electrodes via the percolated pathway in the bulk-heterojunction (BHJ) (Figure 1-9.3). The driving force for charge carrier transport is the internal electric field given by the difference in work functions of the two electrodes [50]. In organic semiconductors, the dominant charge transport mechanism is thermally-activated hopping. In contrast to inorganic semiconductors that can be nearly perfect crystals and exhibit delocalized band transport, organic semiconductors are more amorphous and transport occurs via hopping between localized electronic states [51].

Charge carrier mobility, greatly influenced by the degree of order present in the organic semiconductors, is an important parameter that governs charge transport and recombination. Recombination is one of the biggest loss mechanisms in solar cells, especially non-geminate recombination. Bimolecular recombination, a type of non-geminate recombination, occurs when two free charges of opposite sign meet and recombine. At low mobilities, bimolecular recombination increases. Additionally, recombination increases with thicker active layers, since the path length of charge carriers increases. Therefore, another critical design solar cell design parameter is the active layer thickness.

1.4.4. Charge Carrier Extraction

Charge extraction is the last step in the conversion process (Figure 1-9.4). Between the electrodes and the active layer, two interfacial layers are placed to ensure the formation of an ohmic contact and reduce series resistance and charge recombination. Essentially, the transport layers promote contact selectivity. They facilitate charge transport to the respective electrode (holes to the anode and electrons to the cathode) for collection while also serving the role of a blocking layer for charges of opposite sign.

1.4.5. Equivalent Circuit of OSCs

The equivalent circuit of an organic solar cell can be seen in Figure 1-10. It consists of a current source, diode and resistance connected in parallel; with a second resistance connected in series.

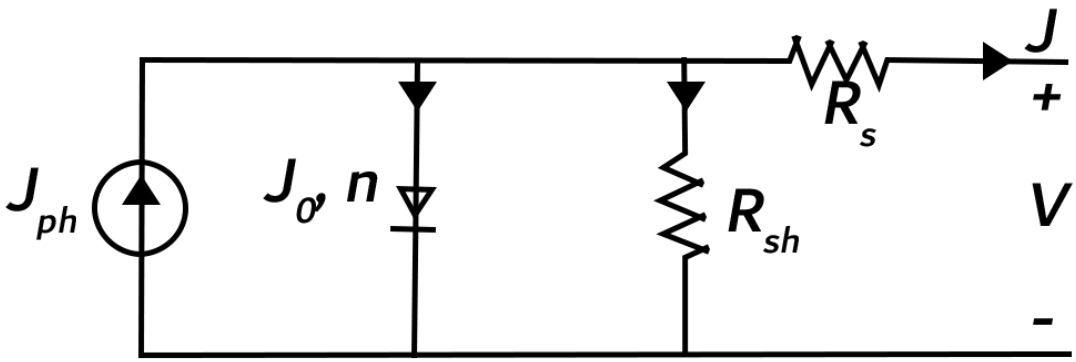

Figure 1-10. Equivalent circuit of a solar cell

In the circuit, J_{ph} is the photocurrent generated in the solar cell under illumination. The photocurrent will depend on the incident light spectrum and intensity, and without illumination, this term will be zero. In parallel to the current source, a diode with an ideality factor of *n* and reverse saturation current, J_0, is connected. Ideality factors greater than one can be attributed to recombination of excitons at the donor-acceptor interface [52]. The series resistance, R_s, arises from resistances of the different layers in the solar cell stack and the resistances between each of their interfaces. The parallel resistance (shunt), R_{sh}, represents leakage currents from pinholes and recombination, for example. Ideally, a solar cell should exhibit a high shunt resistance to prevent an alternative path for the photogenerated current and a low series resistance to prevent power losses limiting the current in the device.

From the equivalent circuit, the J-V characteristic of the solar cell can be modeled by the following equation [53]:

Equation 1.1: $$J = J_0 \left\{ \exp\left[\frac{q(V - A\,J\,R_s)}{n\,k_B\,T}\right] - 1 \right\} + \frac{V - A\,J\,R_s}{R_p} - J_{ph}$$

where k_B is the Boltzmann's constant, q is the elementary charge, T is the temperature of the solar cell, and A is the area of the device. The influence of shunt and series resistances on the J-V characteristic of the solar cell is shown in Figure 1-11.

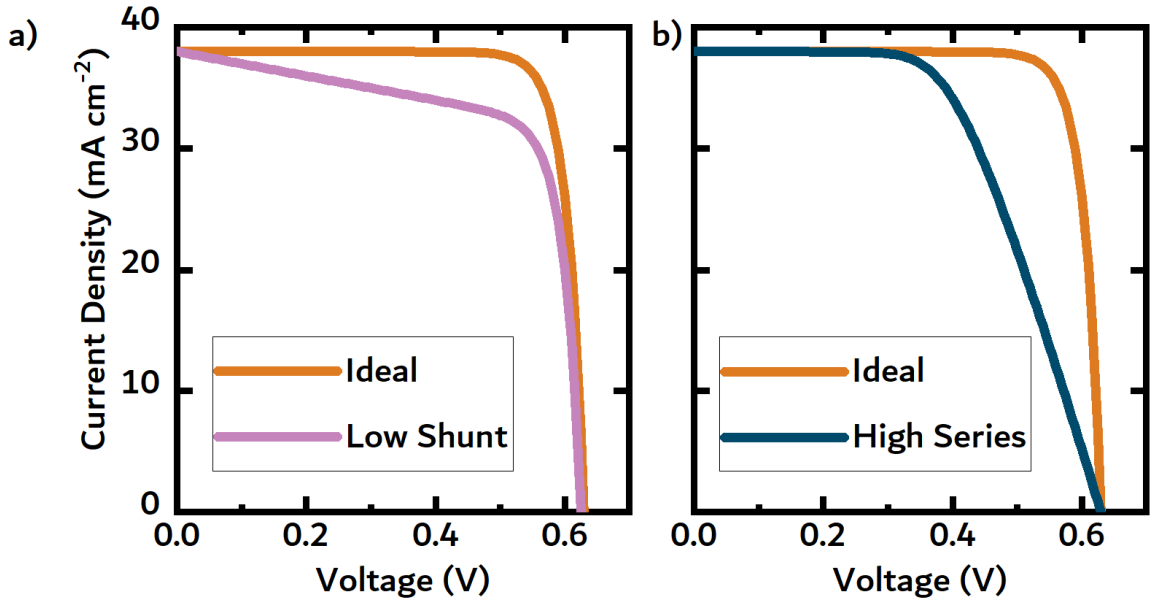

Figure 1-11. The effects of a) low shunt resistance and b) high series resistance on the J-V characteristic of a solar cell.

1.4.6. PV Parameters

The four main parameters of OSCs are the short-circuit current density, J_{SC}, open-circuit voltage, V_{OC}, the fill factor, FF, and power conversion efficiency, PCE. These parameters can be derived from the J-V curve of an OSC, as shown in Figure 1-12.

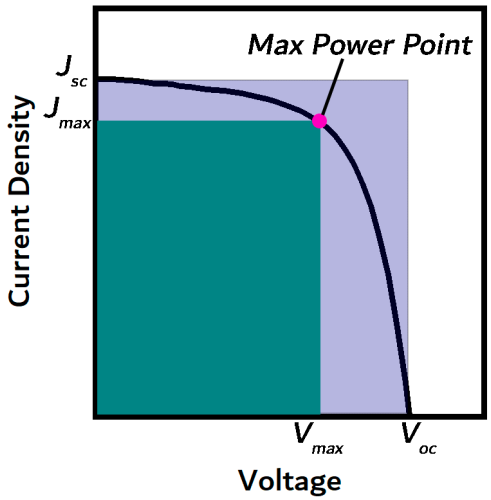

Figure 1-12. J-V Curve of a solar cell

The short-circuit current, where V = 0 V, and open-circuit voltage, where J = 0 mA/cm^2 can be determined from equation 1.1 assuming that the shunt resistance is sufficiently high, series resistance is small, and J_{SC}/J_0 >> 1. With these assumptions, J_{SC} and V_{OC} can be given as:

Equation 1.2: $$J \approx -J_{ph}$$

Equation 1.3: $$V_{oc} \approx \frac{nk_BT}{q} \ln(\frac{J_{ph}}{J_0} + 1)$$

The PCE of a solar cell is defined as the ratio of the electrical power density output by the solar cell to the power density of incident light, P_{in}, on the solar cell:

Equation 1.4: $$\eta = \frac{J_{max}V_{max}}{P_{in}} = FF\frac{J_{sc}V_{oc}}{P_{in}}$$

where $J_{max}V_{max}$ is the maximum power density of solar cell and *FF* is given as:

Equation 1.5: $$FF = \frac{J_{max}V_{max}}{J_{SC}V_{OC}}$$

The *FF* is a measure of how well photogenerated charge carriers are extracted from the device as compared to an ideal solar cell and can be visualized as the 'squareness' of the J-V curve. Charge carrier mobility, parasitic resistances and recombination strongly influence a solar cell's *FF*. Typically, good solar cells have *FF*s higher than 60%. Lin et. al. reported a ternary OSC with a PCE of 18.4%, a *FF* of 78.6%, a J_{SC} of 27.10 mA cm^{-2}, and a V_{OC} of 0.864 V [32].

1.4.7. Organic Photovoltaic Materials

The photoactive layer of state-of-the-art organic solar cells are made up of at least one donor and at least one acceptor material blended together into a bulk heterojunction film. For the donor materials, π-conjugated polymers are typically used. In this thesis, the donor materials studied were poly(3-hexylthiophene) (P3HT), Poly[2-methoxy-5-(2-ethylhexyloxy)-1,4-phenylenevinylene] (MEH-PPV), poly[(2,6-(4,8-bis(5-(2-ethylhexyl)thiophen-2-yl)-benzo[1,2-b:4,5-b′]dithiophene))-alt-(5,5-(1′,3′-di-2-thienyl-5′,7′-bis(2-ethylhexyl)benzo[1′,2′-c:4′,5′-c′]dithiophene-4,8-dione)] (PBDB-T or PCE12), and poly[(2,6-(4,8-bis(5-(2-ethylhexyl-3-fluoro)thiophen-2-yl)-benzo[1,2-b:4,5-b′]dithiophene))-

alt-(5,5-(1′,3′-di-2-thienyl-5′,7′-bis(2-ethylhexyl)benzo[1′,2′-c:4′,5′-c′]dithiophene-4,8-dione)] (PBDBT-T-2F or PCE13) were purchased from 1-material. Poly[[2,3-bis(3-octyloxyphenyl)-5,8-quinoxalinediyl]-2,5-thiophenediyl] (TQ1), poly[4,8-bis(5-(2-ethylhexyl)thiophen-2-yl)benzo[1,2-b;4,5-b′]dithiophene-2,6-diyl-alt-(4-(2-ethylhexyl)-3-fluorothieno[3,4-b]thiophene-)-2-carboxylate-2-6-diyl)] (PTB7-Th or PCE10), poly[(5,6-difluoro-2,1,3-benzothiadiazol-4,7-diyl)-alt-(3,3‴-di(2-octyldodecyl)-2,2′;5′,2″;5″,2‴-quaterthiophen-5,5‴-diyl)] (PffBT4T-2OD or PCE11), and Poly[(2,6-(4,8-bis(5-(2-ethylhexyl-3-chloro)thiophen-2-yl)-benzo[1,2-b:4,5-b']dithiophene))-alt-(5,5-(1',3'-di-2-thienyl-5',7'-bis(2-ethylhexyl)benzo[1',2'-c:4',5'-c']dithiophene-4,8-dione)] (PBDB-T-2Cl or PM7). The structures for some of these donor materials can be seen in Figure 1-13.

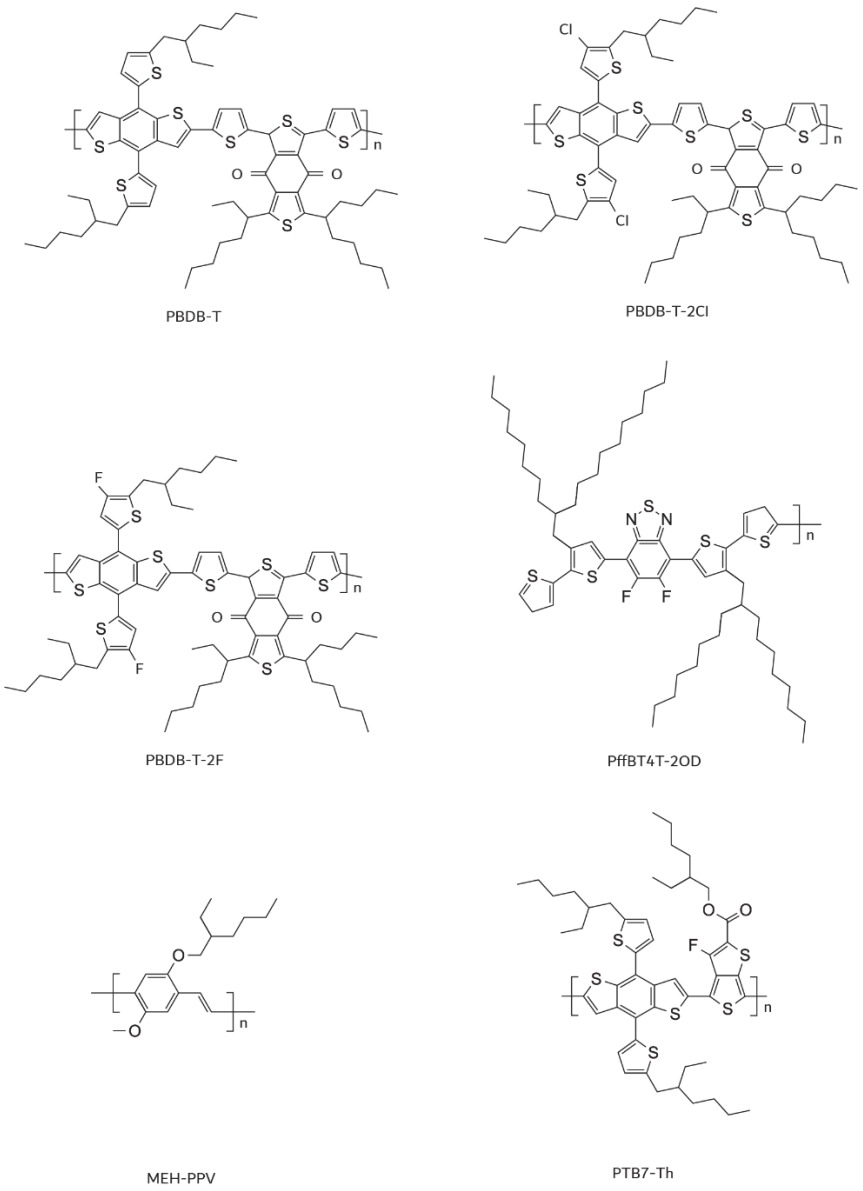

Figure 1-13. Chemical structures of PBDB-T, PBDB-T-2Cl, PBDB-T-2F, PffBT4T-2OD, MEH-PPV, and PTB7-Th

In the inception of organic solar cells, the most commonly used acceptor materials were fullerene derivatives, including [6,6]-Phenyl-C61-butyric acid methyl ester ($PC_{61}BM$) and $PC_{71}BM$ (contains a C_{70} core as opposed to a C_{60} core). However, fullerenes have a number of inherent limitations that hinder performance in an organic solar cell. The energy levels of fullerene derivatives are difficult to alter, they exhibit poor light absorption in the visible and NIR regions, and they suffer from poor thermal stability [40]. Therefore, much work focused on non-fullerene acceptor materials, namely small molecule acceptors, to overcome the shortcomings of fullerene acceptors [39]. In this thesis, apart from $PC_{71}BM$, the acceptor materials investigated were 5,5'-[[4,4,9,9-tetrakis(2-ethylhexyl)-4,9-dihydro-s-indaceno[1,2-b:5,6-b']dithiophene-2,7-diyl]bis(2,1,3-benzothiadiazole-7,4-diylmethylidyne)]bis[3-ethyl-2-thioxo-4-thiazolidinone] (EH-IDTBR), Poly{[N,N′-bis(2-octyldodecyl)-naphthalene-1,4,5,8-bis(dicarboximide)-2,6-diyl]-alt-5,5′-(2,2′-bithiophene)} (N2200), 3,9-bis(2-methylene-(3-(1,1-dicyanomethylene)-indanone))-5,5,11,11-tetrakis(4-hexylphenyl)-dithieno[2,3-d:2’,3’-d’]-s-indaceno[1,2-b:5,6-b’]dithiophene (ITIC), 2,2'-((2Z,2'Z)-((12,13-bis(2-ethylhexyl)-3,9-diundecyl-12,13-dihydro-[1,2,5]thiadiazolo[3,4-e]thieno[2",3’':4’,5']thieno[2',3':4,5]pyrrolo[3,2-g]thieno[2',3':4,5]thieno[3,2-b]indole-2,10-diyl)bis(methanylylidene))bis(5,6-difluoro-3-oxo-2,3-dihydro-1H-indene-2,1-diylidene))dimalononitrile (Y6), and 2-[(2E)-2-[[20-[(Z)-[1-(dicyanomethylidene)-5,6-difluoro-3-oxoinden-2-ylidene]methyl]-12,12,24,24-tetrakis(4-hexylphenyl)-5,9,17,21-tetrathiaheptacyclo[13.9.0.03,13.04,11.06,10.016,23.018,22]tetracosa-1(15),2,4(11),6(10),7,13,16(23),18(22),19-nonaen-8-yl]methylidene]-5,6-difluoro-3-oxoinden-1-ylidene]propanedinitrile (ITIC-4F). The structures for these acceptor materials can be seen in Figure 1-14.

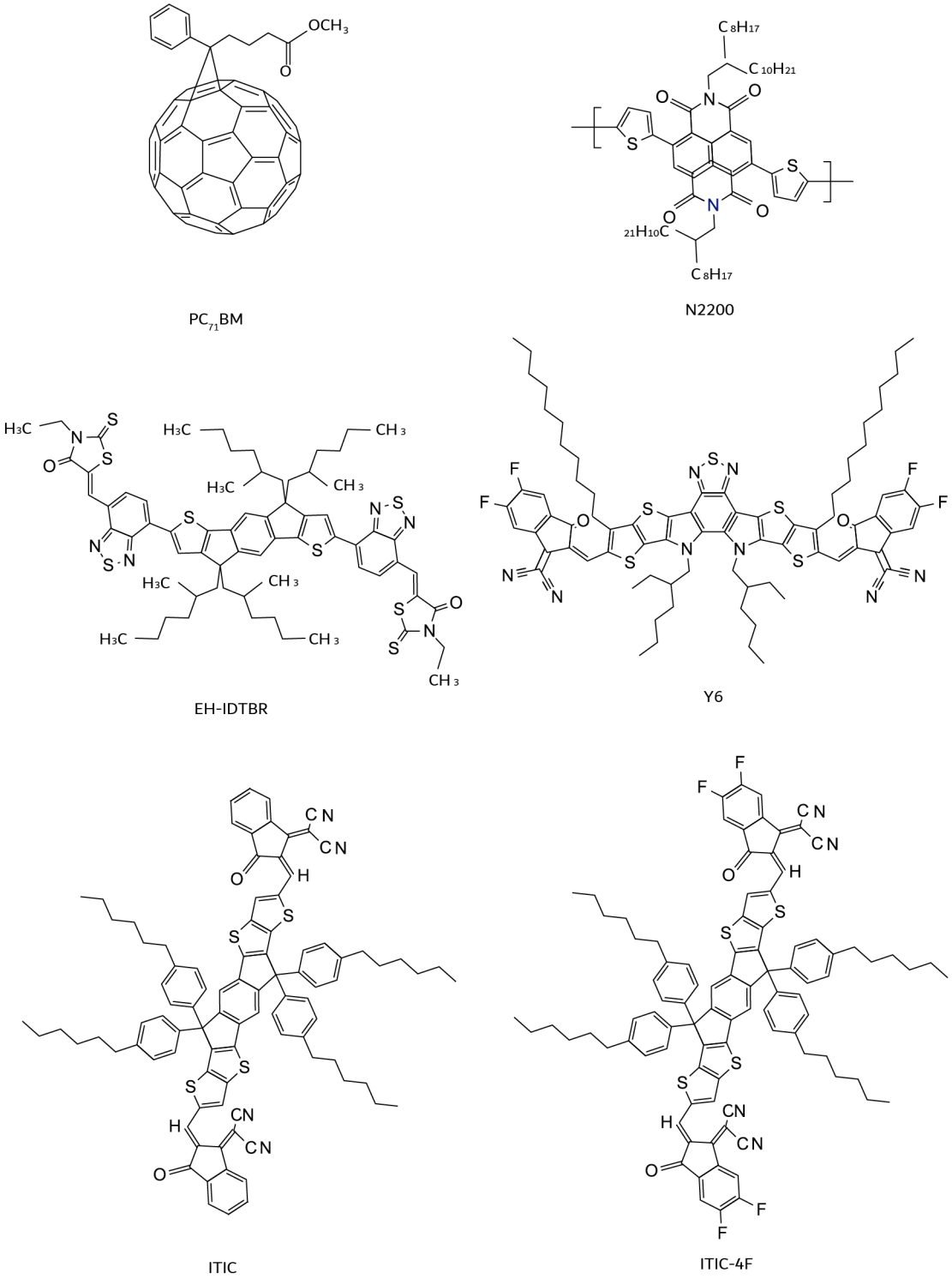

Figure 1-14. Chemical structures for N2200, EH-IDTBR, ITIC, ITIC-4F, PC71BM and Y6

1.5. Thermoelectricity

Thermoelectricity is the phenomenon by which thermal energy is converted directly into electricity, and vice versa. The two effects associated with thermoelectricity are the Seebeck and Peltier effects, which are two manifestations of the same physical process. More precisely, a temperature difference across two ends of a material can be converted into an electric potential via the Seebeck effect (Figure 1-15a). Conversely, an electric potential can be converted into a temperature difference via the Peltier effect (Figure 1-15b). In this thesis, the thermoelectric effect is used in the context of electricity generation, so the emphasis of this section will be on the Seebeck effect, as opposed to the Peltier effect, which is generally discussed in the context of thermoelectric cooling. For discussion on thermoelectric cooling, the reader is referred to a review from Zhao et. al. [54].

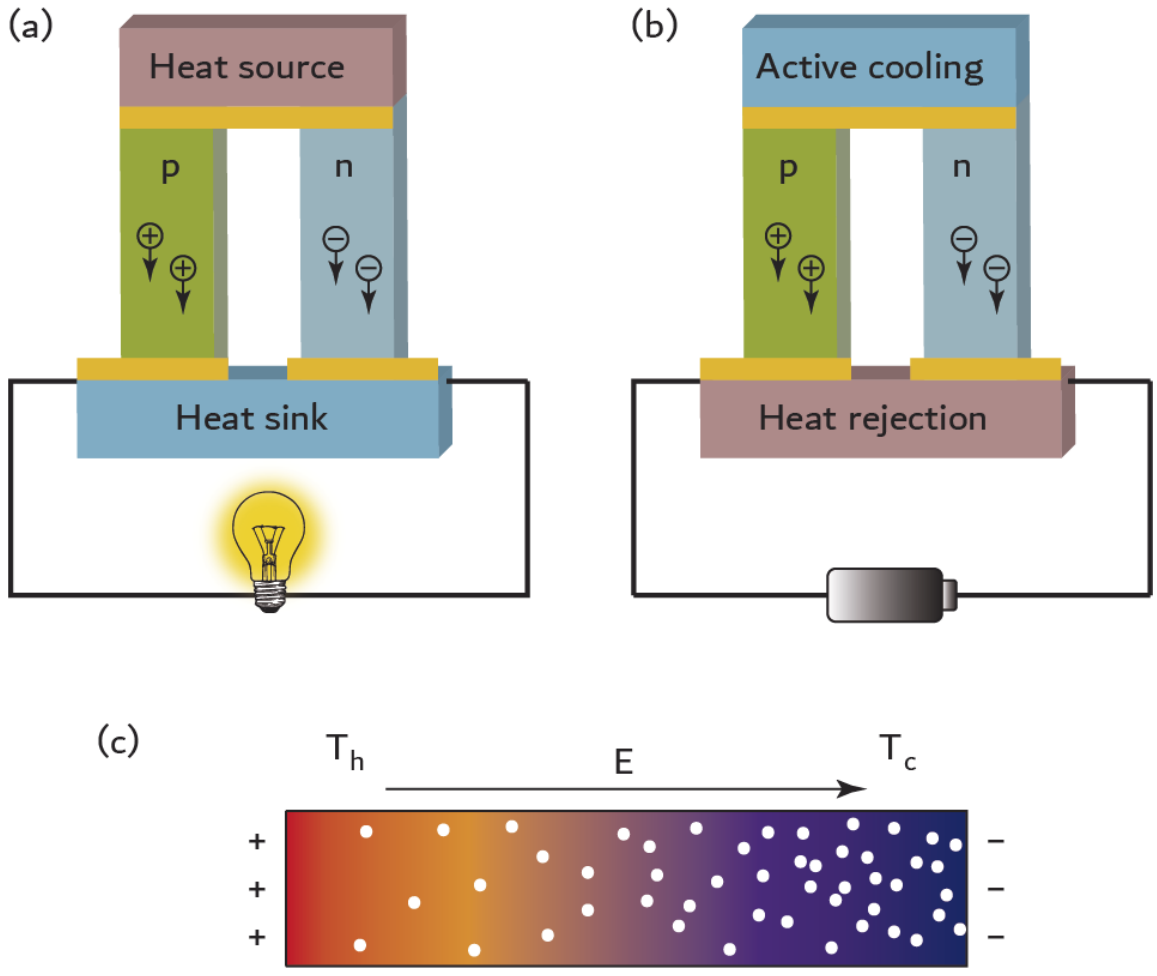

Figure 1-15. Schematic of the TE effect. a) Heat can be converted into electricity via the Seebeck effect; b) Applying a current results in a temperature gradient across the two ends of the thermoelectric device; c) Diffusion of charge carriers and generation of an electric potential as a result of the temperature difference across the thermoelectric material

On the atomic scale, when a temperature gradient is applied across a thermoelectric material, the charge carriers on the hot side possess a higher kinetic energy than those on the cold side, so overall, more hot charge carriers diffuse to the cold side of the device than vice versa (Figure 1-15c). This net migration of charge carriers to the cold side will cause an accumulation of charge on one side and lead to the generation of an electric field across the material. This phenomenon is denominated the Seebeck effect.

1.5.1. TE Parameters

The three main TE parameters are the Seebeck coefficient, electrical conductivity, and thermal conductivity and are influenced by temperature and energetic factors. Good thermoelectric materials exhibit high electrical conductivities and high Seebeck coefficients, while possessing low thermal conductivities. The main approach in the field of organic thermoelectrics is to design a material with a phonon-glass electron-crystal behavior. In this thesis, models such as the Drude model or the Boltzmann transport equation that can be used to predict TE parameters and describe the charge transport in a system will not be discussed in depth. Background information about these models can be found in: [55]–[57].

The Seebeck coefficient is a measure of the induced thermopower across a material in response to a temperature differential, and is defined from a phenomenological point of view as:

Equation 1.6: $$S = \frac{\Delta V}{\Delta T}$$

where ΔT is the temperature difference across the material and ΔV is the electrical potential across the material. TE materials can be p-type, where the majority carriers are holes, or n-type, where the majority carriers are electrons, and the sign of the Seebeck coefficient reflects the majority carriers present in the material. Seebeck coefficients less than zero corresponds to n-type materials while positive Seebeck coefficients correspond to p-type materials.

A generalized physical model of the Seebeck effect was given by Fritzsche [58]:

Equation 1.7: $$S = -\frac{k_B}{q}\int\left(\frac{E-E_F}{k_B T}\right)\frac{\sigma(E)}{\sigma}dE$$

where q is the elementary charge, $E - E_F$ is the energy carried by charge carriers relative to the Fermi energy, and $\sigma(E)$ is the energy dependence of conductivity, or conductivity density of states. In short, S describes the entropy transported per charge within a material and can be calculated in different ways depending on the type of charge carrier transport. Charge transport can occur through wide bands (metallic behavior), narrow bands (heavily doped semiconductors) and localized (disordered) states (organic semiconductors). In this generalized model of the Seebeck effect, the correlation between S and σ can be clearly seen.

The electrical conductivity describes the ability of electrical currents to flow through a material when subject to an electric field, *E*, and is given by Ohm's law:

Equation 1.8: $$J = \sigma E$$

For organic semiconductors, the electrical conductivity is enhanced with increasing temperature since the dominant charge transport mechanism is thermally-activated hopping. In the case of metals, an increase in temperature causes the number of scattering events to increase, thus hampering electrical conductivity.

Typically, the model used to describe charge transport is given as:

Equation 1.9: $$\sigma = \mu(T)\, e\, n(T)$$

where μ is the charge carrier mobility and n is the free carrier concentration. The Drude model works well to describe charge transport in metals, but not in heavily doped semiconductors. Semiclassical band transport theory, *i.e.* the Boltzmann transport equation, taking into account Fermi-Dirac statistics must be used to more accurately describe band transport in disordered systems.

The electrical conductivity in semiconductors can be improved by enhancing charge carrier mobility or increasing the charge carrier density. Mobility in organic semiconductors is related to their molecular and crystal structure and is mainly limited by disorder and defects [59]. While crystalline domains are present in the materials, they are discontinuous and the grain boundaries between domains hinder charge transport. Therefore, tuning domain size and crystallinity may help enhance mobility, and thus electrical conductivity. Alternatively,

increasing free charge carrier concentration via doping can improve the electrical conductivity.

The thermal conductivity of a semiconductors is the sum of the lattice, $\kappa_{Lattice}$, and electronic contributions, $\kappa_{electron}$, given as:

Equation 1.10: $$\kappa = \kappa_{Lattice} + \kappa_{electron}$$

Electrons transport heat in addition to charge and thus contribute to a material's thermal conductivity. For metals and highly doped semiconductors, the Wiedemann-Franz law states that $\kappa_{electron}$ is proportional to the electrical conductivity [60], [61]. For organic semiconductors, the relation between these two parameters is less clear [62].

For conducting polymers, the thermal conductivity is dominated by the lattice vibrations (phonon transport). As a result, organic materials typically possess thermal conductivities lower than 1 W m^{-1} K^{-1} compared to inorganic materials, with thermal conductivities on the order of 10-100 W m^{-1} K^{-1} [63], [64]. However, increasing crystallinity in conducting polymers may enhance thermal conductivity [65]. Additionally, chains of conducting polymers may be oriented during fabrication, resulting in anisotropic thermal and electrical conductivities.

To benchmark the performance of TE materials, the dimensionless figure-of-merit, ***zT***, is given as:

Equation 1.11: $$zT = \frac{S^2\sigma}{\kappa}T$$

where T is the average absolute temperature of the material. Wang et. al. reported a zT of 0.5 for a composite material of poly(3,4-ethylenedioxythiophene):poly(styrenesulfonate) (PEDOT:PSS) and single-wall carbon nanotubes near room temperature, the highest reported zT for organic TE materials. Thermoelectric skutterudites have reported ***zT***s higher than 1 at room temperature, while room temperature ***zT***s for bismuth telluride (Bi_2Te_3) are around 1 [66]–[69]. The task of achieving high zTs is quite challenging because the three parameters are coupled, such that optimization of one parameter usually adversely affects another. Therefore, much effort on improving zTs of organic TE materials has been focused on decoupling the three TE parameters via doping techniques or improving crystallinity [70].

1.5.2. Seebeck coefficient, electrical conductivity, and zT

In organic thermoelectrics, the power factor, $S^2\sigma$, is often used as opposed to the zT because of the intrinsically low thermal conductivites of organic materials and the difficulties associated with thermal conductivity measurements. The Seebeck coefficient and electrical conductivity are measured in-plane, while the thermal conductivity is most easily measured out-of-plane. In samples with high levels of anisotropy, significant differences in thermal conductivities have been reported [71], [72]. Conjugated polymers tend to be oriented in-plane, so in-plane thermal conductivity measurements are critical to report accurate zTs.

Thermoelectric generators (TEGs) are composed of alternating n- and p-type legs connected electrically in series and thermally in parallel. The output voltage of a TEG is given by [73]:

Equation 1.12: $$V_{out} = NS_{TEG}(T_h - T_c)$$

where N is the number of pairs of n- and p-type legs, S_{TEG} is the average Seebeck coefficient of the TEG, T_h is the hot side temperature and T_c is the cold side temperature. If the TEG is connected to an external load, the output power from the TEG is given by:

Equation 1.13: $$P_{TEG} = \frac{V_{out}^2}{(R_L + R_{TEG})} R_L$$

where R_{TEG} is the internal resistance of the TEG and R_L is the resistance of the load. While there has been some debate in literature, Baranowski et. al. demonstrated that the power output from a TEG is maximum when [74]:

Equation 1.14: $$\frac{R_L}{R_{TEG}} = \sqrt{1 + ZT}$$

The efficiency of a TEG can be calculated with the following equation:

Equation 1.15: $$\eta_{TEG} = \frac{P_{TEG}}{P_{thermal}} = \eta_{Carnot} \frac{\sqrt{ZT+1}-1}{\sqrt{ZT+1}+\frac{T_c}{T_h}}$$

where $P_{thermal}$ is the thermal input power, ZT is the device figure-of-merit, and η_{Carnot} is the Carnot limit, defined as:

Equation 1.16: $$\eta_{Carnot} = \frac{T_h - T_c}{T_h}$$

It is important to note that in Equation 1.14, the Z in ZT is capitalized to represent the device figure-of-merit, as opposed to zT (lowercase ***z***), which corresponds to the material's figure of merit. Increasing ZT will monotonically increase η_{TEG}, but the ultimate theoretical efficiency for TEGs, like any other heat engine, is limited to the Carnot limit.

TEGs can have vertical (out-of-plane) or horizontal (in-plane) geometries, with the former being the typical configuration for inorganic TEGs and the latter for organic TEGs. Organic materials tend to be thin films, so a temperature gradient is unable to develop in the vertical direction. Rather, a temperature gradient can develop in the horizontal direction. If the organic TEGs are free-standing or deposited on flexible substrates, the legs can be folded and emulate vertical geometries. For TEGs, two important design parameters that should be considered are leg length and filling factor, defined as the ratio of the area covered by the active thermoelectric material to the hot side. Ideally, legs should be intimately packed to achieve high power density devices. The leg length must be optimized such that electrical losses to resistance (and Joule heating) are minimized yet a large temperature difference across the legs is able to be maintained.

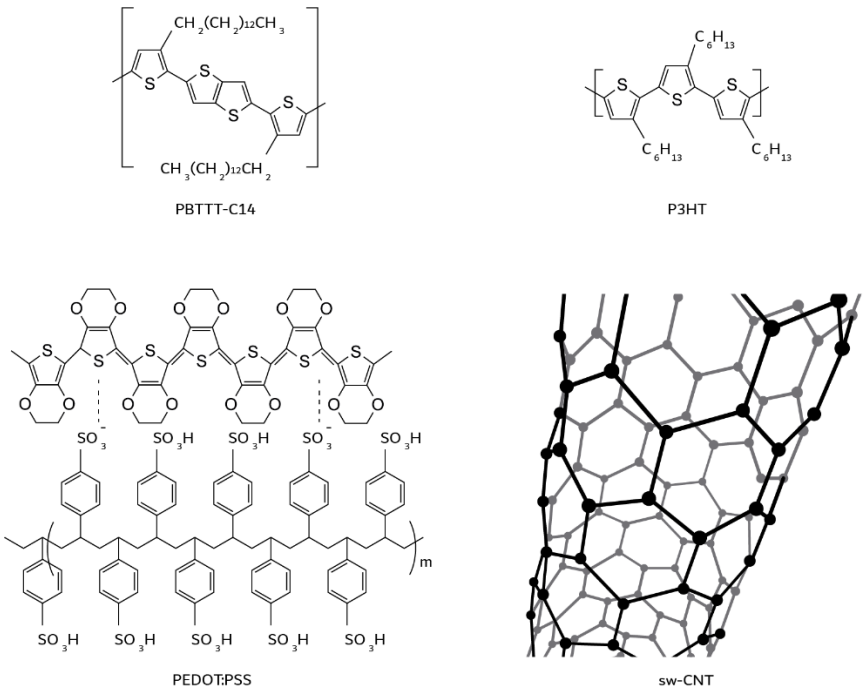

Figure 1-16. Common organic thermoelectric materials

There are four main classes of organic thermoelectric materials: conducting polymers, doped semiconducting polymers, carbon nanostructures, and composite materials. Common conducting polymers used for thermoelectrics include polypyrrole and polyaniline (PANI), while commonly doped semiconducting polymers include polyphenylvinylene, polycarbazole, and polymers based on poly(thiophenes) [65]. Pristine conducting polymers, however, exhibit low electrical conductivities because electron transport happens via thermally-activated hopping through the polymer chains, and thus exhibit low power factors. PEDOT has been one of the most promising organic materials because of its large electrical conductivity compared to other conjugated polymers. The structures of selected thermoelectric materials can be seen in Figure 1-16.

An effective strategy to enhance the thermoelectric performance of semiconducting polymers is via doping techniques, including chemical doping, electrochemical doping and secondary doping. Essentially, doping increases the number of charge carriers, thereby causing the charge transport mechanism to change from thermally-activated hopping to metallic-like (band) transport. Doping changes the position of the Fermi level, shifting it towards the HOMO level in the case of p-type materials and towards the LUMO in n-type materials [75]. Secondary doping, on the other hand, enhances conductivity by changing the morphology of the material using additive solvents. Additive solvents, such as dimethyl

sulfoxide (DMSO), help improve ordering or affect phase separation in mixtures of materials, thereby affecting charge carrier mobility in the materials. Despite the Seebeck coefficient decreasing with increased doping, the enhancement in electrical conductivity can be large enough to lead to higher power factors. It is important to note that obtaining stable n-type materials with large power factors is one of the biggest challenges for organic thermoelectrics.

Single-walled carbon nanotubes (CNTs) have excellent electronic properties, with charge carrier mobilities on the order of 10^5 cm^2 V^{-1} s^{-1} [76]. However, individual CNTs have extremely high thermal conductivities. Depending on the chirality of the CNTs, the CNTs can have a metallic or semiconducting electronic structure, which influences their Seebeck coefficient. Sorted semiconducting CNTs have been theoretically shown to have very high Seebeck coefficients [77]. Although largely determined by the chirality, diameter and electronic structure, the TE properties of CNTs are also affected by the surfactant and processing conditions used to disperse the CNTs [78]. Unlike conjugated polymers, CNT films tend to be porous and have high surface areas, making them easier to dope.

While semi-conducting CNTs possess desirable electrical conductivities and modest to high Seebeck coefficients, the thermal conductivities remain too high to be of use as TE materials. An approach to improving the thermoelectric performance is to mix them with conducting polymers to form composite materials, another class of thermoelectric materials. Composite polymer-CNTs materials may exhibit higher thermoelectric performance because they leverage the high electrical conductivity of the CNTs while suppressing the thermal conductivity by increasing phonon scattering at the heterojunctions [79], [80].

1.5.3. Solar Thermoelectrics

Thermoelectric generators may be well-suited for solar harvesting because they can directly convert both sunlight and solar infrared heat into electricity. Solar cells harvest much of the visible part of the solar spectrum in an efficient manner, but the IR part of the spectrum is essentially useless, and in some cases, detrimental to performance. Compared to other solar heat engines, thermoelectric generators are solid-state devices and the heat-to-electricity conversion process is direct. Other heat engines require a working fluid to be heated and then drive a mechanical turbine to generate electricity. Thus, the number of steps needed to produce electricity imply complex systems.

Solar thermoelectric generators (STEGs) are much simpler systems, comprising three main components: a solar absorber, a TEG, and heat management system. Concentrating optics and vacuum conditions to reduce heat losses can be incorporated as well to enhance STEG conversion efficiency. Kraemer et. al. reported an efficiency of 7.4% for a unicouple STEG based on inorganic materials incorporating thermal and optical concentration [14].

Using organic thermoelectric materials in STEGs may have two key advantages. Firstly, organic thermoelectric materials absorb strongly across the solar spectrum, so there is no need for a solar absorber. The absorption of these materials can be tuned by doping or chemical modification of the material, for example. Secondly, organic materials may be able to make use of the low-grade, diffuse heat available at the Earth's surface in a more cost-effective manner than inorganic materials. Devices based on organic materials can be produced at larger scales, and the complexity of the device is reduced, i.e. no vacuum or active cooling is needed.

1.6. References for Chapter 1

[1] K. Yoshikawa *et al.*, “Silicon heterojunction solar cell with interdigitated back contacts for a photoconversion efficiency over 26%,” vol. 2, no. 5, pp. 1–8, Mar. 2017, doi: 10.1038/nenergy.2017.32.

[2] M. He *et al.*, “Kesterite Solar Cells: Insights into Current Strategies and Challenges,” *Adv. Sci.*, vol. 8, no. 9, p. 2004313, May 2021, doi: 10.1002/ADVS.202004313.

[3] M. L. Petrus *et al.*, “Capturing the Sun: A Review of the Challenges and Perspectives of Perovskite Solar Cells,” *Adv. Energy Mater.*, vol. 7, no. 16, p. 1700264, Aug. 2017, doi: 10.1002/AENM.201700264.

[4] R. Wang, M. Mujahid, Y. Duan, Z.-K. Wang, J. Xue, and Y. Yang, “A Review of Perovskites Solar Cell Stability,” *Adv. Funct. Mater.*, vol. 29, no. 47, p. 1808843, Nov. 2019, doi: 10.1002/ADFM.201808843.

[5] V. T. Chebrolu and H.-J. Kim, “Recent progress in quantum dot sensitized solar cells: an inclusive review of photoanode, sensitizer, electrolyte, and the counter electrode,” *J. Mater. Chem. C*, vol. 7, no. 17, pp. 4911–4933, Apr. 2019, doi: 10.1039/C8TC06476H.

[6] Q. Liu *et al.*, “18% Efficiency organic solar cells,” *Sci. Bull.*, vol. 65, no. 4, pp. 272–275, Feb. 2020, doi: 10.1016/j.scib.2020.01.001.

[7] Y. Lin *et al.*, “Self-Assembled Monolayer Enables Hole Transport Layer-Free Organic Solar Cells with 18% Efficiency and Improved Operational Stability,” *ACS Energy Lett.*, vol. 5, no. 9, pp. 2935–2944, Sep. 2020, doi: 10.1021/ACSENERGYLETT.0C01421.

[8] Y. Cai *et al.*, “A Well-Mixed Phase Formed by Two Compatible Non-Fullerene Acceptors Enables Ternary Organic Solar Cells with Efficiency over 18.6%,” *Adv. Mater.*, p. 2101733, Jul. 2021, doi: 10.1002/ADMA.202101733.

[9] T. M. Razykov, C. S. Ferekides, D. Morel, E. Stefanakos, H. S. Ullal, and H. M. Upadhyaya, “Solar photovoltaic electricity: Current status and future prospects,” *Sol. Energy*, vol. 85, no. 8, pp. 1580–1608, Aug. 2011, doi: 10.1016/J.SOLENER.2010.12.002.

[10] G. W. Crabtree and N. S. Lewis, “Solar energy conversion,” *Phys. Today*, vol. 60, no. 3, p. 37, Mar. 2007, doi: 10.1063/1.2718755.

[11] D. Ginley, M. A. Green, and R. Collins, “Solar Energy Conversion Toward 1 Terawatt,” *MRS Bull.*, vol. 33, no. 4, pp. 355–364, 2008, doi: 10.1557/MRS2008.71.

[12] L. L. Baranowski, G. J. Snyder, and E. S. Toberer, “Concentrated solar thermoelectric generators,” *Energy Environ. Sci.*, vol. 5, no. 10, pp. 9055–9067, Sep. 2012, doi: 10.1039/C2EE22248E.

[13] D. Kraemer *et al.*, “High-performance flat-panel solar thermoelectric generators with high thermal concentration,” *Nat. Mater.*, vol. 10, no. 7, p. 532, May 2011, doi: 10.1038/nmat3013.

[14] D. Kraemer *et al.*, “Concentrating solar thermoelectric generators with a peak efficiency of 7.4%,” *Nat. Energy*, vol. 1, no. 11, p. 16153, Sep. 2016, doi: 10.1038/nenergy.2016.153.

[15] J. P. Jurado, B. Dörling, O. Zapata-Arteaga, A. Roig, A. Mihi, and M. Campoy-Quiles, “Solar Harvesting: a Unique Opportunity for Organic Thermoelectrics?,” *Adv. Energy Mater.*, vol. 9, no. 45, p. 1902385, Dec. 2019, doi: 10.1002/aenm.201902385.

[16] “Data overview - IEA.” [Online]. Available: https://www.iea.org/data-and-statistics?country=WORLD&fuel=Energy consumption&indicator=TFCbySource. [Accessed: 17-Jul-2021].

[17] R. Perez and M. Perez, “A fundamental look at energy reserves for the planet.,” *Int. Energy Agency SHC Program. Sol. Updat.*, vol. 50, no. April 2009, pp. 2–3, 2009. Retreived from https://research.asrc.albany.edu/people/faculty/perez/Kit/pdf/a-fundamental-look-at%20the-planetary-energy-reserves.pdf

[18] “Crystalline Silicon Photovoltaics Research | Department of Energy.” [Online]. Available: https://www.energy.gov/eere/solar/crystalline-silicon-photovoltaics-research. [Accessed: 17-Jul-2021].

[19] M. A. Green and S. P. Bremner, “Energy conversion approaches and materials for high-efficiency photovoltaics,” *Nat. Mater.*, vol. 16, no. 1, p. 23, Dec. 2016, doi: 10.1038/nmat4676.

[20] A. Al-Ashouri *et al.*, “Monolithic perovskite/silicon tandem solar cell with >29% efficiency by enhanced hole extraction,” *Science (80-.).*, vol. 370, no. 6522, pp. 1300–1309, Dec. 2020, doi: 10.1126/SCIENCE.ABD4016.

[21] G. Li, W.-H. Chang, and Y. Yang, “Low-bandgap conjugated polymers enabling solution-processable tandem solar cells,” *Nat. Rev. Mater. 2017 28*, vol. 2, no. 8, pp. 1–13, Jul. 2017, doi: 10.1038/natrevmats.2017.43.

[22] J. Wang *et al.*, “A Tandem Organic Photovoltaic Cell with 19.6% Efficiency Enabled by Light Distribution Control,” *Adv. Mater.*, p. 2102787, 2021, doi: 10.1002/ADMA.202102787.

[23] J. F. Geisz *et al.*, “Six-junction III–V solar cells with 47.1% conversion efficiency under 143 Suns concentration,” *Nat. Energy 2020 54*, vol. 5, no. 4, pp. 326–335, Apr. 2020, doi: 10.1038/s41560-020-0598-5.

[24] T. Trupke, M. A. Green, and P. Würfel, “Improving solar cell efficiencies by up-conversion of sub-band-gap light,” *J. Appl. Phys.*, vol. 92, no. 7, p. 4117, Sep. 2002, doi: 10.1063/1.1505677.

[25] S. Asahi, H. Teranishi, K. Kusaki, T. Kaizu, and T. Kita, “Two-step photon up-conversion solar cells,” *Nat. Commun. 2017 81*, vol. 8, no. 1, pp. 1–9, Apr. 2017, doi: 10.1038/ncomms14962.

[26] Z. Omair *et al.*, “Ultraefficient thermophotovoltaic power conversion by band-edge spectral filtering,” *Proc. Natl. Acad. Sci.*, vol. 116, no. 31, pp. 15356–15361, Jul. 2019, doi: 10.1073/PNAS.1903001116.

[27] M. C. Scharber and N. S. Sariciftci, “Low Band Gap Conjugated Semiconducting Polymers,” *Adv. Mater. Technol.*, vol. 6, no. 4, p. 2000857, Apr. 2021, doi: 10.1002/ADMT.202000857.

[28] C. Wang *et al.*, “Low Band Gap Polymer Solar Cells With Minimal Voltage Losses,” *Adv. Energy Mater.*, vol. 6, no. 18, p. 1600148, Sep. 2016, doi: 10.1002/AENM.201600148.

[29] T. Bauer, N. Pfleger, N. Breidenbach, M. Eck, D. Laing, and S. Kaesche, “Material aspects of Solar Salt for sensible heat storage,” *Appl. Energy*, vol. 111, pp. 1114–1119, Nov. 2013, doi: 10.1016/J.APENERGY.2013.04.072.

[30] Y. ting Wu, N. Ren, T. Wang, and C. fang Ma, “Experimental study on optimized composition of mixed carbonate salt for sensible heat storage in solar thermal power plant,” *Sol. Energy*, vol. 85, no. 9, pp. 1957–1966, Sep. 2011, doi: 10.1016/J.SOLENER.2011.05.004.

[31] M. Zhang *et al.*, “Single-layered organic photovoltaics with double cascading charge transport pathways: 18% efficiencies,” *Nat. Commun. 2021 121*, vol. 12, no. 1, pp. 1–10, Jan. 2021, doi: 10.1038/s41467-020-20580-8.

[32] Y. Lin *et al.*, “18.4 % Organic Solar Cells Using a High Ionization Energy Self-Assembled Monolayer as Hole-Extraction Interlayer,” *ChemSusChem*, 2021, doi: 10.1002/CSSC.202100707.

[33] Y. Cui *et al.*, “Single-Junction Organic Photovoltaic Cell with 19% Efficiency,” *Adv. Mater.*, p. 2102420, Aug. 2021, doi: 10.1002/ADMA.202102420.

[34] F. Machui *et al.*, “Cost analysis of roll-to-roll fabricated ITO free single and tandem organic solar modules based on data from manufacture,” *Energy Environ. Sci.*, vol. 7, no. 9, pp. 2792–2802, Aug. 2014, doi: 10.1039/C4EE01222D.

[35] N. Espinosa, M. Hösel, D. Angmo, and F. C. Krebs, “Solar cells with one-day energy payback for the factories of the future,” *Energy Environ. Sci.*, vol. 5, no. 1, pp. 5117–5132, Jan. 2012, doi: 10.1039/C1EE02728J.

[36] M. Kaltenbrunner *et al.*, “Ultrathin and lightweight organic solar cells with high flexibility,” *Nat. Commun. 2012 31*, vol. 3, no. 1, pp. 1–7, Apr. 2012, doi: 10.1038/ncomms1772.

[37] C. Deibel, A. Baumann, and V. Dyakonov, “Photogeneration and Recombination in

Polymer Solar Cells," *Phys. Org. Semicond.*, pp. 575–602, Jan. 2013, doi: 10.1002/9783527654949.CH17.

[38] R. Zhou *et al.*, "All-small-molecule organic solar cells with over 14% efficiency by optimizing hierarchical morphologies," *Nat. Commun. 2019 101*, vol. 10, no. 1, pp. 1–9, Nov. 2019, doi: 10.1038/s41467-019-13292-1.

[39] C. Yan *et al.*, "Non-fullerene acceptors for organic solar cells," *Nat. Rev. Mater. 2018 33*, vol. 3, no. 3, pp. 1–19, Feb. 2018, doi: 10.1038/natrevmats.2018.3.

[40] E. M. Speller *et al.*, "From fullerene acceptors to non-fullerene acceptors: prospects and challenges in the stability of organic solar cells," *J. Mater. Chem. A*, vol. 7, no. 41, pp. 23361–23377, Oct. 2019, doi: 10.1039/C9TA05235F.

[41] S. Holliday *et al.*, "High-efficiency and air-stable P3HT-based polymer solar cells with a new non-fullerene acceptor," *Nat. Commun. 2016 71*, vol. 7, no. 1, pp. 1–11, Jun. 2016, doi: 10.1038/ncomms11585.

[42] S. Rafique, S. M. Abdullah, K. Sulaiman, and M. Iwamoto, "Fundamentals of bulk heterojunction organic solar cells: An overview of stability/degradation issues and strategies for improvement," *Renew. Sustain. Energy Rev.*, vol. 84, pp. 43–53, Mar. 2018, doi: 10.1016/J.RSER.2017.12.008.

[43] P. W. M. Blom, V. D. Mihailetchi, L. J. A. Koster, and D. E. Markov, "Device Physics of Polymer:Fullerene Bulk Heterojunction Solar Cells," *Adv. Mater.*, vol. 19, no. 12, pp. 1551–1566, Jun. 2007, doi: 10.1002/ADMA.200601093.

[44] H.-H. Gao *et al.*, "A New Nonfullerene Acceptor with Near Infrared Absorption for High Performance Ternary-Blend Organic Solar Cells with Efficiency over 13%," *Adv. Sci.*, vol. 5, no. 6, p. 1800307, Jun. 2018, doi: 10.1002/ADVS.201800307.

[45] A. Laventure and G. C. Welch, "A tetrachlorinated molecular non-fullerene acceptor for high performance near-IR absorbing organic solar cells," *J. Mater. Chem. C*, vol. 6, no. 34, pp. 9060–9064, Aug. 2018, doi: 10.1039/C8TC02701C.

[46] R. Long and O. V. Prezhdo, "Asymmetry in the Electron and Hole Transfer at a Polymer–Carbon Nanotube Heterojunction," *Nano Lett.*, vol. 14, no. 6, pp. 3335–3341, Jun. 2014, doi: 10.1021/NL500792A.

[47] J. J. M. Halls, K. Pichler, R. H. Friend, S. C. Moratti, and A. B. Holmes, "Exciton diffusion and dissociation in a poly(p-phenylenevinylene)/C60 heterojunction photovoltaic cell," *Appl. Phys. Lett.*, vol. 68, no. 22, p. 3120, Jun. 1998, doi: 10.1063/1.115797.

[48] H. M. Rad, F. Zhu, and J. Singh, "Profiling exciton generation and recombination in conventional and inverted bulk heterojunction organic solar cells," *J. Appl. Phys.*, vol. 124, no. 8, p. 083103, Aug. 2018, doi: 10.1063/1.5031062.

[49] L. E. de Sousa, F. T. Bueno, D. A. da S. Filho, L. A. R. Junior, and P. H. de O. Neto,

"Dynamical exciton decay in organic materials: the role of bimolecular recombination," *Phys. Chem. Chem. Phys.*, vol. 21, no. 4, pp. 1711–1716, Jan. 2019, doi: 10.1039/C8CP05951A.

[50] Y. Zhou, M. Eck, and M. Krüger, "Bulk-heterojunction hybrid solar cells based on colloidal nanocrystals and conjugated polymers," *Energy Environ. Sci.*, vol. 3, no. 12, pp. 1851–1864, Nov. 2010, doi: 10.1039/C0EE00143K.

[51] X. Shi, M. Hu, S. Dan, J. Huang, and Y. Ai, "Electric field effects on the charge transport in organic semiconductors based on improved variable-range hopping theory," *Chem. Phys. Lett.*, vol. 764, p. 138275, Feb. 2021, doi: 10.1016/J.CPLETT.2020.138275.

[52] A. Rana *et al.*, "Non-approximated series resistance evaluation by considering high ideality factor in organic solar cell," *AIP Adv.*, vol. 8, no. 12, p. 125121, Dec. 2018, doi: 10.1063/1.5053584.

[53] J. Nelson, "The Physics of Solar Cells," *Phys. Sol. Cells*, May 2003, doi: 10.1142/P276.

[54] D. Zhao and G. Tan, "A review of thermoelectric cooling: Materials, modeling and applications," *Appl. Therm. Eng.*, vol. 66, no. 1–2, pp. 15–24, May 2014, doi: 10.1016/J.APPLTHERMALENG.2014.01.074.

[55] M. Fiorentini and N. Bonini, "Thermoelectric coefficients of n-doped silicon from first principles via the solution of the Boltzmann transport equation," *Phys. Rev. B*, vol. 94, no. 8, p. 85204, Aug. 2016, doi: 10.1103/PhysRevB.94.085204.

[56] A. Cantarero and F. X. Àlvarez, "Thermoelectric Effects: Semiclassical and Quantum Approaches from the Boltzmann Transport Equation," pp. 1–39, 2014, doi: 10.1007/978-3-319-02012-9_1.

[57] A. Bulusu and D. G. Walker, "Review of electronic transport models for thermoelectric materials," *Superlattices Microstruct.*, vol. 44, no. 1, pp. 1–36, Jul. 2008, doi: 10.1016/J.SPMI.2008.02.008.

[58] H. Fritzsche, "A general expression for the thermoelectric power," *Solid State Commun.*, vol. 9, no. 21, pp. 1813–1815, Nov. 1971, doi: 10.1016/0038-1098(71)90096-2.

[59] S. Fratini, M. Nikolka, A. Salleo, G. Schweicher, and H. Sirringhaus, "Charge transport in high-mobility conjugated polymers and molecular semiconductors," *Nat. Mater. 2020 195*, vol. 19, no. 5, pp. 491–502, Apr. 2020, doi: 10.1038/s41563-020-0647-2.

[60] D. Scheunemann and M. Kemerink, "Non-Wiedemann-Franz behavior of the thermal conductivity of organic semiconductors," *Phys. Rev. B*, vol. 101, no. 7, p. 075206, Feb. 2020, doi: 10.1103/PhysRevB.101.075206.

[61] O. Zapata-Arteaga, A. Perevedentsev, S. Marina, J. Martin, J. S. Reparaz, and M. Campoy-Quiles, “Reduction of the Lattice Thermal Conductivity of Polymer Semiconductors by Molecular Doping,” *ACS Energy Lett.*, vol. 5, no. 9, pp. 2972–2978, Sep. 2020, doi: 10.1021/ACSENERGYLETT.0C01410.

[62] G.-H. H. Kim, L. Shao, K. Zhang, and K. P. Pipe, “Engineered doping of organic semiconductors for enhanced thermoelectric efficiency,” *Nat. Mater.*, vol. 12, no. 8, p. 719, May 2013, doi: 10.1038/nmat3635.

[63] H. R. Shanks, P. D. Maycock, P. H. Sidles, and G. C. Danielson, “Thermal Conductivity of Silicon from 300 to 1400\ifmmode^\circ\else\textdegree\fi{}K,” *Phys. Rev.*, vol. 130, no. 5, pp. 1743–1748, Jun. 1963, doi: 10.1103/PhysRev.130.1743.

[64] Y. Zhang, Y.-J. Heo, M. Park, and S.-J. Park, “Recent Advances in Organic Thermoelectric Materials: Principle Mechanisms and Emerging Carbon-Based Green Energy Materials,” *Polym. 2019, Vol. 11, Page 167*, vol. 11, no. 1, p. 167, Jan. 2019, doi: 10.3390/POLYM11010167.

[65] O. Bubnova and X. Crispin, “Towards polymer-based organic thermoelectric generators,” *Energy Environ. Sci.*, vol. 5, no. 11, pp. 9345–9362, Oct. 2012, doi: 10.1039/C2EE22777K.

[66] K. Biswas, M. S. Good, K. C. Roberts, M. A. Subramanian, and T. J. Hendricks, “Thermoelectric and structural properties of high-performance In-based skutterudites for high-temperature energy recovery,” *J. Mater. Res.*, vol. 26, no. 15, pp. 1827–1835, Aug. 2011, doi: 10.1557/JMR.2011.163.

[67] H. Li, X. Tang, Q. Zhang, and C. Uher, “Rapid preparation method of bulk nanostructured Yb0.3Co4Sb12+y compounds and their improved thermoelectric performance,” *Appl. Phys. Lett.*, vol. 93, no. 25, p. 252109, Dec. 2008, doi: 10.1063/1.3054158.

[68] G. Rogl *et al.*, “In-doped multifilled n-type skutterudites with ZT = 1.8,” *Acta Mater.*, vol. 95, pp. 201–211, Aug. 2015, doi: 10.1016/J.ACTAMAT.2015.05.024.

[69] I. T. Witting *et al.*, “The Thermoelectric Properties of Bismuth Telluride,” *Adv. Electron. Mater.*, vol. 5, no. 6, p. 1800904, Jun. 2019, doi: 10.1002/AELM.201800904.

[70] H. Wang and C. Yu, “Organic Thermoelectrics: Materials Preparation, Performance Optimization, and Device Integration,” *Joule*, vol. 3, no. 1, pp. 53–80, Jan. 2019, doi: 10.1016/J.JOULE.2018.10.012.

[71] K. Kurabayashi, M. Asheghi, M. Touzelbaev, and K. E. Goodson, “Measurement of the thermal conductivity anisotropy in polyimide films,” *J. Microelectromechanical Syst.*, vol. 8, no. 2, pp. 180–191, Jun. 1999, doi: 10.1109/84.767114.

[72] S. N. Patel and M. L. Chabinyc, “Anisotropies and the thermoelectric properties of semiconducting polymers,” *J. Appl. Polym. Sci.*, vol. 134, no. 3, p. 44403, Jan. 2017,

doi: 10.1002/app.44403.

[73] M.-Z. Yang, C.-C. Wu, C.-L. Dai, and W.-J. Tsai, “Energy Harvesting Thermoelectric Generators Manufactured Using the Complementary Metal Oxide Semiconductor Process,” *Sensors 2013, Vol. 13, Pages 2359-2367*, vol. 13, no. 2, pp. 2359–2367, Feb. 2013, doi: 10.3390/S130202359.

[74] L. L. Baranowski, G. J. Snyder, and E. S. Toberer, “Response to ‘Comment on “Effective thermal conductivity in thermoelectric materials”’ [J. Appl. Phys. 113, 204904 (2013)],” *J. Appl. Phys.*, vol. 115, no. 12, p. 126102, Mar. 2014, doi: 10.1063/1.4869140.

[75] Berthold Wegner *et al.*, “Predicting the yield of ion pair formation in molecular electrical doping: redox-potentials versus ionization energy/electron affinity,” *J. Mater. Chem. C*, vol. 7, no. 44, pp. 13839–13848, Nov. 2019, doi: 10.1039/C9TC04500G.

[76] T. Dürkop, S. A. Getty, and Enrique Cobas, and M. S. Fuhrer*, “Extraordinary Mobility in Semiconducting Carbon Nanotubes,” *Nano Lett.*, vol. 4, no. 1, pp. 35–39, Jan. 2003, doi: 10.1021/NL034841Q.

[77] A. D. Avery *et al.*, “Tailored semiconducting carbon nanotube networks with enhanced thermoelectric properties,” *Nat. Energy 2016 14*, vol. 1, no. 4, pp. 1–9, Apr. 2016, doi: 10.1038/nenergy.2016.33.

[78] Y. Ryu, L. Yin, and C. Yu, “Dramatic electrical conductivity improvement of carbon nanotube networks by simultaneous de-bundling and hole-doping with chlorosulfonic acid,” *J. Mater. Chem.*, vol. 22, no. 14, pp. 6959–6964, Mar. 2012, doi: 10.1039/C2JM16000E.

[79] H. Wang *et al.*, “Thermally Driven Large N-Type Voltage Responses from Hybrids of Carbon Nanotubes and Poly(3,4-ethylenedioxythiophene) with Tetrakis(dimethylamino)ethylene,” *Adv. Mater.*, vol. 27, no. 43, pp. 6855–6861, Nov. 2015, doi: 10.1002/ADMA.201502950.

[80] L. M. Cowen, J. Atoyo, M. J. Carnie, D. Baran, and B. C. Schroeder, “Review—Organic Materials for Thermoelectric Energy Generation,” *ECS J. Solid State Sci. Technol.*, vol. 6, no. 3, p. N3080, Jan. 2017, doi: 10.1149/2.0121703JSS.

Chapter 2. Methodology and experimental description

2.1. Sample preparation

2.1.1. Thermoelectric films

Carbon nanotube buckypapers

SG65i CoMoCAT single-wall carbon nanotubes were bought from Sigma-Aldrich. eDIPS CNTs were bought from Meijo Nano Carbon. The CNTs were dispersed in an aqueous solution of sodium dodecylbenzenesulfonate (SDBS). Fifty milliliter SDBS solutions with an initial concentration of 1 mg mL^{-1} were mixed with 10 mg of CNTs. The dispersions were sonicated at in a bath sonicator with ice and then centrifuged at 6000 rpm for 6 h. Once dispersed, the dispersion was filtered through porous filter paper (polyvinylidene fluoride (PVDF) membranes with a 0.2 μm pore size) to achieve thick buckypaper films. Buckypaper thicker than ≈5 μm can easily be removed from the supporting filter paper, giving freestanding samples.

The composite eDIPS with bacterial cellulose samples were prepared following the work of Abol-Fotouh [1]. In summary, bacterial cellulose fibers are grown in an aqueous medium in the presence of dispersed CNTs, forming well-intermixed films. After washing and drying, the ≈10 μm films resemble buckypapers, yet contain only about 10 wt% CNTs, and correspondingly exhibit lower electrical and thermal conductivities. These samples were prepared by Dr. B. Dörling and Dr. D. Abol-Fotouh (in Prof. Anna Roig Group at ICMAB-CSIC).

2.1.2. Freestanding PEDOT:PSS films

An aqueous dispersion of PEDOT:PSS (Heraeus Clevios AI 4083) was bought from Heraeus. Thick, freestanding films (>5 μm) were prepared by drop-casting the aqueous PEDOT:PSS onto PET substrates and allowing them to dry. Due to the poor adhesion of PEDOT:PSS on PET substrates, freestanding films of PEDOT:PSS can be achieved by carefully peeling these thick dried PEDOT:PSS films from the PET substrates. For the DMSO-treated films, DMSO was purchased from Sigma-Aldrich and added directly (5%, v/v) to the polymer dispersion. The DMSO/PEDOT:PSS dispersion was then drop-casted in a similar fashion to the pristine PEDOT:PSS films.

2.1.3. TE polymer films

Regio-regular P3HT and poly[2,5-bis(3-tetradecylthiophen-2-yl)thieno[3,2-b]thiophene] (PBTTT-C_{14}) were purchased from Sigma-Aldrich. P3HT was dissolved in chloroform (CF) at a concentration of 7.5 mg mL^{-1}, and thin films were spin-coated on glass substrates. Thick, freestanding films of P3HT were obtained by drop-casting in a similar fashion to the freestanding PEDOT:PSS films. PBTTT-C_{14} was dissolved in chlorobenzene (CB) at a concentration of 20 mg mL^{-1}. Solutions were stirred at 110 °C for three hours and blade coated (Zehntner ZAA 2300) using a preheated blade coater at 110 °C. A blade height of 200 µm and a speed of 30 mm s^{-1} were used. Finally, the polymer films were thermally annealed for 30 minutes at 180 °C and then cooled slowly to room temperature. The doped PBTTT-C_{14} samples were prepared by Dr. O. Zapata-Arteaga in a custom-built doping vessel consisting of a 200 mL modified reactor beaker with an inbuilt heating cartridge to control the film temperature during dopant evaporation as described by Zapata-Arteaga et. al. [2]. The temperature was measured with two k-type thermocouples attached to the heating cartridge and the bottom of the beaker, respectively. Then, approximately 5 mg of 2,3,5,6-tetrafluoro-2,5-cyclohexadiene-1,4-diylidene)dimalononitrile (F_4TCNQ) purchased from Sigma-Aldrich, placed on the bottom of the beaker was preheated to 210 °C. The polymer films were placed on the heating cartridge facing down towards the F_4TCNQ and heated to 130 °C. The system was then sealed and evacuated to 70 kPa. Film thickness was measured using a digital micrometer (Mitutoyo High-Accuracy Digimatic).

2.1.4. Solar cell filters

Figure 2-1. Picture of a solar cell filter

Optically-thick, freestanding filters made of the relevant materials were used instead of complete photovoltaic cells to evaluate the role of the active layer bandgap on the performance of hybrid PV-TE devices. For the glass filter, a glass substrate was cleaned in ethanol and used without further processing. For the glass with indium tin oxide (ITO) filter, a glass substrate with ITO purchased from Ossila was cleaned with ethanol and used as is. For the glass with zinc oxide (ZnO) filter, ZnO nanoparticle solution was bought from Avantama. A glass substrate was rinsed in ethanol and a layer of ZnO was deposited by spin-coating at an RPM of 3000 for 30 seconds. For the glass/ITO/ZnO, a glass substrate with ITO was cleaned with ethanol, and a layer of ZnO was deposited by spin-coating. For the rest of the filters, all materials were dissolved in chlorobenzene (CB) at a concentration of approximately 30 mg mL^{-1}. Poly(sodium 4-styrenesulfonate) (pNaSS) purchased from Sigma-Aldrich was dissolved in an aqueous solution of Triton X100 (1% v/v) also purchased from Sigma-Aldrich. A glass substrate was cleaned with ethanol, and then a thin layer of pNaSS was deposited through spin-coating. Once dry, a thick polymer layer was deposited on top of the pNaSS layer through drop-casting 150 µL of polymer solution or small-molecule solution. Finally, the samples were submerged in water to dissolve the pNaSS layer, releasing a freestanding layer of the filter materials. Filters were made of the following materials with increasing band gap: poly(9,9-dioctylfluorene) (PFO), Poly[2-methoxy-5-(2-ethylhexyloxy)-1,4-phenylenevinylene] (MEH-PPV), poly(9,9-dioctylfluorene-alt-benzothiadiazole) (PFBT), poly(3-hexylthiophene-2,5-diyl) (P3HT), poly[(2,6-(4,8-bis(5-(2-ethylhexyl)thiophen-2-yl)-benzo[1,2-*b*:4,5-*b*′]dithiophene))-*alt*-(5,5-(1′,3′-di-2-thienyl-5′,7′-bis(2-ethylhexyl)benzo[1′,2′-*c*:4′,5′-*c*′]dithiophene-4,8-dione)] (PBDB-T or PCE12), poly[(2,6-(4,8-bis(5-(2-ethylhexyl-3-fluoro)thiophen-2-yl)-benzo[1,2-*b*:4,5-*b*′]dithiophene))-*alt*-(5,5-(1′,3′-di-2-thienyl-5′,7′-bis(2-ethylhexyl)benzo[1′,2′-*c*:4′,5′-*c*′]dithiophene-4,8-dione)] (PBDBT-T-2F or PCE13), Poly[[2,3-bis(3-octyloxyphenyl)-5,8-quinoxalinediyl]-2,5-thiophenediyl] (TQ1), poly[4,8-bis(5-(2-ethylhexyl)thiophen-2-yl)benzo[1,2-*b*;4,5-*b*′]dithiophene-2,6-diyl-*alt*-(4-(2-ethylhexyl)-3-fluorothieno[3,4-*b*]thiophene-)-2-carboxylate-2-6-diyl)] (PTB7-Th or PCE10), poly[(5,6-difluoro-2,1,3-benzothiadiazol-4,7-diyl)-*alt*-(3,3‴-di(2-octyldodecyl)-2,2′;5′,2″;5″,2‴-quaterthiophen-5,5‴-diyl)] (PffBT4T-2OD or PCE11), poly([*N*,*N*′-bis(2-octyldodecyl)-naphthalene-1,4,5,8-bis(dicarboximide)-2,6-diyl]-*alt*-5,5′-(2,2′-bithiophene)) (N2200). PFBT was bought from Sigma-Aldrich. TQ1, PCE10, PCE11, N2200), and PFO were purchased from Ossila. MEH-PPV, PBDB-T, and PBDBT-T-2F were purchased from 1-material.

2.1.5. Solar cells

The materials (with a donor acceptor ratio of 1:1) were dissolved in o-xylene with a concentration of 15 mg mL^{-1}. Pre-patterned ITO substrates were cleaned with sequential ultrasonication baths (10 mins) in acetone, an aqueous Hellmanex solution (from Ossila), isopropanol, and sodium hydroxide (10 vol%). They were rinsed in DI water and dried with N_2. The bottom transport layer, either PEDOT:PSS (HTL Solar purchased from Ossila) or ZnO depending on the device architecture, was deposited using an automatic blade coater Zehntner ZAA 2300 with an aluminum applicator Zehntner ZUA 2000, in ambient conditions and at a constant speed of 5 mm s^{-1}. For ZnO, the drop volume used was 50 µL, and the temperature was set to 40 °C. All active layer materials were deposited using a second blade coater equipment (same brand and model) that included custom-made electronics to enable speed profiles, inside a nitrogen-filled and dry glove box, at 80 °C, while setting a blade gap of 200 µm. The drop volume used was 75 µL for the photoactive layer blends. The speed of the blade was set to decelerate linearly from 80 to 5 mm s^{-1} to produce samples with thickness gradients, similar to the approach described by Nickel et al [3]. The second transport layer and electrode, either Ca/Ag or MoO_3/Ag, were thermally evaporated at a rate of 0.1 Å s^{-1} for the transport layer and 0.5 Å s^{-1} for the electrode. Samples were encapsulated using a cut glass slide and epoxy resin, then cured with an UV lamp (UVP, 4W lamp) for 5-10 minutes. Commercial Silicon solar cells were purchased from AOSHIKE and commercial organic solar cells were purchased from Infinity PV.

The thicknesses of the devices were measured using a Alpha-Step D-500 stylus profiler from KLA. The thicknesses of the PEDOT:PSS and ZnO layers were found to be between 30-35 µm. For the thermally evaporated layers, 10 nm of Ca or MoO_3 were evaporated on top of the photoactive layer (PAL), while the evaporated Ag layer had a thickness of 150 nm.

2.1.6. Mobility devices

The devices for the mobility measurements were made in a similar fashion to the solar cells, with the only difference being that the photoactive layer was sandwiched between the same type of transport layer (either ETL or HTL) on either side: glass/ITO (Indium Tin Oxide)/transport layer (ETL or HTL)/photoactive layer (PAL)/ transport layer (ETL or HTL)/top electrode. For the hole-only devices, the devices had a structure of glass/ITO/PEDOT:PSS (HTL Solar)/PAL/MoO_3/Ag. For the electron-only devices, the devices had a structure of glass/ITO/ZnO/PAL/Ca/Ag.

2.2. Experimental setups

2.2.1. Seebeck measurements

For the normal Seebeck measurements, a setup rig built by Dr. B. Dörling was used. Briefly, a normal heat source (a Kofler bench in this case) was used to heat one side of the TE material, while the other side was left unheated. Two type K thermocouples and crocodile clips were placed on the ends of the TE materials. A Keithley 2400 source measure was used to record the voltage across the sample, and a Raspberry Pi and custom python program recorded hot side temperature, cold side temperature and the voltage from the source meter. The measured voltage was plotted temperature difference, and the average Seebeck coefficient was extracted from the slope of V against ΔT, as can be seen in Figure 2-2.

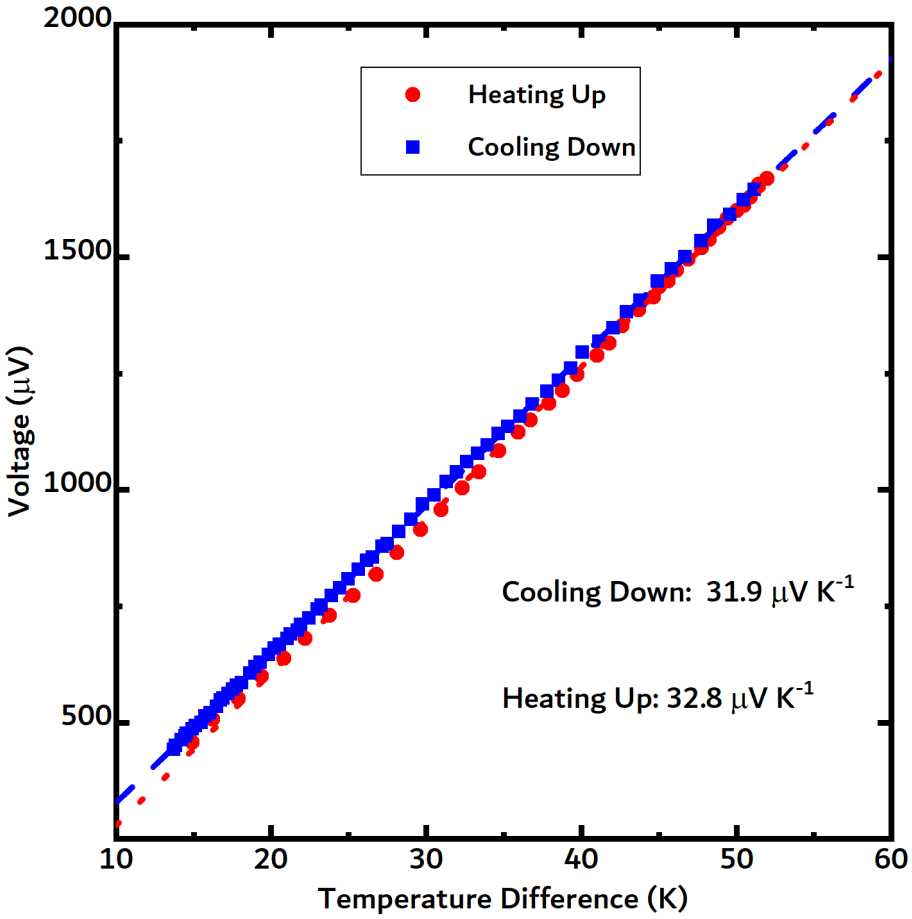

Figure 2-2. Example Seebeck coefficient measurement of a film of CoMoCAT CNTs. The red circles represent the data points when the sample was heated, while the blue squares represent the data points when the sample was cooled. The blue dashed line is the fit of the cooling down curve, while the red dotted line is the fit of the heating up curve.

For the Photo-Seebeck measurements, a AAA solar simulator (SAN-EI Electric, XES-100S1) was used as the heat source instead of the Kofler bench. One side of the TE material was exposed to illumination while the other was shadowed. Two type T thermocouples were placed on the ends of the TE materials. A custom multiplexer controlled by a Raspberry Pi was designed to switch the connections to a Keithley 2400 source meter to measure hot side temperature, cold side temperature and the voltage across the TE material. A LabVIEW program was used to control the measurement. The average Seebeck coefficient was extracted from the plot of voltage against temperature difference.

2.2.2. Photothermal measurements

An Optris PI 450 IR camera was used to record temperature response. Depending on the experiment, the freestanding films were mechanically supported by an annular metal ring or a 3D printed support. In most cases, the materials were illuminated for 5 minutes to allow the materials to reach a steady-state temperature. The emissivities of the organic materials were found to be 0.95 after a calibration step. To determine the emissivity, a sample was heated using a normal heat source, and a thermocouple was used to measured the temperature. The emissivity was changed until the temperature of the IR camera matched the temperature of the thermocouple.

2.2.3. Fourier Transform Infrared Spectroscopy

Film absorbance was measured on spin-coated thin samples and the solar cell filters, using a Fourier transform infrared (FTIR) spectrometer (Bruker Vertex 70) attached to an optical microscope (Hyperion).

2.2.4. Electrical characterization

The IV characterization of the solar cells was performed using a Keithley 2400 source meter. The same sourcemeter was used to perform the space-charge limited current (SCLC) experiments and the electrical measurements (PV curves) for the SOTEG [4], [5].

2.2.5. External Quantum Efficiency

The custom-built external quantum efficiency EQE setup consists of a Supercontinuum White laser (Fianium PM-SC) coupled to a Fianium monochromator (LLTFContrastTM), with the power calibrated by a broad-band silicon photodetector (Thorlabs S120 V 200–1100 nm 50 mW). The EQE wavelength scan was done from 400 nm to 1100 nm every nm followed by a no-light measurement of the dark current of each device. The electric characterization was performed with a Keithley 2450 Sourcemeter.

2.3. References for Chapter 2

[1] D. Abol-Fotouh *et al.*, “Farming thermoelectric paper,” *Energy Environ. Sci.*, vol. 12, no. 2, pp. 716–726, 2019, doi: 10.1039/C8EE03112F.

[2] O. Zapata-Arteaga, A. Perevedentsev, S. Marina, J. Martin, J. S. Reparaz, and M. Campoy-Quiles, “Reduction of the Lattice Thermal Conductivity of Polymer Semiconductors by Molecular Doping,” *ACS Energy Lett.*, vol. 5, no. 9, pp. 2972–2978, Sep. 2020, doi: 10.1021/ACSENERGYLETT.0C01410.

[3] F. Nickel *et al.*, “Spatial mapping of photocurrents in organic solar cells comprising wedge-shaped absorber layers for an efficient material screening,” *Sol. Energy Mater. Sol. Cells*, vol. 104, pp. 18–22, Sep. 2012, doi: 10.1016/J.SOLMAT.2012.04.026.

[4] B. Ebenhoch, S. A. J. Thomson, K. Genevičius, G. Juška, and I. D. W. Samuel, “Charge carrier mobility of the organic photovoltaic materials PTB7 and PC71BM and its influence on device performance,” *Org. Electron.*, vol. 22, pp. 62–68, Jul. 2015 doi: 10.1016/j.orgel.2015.03.013.

[5] J. Yuan *et al.*, “Single-Junction Organic Solar Cell with over 15% Efficiency Using Fused-Ring Acceptor with Electron-Deficient Core,” *Joule*, vol. 3, no. 4, pp. 1140–1151, Apr. 2019, doi: 10.1016/J.JOULE.2019.01.004.

Chapter 3. Solar Organic Thermoelectric Generators (SOTEGs)

3.1. Solar Organic Thermoelectrics

Solar thermoelectric generators (STEGs) convert solar energy into heat and then heat into electricity via the Seebeck effect. The primary advantage of STEGs compared to other solar thermal energy conversion technologies is that they are scalable, solid-state heat engines capable of directly converting sunlight into electricity, foregoing the need for moving parts. Traditionally, STEGs based on inorganic materials consist of three subsystems: a solar absorber, the TEG, and the heat dissipation system. STEGs incorporate optical and thermal concentration to achieve high working temperatures on the hot end of the device, a necessity for high-efficiency devices. Additionally, state-of-the-art STEGs use radiation shields, active cooling and vacuum insulation, components which increases device complexity. The solar-to-electricity record efficiency for such devices is 9.6%, as reported by Kraemer et al. [1].

Using organic materials to develop organic STEGs (SOTEGs) may be an interesting approach to overcome some of the shortcomings of inorganic materials. Many common organic TE materials possess strong absorption in the solar spectrum, so using organic materials would eliminate the need for a separate solar absorber. Because the energy that arrives at the Earth's surface is diffuse, the heat is too low-grade, making most inorganic solar-thermal applications unfeasible. Organic TEs, however, are made from materials that are cheap, low toxic, highly abundant, and solution processable and can be printed onto large surfaces. SOTEGs can have a lower level of device complexity with respect to STEGs based on inorganic materials. Vacuum, radiation shields, and active cooling are not needed to capture the otherwise wasted, low-grade heat. Furthermore, the optical properties of organic materials can be readily tuned via doping, allowing SOTEGs to be integrated with semi-transparent solar cells to capture unused solar infrared radiation (see next chapter).

In this chapter, the efficiency limit of SOTEGs is evaluated by drawing on standard theory and experimental data. Later, the photothermal conversion capability of benchmark organic TE materials in terms of the temperature rise upon illumination as well as the appearance of nonthermal photoinduced effects is investigated. Lastly, a number of device geometries are proposed and the power output as a function of geometrical factors such as leg length,

the ratio between illuminated and shadowed area, and light concentration are determined. Part of the work in this chapter was published in Jurado et al. [2] and Liu et al. [3].

3.1.1. SOTEG Limits

In this chapter we evaluated the efficiency limit in SOTEGs. Ultimately, SOTEGs are limited by the Carnot efficiency, but the various conversion processes also influence conversion efficiency. The overall efficiency of a SOTEG is given by:

Equation 3.1: $$\eta = \eta_{opt}\eta_{abs}\eta_{teg}\eta_{aux}$$

where η_{opt} is the optical efficiency, η_{abs} is the absorber efficiency, η_{teg} is the efficiency of a TE generator, and η_{aux} is the auxiliary efficiency [1].

3.1.2. Optical Efficiency

For devices with optical concentration, the optical efficiency of the focusing lens, defined as the fraction of radiant power at its input aperture which reaches its output aperture, is limited by optical losses such as those from reflection, absorption, scattering or transmission of incident light, as shown in Figure 3-1 [4]. For reference, a lens made from NB-K has a transmittance of 92% from 250 to 4000 nm [1].

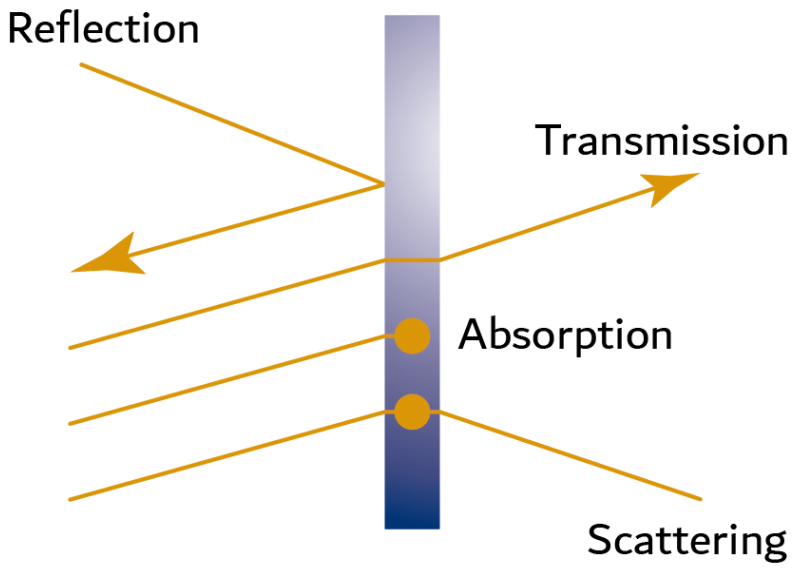

Figure 3-1. Optical losses associated with concentrating optics, such as a lens

3.1.3. Absorber Efficiency

The absorber efficiency is defined as the ratio of total incident solar radiation to the useful heat gain by the SOTEG. Incident radiation can either be reflected (1a in Figure 2-2), transmitted (1b) or absorbed. Because organic thermoelectric materials are semiconductors, they can absorb photons possessing energy higher than their band gap. However, not every photon is absorbed and converted into heat. Absorption of a photon can give rise to an electron-hole pair (2a). If the electron-hole pair does not separate, it can recombine radiatively or non-radiatively. In radiative recombination, the electron-hole pair will recombine and emit low-energy photons (2b). In non-radiative recombination, the electron-hole pair will thermalize and give off heat (2c). Photons with energies much higher than the band gap of the semiconductor generate charge carriers with excess energy, which can relax and release heat (2d).

Photons with energy below the band gap cannot be absorbed by the material and are generally lost to transmission. Energy given off as radiation, as well as the photons that recombine radiatively, limit absorber efficiency. It is interesting to note that solar cell efficiency is limited by non-radiative and radiative recombination, but non-radiative recombination is desired for SOTEGs. A structured graphene metamaterial was reported to have a solar-to-thermal conversion efficiency of 90.1% [5].

3.1.4. TEG efficiency and auxiliary efficiency

The TEG efficiency, as defined in eq. 1.15, is directly influenced by the Seebeck coefficients, electrical conductivities and thermal conductivities of the materials used in the devices. In addition to the properties of the materials, the TEG efficiency takes into account any parasitic thermal and electrical losses that negatively affect device performance including conduction losses through electrical contacts (3a), convection (3b), radiation losses (3c), losses that arise from the presence of traps (3d), and joule heating (3e). The auxiliary efficiency refers to parasitic losses arising from cooling the system, or pumping a working fluid through the system, for example.

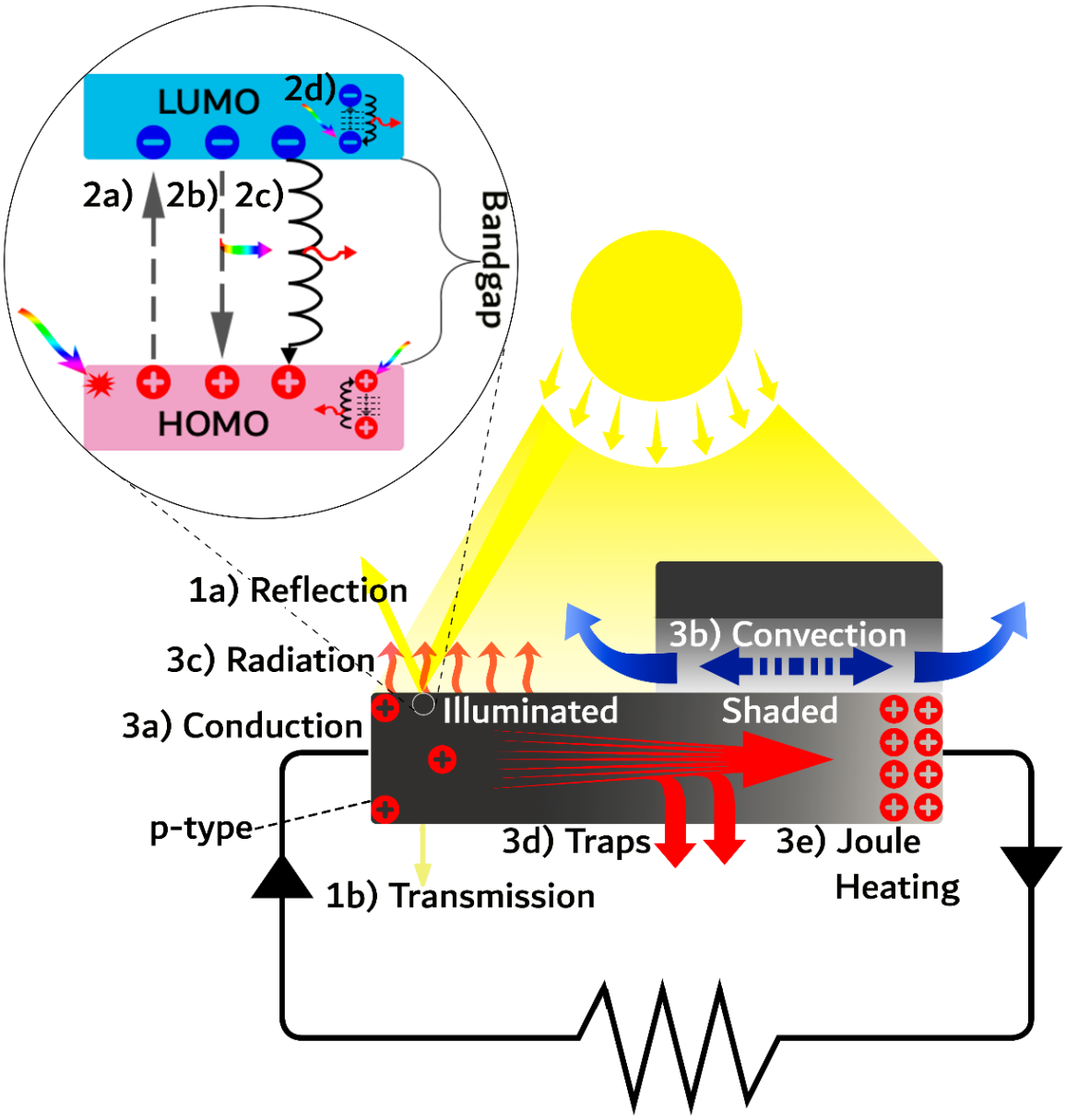

Figure 3-2. Associated processes and loss mechanisms in a SOTEG leg. Optical loss mechanisms: 1a) reflected light, 1b) transmitted light; absorption processes and losses: 2a) exciton formation, 2b) radiative recombination via photoluminescence, 2c) nonradiative recombination, 2d) thermalization losses; heat loss mechanisms: 3a) Conduction, 3b) Convection, 3c) radiation, 3d) traps, 3e) Joule heating. The figure was adapted from Jurado et al. [2].

3.2. SOTEG Solar Absorber Characterization

The photothermal conversion capability of benchmark organic TE materials was explored by characterizing their absorption spectra and measuring the temperature rise upon illumination. In this chapter, we considered commonly-used organic materials, spanning the four main classes of organic TE materials, namely: conducting polymers, doped

semiconducting polymers, carbon nanotubes (CNTs) and CNT-polymer composites. Specifically, we investigated semiconducting polymers such as poly(3-hexylthiophene-2,5-diyl) (P3HT), poly[2,5-bis(3-tetradecylthiophen-2-yl)thieno[3,2-b]thiophene] (PBTTT), PBTTT vapor-doped with 2,3,5,6-Tetrafluoro-7,7,8,8-tetracyanoquino-dimethane (F_4TCNQ); conducting polymers including PEDOT:PSS, and dimethyl sulfoxide (DMSO) treated PEDOT:PSS; single-wall carbon nanotubes of the CoMoCAT and eDIPS varieties and CNT:polymer composites including CoMoCAT:P3HT and eDIPS:cellulose [6]–[21]. Additionally, we examined the insulating polymer polylactic acid (PLA). The reported Seebeck and electrical conductivities of some of the previously mentioned materials can be found in Table 3.1. The thermal conductivity is introduced later in the chapter, but the thermal conductivities of the materials are shown in Table 3.2. Using the reported literature values, the *zT* for the materials are calculated.

Table 3.1. Reported TE parameters of selected organic materials

Material	**Seebeck (μV K^{-1})**	**Electrical Conductivity (S cm^{-1})**	**Calculated *zTs***	**Reference**
P3HT	1000	7.1E-6	1.1E-6	[12], [22]
PBTTT-C_{14}	-	4E-5	-	[15]
PEDOT:PSS	10-200	14	0.055	[23]
F_4TCNQ-doped PBTTT (25 mol%)	60 ± 9	3 - 68	0.036	[24], [25]
DMSO-treated PEDOT:PSS	15	13.4-1370	0.022	[26]–[28]
CoMoCAT CNTs	30	0.1-750	0.002	[11], [29]
eDIPS CNTs	30-50	300-2250	0.006	[11]
SW-CNT:P3HT (42% wt CNTs)	42	10	0.003	[12]
SW-CNT:cellulose (10% wt CNTs)	42	50	0.001	[13]

3.2.1. Absorption

Solar absorbers must be able to absorb sunlight and convert absorbed sunlight into heat. Ideal solar absorbers exhibit broadband absorption across the solar spectrum and little

emittance in the mid-IR regime to prevent radiation losses [30]. It is well reported in literature that common organic thermoelectric materials exhibit strong absorption in the solar spectrum [2], [25], [31], [32]. In this thesis, Fourier Transfrom Infrared (FTIR) spectroscopy was used to characterize the absorption spectra of several (semi-)conducting polymers and carbon nanotubes, as seen in Figure 3-3a and 3-3b. Semiconducting polymers have their absorption peaks in the UV and visible region of the solar spectrum [33]–[35]. P3HT and PBTTT exhibit their absorption peaks between 400 and 650 nm (Figure 3-3a). Doped polymers, such as PBTTT vapor-doped with F_4TCNQ shown in Figure 3-3a, can exhibit even broader absorption up to the NIR region, as result of polaron absorption or absorption of charge transfer complexes [17], [36], [37]. Conducting polymers, like PEDOT:PSS in Figure 3-3a, exhibit weak absorption in the UV and visible regions of the solar spectrum but exhibit strong absorption in the NIR region due to a Drude tail of free carriers [38], [39]. CNTs and their composites (Figure 3-3b) are capable of absorbing across the entire solar spectrum [2]. The electronic properties of CNTs can be metallic or semiconducting and depend strongly on their geometrical structure [40]. Because CNT raw materials typically are a mixture of CNTs of different structure, they exhibit broadband absorption across the entire solar spectrum. The CoMoCAT CNT absorption spectrum has more discernible peaks, since it has less residual catalyst material, and a higher concentration of a few semiconducting CNTs with specific chiral vector.

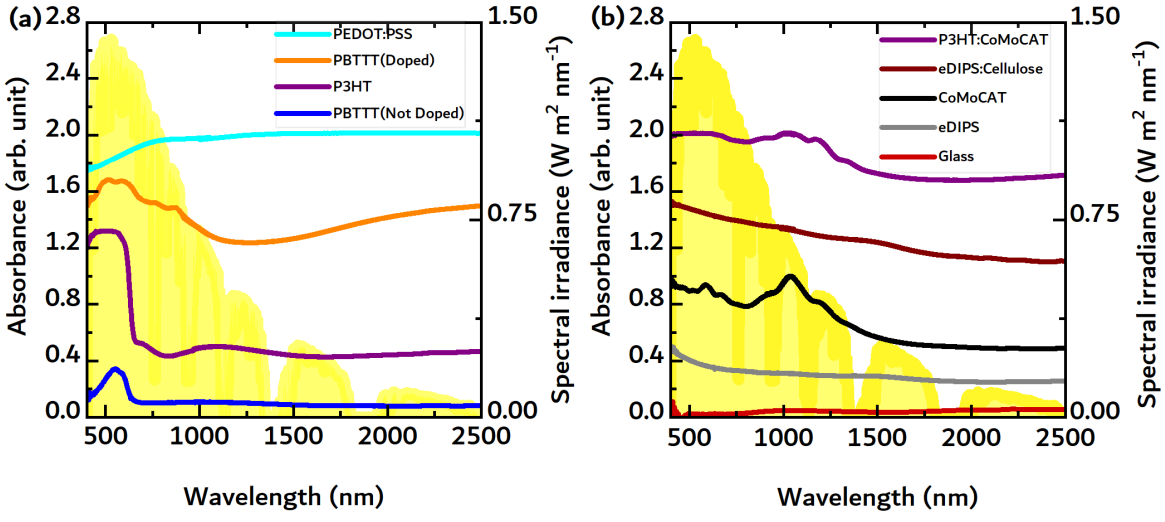

Figure 3-3. a) Absorbance of (Semi-)conducting polymers: Vis–NIR spectra of P3HT (violet), PEDOT:PSS (cyan), undoped PBTTT (blue) and PBTTT doped with F4TCNQ (orange) plotted together with the AM 1.5 solar spectrum. b) Absorbance of CNTs and composites: Vis–NIR spectra of a glass substrate (red), CoMoCAT CNTs (black), P3HT:CoMoCAT composite (purple), eDIPS CNTs (gray) and eDIPS:cellulose composite (wine) with the AM 1.5 solar spectrum. The spectra has been shifted. The Figure has been adapted from Jurado et al. [2].

3.2.2. Thickness

The thickness of the solar absorber directly influences the amount of incident solar radiation absorbed, thus affecting how hot a solar absorber can get. To probe the impact of thickness on temperature rise, photothermal simulations were carried out in COMSOL Multiphysics (v5.3a) using the Finite Element Method (FEM). First, the 1D transfer-matrix method was used to calculate the heat dissipated as a result of optical absorption under AM1.5 conditions [41]. Gasiorowski et al. reported the refractive index for pristine PEDOT:PSS up to ≈1700 nm, and the values for the refractive index were extrapolated out to 3000 nm [38]. Next, the 1-D heat transfer model in COMSOL along with the calculated dissipated heat in the previous step was used to calculate the steady-state temperature of the free-standing materials. The emissivity and thermal conductivity were set to 0.95 and 0.2 W m^{-1} K^{-1}, respectively [42]–[45]. The convection coefficient was assumed to be 12 W m^{-2} K^{-1} , which corresponds to natural convection in air [46]. It is important to note that the convection coefficient depends on the geometry of the surface and the properties of the convective fluid, in this case, air at an ambient temperature of 293K. The initial temperature of the film was set to be 293K. Finally, the thickness of the film was swept from 100 nm to 100 µm to investigate the influence of thickness on steady-state temperate under illumination.

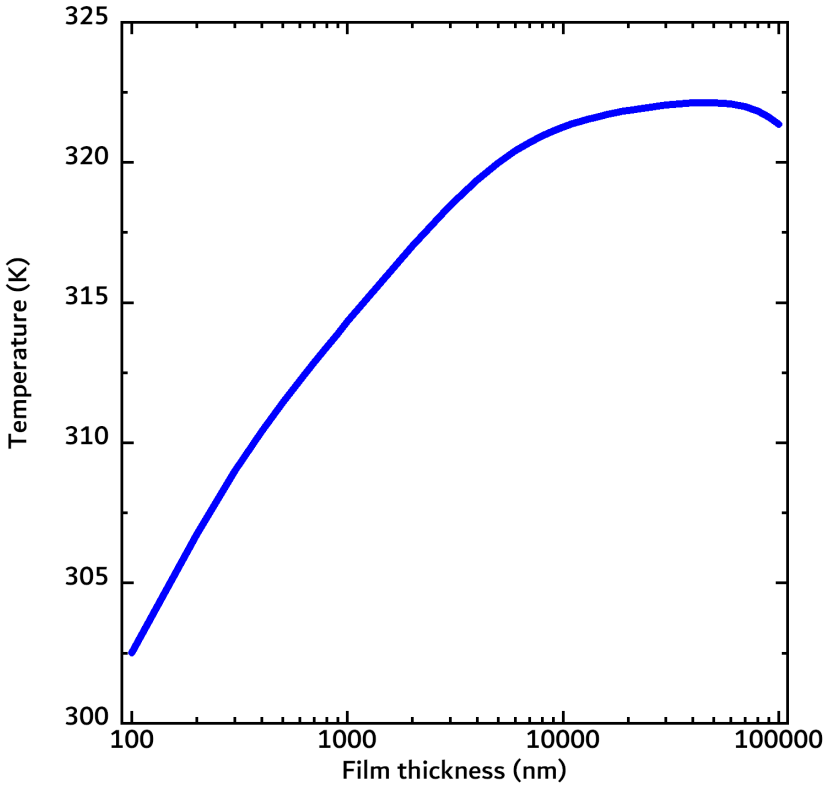

Figure 3-4. Calculated steady-state temperatures for PEDOT:PSS as a function of film thickness

The average steady-state temperature of the film as a function of film thickness is shown in Figure 3-4. Temperature rises steadily up to ≈ 10 μm, after which it reaches a plateau. The increased temperature comes as a result of greater absorbance. For extremely thick films (>80 μm, much greater than the penetration depth at all wavelengths), the temperature begins to drop since the unheated part of the film acts as a heat sink.

3.2.3. Thermal Conductivity

The thermal conductivity of a material also influences a material's photothermal response. Conductivity losses through electrical contacts and support materials are inevitable in a working device, but heat losses as a result of conduction can be mitigated with materials possessing low thermal conductivities. The thermal conductivities of common organic thermoelectric materials along with PLA, a potential support material for thermoelectric devices, are shown in Table 3.2.

Table 3.2. Thermal conductivities of common organic TE materials

Material	**Thermal Conductivity (W m^{-1} K^{-1})**	**Measurement direction**	**References**
PEDOT:PSS	0.2	out-of-plane	[47], [48]
	0.5	in-plane	
5% DMSO-treated PEDOT:PSS	0.42 ± 0.07	in-plane	[49]
	1.1	in-plane	[50]
	0.30 ± 0.07	out-of-plane	
PBTTT-C14	0.39	out-of-plane	[51]
	0.23	in-plane	[50]
	~0.6-0.8	in-plane	[52]
F_4TCNQ-Doped PBTTT-C14	~0.2	out-of-plane	[52]
P3HT	0.189 ± 0.023	out-of-plane	[53]
PLA	0.111	-	[54]
CoMoCAT CNTs	8.5	in-plane	[13]
eDIPS	27	in-plane	[13]
eDIPS:cellulose	2.7	in-plane	[13]

To probe the influence of thermal conductivity on photothermal response, a 3D printer was used to print small rectangles (5 mm thick) made of black polylactic acid (PLA). Although PLA is not a thermoelectric material, PLA could be incorporated as a structural material in a SOTEG. These pieces were 3D printed varying the infill density to emulate porosity and thus reduce the thermal conductivity. Next, the photothermal response of the PLA slabs was investigated using a solar simulator as a radiation source and an IR camera to probe the temperature of the slabs in ambient room conditions. The slabs were constantly illuminated until reaching a steady-state temperature (Figure 3-5a). As expected, the most porous PLA sample achieved a steady-state temperature (Figure 3-5b) about 35% higher than the dense PLA sample.

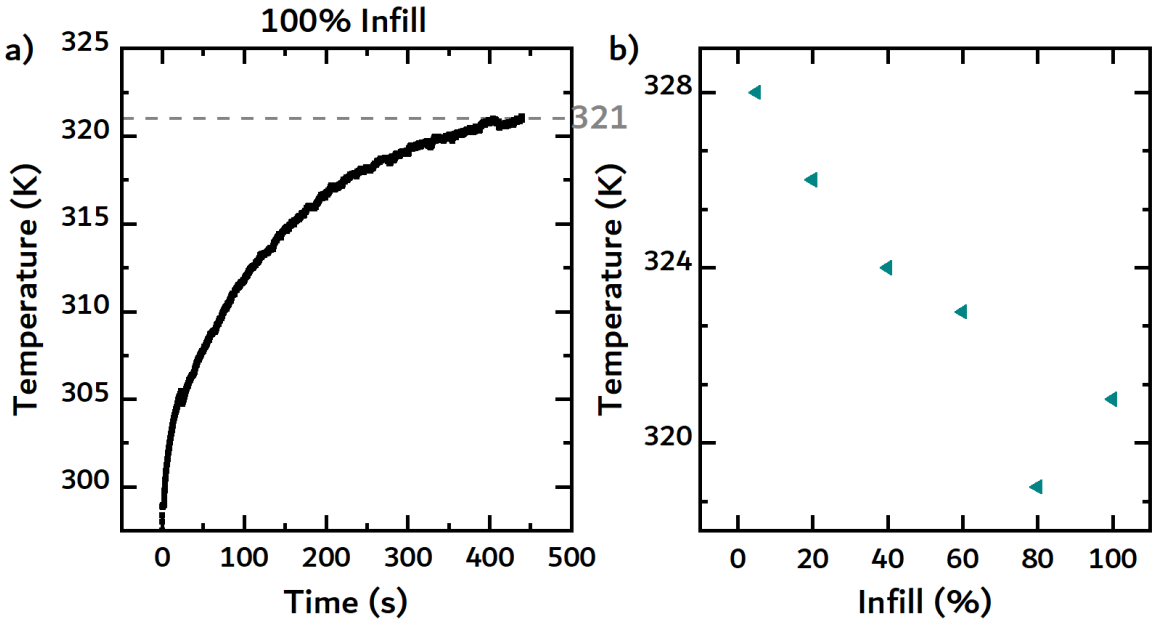

Figure 3-5. a) Example of temperature evolution of a PLA with an infill density of 100% under 1 sun. b) Steady-state temperature of PLA slabs as a function of infill density under 1 sun

Besides PLA, the photothermal responses for common thermoelectric materials were characterized. Metal rings were used to support the free-standing films, and the temperature of the materials was probed in the non-supported part of the film (Figure 3-6a) The power of the solar simulator was adjusted to change the irradiance up to 2.5 suns.

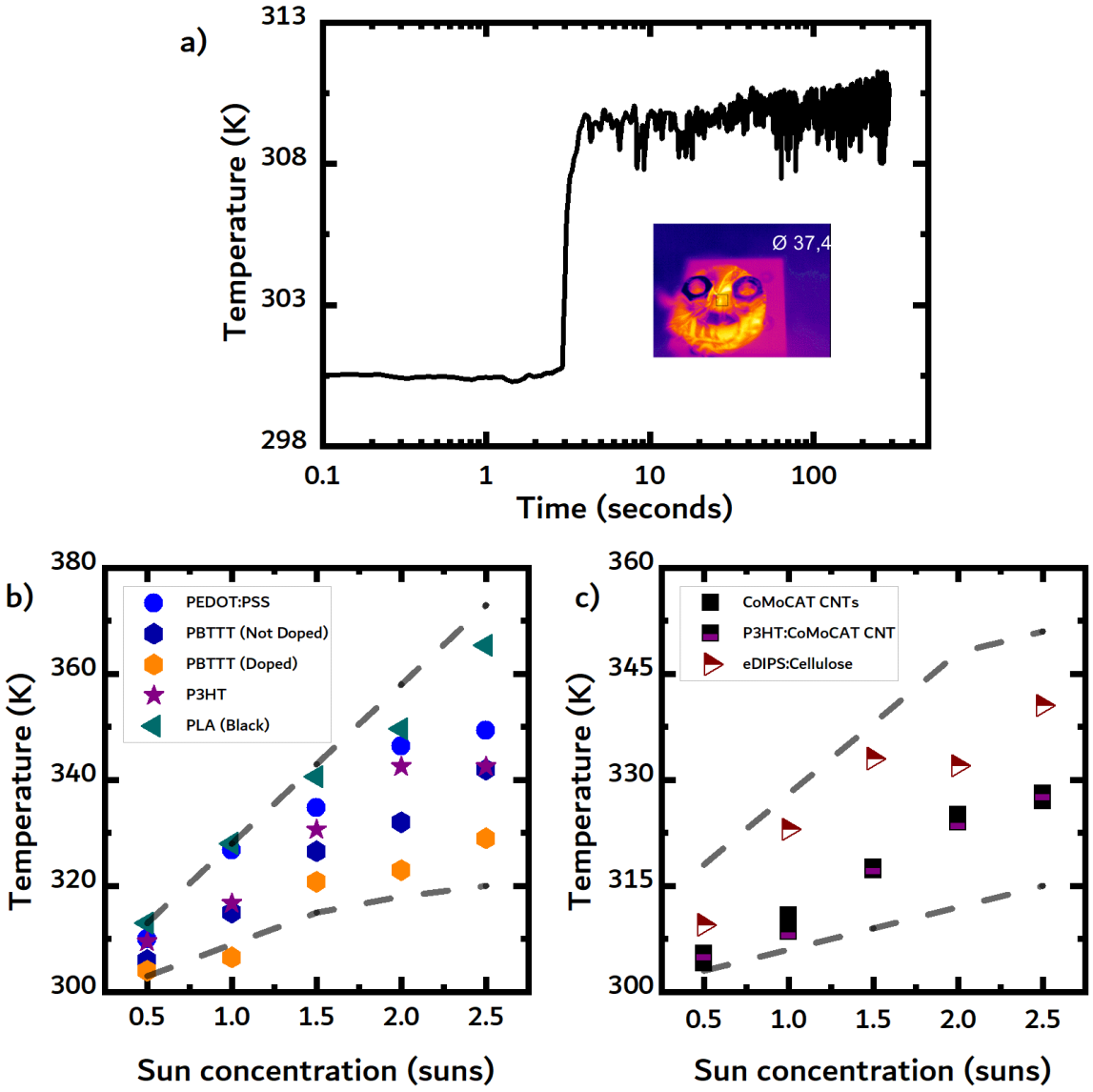

Figure 3-6. a) Temperature evolution of CoMoCAT CNTs under 1 sun with a corresponding thermal image. The black box represents the measurement area. b) Temperature rise of free-standing polymer and c) free-standing CNT samples versus irradiance. The gray dashed lines are a guide for the reader. The figure was adapted from Jurado et al. [2].

Table 3.3. Sample thickness and steady-state temperature achieved under 1 sun

Sample	Thickness (μm)	Temp (K)
P3HT:CoMoCAT CNTs	5.7	308.5
F_4TCNQ-Doped PBTTT	2.9	306.5
CoMoCAT CNTs	7.5	310.8
P3HT	24.4	316.7
PEDOT:PSS	52.5	326.8
PBTTT	19.4	315
eDIPS:cellulose	10	323
PLA	5000	328

The steady-state temperature of the polymers under illumination in ambient conditions as a function of irradiance can be seen in Figure 3-6b. The 3D-printed black PLA and PEDOT:PSS achieved the highest steady-state temperatures. PEDOT:PSS, with a thickness of 46 μm, heated up to around 75 °C under 2 sun. PEDOT:PSS exhibits broadband absorption in the NIR, and the thickness of the PEDOT:PSS likely enhanced its ability to absorb incident irradiation also in the visible, thus leading to the large increase in temperature. The thicknesses for all the samples used along with their achieved temperatures are listed in Table 3.3.

The impact of thickness can be seen by comparing pristine PBTTT and F_4CNTQ-doped PBTTT (19 μm for PBTTT and 3 μm for F_4CNTQ-doped PBTTT). Pristine PBTTT heated up to 60 °C, while F_4CNTQ-doped PBTTT heated up to 50°C under 2 sun. Doping broadens the absorption spectrum of organic semiconductors, but organic semiconductors can only be effectively doped in thin films, which significantly hampers light absorption.

Of the carbon nanotubes samples, the composite eDIPS with cellulose sample heated up the most (Figure 3-6c). The CNTs are grown with cellulose to create a porous composite paper. Cellulose has a low thermal conductivity, so the composite has a low thermal conductivity compared to the other CNT-based materials. Abol-Fotouh et. al reported the in-plane thermal conductivities of pure eDIPS and eDIPS:cellulose composites with a given cellulose/CNT ratio to be 27 W m^{-1} K^{-1} and 2.7 W m^{-1} K^{-1}, respectively [13]. The lower thermal conductivity is likely reducing the conduction losses to the contacts as observed from comparing images from the IR camera, allowing the sample to achieve higher temperatures.

In a real solar organic thermoelectric generator, increasing the temperature difference between the hot and cold sides of the device will enhance the performance of the device, since the TEG efficiency will improve as shown in Eq. 1.14 in chapter 1. From the results in Figures 3-6b and 3-6c, optical concentration is one strategy to increase temperature difference, however, convection and conduction losses at higher temperatures become more prevalent in ambient conditions. Below 2 sun, the steady-state temperature increased steadily. Above 2 sun, the steady-state temperature started to level off, which likely indicates the increasing impact of convection and conduction effects. With increasing material temperature, the temperature difference between the material and the ambient air also increases, thus creating convection currents that reduce temperature. Vacuum conditions become necessary to reduce convection, implying an added degree of complexity to the system [1], [55]. It should also be noted that the measurements are reversible, i.e. no apparent permanent change was made to the thermoelectric materials upon illumination with concentrated light.

3.3. Photoconductivity in Organic Thermoelectrics

Solar thermoelectric generators (STEGs) use light as a heat source, as opposed to traditional thermoelectric generators that use waste heat. Light effects, such as photoconductivity, may also appear in parallel to the thermoelectric effect [56], [57]. Since the materials are semiconductors, an incident photon with energy exceeding that of the materials bandgap can excite carriers. When the absorption results in the generation of a hole-electron pair, no net charge is gained in the material. Unlike in organic solar cells, any photogenerated charge carrier pairs that may arise in STEGs are not separated and collected at their respective electrodes. Rather, they will both diffuse towards the cold side of the TE leg, resulting in zero net current. On the other hand, carriers from states within the material's bandgap (traps), can lead to the generation of extra, photogenerated charges. Recalling equation 1.9, these extra charges could enhance the electrical conductivity, and in turn, enhance the thermoelectric performance of the material. Alternatively, the mobility of a charge located in the conduction band could be enhanced by the additional energy provided upon photon absorption, thus increasing conductivity.

To probe the existence of photoconductivity effects, the resistance of the sample was measured continuously using a two-point method while the illumination of the solar simulator was cycled on and off. The temperature (wine-colored line) and resistance (dark blue line) response of pristine PEDOT:PSS and CoMoCAT CNTs under illumination is

shown in Figures 3-7a and 3-7b, respectively. For PEDOT:PSS, illumination causes the electrical conductivity to increase instantaneously, a phenomenon reported by Xing et. al. [58]. The instantaneous increase in conductivity is attributed to photoconductivity, which arises from an increase in the charge carrier mobility. With continued illumination, the temperature increases, but the electrical conductivity decreases, indicative of a metallic conductor. PEDOT systems have been reported to exhibit metallic behavior in literature [59]–[61], and to confirm the metallic behavior of the PEDOT:PSS used, the PEDOT:PSS sample was heated and the resistance was recorded (Figure 3-7c). The conductivity of the PEDOT:PSS sample decreased with temperature, confirming metallic behavior. In the case of CoMoCAT CNTs, a small photoconductivity effect can be observed, with resistance decreasing by 1.5% under illumination.

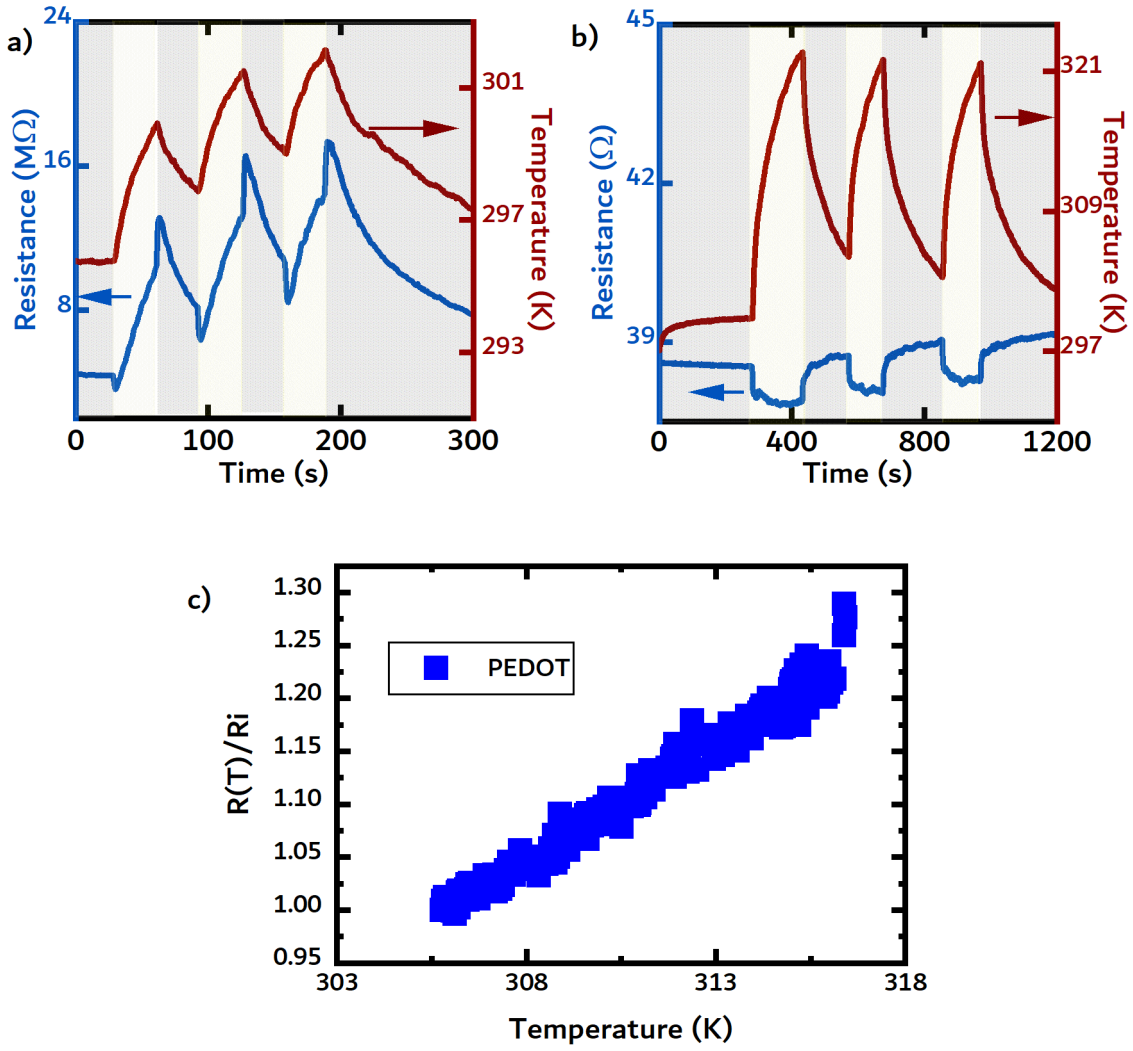

Figure 3-7. Temporal resistance (blue) and temperature (red) response of a) PEDOT:PSS and b) CoMoCAT CNTs under 1 sun. The yellow and shaded regions indicate the time when the materials were illuminated and in dark, respectively. c) Normalized resistance of pristine PEDOT:PSS as a function of temperature. The figure was adapted from Jurado et al. [2].

3.3.1. Photo-Seebeck effect

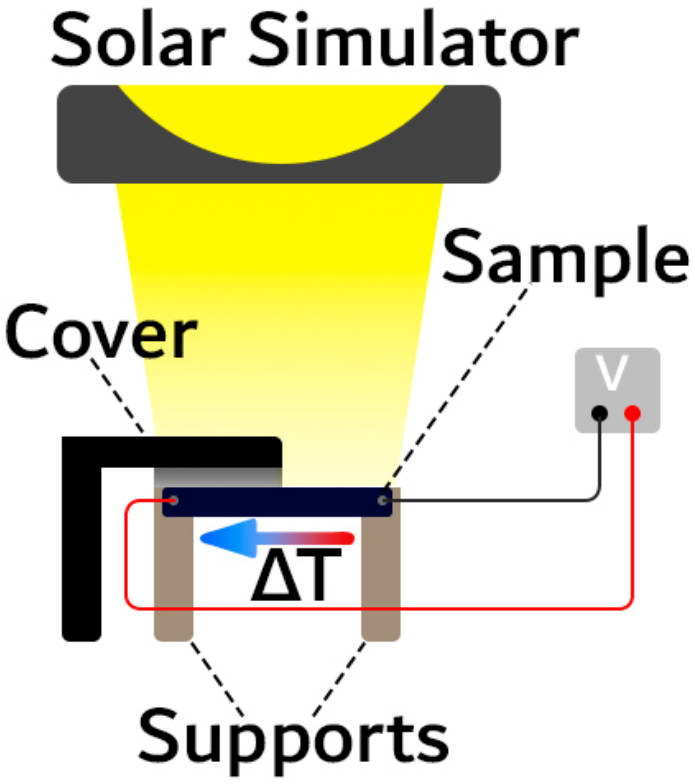

Figure 3-8. Schematic of the photo-Seebeck experiment. Adapted from Jurado et al. [2].

A custom-made setup was built to probe the photo-Seebeck effect (Figure 3-8). Briefly, one end of the sample was illuminated while the other end was covered. The sample was illuminated, and the temperature and Seebeck voltage were recorded with thermocouples contacted at each end of the sample. Once the sample reached a steady-state temperature, the illumination was turned off, and temperature and the Seebeck voltages were recorded as the sample cooled. The experiment was repeated using a conventional heat source (in this case, a hot plate), and the Seebeck coefficients from both experiments were compared. The Seebeck coefficient of pristine PEDOT:PSS was difficult to measure likely due to the adsorption of water by PEDOT:PSS [62], so the pristine PEDOT:PSS was treated with DMSO.

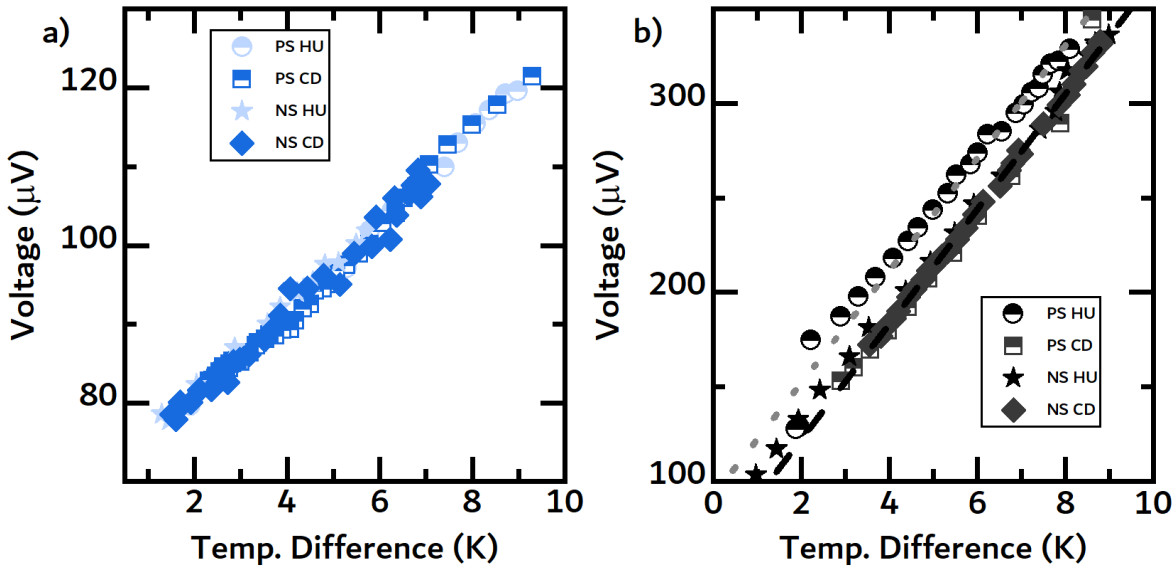

Figure 3-9. a) Photo-Seebeck (PS).) and "normal" Seebeck (NS) measurement for DMSO-treated PEDOT:PSS. The Seebeck voltage was continuously measured as the materials were heated up (HU) and cooled down (CD). b) Photo-Seebeck and "normal" Seebeck measurement for CoMoCAT CNTs. The dotted gray line is a linear fit for the PS HU data set, while the dashed black line is the linear fit for the three other data sets.

For both materials, there were no observable photoinduced effects in the Seebeck coefficients. Figures 3-9a and b show the recorded Seebeck voltages against temperature difference for the DMSO-treated PEDOT:PSS and CoMoCAT CNTs samples, respectively. The Seebeck coefficients for the CoMoCAT CNTs and DMSO-treated PEDOT:PSS samples were found to be around 30 μV K^{-1} and 5.6 μV K^{-1}, respectively. For the CoMoCAT CNTs, there is a slight difference in the Seebeck coefficient when light is used as a heat source. The linear fit of the data (gray dotted line) reveals a Seebeck coefficient of 29.70 ± 0.87 μV K^{-1} compared to a Seebeck coefficient of 30.40 ± 0.78 μV K^{-1} measured when a traditional heat source is used. For the DMSO-treated PEDOT:PSS, the Seebeck coefficients were found to be similar independent of the heat source. In conclusion, the photoinduced charge carrier density does not negatively impact the Seebeck coefficient, and the major effect of light absorption on the studied organic TE materials is to increase temperature, with no significant secondary effects observed.

3.4. Design of Solar Organic Thermoelectric Generators

In this section of the chapter, planar and vertical device geometries are discussed. Traditional STEGs based on inorganic materials have vertical geometries, but the flexible nature of organic materials allows for innumerable device architectures, all based on a

planar geometry. Vertical devices likely possess superior light absorption compared to planar devices, since thickness enhances light absorption. Additionally, vertical devices have a high packing density, which can lead to high output voltages [63]. Planar devices, on the other hand, have lower filling factors and if supported on a flexible substrate, are susceptible to thermal losses. However, organic TEGs can emulate vertical devices because of their flexible nature and are more readily integrated into applications requiring devices with conformal geometries.

3.4.1. Planar Devices

Organic TEs are mainly only able to develop significant temperature differences in the lateral direction because they are mainly thin-film materials. However, the flexibility of organic materials can be harnessed to design many possible device geometries for SOTEGs based on the constraint of a planar geometry device. Essentially, one end of the device must be exposed to the Sun while the other end must be covered to generate the temperature difference, but the materials can be bent or folded in numerous ways, as show in Figure 3-10. In one design, the device could be placed on the edge of a brick or block of cement, as seen in Figure 3-10a. The top surface would be exposed to direct sunlight, while the lateral side can be shaded. Figure 3-10b shows a T-shaped device that can be stuck into the soil. In this design, the soil could act as a heat sink generating a temperature difference between the top side exposed to direct sunlight and the lateral legs stuck into the soil. Alternatively, it could be attached to the underside of a transparent hot surface, such as an organic solar cell. In this configuration, the lateral parts act as the fins of a heat sink. Figure 3-10c shows an S-shaped device. Direct sunlight heats the exposed top surface, while the bottom part of the device remains covered, thus generating a temperature difference. It would be necessary to pay special attention to the electrical contacts in this configuration, as additional, unwanted resistances may result from too long or too small electrical interconnects.

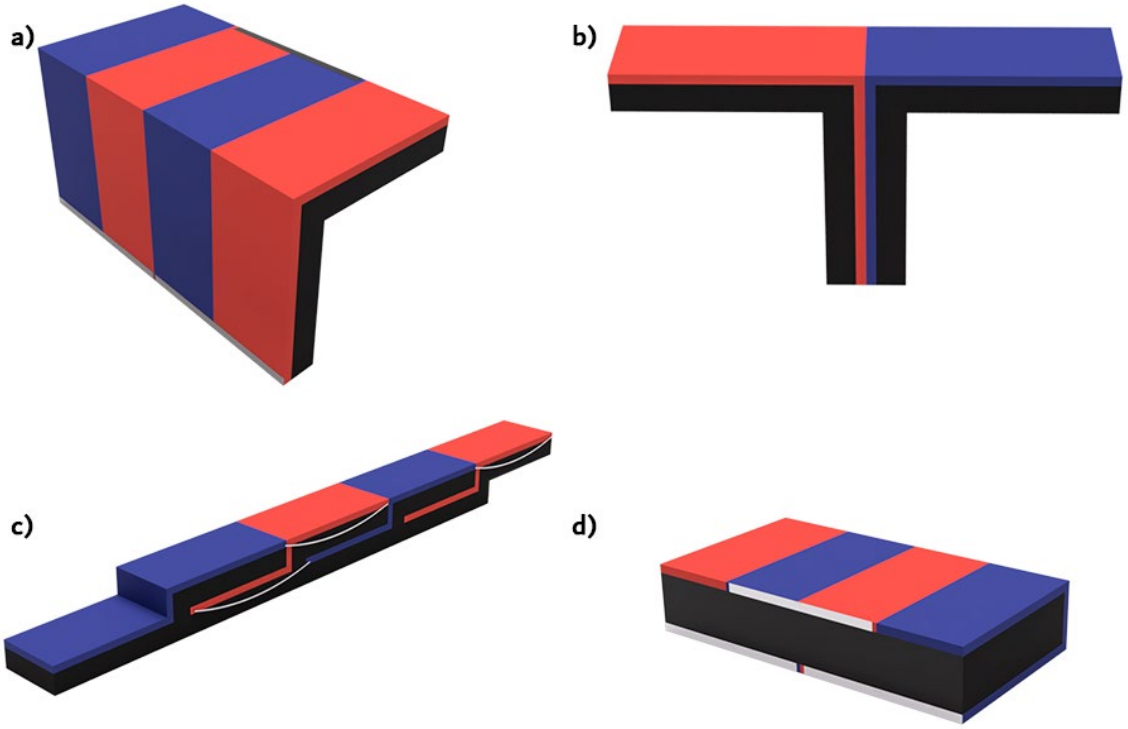

Figure 3-10. Possible device architectures of planar SOTEGs. a) L-shaped device where the top part is exposed to sunlight. b) T-shaped device where the top part is exposed to sunlight and the bottom part can be stuck into soil, for example. c) S-shaped devices where the top part is exposed to sunlight and positioned to cover the bottom part. d) U-shaped devices where the top part is exposed to sunlight and the bottom part is in contact with the ground.

Several geometrical parameters, namely illuminated area, load resistance and leg length, affect the power output of a single SOTEG leg. Prudent SOTEG device designs should account for these parameters to optimize power output, so the work in the next section focused around investigating these parameters. Using a custom-built setup shown in Figure 3-11, the materials were illuminated using a solar simulator and the illuminated area of each sample was varied using a translation stage and a cover. Before beginning the measurement, the internal resistance of the material was measured, and a variable resistance matched to the internal resistance of the material was connected to the sample. A nanovoltmeter measured the voltage drop across the load resistor to measure the power generated by the material. Additionally, the V_{OC} of the material was recorded by disconnecting the load resistance and measuring the voltage drop across the material.

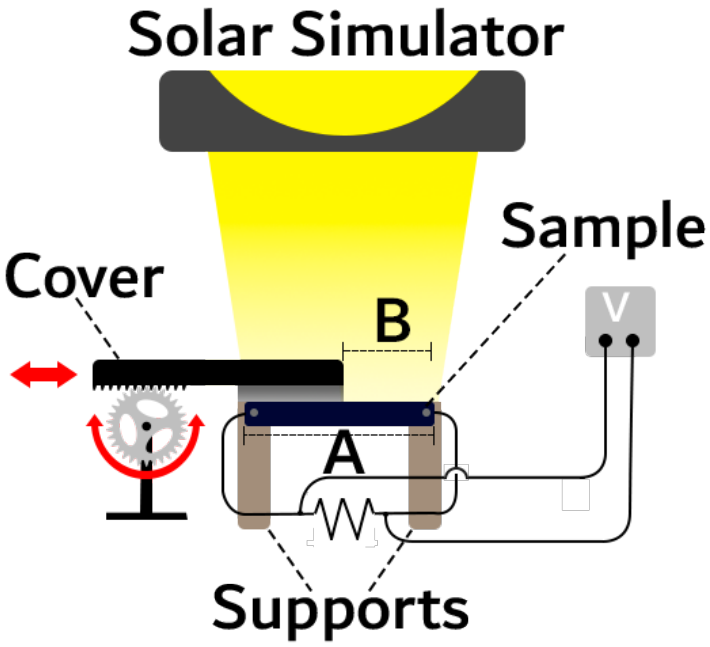

Figure 3-11. Schematic of the power output experiment where A is the area of the entire leg and B is the illuminated area.

The measured voltages and power output for each sample as a function of illuminated area under 2 sun are shown in Figure 3-12. It is important to note that the two measurement points at 0% and 100% illuminated area account for heat sink effects arising from the electrodes. At 0% illumination, although the sample was not illuminated, one of the electrodes was illuminated, causing a temperature difference to arise between the two ends of the sample. So the measurement point at 0% illuminated area was done in dark conditions. At 100% illumination, the entire sample was illuminated, but one of the electrodes was partially covered. Therefore, the sample and electrodes were completely illuminated to ensure the electrodes did not cause a temperature difference across the ends of the samples.

For the CNT samples (Figures 3-12a and c), the composite sample had a slightly higher power output then the pristine CNTs sample. Likely, the low thermal conductivity introduced by the cellulose compensates the reduced electrical conductivity. Only 40% of the material (5 -6 centimeters aproximately) needs to be illuminated to achieve maximum power. For the PEDOT samples (Figures 3-12b and d), the measured powers were extremely small compared to the powers measured for the CNT-based samples (on the order of picowatts compared to nanowatts). The voltages measured for the pristine PEDOT:PSS sample have the opposite polarity, and are on the order on mVs, which can likely be attributed to an ionic Seebeck effect [23].

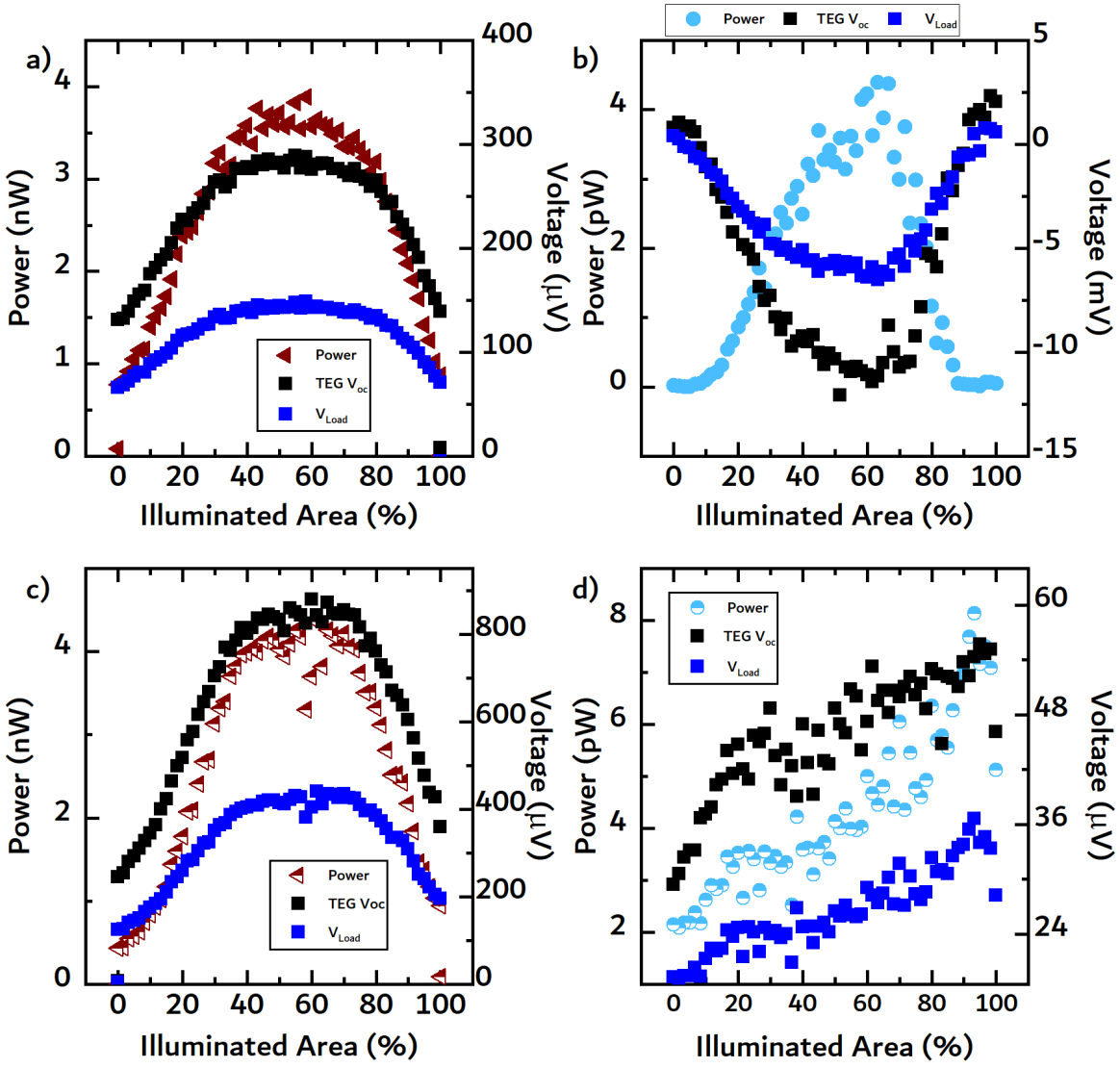

Figure 3-12. Voltage measured across the load, open circuit voltage and calculated power output as a function of illuminated area for a) pure eDIPS, b) pure PEDOT:PSS, c) eDIPS:Cellulose, and d) DMSO-treated PEDOT:PSS.

The P-V curves of the pristine eDIPS sample for different amounts of illuminated area are shown in Figure 3-13a. Maximum power was obtained when the load resistance is nearly matched to the resistance of the leg (approximately 5.7 ohms). To investigate the influence of leg length, a sample of pure eDIPS was cut multiple times, and the power extracted was measured (Figure 3-13b). The amount of area that needs to be illuminated is likely to be dependent on sample length. Figure 3-13c plots the illuminated area at P_{max} against sample length. At shorter leg lengths, more area needs to be illuminated. This can likely be explained by changes in the resistance and the thermovoltage that develops across the material. The resistance of the sample decreases as the leg is shortened, but the thermovoltage across the sample changes due to thermal losses. At long lengths, the

resistance limits the amount of power generated. At medium leg lengths, the thermovoltage is maintained, so the reduction in resistance leads to an increase in the amount of power generated. At very small lengths, the thermovoltage across the sample began to decrease due to thermal equilibration, thus leading to a decrease in the amount of power generated.

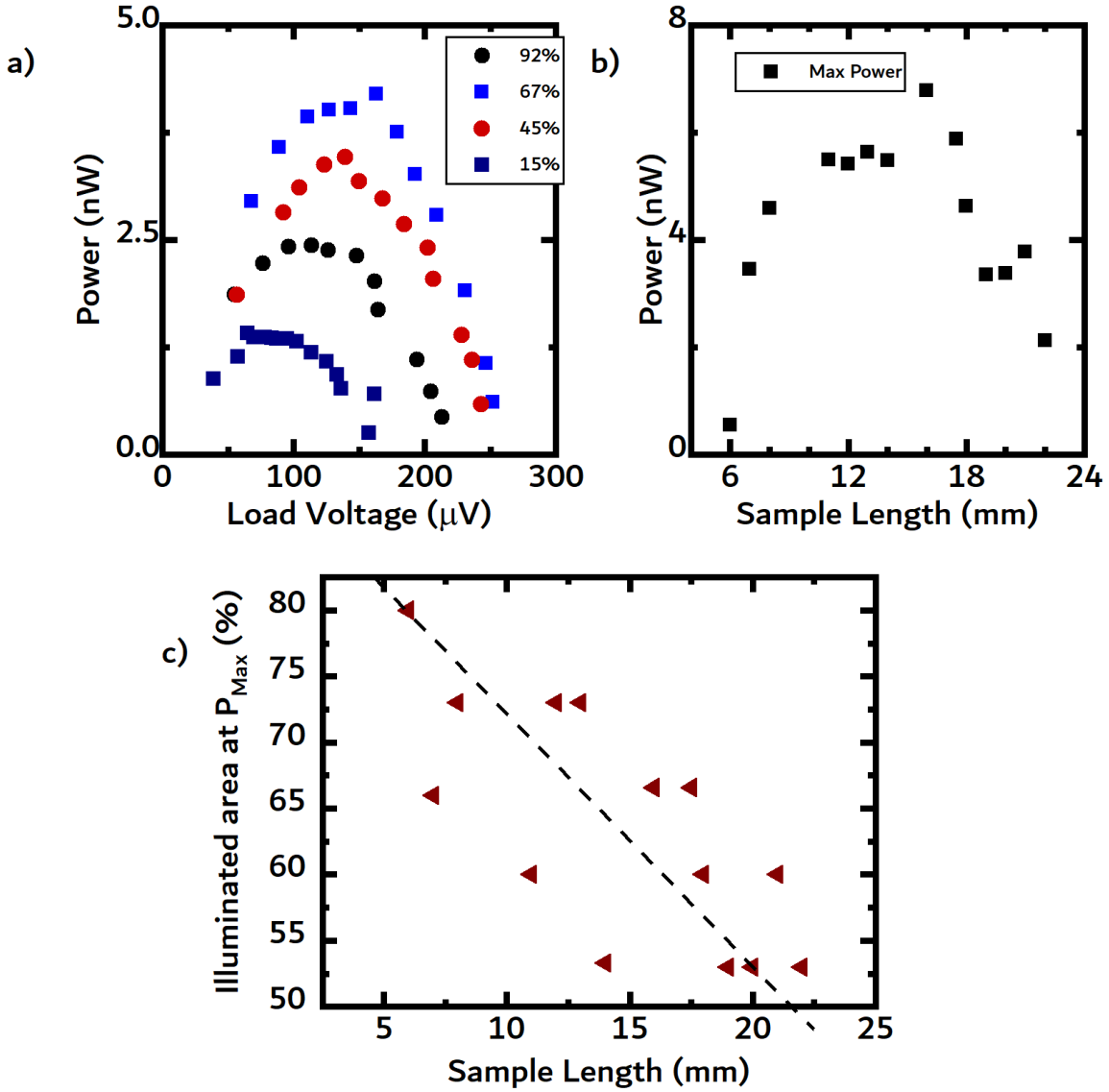

Figure 3-13. a) Power curves for eDIPS CNTs for different amounts of illuminated area. b) Power as a function of the distance between electrodes (leg length). c) Sample length vs illuminated area where maximum power output is achieved.

3.4.2. Vertical Devices

For solar thermoelectrics, vertical devices are particularly interesting because light absorption will likely be enhanced in a vertical configuration. In vertical devices, the legs are thick, which is ideal for light absorption. Thicker devices absorb more light, thereby enhancing temperature rise at the hot end. A higher operating temperature difference will lead to higher thermoelectric efficiencies. Vertical structures with organic materials are difficult to fabricate despite the potential advantages they might offer. The deposition techniques used for solution-processed materials, such as blade-coating and drop-casting, typically only allow for thin-films to be obtained. Foaming techniques involving gas depressurization or supercritical fluids, for example, can be used to achieve porous materials [64], [65]. In this thesis, porous materials were not investigated, but they could be used to make vertical devices.

For materials supported on a substrate, the filling factor, defined as the ratio between the active layer and the thickness of the substrate, would be small if the sample is simply rotated 90 degrees. Assuming an active layer thickness of 10 μm and a substrate thickness of 100 μm, the filling factor would be 10%.

The work in this section was carried out in collaboration with Schroeder Research Group at University College London. The collaborators synthesized novel organometallic coordination polymers (OMCPs), which have polymer structures containing metal cation centers linked by organic ligands. Three OCMPs were synthesized by the collaborators: Poly(nickel-ethylenetetrathiolate) (Ni-ett), poly(nickel-[2,2′-bi(1,3-dithiolylidene)]-4,4′,5,5′-tetrakis(thiolate)) (Ni-diett), and poly(nickel-benzene-1,2,4,5-tetrakis(thiolate) (Ni-btt). Their chemical structures are shown in Figure 3-14. Apart from compositional, structural, and electronic structure characterization, the collaborators also characterized the Seebeck coefficient and electrical conductivity of the materials, as shown in Table 3.4. The work carried out in this thesis focused on characterizing the thermal conductivity using Raman thermometry and the photothermal properties of the materials. The reader is referred to the published work by Liu et al. [3].

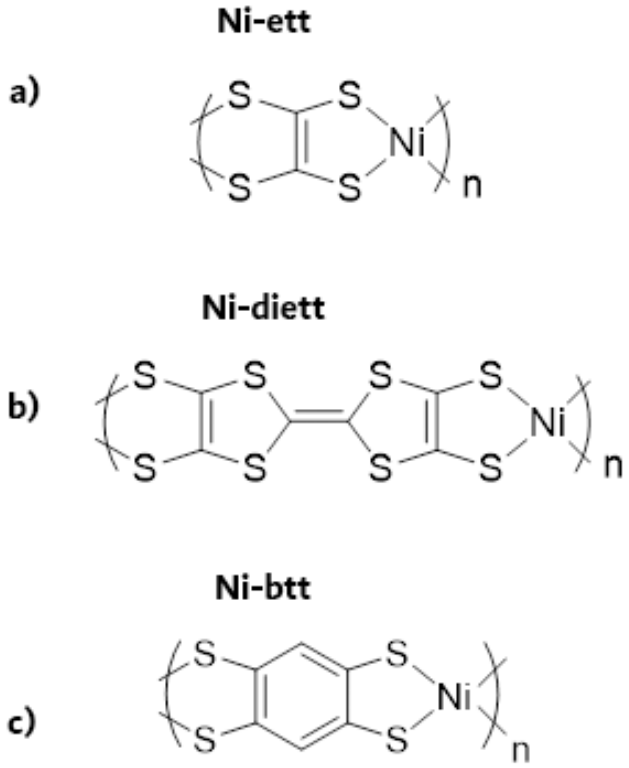

Figure 3-14. Structures of the three synthesized OCMPs by Liu et al. [3] : a) Ni-ett, b) Ni-diett, and c) Ni-btt

Table 3.4. Reported thermoelectric properties of the OMCPs

Material	**Electrical conductivity (S cm^{-1})**	**Seebeck coeffcient (μV K^{-1})**	**Power factor (μW m^{-1} K^{-1})**
Ni-ett	7.49 ± 0.05	−86.1 ± 1.2	5.55 ± 0.19
Ni-diett	5.70 ± 0.05	−40.2 ± 1.6	0.94 ± 0.08
Ni-btt	7.11 ± 0.01	12.7 ± 1.2	0.12 ± 0.02

3.4.2.1. Thermal Conductivity Characterization of OMCPs with Raman Thermometry

Raman thermometry is a thermal characterization technique which makes use of Raman scattering phenomena to determine the local temperature of a material. In single-laser Raman thermometry, monochromatic light from a laser, acting as a heat source, is focused on the material, and the back scattered light is collected by a Raman spectrometer [66]. The local heating is controlled by the laser power, which also influences the temperature-dependent Raman spectra. In order to calculate the thermal conductivity of a material, two steps are needed. In a first step, the shift in the spectral positions of the Raman peaks is recorded as a function of laser power. In a second step, an external heat source is used to

vary the temperature of a sample, and the shift in the spectral positions of the Raman peaks is once again recorded for very low laser powers. From these two steps, the Raman shift by the material can be related to local temperature rise. Assuming a semi-infinite medium, the thermal conductivity can be calculated from the following equation:

Equation 3.2. $$\kappa = \frac{P_{abs}}{\pi R \Delta T}$$

where P_{abs} is the laser power absorbed by the sample, R is the Gaussian spot radius, k is thermal conductivity of the specimen, and ΔT is the temperature rise in the laser spot region. In this measurement, given the thickness of the samples (mm) and their low reflectivity, it is reasonable to assume all incident laser radiation is absorbed by the material, so P_{abs} is taken to be the incident laser radiation, measured with a power meter at the sample location. In conclusion, the thermal conductivity is obtained by measuring the temperature rise within the laser spot as a function of the laser power absorbed by the sample.

Each sample was polished using fine grained sand paper, and three independent points for each sample were measured and averaged to arrive at the reported thermal conductivities in Table 3.5. Typical Raman spectra for the Ni-diett sample at different absorbed power are shown in Figure 3-15a. The peaks around 360 cm^{-1} and 490 cm^{-1} become redshifted at increasing power. Figure 3-15b shows the calibrated temperature rise at one point for all three samples as a function of the absorbed power. From this plot, the thermal conductivities can be extracted.

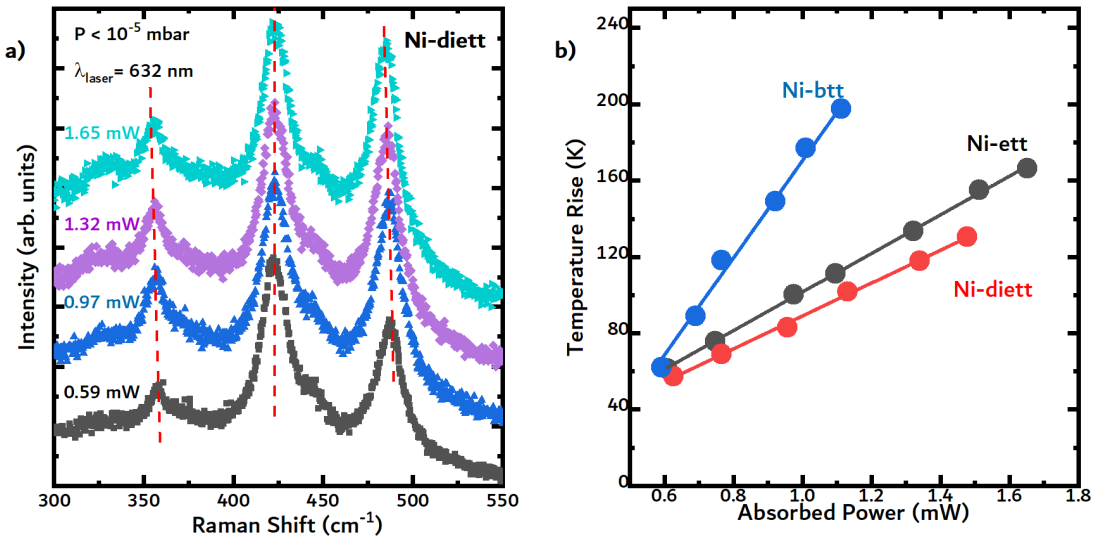

Figure 3-15. a) The representative Raman spectra of the Ni-diett sample at different absorbed powers. Note that only the peaks around 360 cm-1 and 490 cm-1 exhibit a redshift as the absorbed power increases. b) The

calibrated temperature rise of each sample as a function of the absorbed power. This figure was adapted from Liu et al. [3].

Table 3.5. Measured thermal conductivities for the OCMPs

(Units in W m^{-1} K^{-1})	Ni-ett	Ni-diett	Ni-btt
Point 1	1.67	1.25	0.64
Point 2	1.53	1.93	1.61
Point 3	1.92	1.37	1.43
Average	1.71	1.51	1.23
Stdev	0.2	0.36	0.52

All three OMCP materials show relatively low thermal conductivities (<2 W m^{-1} K^{-1}) in freestanding pellets, with the lowest value recorded for Ni-btt (1.2 ± 0.5 W m^{-1} K^{-1}) and a slightly higher value for Ni-diett (1.5 ± 0.4 W m^{-1} K^{-1}) and the highest value for Ni-ett (1.7 ± 0.2 W m^{-1} K^{-1}). The origin of the differences can likely be attributed to differences in the surface topography of the samples, rather than from differences in the molecular structure. The optical images of the samples are shown in Appendix A, Figure A.1. From the optical images, there are clear inhomogeneties in the surface roughness of all samples. In the Ni-ett sample, smooth and rough domains can be seen (Figure A.1a). The Ni-diett sample has an almost porous-like structure (Figure A.1b), while the Ni-btt sample has a rough surface structure (Figure A.1c). The inhomogeneties in surface roughness of the samples are likely responsible for the differences in thermal conductivities. These inhomogeneties could indicate there are local variations in the thermal conductivities within the samples. Further details on the Raman analysis of these samples can be found in the Appendix A.

3.4.2.2. Photothermal Characterization of OMCPs

The OMCPs from Liu et al were used to study vertical devices. The particles of the OMCPs were compressed into thick pellets (aprox. 2 mm), and the photothermal properties of the materials were characterized. OMCPs, as opposed to organic materials, suffer from poor solubility, and thus fabricating shape conformal materials is difficult [3].

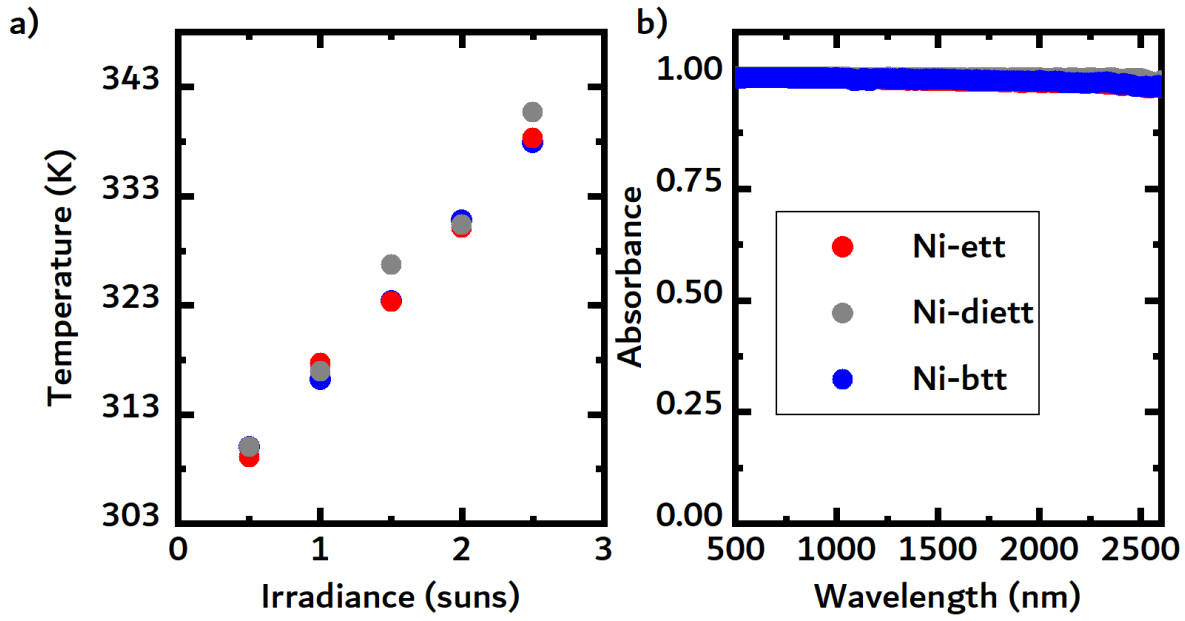

Figure 3-16. a) Temperature rise of OMCPs pellets versus Irrandiance. b) Vis–NIR spectra of the three OMCPs.

The three OMCPs heated up similarly under illumination (around 340 K under 2.5 sun) and strongly absorb across the solar spectrum (Figures 3-16a and b, respectively). The thermal conductivity measurements of the OMCPs will be discussed in further detail in the following section, but the OMCPs have similar thermal conductivities to the CNT:cellulose sample. The OMCPs displayed thermal conductivities in the range of 1.2 to 1.8 W m^{-1} K^{-1}, compared to the CNT:cellulose sample with a slightly higher thermal conductivity of 2.7 W m^{-1} K^{-1}. Both sets of samples achieved temperatures around 340 K under 2.5 sun.

In a simple experiment to probe the feasibility of vertical devices, the Ni-btt pellet was attached to a heat sink and placed under the solar simulator. The voltage between the top and bottom of the sample was recorded as illumination at 1 sun conditions was cycled on and off (Figure 3-17). Under illumination, the thermovoltage was found to be 120 μV. Using the absolute value of the reported Seebeck coefficient at 300 K (40 μV K^{-1}), the temperature difference between the top and bottom side of the sample was calculated to be 3 K. Although the temperature difference is small, further work can be done to enhance this temperature difference. For example, one straight-forward strategy to improve the temperature difference would be to produce thicker pellets, which is something that can readily be achieved.

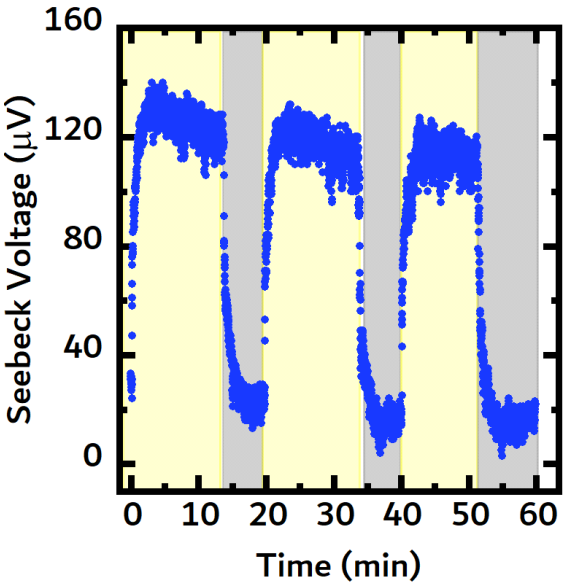

Figure 3-17. Temporal voltage response of the Ni-btt under 1 sun illumination

3.4.3. Comparison of geometries

When comparing the two geometries, the thickness of the TE legs in vertical devices is comparable equivalent to the length of the TE legs in planar devices. As discussed earlier, there is a tradeoff between electrical resistance and thermovoltage with leg length, recalling Figure 3-13b. At optimal lengths, the reduction in electrical resistance compared to long leg lengths enhances power output with little or no effect on the thermovoltage. At shorter leg lengths (<10 mm), the reduction in electrical resistance no longer compensates the reduction in thermovoltage, so power output drops. The same principle is true for the thickness of TE legs in vertical devices. There is an optimal leg thickness, and likely the 2 mm thick OMCP pellets are too thin. An appreciable temperature difference is unable to develop across the thickness of the pellet, hence the small Seebeck voltage. Although the thermal conductivities and electrical conductivities of the OMCP pellet is different from the CNT sample used in the leg length experiment, it is reasonable to conclude that significantly thicker pellets would help lead to a higher temperature difference across the TE leg, and ultimately better TE performance.

For the continuation of the work in this chapter, the planar geometry was chosen as the more suitable geometry. The devices discussed in the next section have been based off of planar geometries.

3.4.4. Devices with Mirror Concentration

Incorporating mirrors into SOTEGs is a strategy to concentrate incident solar radiation on to one end of the SOTEG. Concentration to 2 sun may be ideal because the TEG efficiency will be higher due to the increased temperature rise of the materials without significant heat losses to convection and conduction. Apart from concentration, the mirrors can be used to cover the other end of the SOTEG.

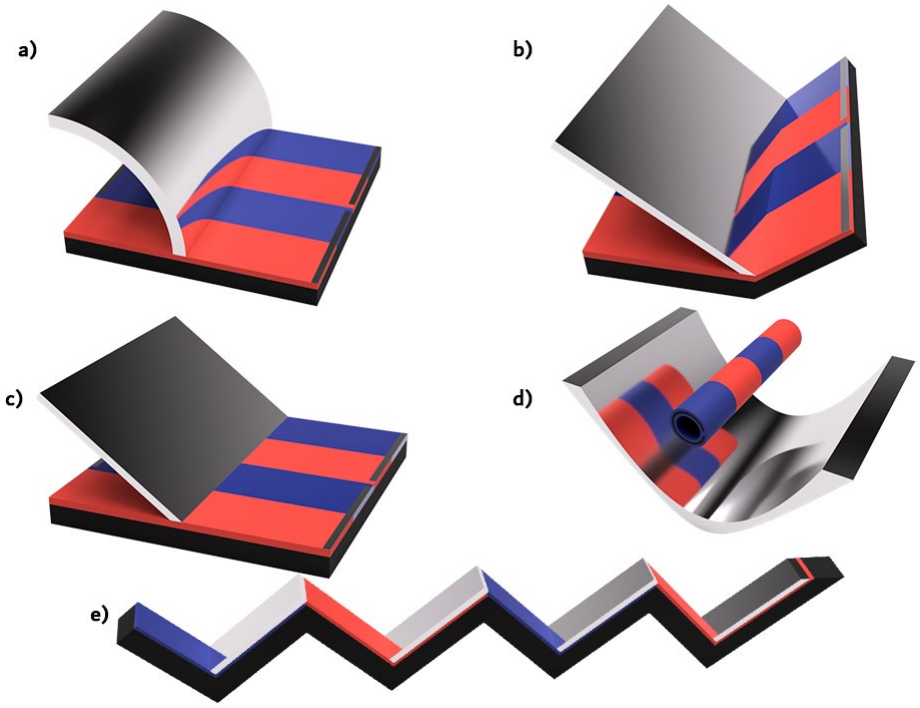

Figure 3-18. Possible device architectures of organic SOTEGs with concentrators. a) Device with a non-flat mirror where a mirror concentrates sunlight on to the exposed part of the device while covering the other part. b) Bent device with a flat mirror that concentrates the sun onto one part while covering the other part. c) Device with a flat mirror that concentrates the sun onto one part while covering the other part. d) Device using a parabolic mirror that concentrates the sun onto one part. e) Accordion-like device where mirrors concentrate light onto certain parts of the device while covering other parts. This figure was adapted from Jurado et al. [2].

The amount of concentration will depend on factors such as the incidence angle of radiation, SOTEG leg length, and the angle between the mirror and the exposed part of the SOTEG. For the case of a bent SOTEG like the one shown in Figure 3-18b, the amount of light concentrated onto the exposed part of the SOTEG can be calculated from:

Equation 3.3. $$C = \frac{L_1 + L_2}{L_1}$$

where L_1 is the base length of the exposed part and L_2 is the base length of the covered part. For reference, a schematic of the device can be seen in Figure 3-19.

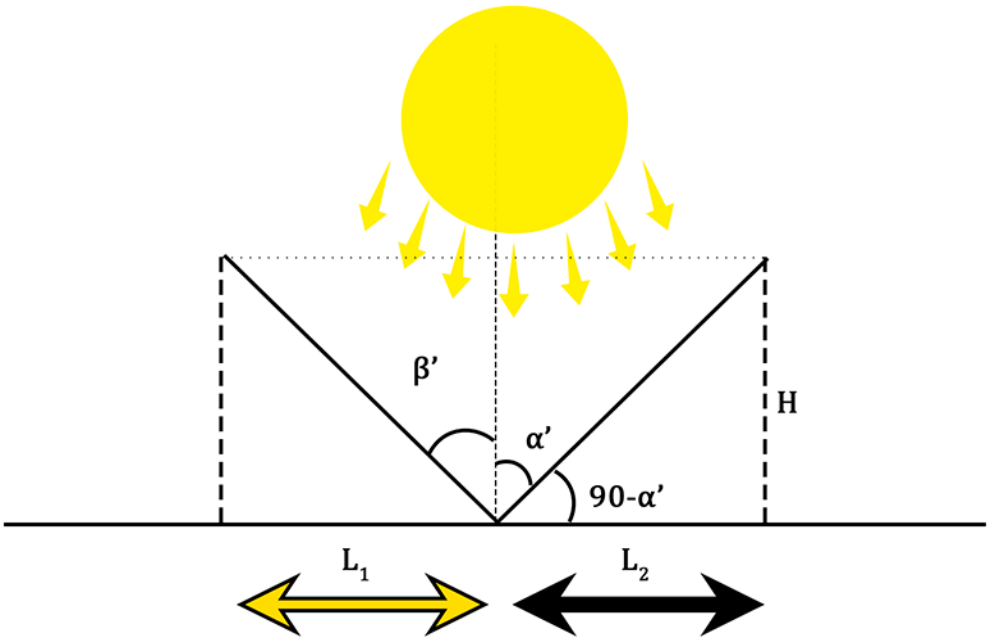

Figure 3-19. Schematic of a SOTEG with a concentrating mirror. This figure was adapted from Jurado et al. [2].

From geometry, the exposed and covered leg lengths can be found:

Equation 3.4. $$\tan\beta' = \frac{L_1}{H}$$

Equation 3.5. $$\tan\alpha' = \frac{L_2}{H}$$

Combining equations 2.3-2.5, C can be written in terms of α' and β':

Equation 3.6. $$C = 1 + \frac{\tan\alpha'}{\tan\beta'}$$

When α' is equal to β', the device has a symmetric V-shaped geometry and the concentration factor is 2. This device architecture has been demonstrated in organic solar cells, where the efficiency was enhanced with opening angle compared with planar solar cells [67].

For the case of a device with the geometry shown in Figure 3-18c, the calculations for concentration are slightly more complex. A schematic of the SOTEG device is shown in Figure 3-20.

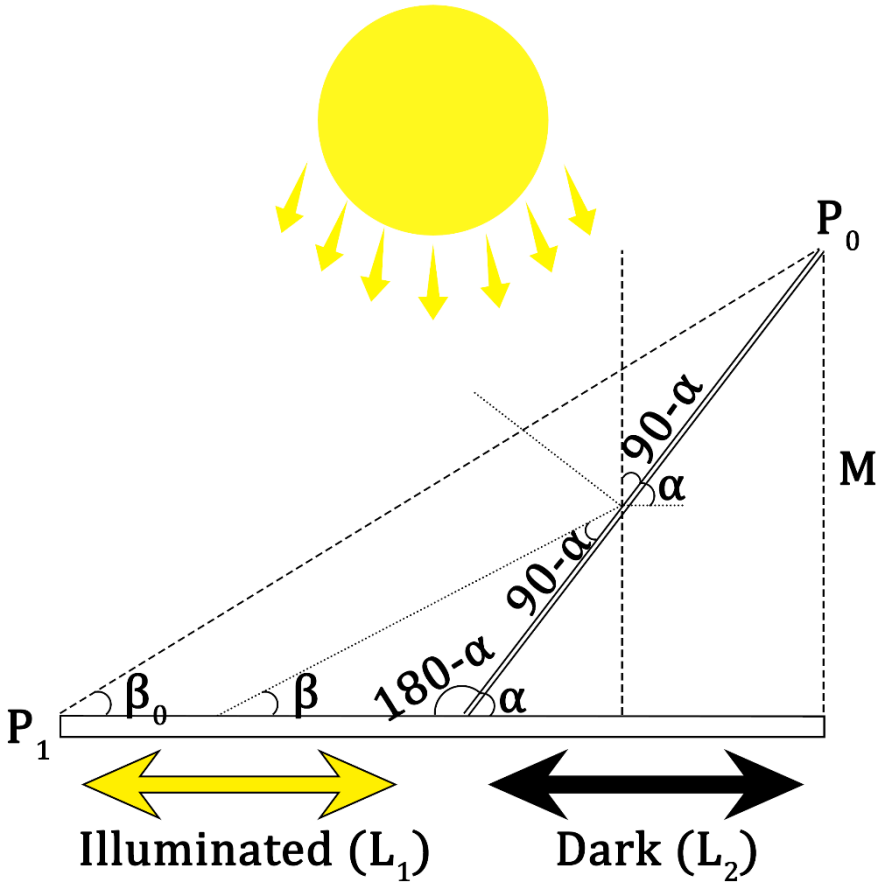

Figure 3-20. Schematic representation of a SOTEG of an alternative configuration incorporating a concentrating mirror. This figure was adapted from Jurado et al. [2].

With this geometry, max concentration occurs when light is reflected from P_0 to P_1 and can defined as:

Equation 3.7. $$C_{Max} = \frac{L_1+L_2}{L_1} = \frac{L}{L_1}$$

where L_1 is the length of the illuminated side, L_2 is the length of the shaded side, and L is the total length of the device. From geometry:

Equation 3.8. $$\tan\beta_0 = \frac{M}{L} = \frac{L_2 \tan\alpha}{L}$$

β can be solved from:

Equation 3.9. $$\beta + (180° - \alpha) + (90° - \alpha) = 180°$$

rearranging for β

Equation 3.10. $$\beta = (2\alpha - 90°)$$

Next, α can be solved from:

Equation 3.11. $$\tan\beta = \tan(2\alpha - 90°) = \frac{\tan(2\alpha) - \tan(90°)}{1 + \tan(2\alpha)\tan(90°)}$$

Because tan 90° is equal to infinity, the right hand side can be simplified to:

Equation 3.12. $$\tan\beta \cong -\frac{1}{\tan(2\alpha)} = \frac{\tan^2(\alpha - 1)}{2\tan\alpha}$$

Summarily, β_0 can be solved:

Equation 3.13. $$\tan\beta_0 = \tan(2\alpha_0 - 90°) = \frac{\tan^2(\alpha_0 - 1)}{2\tan\alpha_0} = \frac{L_2\tan\alpha_0}{L}$$

Which can be simplified to

Equation 3.14. $$\tan^2(\alpha_0 - 1) = \frac{2L_2\tan^2\alpha_0}{L}$$

Solving for α_0

Equation 3.15. $$\alpha_0 = \operatorname{atan}\sqrt{\frac{C_{Max}}{2 - C_{Max}}}$$

This equation has real solutions only when L_2 is less than L_1, which means the theoretical maximum concentration for this geometry is 2.

3.5. Proof of Concept device

A proof-of-concept SOTEG consisting of 6 legs and a concentrating mirror was fabricated using an architecture similar to Figure 3-18b. Figure 3-21 shows an artistic representation of the device. The p-type legs were chosen to be eDIPS, while the n-type legs were eDIPS doped with polyethylenimine (PEI) [11], [68]–[70]. From the earlier experiments on leg length, the legs were chosen to be 1.5 cm in length and 0.8 cm in width. The measured Seebeck coefficients for the pristine eDIPS and PEI-doped eDIPS were 45 and −35 μV K^{-1},

respectively (Figure 3-22), leading to an overall Seebeck coefficient for the device of 240 μV K^{-1}. Black PLA was chosen as the support material, and the legs were carefully interconnected using silver paste. An actual photo of the device can be seen in Figure 3-23.

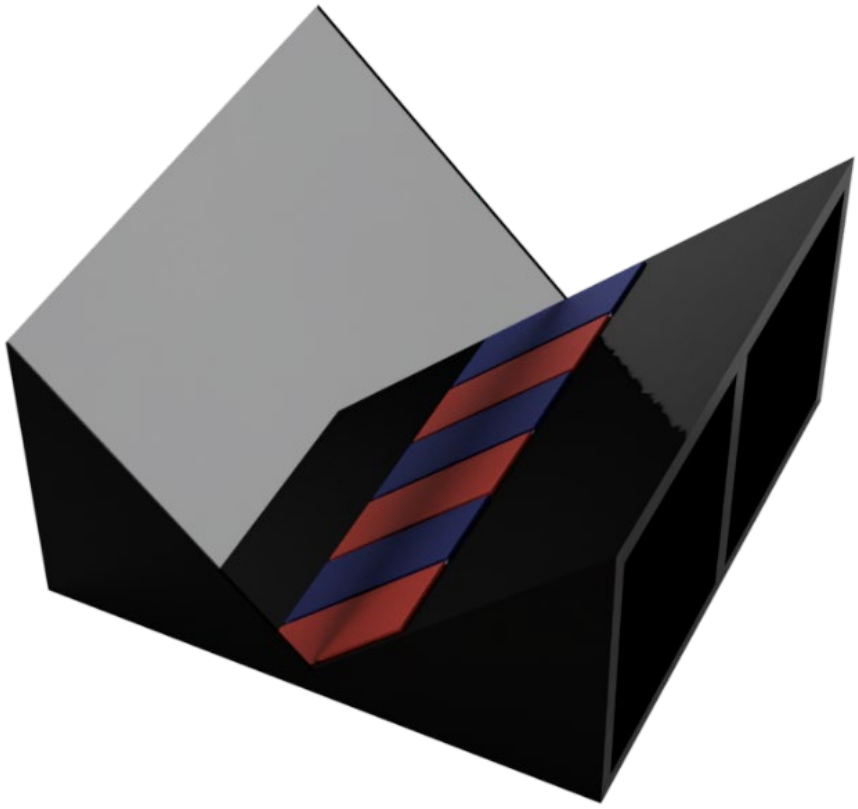

Figure 3-21. An artistic representation of the proof-of-concept device. This figure was adapted from Jurado et al. [2].

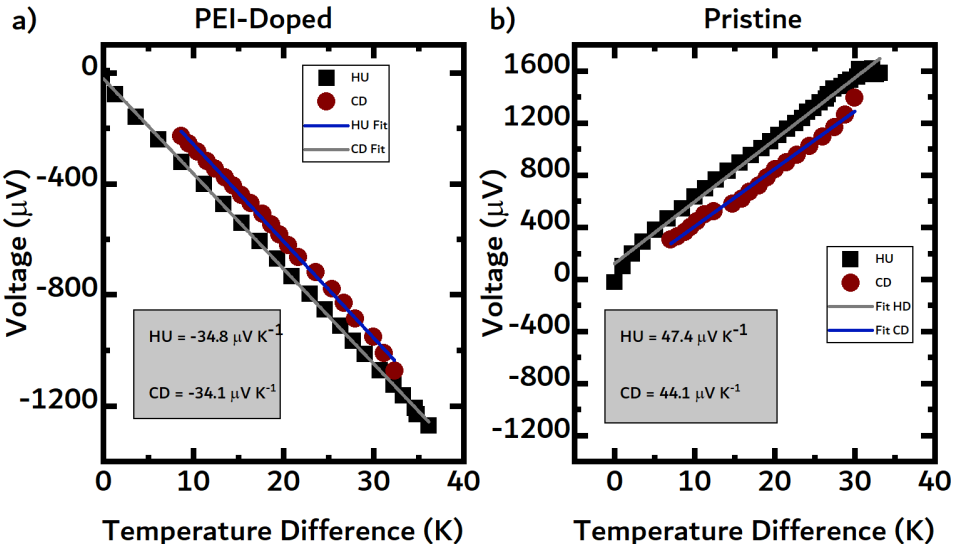

Figure 3-22. Seebeck measurement for a) PEI-Doped eDIPS and b) pristine eDIPS. The Seebeck voltage was continuously measured as the materials were heated (HU) and cooled (CD).

Figure 3-23. Photo of the actual proof-of-concept device

The power output and V_{OC} of the SOTEG were measured as a function of concentration (Figure 3-24a), and the P-V curves were recorded under 3 different irradiance conditions (3-24b). The unoptimized SOTEG generates around 0.18 μW of power under 1 sun, which due to the presence of the concentrating mirror that also covers one end of the SOTEG, becomes effectively 2 suns. The internal resistance of the SOTEG slightly increased with time, which could indicate an increase in contact resistance in the internal connections due to degradation or de-doping of the n-type materials, for example.

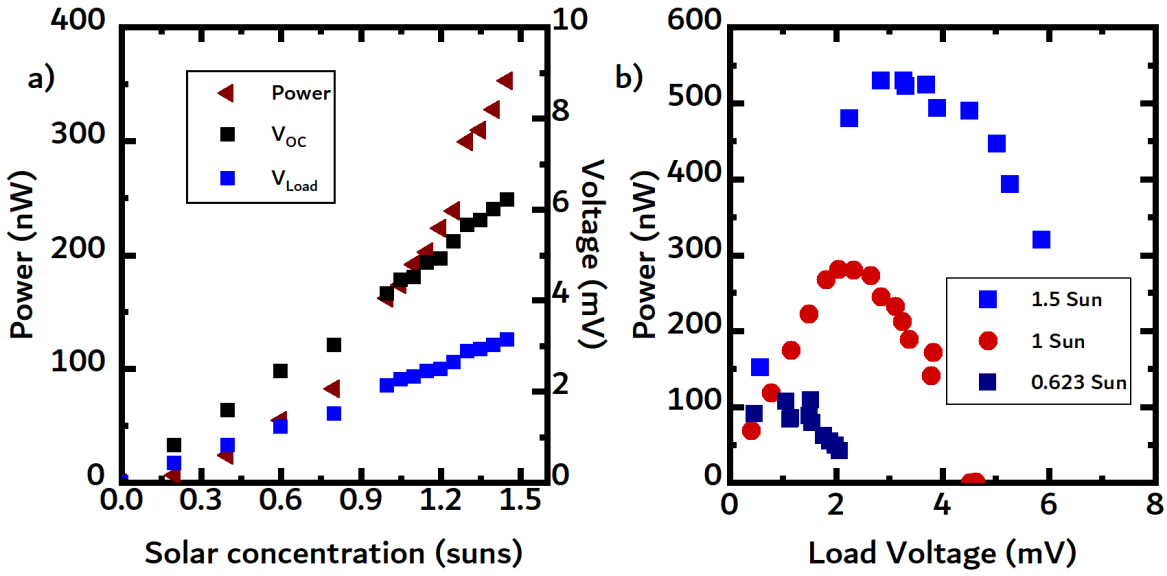

Figure 3-24. Electrical characterization of the proof-of-concept device. a) Voltage across the load, V_{OC}, and power as a function of irradiance

To check the reliability of the results, the experiment was repeated without the concentrating mirror and the expected Seebeck voltage was calculated and compared to the measured Seebeck voltage. The power generated by the SOTEG without the mirror was around 0.08 μW compared to 0.18 μW with the mirror. Looking at the measured Seebeck voltage, the upper and lower limits for the expected Seebeck voltage for the SOTEG were calculated. In the case of 1 sun conditions, the measured Seebeck voltage was 4140 μV. As previously discussed, the Seebeck coefficient of the device was expected to be 240 μV K^{-1}. Under 1 sun, the achieved steady state temperature rise for eDIPS is expected to be similar to that of CoMoCAT CNTs, so around 14 K. The PLA, on the other hand, heated up 30 K under 1 sun. Because the eDIPS legs are in intimate contact with the PLA, the PLA is expected to contribute to the heating of the SOTEG legs due to absorption. Therefore, the temperature increase of the hot side should lie somewhere between 14 (lower limit) and 30 (upper limit) K. The Seebeck voltages for both cases were calculated (Equations 3.16 and 3.17,

respectively), and it can be seen that the measured Seebeck voltage lies between these two limits. It is important to note that the SOTEG began to degrade after a few days, as lower power output was observed. The degradation can likely be attributed to the dedoping of the PEI-doped legs in the SOTEG [11].

Equation 3.16. $$S_{Lower\ Limit} = 14K * 240\frac{\mu V}{K} = 3360\mu V$$

Equation 3.17. $$S_{Lower\ Limit} = 30K * 240\frac{\mu V}{K} = 7200\mu V$$

3.6. Chapter Conclusions

In this chapter, organic TE materials were shown to be able to harvest solar radiation. Organic TE materials are capable of absorbing incident solar radiation across the solar spectrum, as shown by the FTIR absorption experiments. The photothermal experiments demonstrated that the temperature of organic TE materials can rise more than 50 K under a concentration factor of 2. Thus, organic TE materials can simultaneously be used as a solar absorber, resulting in simple device geometries.

Small photoconductivity effects were observed in a mat of CoMoCAT CNTs and a free-standing, pristine PEDOT:PSS film, with no noticeable change of the Seebeck coefficient under illumination. Furthermore, the influence of two critical design parameters, namely illuminated area and leg length, on power output were investigated. A reduction in leg length may enhance power output by reducing electrical resistance, but at short leg lengths, the reduction in electrical resistance no longer compensates the reduction in thermovoltage associated to thermal losses. Thermalization of both sides of the thermoelectric leg are particularly strong in vertical devices if thickness is not sufficiently large.

Next, several possible device architectures for SOTEGs that incorporate concentrating mirrors were presented. In the final section, a proof-of-concept SOTEG with 6 legs was fabricated, outputting 180 nW under 2 suns. The proof-of-concept demonstrates the strong potential of organics to yield simple and efficient SOTEG devices.

3.7. References for Chapter 3

[1] D. Kraemer *et al.*, “Concentrating solar thermoelectric generators with a peak efficiency of 7.4%,” *Nat. Energy*, vol. 1, no. 11, p. 16153, Sep. 2016, doi: 10.1038/nenergy.2016.153.

[2] J. P. Jurado, B. Dörling, O. Zapata-Arteaga, A. Roig, A. Mihi, and M. Campoy-Quiles, “Solar Harvesting: a Unique Opportunity for Organic Thermoelectrics?,” *Adv. Energy Mater.*, vol. 9, no. 45, p. 1902385, Dec. 2019, doi: 10.1002/aenm.201902385.

[3] Z. Liu *et al.*, “Controlling the Thermoelectric Properties of Organometallic Coordination Polymers via Ligand Design,” *Adv. Funct. Mater.*, vol. 30, no. 32, p. 2003106, Aug. 2020, doi: 10.1002/ADFM.202003106.

[4] M. Victoria, S. Askins, R. Herrero, I. Antón, and G. Sala, “Assessment of the optical efficiency of a primary lens to be used in a CPV system,” *Sol. Energy*, vol. 134, pp. 406–415, Sep. 2016, doi: 10.1016/J.SOLENER.2016.05.016.

[5] K.-T. Lin, H. Lin, T. Yang, and B. Jia, “Structured graphene metamaterial selective absorbers for high efficiency and omnidirectional solar thermal energy conversion,” *Nat. Commun. 2020 111*, vol. 11, no. 1, pp. 1–10, Mar. 2020, doi: 10.1038/s41467-020-15116-z.

[6] E. Lim, K. A. Peterson, G. M. Su, and M. L. Chabinyc, “Thermoelectric Properties of Poly(3-hexylthiophene) (P3HT) Doped with 2,3,5,6-Tetrafluoro-7,7,8,8-tetracyanoquinodimethane (F4TCNQ) by Vapor-Phase Infiltration,” *Chem. Mater.*, vol. 30, no. 3, pp. 998–1010, Feb. 2018, doi: 10.1021/ACS.CHEMMATER.7B04849.

[7] S. Qu *et al.*, “Highly anisotropic P3HT films with enhanced thermoelectric performance via organic small molecule epitaxy,” *NPG Asia Mater. 2016 87*, vol. 8, no. 7, pp. e292–e292, Jul. 2016, doi: 10.1038/am.2016.97.

[8] A. D. Avery *et al.*, “Tailored semiconducting carbon nanotube networks with enhanced thermoelectric properties,” *Nat. Energy 2016 14*, vol. 1, no. 4, pp. 1–9, Apr. 2016, doi: 10.1038/nenergy.2016.33.

[9] D. Hayashi *et al.*, “Thermoelectric properties of single-wall carbon nanotube films: Effects of diameter and wet environment,” *Appl. Phys. Express*, vol. 9, no. 2, p. 025102, Jan. 2016, doi: 10.7567/APEX.9.025102.

[10] B. Dörling, X. Rodríguez-Martínez, I. Álvarez-Corzo, J. S. Reparaz, and M. Campoy-Quiles, “Soluble alkali-metal carbon nanotube salts for n-type thermoelectric composites with improved stability,” *Appl. Phys. Lett.*, vol. 118, no. 21, p. 213901, May 2021, doi: 10.1063/5.0047338.

[11] F. Abdallah *et al.*, “Investigating Thermoelectric Stability under Encapsulation Using

PEI-Doped CNT Films as a Model System," *Adv. Mater. Technol.*, vol. 5, no. 7, p. 2000256, Jul. 2020, doi: 10.1002/ADMT.202000256.

[12] C. Bounioux *et al.*, "Thermoelectric composites of poly(3-hexylthiophene) and carbon nanotubes with a large power factor," *Energy Environ. Sci.*, vol. 6, no. 3, pp. 918–925, Feb. 2013, doi: 10.1039/C2EE23406H.

[13] D. Abol-Fotouh *et al.*, "Farming thermoelectric paper," *Energy Environ. Sci.*, vol. 12, no. 2, pp. 716–726, 2019, doi: 10.1039/C8EE03112F.

[14] Q. Zhang, Y. Sun, F. Jiao, J. Zhang, W. Xu, and D. Zhu, "Effects of structural order in the pristine state on the thermoelectric power-factor of doped PBTTT films," *Synth. Met.*, vol. 162, no. 9–10, pp. 788–793, Jun. 2012, doi: 10.1016/J.SYNTHMET.2012.03.003.

[15] J. E. Cochran *et al.*, "Molecular Interactions and Ordering in Electrically Doped Polymers: Blends of PBTTT and F4TCNQ," *Macromolecules*, vol. 47, no. 19, pp. 6836–6846, Oct. 2014, doi: 10.1021/ma501547h.

[16] A. Abutaha *et al.*, "Correlating charge and thermoelectric transport to paracrystallinity in conducting polymers," *Nat. Commun. 2020 111*, vol. 11, no. 1, pp. 1–8, Apr. 2020, doi: 10.1038/s41467-020-15399-2.

[17] S. N. Patel *et al.*, "Morphology controls the thermoelectric power factor of a doped semiconducting polymer," *Sci. Adv.*, vol. 3, no. 6, p. e1700434, Jun. 2017, doi: 10.1126/sciadv.1700434.

[18] Q. Li, Q. Zhou, L. Wen, and W. Liu, "Enhanced thermoelectric performances of flexible PEDOT:PSS film by synergistically tuning the ordering structure and oxidation state," *J. Mater.*, vol. 6, no. 1, pp. 119–127, Mar. 2020, doi: 10.1016/J.JMAT.2020.01.001.

[19] R. Yue and J. Xu, "Poly(3,4-ethylenedioxythiophene) as promising organic thermoelectric materials: A mini-review," *Synth. Met.*, vol. 162, no. 11–12, pp. 912–917, Jul. 2012, doi: 10.1016/J.SYNTHMET.2012.04.005.

[20] C. Badre, L. Marquant, A. M. Alsayed, and L. A. Hough, "Highly Conductive Poly(3,4-ethylenedioxythiophene):Poly (styrenesulfonate) Films Using 1-Ethyl-3-methylimidazolium Tetracyanoborate Ionic Liquid," *Adv. Funct. Mater.*, vol. 22, no. 13, pp. 2723–2727, Jul. 2012, doi: 10.1002/ADFM.201200225.

[21] J. Luo *et al.*, "Chemical post-treatment and thermoelectric properties of poly(3,4-ethylenedioxylthiophene):poly(styrenesulfonate) thin films," *J. Appl. Phys.*, vol. 115, no. 5, p. 054908, Feb. 2014, doi: 10.1063/1.4864749.

[22] H. Zhu, C. Liu, H. Song, J. Xu, F. Kong, and J. Wang, "Thermoelectric performance of poly(3-hexylthiophene) films doped by iodine vapor with promising high seebeck coefficient," *Electron. Mater. Lett. 2014 102*, vol. 10, no. 2, pp. 427–431, Mar. 2014, doi: 10.1007/S13391-013-3150-Y.

[23] H. Wang, U. Ail, R. Gabrielsson, M. Berggren, and X. Crispin, “Ionic Seebeck Effect in Conducting Polymers,” *Adv. Energy Mater.*, vol. 5, no. 11, p. 1500044, Jun. 2015, doi: 10.1002/AENM.201500044.

[24] A. M. Glaudell, J. E. Cochran, S. N. Patel, and M. L. Chabinyc, “Impact of the Doping Method on Conductivity and Thermopower in Semiconducting Polythiophenes,” *Adv. Energy Mater.*, vol. 5, no. 4, p. 1401072, Feb. 2015, doi: 10.1002/aenm.201401072.

[25] O. Zapata-Arteaga, A. Perevedentsev, S. Marina, J. Martin, J. S. Reparaz, and M. Campoy-Quiles, “Reduction of the Lattice Thermal Conductivity of Polymer Semiconductors by Molecular Doping,” *ACS Energy Lett.*, vol. 5, no. 9, pp. 2972–2978, Sep. 2020, doi: 10.1021/ACSENERGYLETT.0C01410.

[26] Y. Xu *et al.*, “Morphological modulation to improve thermoelectric performances of PEDOT:PSS films by DMSO vapor post-treatment,” *Synth. Met.*, vol. 271, p. 116628, Jan. 2021, doi: 10.1016/J.SYNTHMET.2020.116628.

[27] S. Ichikawa and N. Toshima, “Improvement of thermoelectric properties of composite films of PEDOT-PSS with xylitol by means of stretching and solvent treatment,” *Polym. J. 2015 477*, vol. 47, no. 7, pp. 522–526, May 2015, doi: 10.1038/pj.2015.28.

[28] J. S. Yeo, J. M. Yun, D. Y. Kim, S. S. Kim, and S. I. Na, “Successive solvent-treated PEDOT:PSS electrodes for flexible ITO-free organic photovoltaics,” *Sol. Energy Mater. Sol. Cells*, vol. 114, pp. 104–109, Jul. 2013, doi: 10.1016/J.SOLMAT.2013.02.031.

[29] B. Dörling, S. Sandoval, P. Kankla, A. Fuertes, G. Tobias, and M. Campoy-Quiles, “Exploring different doping mechanisms in thermoelectric polymer/carbon nanotube composites,” *Synth. Met.*, vol. 225, pp. 70–75, Mar. 2017, doi: 10.1016/J.SYNTHMET.2017.01.002.

[30] H. Wang, V. Prasad Sivan, A. Mitchell, G. Rosengarten, P. Phelan, and L. Wang, “Highly efficient selective metamaterial absorber for high-temperature solar thermal energy harvesting,” *Sol. Energy Mater. Sol. Cells*, vol. 137, pp. 235–242, Jun. 2015, doi: 10.1016/J.SOLMAT.2015.02.019.

[31] Khosrow Rahimi, Ioan Botiz, J. O. Agumba, Sajedeh Motamen, Natalie Stingelin, and Günter Reiter, “Light absorption of poly(3-hexylthiophene) single crystals,” *RSC Adv.*, vol. 4, no. 22, pp. 11121–11123, Feb. 2014, doi: 10.1039/C3RA47064D.

[32] J. Luo *et al.*, “Enhancement of the thermoelectric properties of PEDOT:PSS thin films by post-treatment,” *J. Mater. Chem. A*, vol. 1, no. 26, pp. 7576–7583, Jun. 2013, doi: 10.1039/C3TA11209H.

[33] M. S. Vezie *et al.*, “Exploring the origin of high optical absorption in conjugated polymers,” *Nat. Mater.*, vol. 15, p. 746, May 2016.

[34] B. Tang *et al.*, “Restricting the liquid–liquid phase separation of PTB7-Th:PF12TBT:PC71BM by enhanced PTB7-Th solution aggregation to optimize the

interpenetrating network," *RSC Adv.*, vol. 7, no. 29, pp. 17913–17922, Mar. 2017, doi: 10.1039/C6RA28306C.

[35] C. Sun *et al.*, "A low cost and high performance polymer donor material for polymer solar cells," *Nat. Commun. 2018 91*, vol. 9, no. 1, pp. 1–10, Feb. 2018, doi: 10.1038/s41467-018-03207-x.

[36] A. E. Mansour *et al.*, "The optical signatures of molecular-doping induced polarons in poly(3-hexylthiophene-2,5-diyl): individual polymer chains versus aggregates," *J. Mater. Chem. C*, vol. 8, no. 8, pp. 2870–2879, Feb. 2020, doi: 10.1039/C9TC06509A.

[37] D. A. Stanfield, Y. Wu, S. H. Tolbert, and B. J. Schwartz, "Controlling the Formation of Charge Transfer Complexes in Chemically Doped Semiconducting Polymers," *Chem. Mater.*, vol. 33, no. 7, pp. 2343–2356, Apr. 2021, doi: 10.1021/ACS.CHEMMATER.0C04471.

[38] J. Gasiorowski, R. Menon, K. Hingerl, M. Dachev, and N. S. Sariciftci, "Surface morphology, optical properties and conductivity changes of poly(3,4-ethylenedioxythiophene):poly(styrenesulfonate) by using additives," *Thin Solid Films*, vol. 536, no. 100, pp. 211–215, Jun. 2013, doi: 10.1016/j.tsf.2013.03.124.

[39] S. Logothetidis, "Ellipsometry of Functional Organic Surfaces and Films," in *Ellipsometry of Functional Organic Surfaces and Films*, K. Hinrichs and K.-J. Eichhorn, Eds. Berlin, Heidelberg: Springer, 2014.

[40] E. Tetik, F. Karadağ, M. Karaaslan, and İ. Çömez, " The Electronic Properties of the Graphene and Carbon Nanotubes: Ab Initio Density Functional Theory Investigation ," *ISRN Nanotechnol.*, vol. 2012, pp. 1–7, Apr. 2012, doi: 10.5402/2012/416417.

[41] G. F. Burkhard, E. T. Hoke, and M. D. McGehee, "Accounting for Interference, Scattering, and Electrode Absorption to Make Accurate Internal Quantum Efficiency Measurements in Organic and Other Thin Solar Cells," *Adv. Mater.*, vol. 22, no. 30, pp. 3293–3297, Aug. 2010, doi: 10.1002/adma.201000883.

[42] "Emissivity - Non-Metals." [Online]. Available: https://www.flukeprocessinstruments.com/en-us/service-and-support/knowledge-center/infrared-technology/emissivity-non-metals. [Accessed: 20-Jun-2021].

[43] J. C. Duda, P. E. Hopkins, Y. Shen, and M. C. Gupta, "Thermal transport in organic semiconducting polymers," *Appl. Phys. Lett.*, vol. 102, no. 25, p. 251912, Jun. 2013, doi: 10.1063/1.4812234.

[44] P. M. Smith, L. Su, W. Gong, N. Nakamura, B. Reeja-Jayan, and S. Shen, "Thermal conductivity of poly(3,4-ethylenedioxythiophene) films engineered by oxidative chemical vapor deposition (oCVD)," *RSC Adv.*, vol. 8, no. 35, pp. 19348–19352, May 2018, doi: 10.1039/C8RA03302A.

[45] C. T. Yang, H. I. Hsiang, T. S. Huang, P. C. Huang, and Y. K. Han, "Thermal conductivity and dielectric properties of PEDOT:PSS-AlN filler reinforced water-

soluble polymer composites," *Ceram. Int.*, vol. 43, pp. S710–S716, Aug. 2017, doi: 10.1016/J.CERAMINT.2017.05.271.

[46] "Convective Heat Transfer," *Engineering ToolBoc*, 2003. [Online]. Available: https://www.engineeringtoolbox.com/convective-heat-transfer-d_430.html. [Accessed: 20-Jun-2020].

[47] N. Toshima and N. Jiravanichanun, "Improvement of Thermoelectric Properties of PEDOT/PSS Films by Addition of Gold Nanoparticles: Enhancement of Seebeck Coefficient," *J. Electron. Mater.*, vol. 42, no. 7, pp. 1882–1887, 2013, doi: 10.1007/s11664-012-2458-y.

[48] A. Weathers *et al.*, "Significant Electronic Thermal Transport in the Conducting Polymer Poly(3,4-ethylenedioxythiophene)," *Adv. Mater.*, vol. 27, no. 12, pp. 2101–2106, Mar. 2015, doi: 10.1002/adma.201404738.

[49] J. Liu, X. Wang, D. Li, N. E. Coates, R. A. Segalman, and D. G. Cahill, "Thermal Conductivity and Elastic Constants of PEDOT:PSS with High Electrical Conductivity," *Macromolecules*, vol. 48, no. 3, pp. 585–591, Feb. 2015, doi: 10.1021/ma502099t.

[50] G.-H. H. Kim, L. Shao, K. Zhang, and K. P. Pipe, "Engineered doping of organic semiconductors for enhanced thermoelectric efficiency," *Nat. Mater.*, vol. 12, no. 8, p. 719, May 2013, doi: 10.1038/nmat3635.

[51] H. Ushirokita and H. Tada, "In-plane Thermal Conductivity Measurement of Conjugated Polymer Films by Membrane-based AC Calorimetry," *Chem. Lett.*, vol. 45, no. 7, pp. 735–737, Apr. 2016, doi: 10.1246/cl.160175.

[52] O. Zapata-Arteaga, B. Dörling, A. Perevedentsev, J. Martín, J. S. Reparaz, and M. Campoy-Quiles, "Closing the Stability-Performance Gap in Organic Thermoelectrics by Adjusting the Partial to Integer Charge Transfer Ratio," *Macromolecules*, vol. 53, no. 2, pp. 609–620, Jan. 2020, doi: 10.1021/acs.macromol.9b02263.

[53] S. Rausch, D. Rauh, C. Deibel, S. Vidi, and H. P. Ebert, "Thin-Film Thermal-Conductivity Measurement on Semi-Conducting Polymer Material Using the 3$ω$ Technique," *Int. J. Thermophys.*, vol. 34, no. 5, pp. 820–830, May 2013, doi: 10.1007/s10765-012-1174-4.

[54] S. Farah and D. G. Anderson, "Physical and mechanical properties of PLA, and their functions in widespread applications — A comprehensive review," *Adv. Drug Deliv. Rev.*, vol. 107, pp. 367–392, Dec. 2016, doi: 10.1016/J.ADDR.2016.06.012.

[55] D. Kraemer *et al.*, "High-performance flat-panel solar thermoelectric generators with high thermal concentration," *Nat. Mater.*, vol. 10, no. 7, p. 532, May 2011, doi: 10.1038/nmat3013.

[56] A. Horikawa, T. Igarashi, I. Terasaki, and R. Okazaki, "Photo-Seebeck effect in polycrystalline ZnO," *J. Appl. Phys.*, vol. 118, no. 9, p. 095101, Sep. 2015, doi: 10.1063/1.4929638.

[57] Y. Shiraishi, R. Okazaki, H. Taniguchi, and I. Terasaki, “Photo-Seebeck effect in ZnS,” *Jpn. J. Appl. Phys.*, vol. 54, no. 3, p. 031203, Feb. 2015, doi: 10.7567/JJAP.54.031203.

[58] Y. Xing, M. Qian, G. Wang, G. Zhang, D. Guo, and J. Wu, “UV irradiation induced conductivity improvement in poly(3,4-ethylenedioxythiophene):poly(styrenesulfonate) film,” *Sci. China Technol. Sci.*, vol. 57, no. 1, pp. 44–48, Dec. 2014, doi: 10.1007/s11431-013-5426-8.

[59] D. Farka *et al.*, “Anderson-Localization and the Mott–Ioffe–Regel Limit in Glassy-Metallic PEDOT,” *Adv. Electron. Mater.*, vol. 3, no. 7, p. 1700050, Jul. 2017, doi: 10.1002/AELM.201700050.

[60] N. Massonnet, A. Carella, A. de Geyer, J. Faure-Vincent, and J.-P. Simonato, “Metallic behaviour of acid doped highly conductive polymers,” *Chem. Sci.*, vol. 6, no. 1, pp. 412–417, Dec. 2014, doi: 10.1039/C4SC02463J.

[61] O. Bubnova *et al.*, “Semi-metallic polymers,” *Nat. Mater. 2014 132*, vol. 13, no. 2, pp. 190–194, Dec. 2013, doi: 10.1038/nmat3824.

[62] E. S. Muckley, C. B. Jacobs, R. Kumar, and I. N. Ivanov, “Effect of water adsorption on ionic and electronic transport in PEDOT:PSS (Conference Presentation),” vol. 10364, p. 103640R, Sep. 2017, doi: 10.1117/12.2274496.

[63] Z. Lin and M. He, *Organic thermoelectric materials*. Royal Society of Chemistry, 2019.

[64] M. Haurat and M. Dumon, “Amorphous Polymers’ Foaming and Blends with Organic Foaming-Aid Structured Additives in Supercritical CO2, a Way to Fabricate Porous Polymers from Macro to Nano Porosities in Batch or Continuous Processes,” *Mol. 2020, Vol. 25, Page 5320*, vol. 25, no. 22, p. 5320, Nov. 2020, doi: 10.3390/MOLECULES25225320.

[65] J. L. Blackburn, A. J. Ferguson, C. Cho, and J. C. Grunlan, “Carbon-Nanotube-Based Thermoelectric Materials and Devices,” *Adv. Mater.*, vol. 30, no. 11, p. 1704386, Mar. 2018, doi: 10.1002/adma.201704386.

[66] S. Sandell, E. Chávez-Ángel, A. El Sachat, J. He, C. M. Sotomayor Torres, and J. Maire, “Thermoreflectance techniques and Raman thermometry for thermal property characterization of nanostructures,” *J. Appl. Phys.*, vol. 128, no. 13, Oct. 2020, doi: 10.1063/5.0020239.

[67] Y. Zhou, F. Zhang, K. Tvingstedt, W. Tian, and O. Inganäs, “Multifolded polymer solar cells on flexible substrates,” *Appl. Phys. Lett.*, vol. 93, no. 3, p. 33302, Jul. 2008, doi: 10.1063/1.2957995.

[68] Moonsub Shim, Ali Javey, and Nadine Wong Shi Kam, and H. Dai*, “Polymer Functionalization for Air-Stable n-Type Carbon Nanotube Field-Effect Transistors,” *J. Am. Chem. Soc.*, vol. 123, no. 46, pp. 11512–11513, Nov. 2001, doi:

10.1021/JA0169670.

[69] D. D. Freeman, K. Choi, and C. Yu, “N-Type Thermoelectric Performance of Functionalized Carbon Nanotube-Filled Polymer Composites,” *PLoS One*, vol. 7, no. 11, p. e47822, Nov. 2012, doi: 10.1371/JOURNAL.PONE.0047822.

[70] C. Yu, A. Murali, K. Choi, and Y. Ryu, “Air-stable fabric thermoelectric modules made of N- and P-type carbon nanotubes,” *Energy Environ. Sci.*, vol. 5, no. 11, pp. 9481–9486, 2012, doi: 10.1039/C2EE22838F.

Chapter 4. Geometries for Hybrid Photovoltaic-Thermoelectric devices

OSCs mainly make use of the UV-Vis part of the solar spectrum. New non-fullerene acceptors have pushed absorption into the NIR part of the solar spectrum, but a significant part of the NIR is not harvested by OSCs. Coupling thermoelectrics with OSCs in a hybrid device may be a strategy to enhance solar energy conversion, capturing the fraction of light and infrared heat not used by OSCs. In the previous chapter, it was demonstrated that organic thermoelectric generators can directly convert light and infrared heat into electricity in a steady-state harvesting approach. In this chapter, geometries for all-organic hybrid PV-TE devices are investigated. The work from this chapter was published by Jurado et al. [1].

4.1. Geometries for Hybrid PV-TE Devices

4.1.1. Device Geometries

A working solar cell is unable to convert all incident sunlight to electricity because of optical and electrical loss mechanisms. The Shockly-Queisser limit defines the thermodynamic limit for single-junction solar cells, which are limited to 33.7% [2]. Rather, a fraction of the incident light is lost due to reflection at the front of the solar cell and reflection from the back electrodes [3]. Additionally, another fraction of the incident light is also transformed into heat, Q_{PV}, via non-radiative mechanisms, and the rest of the incident light can be transformed into useable power, P_{PV}. In addition to non-radiative loss, radiative losses will limit solar cell performance [2], [4], [5].

One of the most widely reported approaches to couple a TEG with a solar cell is to place a solar cell in intimate contact with the backside of a solar cell [6]–[9]. In this chapter, three device geometries are investigated and are shown in Figure 4-1: a) a non-contact reflection geometry, b) a non-contact transmission, and c-d) a contact transmission geometry. These geometries were chosen because of their simplicity. In a reflection geometry, an opaque solar cell is placed at an angle to reflect incident light, $P_{R,PV}$, towards the SOTEG. The SOTEG in a reflection geometry can convert the reflected light from the solar cell into thermal energy and then to useable power, P_{TEG}. Heat from the SOTEG can also be lost to the environment, Q_R, due to convection or radiation, for example. In this geometry, light transmitted by the solar cell or light reflected by the solar cell that is not reflected towards

the SOTEG, is considered a loss mechanism, $P_{L,PV}$. Similarly for the SOTEG, light transmitted through the SOTEG or reflected by the SOTEG is a loss mechanism, $P_{L,TEG}$. In a non-contact transmission geometry, a semi-transparent solar cell is placed above the thermoelectric, allowing a fraction of light to be transmitted by the solar cell, $P_{T,PV}$, to the SOTEG, which can absorb the transmitted light. Reflection from the solar cell, $P_{L,PV}$, and heat generated by the solar cell, Q_{PV}, are considered loss mechanisms in this geometry, as well as light reflected or transmitted by the SOTEG.

In a contact geometry, the solar cell, either opaque or semi-transparent, is placed in direct contact with the SOTEG. As a result, the heat from the solar cell can be partially transferred to the SOTEG. In the case that a semi-transparent solar cell is used, the sub-band gap photons and any non-absorbed light transmitted by the solar cell could potentially be absorbed by the SOTEG. As previously mentioned, the solar cell will inevitably convert a percentage of incoming light into waste heat through non-radiative recombination. The SOTEG can partially convert the waste heat from the solar cell into electricity. If solar cell performance is enhanced with increasing temperature, using a contact geometry would be beneficial. The intimate contact between the SOTEG and the solar cell will cause an increase in the thermal resistance – i.e. reduce convection – at the backend of the solar cell, thereby increasing the temperature of the solar cell provided that the SOTEG provides sufficient thermal insulation, i.e. it possesses a low thermal conductivity. The gain in temperature will improve solar cell efficiency, and the thermal energy converted by the SOTEG will further raise the overall device efficiency. For the SOTEG device, both planar (Figure 4-1c) and vertical (Figure 4-1d) device geometries are considered. As mentioned in the previous chapter, vertical devices offer enhanced light absorption compared to planar devices but are difficult to fabricate.

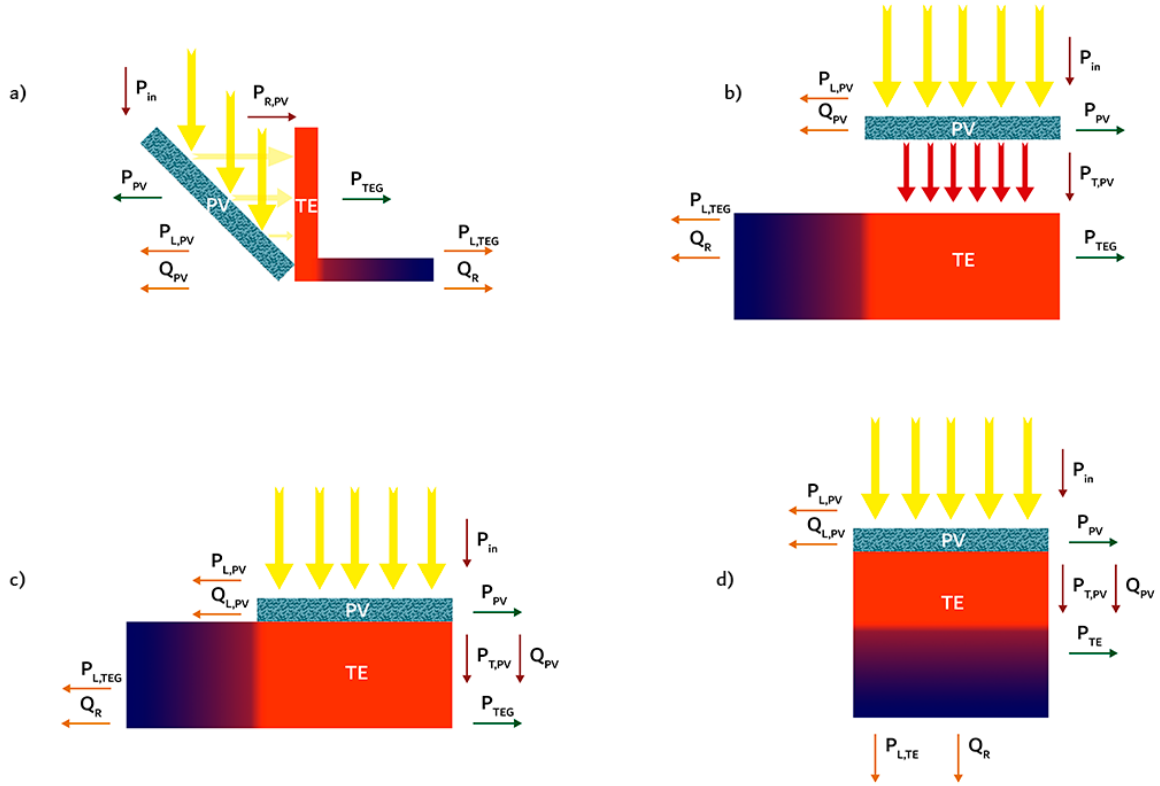

Figure 4-1. a) Non-contact reflection geometry; the solar cell is placed at an angle such that the reflected fraction of the incident light is directed towards the TEG; b) non-contact transmission geometry; the semi-transparent solar cell is physically separated from the TEG, and the transmitted fraction of the incident light can be absorbed by the TEG; c) contact geometry; the solar cell (either semi-transparent or opaque) is in direct contact with the thermoelectric generator; d) contact geometry with a vertical TEG device. The associated process and loss mechanisms of the hybrid device: incident solar radiation on the solar cell and reflected light from the back end of the hybrid device, Pin; optical power losses from the solar cell, PL,PV; thermal losses from the solar cell, QL,PV; power output from the solar cell, PPV; transmitted light from the solar cell to the TEG, PT,PV; heat transferred from the solar cell to the TEG, QPV; optical power losses from the TEG, PL,TEG; thermal losses from the TEG, QR; power output from the TEG, PTEG. The figure has been adapted from Jurado et al. [1].

4.1.2. Mathematical framework

The efficiency of a hybrid PV-TE device is described mathematically in this section. The overall output power from a hybrid PV-TE device is given by:

Equation 4.1. $$P_{H,out} = P_{PV} + P_{TEG}$$

where P_{PV} is output power from the solar cell and P_{TEG} is output power from the TEG. Alternatively, Equation 4.1 can be written in terms of efficiency:

Equation 4.2. $$\eta_H(T) = \eta_{PV}(T) + \eta_{TEG}(T)$$

where η_H is the overall efficiency of the hybrid device, η_{PV} is the solar cell efficiency, and η_{TEG} is the efficiency of the TEG. Solar cell efficiency is dependent on many factors previously discussed in chapter 1.3, but it is important to emphasize the temperature dependence of solar cell efficiency in Equation 4.2, which can significantly change when coupled with a TEG.

4.1.3. Non-contact Geometries

For devices with non-contact modes (reflection and transmission geometries), the heat generated by the solar cell will not contribute to the SOTEG efficiency, since there is a gap left between the solar cell and the SOTEG. Only transmitted or reflected light from the solar cell that is absorbed by the TEG can be converted. In these geometries, it is assumed that $\eta_{TEG} = \eta_{SOTEG}$, where SOTEG efficiency was discussed previously in Chapter 3. Assuming no optical concentration and no auxiliary losses in the device, Equation 3.1 can be reduced to:

Equation 4.3. $$\eta_{SOTEG} = \eta_{abs}\eta_{teg} = \eta_{teg}\eta_{TEG,PT}\tau$$

where τ is the transmittance from a PV cell. For reflection mode, τ is set to R, which is the reflectance. The middle term in Equation 3.3, $\eta_{TEG,PT}$, refers to the TEG's photothermal efficiency, and is defined here as the ratio of heat generated through absorption of transmitted or reflected light to light power, either transmitted or reflected, from the solar cell. For the reflection geometry,

Equation 4.4. $$\eta_{TEG,PT} = \frac{Q_{PT,TEG}}{P_{R,PV}}$$

For the non-contact transmission geometry,

Equation 4.5. $$\eta_{TEG,PT} = \frac{Q_{PT,TEG}}{P_{T,PV}}$$

For the reflection geometry, we consider an opaque cell and neglect the small emissivity of the cell at room temperature. In this case, the hybrid device efficiency becomes:

Equation 4.6. $$\eta_H{}^{Reflection\ Geometry} = \eta_{PV} + R\eta_{teg}\eta_{abs}$$

where R is the reflectance from the PV cell. For the non-contact transmission geometry:

Equation 4.7. $\eta_H{}^{Transmission\ Geometry} = \eta_{PV} + \tau\eta_{teg}\eta_{abs}$

4.1.4. Contact Geometries

For the case of hybrid devices with a contact geometry, the SOTEG converts thermal and optical energy into electricity. Therefore, the SOTEG efficiency can be defined as:

Equation 4.8. $\eta_{TEG}(T) = \eta_{TEG}^{opt} + \eta_{TEG}^{heat}$

In this geometry, a solar cell's light-to-heat, or photothermal, efficiency must be considered, since the heat generated by the solar cell contributes to the energy the SOTEG can convert into electricity. The photothermal efficiency of a solar cell can be written as:

Equation 4.9. $\eta_{PV,PT} = (1 - \eta_{PV})\eta_{opt,PV}$

where $\eta_{opt,PV}$ is the optical efficiency of the solar cell, which accounts for the sum of reflectance, transmittance and emission losses:

Equation 4.10. $\eta_{opt,PV} = R + \tau + E$

If opaque solar cells are used, $\eta_{TEG}^{opt} = 0$ because the solar cell transmits no light. Therefore, the efficiency for a device in contact mode incorporating an opaque solar cell can be given as:

Equation 4.11. $\eta_H{}^{Contact\ Opaque} = \eta_{PV}(T) + (1 - \eta_{PV})\,\eta_{opt,PV}\eta_{H,coupling}\eta_{teg}$

where $\eta_{H,coupling}$ is a coupling term to describe the SOTEG's ability to harvest the waste heat generated by the solar cell.

In the case of a device in contact mode incorporating a semitransparent solar cell, the device efficiency can be written as:

Equation 4.12. $\eta_H{}^{Contact\ ST} = \eta_{PV}(T) + \eta_{teg}(\eta_{TEG,PT}\tau + (1 - \eta_{PV})\eta_{opt,PV}\eta_{H,coupling})$

4.2. Experimental approach and materials

In this section of the thesis, the three geometries were compared by drawing upon experimental data. In a first step, the energy available to be converted by the SOTEG in a hybrid device was quantified by measuring the reflection and transmission spectra of the OSC materials using FTIR spectroscopy. Next, photothermal experiments similar to those detailed in chapter 3 were conducted to measure the temperature rise of the materials under 1 sun. Finally, the TEG efficiencies for the three device geometries were calculated using the experimental results.

There are a large number of OSC materials reported in literature, but to evaluate the potential of organic-based hybrid devices in a general manner, a number of OSC materials with different band gaps were selected. Optically-thick, free-standing filters of ten different polymers (Table 4.1) were fabricated to emulate solar cells. Additionally, two commercial solar cells, an organic solar cell from Infinity PV and a polycrystalline silicon cell, as well as support and other materials found in the solar cell stack were used. For the non-contact geometries, the TE materials used and their thicknesses can be found in Table 4.2.

Table 4.1. List of the OSC layers used in this study and their band gap or absorption edge

Solar Cell Filters	Band gap or absorption edge	Thickness (μm)
PFO	485 nm	3.2
MEH-PPV	583 nm	18
PFBT	638 nm	23
P3HT	660 nm	25.2
PCE12	703 nm	19.2
PCE13	717 nm	13.2
TQ1	757 nm	9.9
PCE10	773 nm	8.2
PCE11	829 nm	28
N2200	866 nm	50
Bare Glass	-	11360
Glass with ITO	-	11460
Glass with ZnO	-	11390
Glass with ITO and ZnO	-	11490

Table 4.2. List of TE materials used and their thicknesses

TE Material	Thickness
PEDOT:PSS	52.5 μm
F_4TNCQ-Doped PBTT	2.9 μm
eDIPS	9 μm
eDIPS:cellulose	10 μm

4.3. Reflectance and Transmittance of Common OSC materials

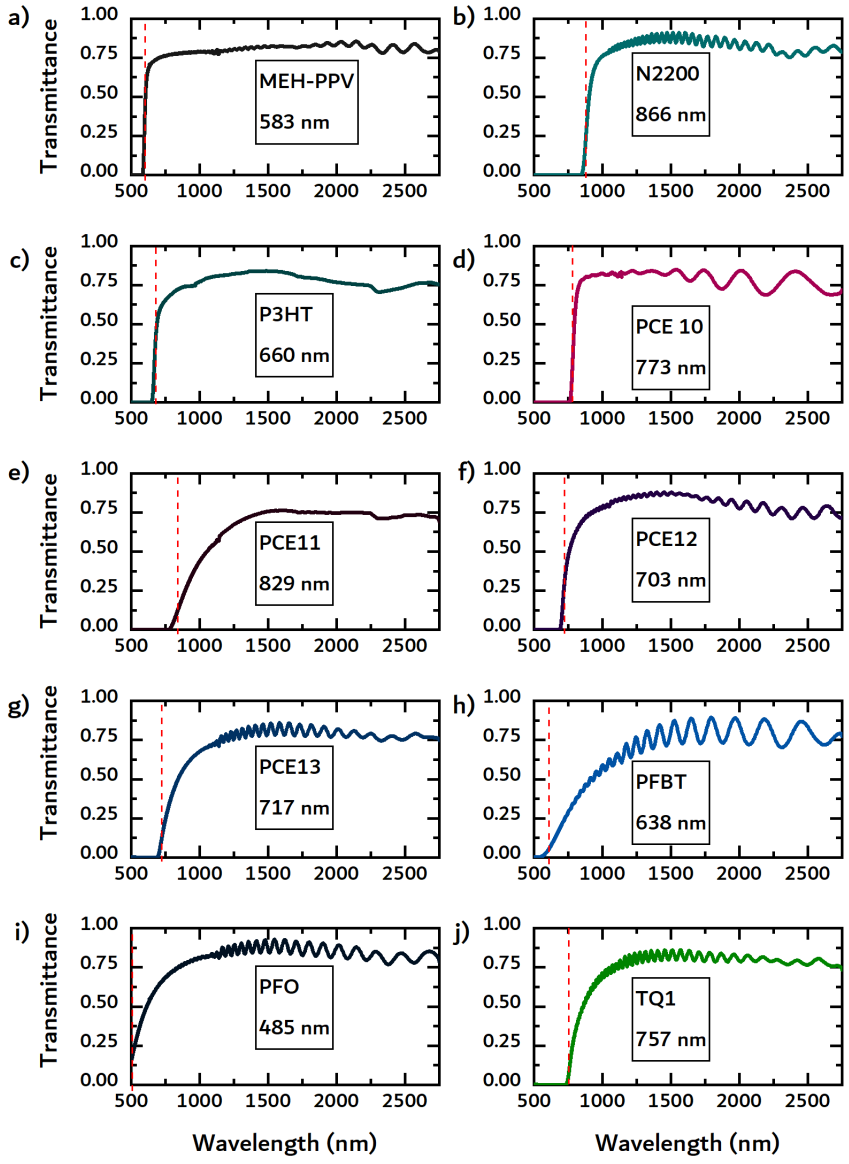

Figure 4-2. Transmittance data for. a) MEH-PPV; b) N2200; c) P3HT; d) PCE10; e) PCE11; f) PCE12; g) PCE13; h) PFBT; i) PFO; and j) TQ1. The number in the label box corresponds to the absorption edge in nanometers. The figure has been adapted from Jurado et al. [1].

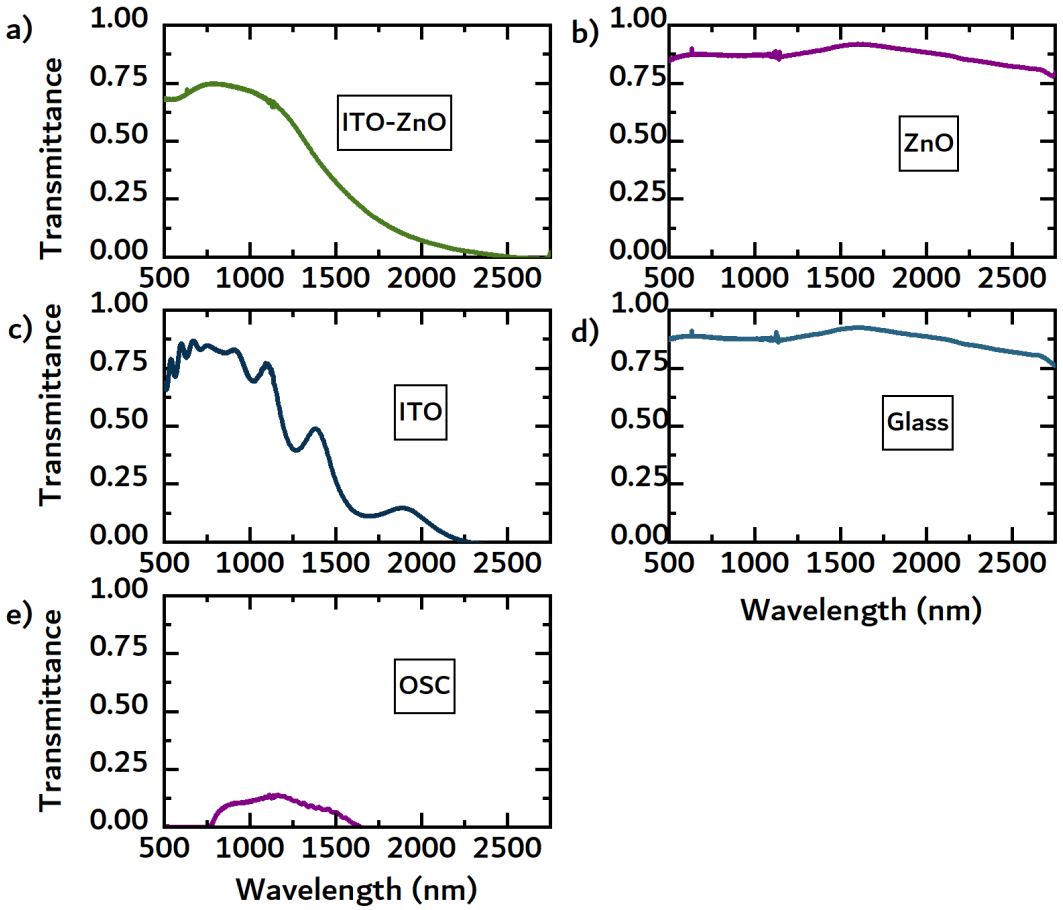

Figure 4-3. Transmittance data for a) a glass substrate with ITO and ZnO layers; b) a glass substrate with ZnO; c) a glass substrate with ITO; d) a bare glass substrate; and e) a commercial infinityPV OSC module. The figure has been adapted from Jurado et al. [1].

Figures 4-2 and 4-3 show the transmittance spectra for the selected OSC active layer materials and for the other materials (glass, glass with ITO, glass with ZnO, glass with ITO and ZnO, and commercial OSC module), respectively. For the OSC active layer materials, the cut-on wavelength, defined as the point where transmittance exceeds 10%, is clearly seen and marked with a red, dashed line. In the case of P3HT, the cut-on wavelength is 660 nm for example. It can clearly be seen in Figure 4-2 that the active layer materials transmit a large portion of the NIR radiation since the band gap for most OSCs is below 900 nm. Of the other materials, bare glass and the glass coated with ZnO transmit the most. The glass with ITO sample exhibited high transmittance in the UV-Vis region yet poor transmittance in the NIR region due to absorption by free electrons (Drude tail) [10]. The commercial OSC module exhibited poor transmittance in all regions. From the figures, some samples exhibit an oscillatory pattern for wavelengths greater than the band gap wavelength, which can be attributed to interference effects due to film thickness, listed in Table 4.1.

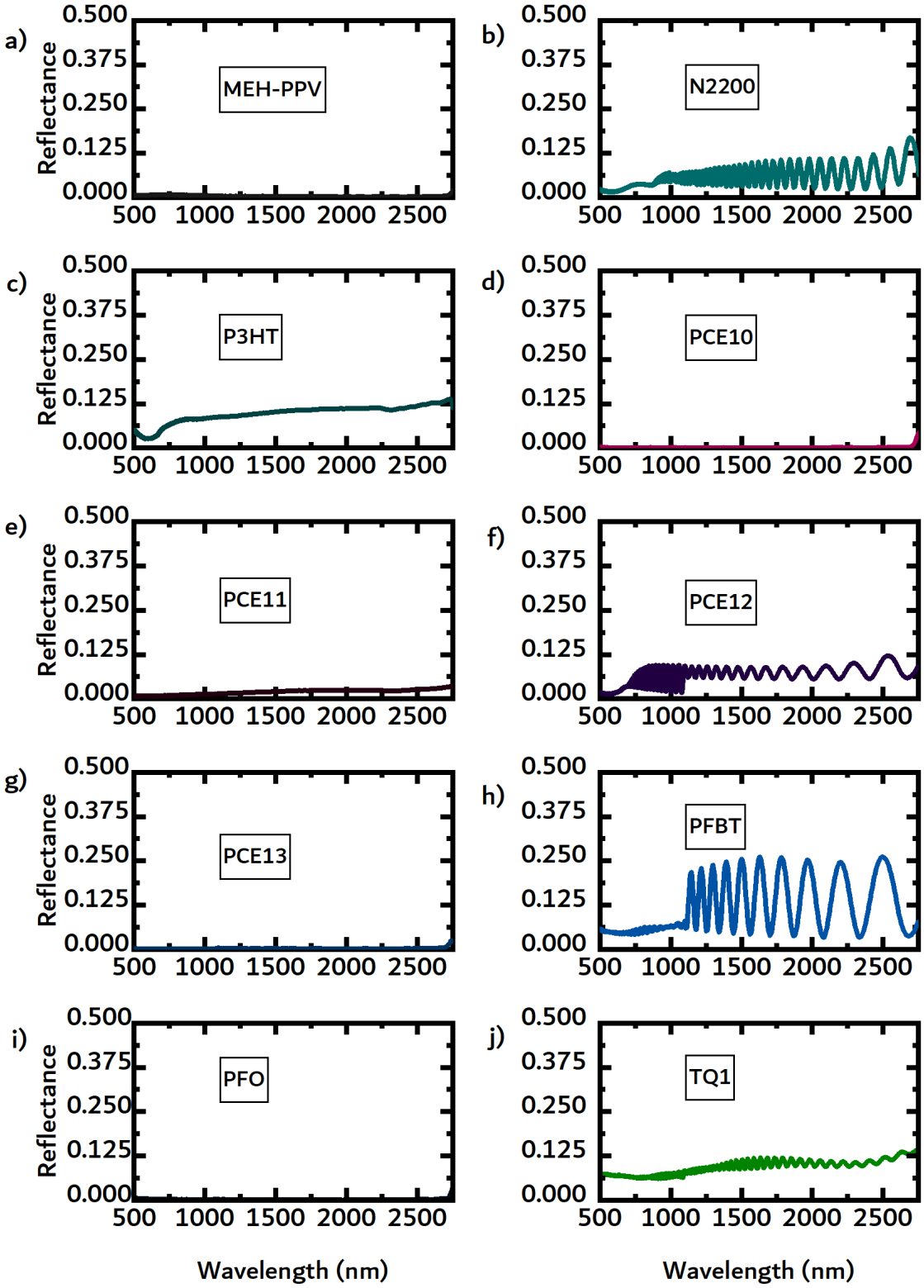

Figure 4-4. Specular reflectance data for a) MEH-PPV; b) N2200; c) P3HT; d) PCE10; e) PCE11; f) PCE12; g) PCE13; h) PFBT; i) PFO; and j) TQ1. The figure has been adapted from Jurado et al. [1].

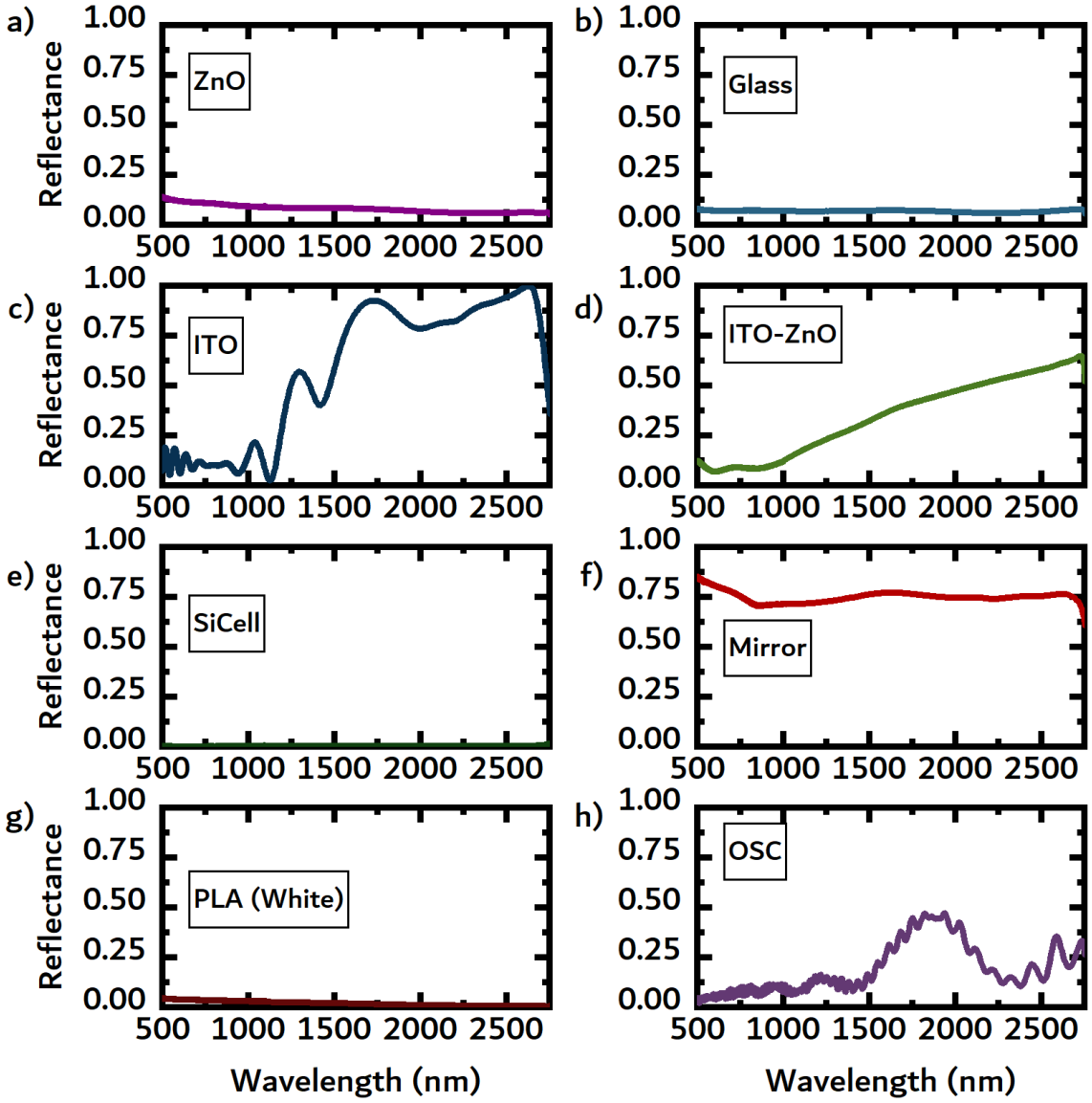

Figure 4-5. Specular reflectance data for a) a glass substrate with ZnO, b) a bare glass substrate c) a glass substrate with ITO; d) a glass substrate with ITO and ZnO layers; e) a commercial silicon module; f) a commercial mirror; g) a 3-D printed white PLA block; and h) a commercial infinityPV OSC module. The figure has been adapted from Jurado et al. [1].

Figures 4-4 and 4-5 show the normal incidence reflectance spectra for the selected OSC active layer materials and for the other materials, respectively. In this experiment, a commercial mirror was measured as a reference. The active layer materials, as seen in Figure 4-4, generally exhibit low reflectance. The low reflectance, at least in part, could be due to the large scattering exhibited by the free standing films, which arises from film roughness. Glass with ITO (Figure 4-5c) and glass with ITO and ZnO (Figure 4-5d) exhibit

higher reflectance in the NIR region. The commercial silicon cell exhibits extremely low reflectance likely due to surface texturization.

4.4. Photothermal Experiments

It is clear to see that some incident radiation is reflected and transmitted. In addition to transmittance and reflectance data, a useful approach to compare the three geometries is by evaluating temperature rise under illumination of the solar cells and the solar cell filters. For the three geometries, an infrared camera was used to record temperature under illumination, but the measurement was slightly different in each case. For the contact geometry, the commercial PV modules and solar cell filters were placed under the solar simulator and illuminated under 1 sun conditions while temperature and efficiency were continuously recorded. In this geometry, the solar cell is in direct contact with the TEG and is essentially a heat reservoir. Temperature rise of the two commercial modules is here used as a proxy of the efficiency of converting light into heat in the solar cell, i.e. $\eta_{PV,PT}$.

The temperature and efficiency response of the commercial silicon and OSC modules are shown in Figures 4-6a and 4-6b, respectively. For the silicon cell, a temperature rise of approximately 30 K caused the efficiency to drop by more than 1.5 percentage points. For the commercial OSC module, solar cell efficiency increased by almost 20% as the temperature increased by over 30 K. Because the OSC module was flexible, the OSC was supported with a block of white PLA. When the white PLA block was removed (black line), the OSC module did not reach as high a temperature as it did when in contact with the white PLA block (navy line). Likely, the PLA block helps reduce convection losses at the back end of the OSC module. The origin of the enhancement in efficiency due to temperature could be due to an increase in the mobility of charge carriers [11], [12]. Organic semiconductors have temperature-dependent mobility because charge transport is influenced by temperature (temperature-activated hopping). At higher temperature, charge transport is enhanced in the active layer and/or the solar cell's ITO-free front electrode. Figure 4-6b shows the efficiency of the OSC module as a function of temperature. As this is a very interesting effect, it will be studied in depth in the next chapter.

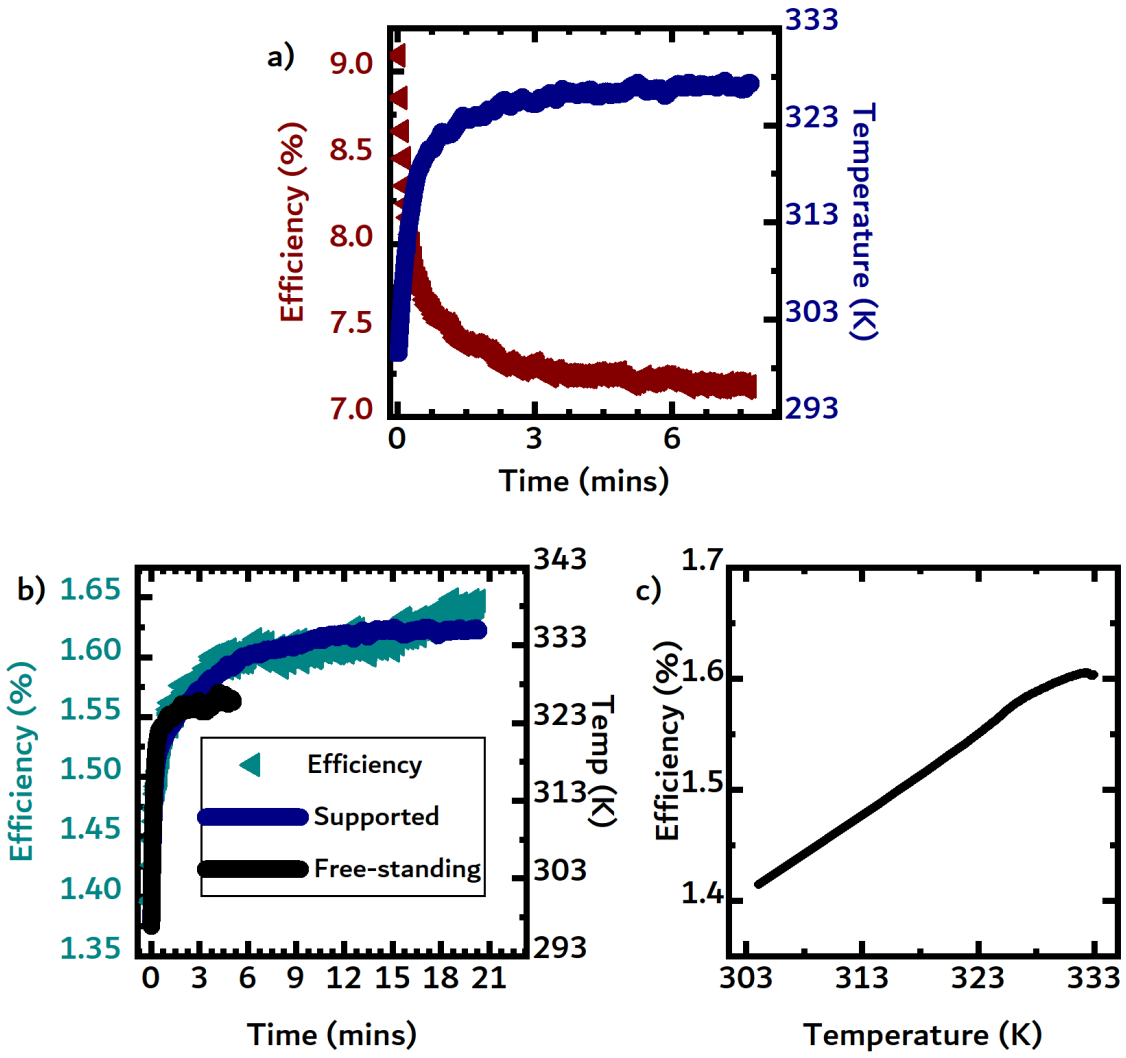

Figure 4-6. a) Efficiency and temperature evolution under continuous 1 sun illumination for a commercial silicon cell. b) Temperature evolution of the free-standing infinityPV OSC module (black line); temperature (blue line) and efficiency (cyan triangles) evolution of the same commercial module, supported on the back side with a block of white PLA. c) Efficiency as a function of temperature for the infinityPV OSC module. The figure has been adapted from Jurado et al. [1].

In a real device using a contact geometry, the surface temperatures of the thermoelectric materials should be measured. However, given the difficulties of accurately measuring the surface temperature of the thermoelectric materials in direct contact with the solar cell, the surface temperatures of the solar cell filters were measured. These temperatures likely can be considered the lower limit, since losses to convection will likely be reduced when another material is placed in contact with the filters (leading to higher temperatures). Additionally, the thermoelectric materials can absorb a part of the light transmitted by the filters, which can also lead to higher temperatures. The steady-state temperatures achieved by the free-standing solar cell filters as well as the commercial solar cell modules are shown in Figure

4-7. As discussed in the previous chapter, temperature rise depends on both a material's absorption spectrum and thickness. The temperature of the silicon solar cell was measured from the front and the back to ensure no significant temperature gradient developed in the thickness direction of the cell, since it was much thicker than the other materials. The commercial OSC module achieved the highest temperature (327 K), which could be due to a reduction of convection losses as a result of the (Polyethylene Terephthalate) PET encapsulation. Of the solar cell filters, N2200, a common non-fullerene acceptor, heated up the most. N2200 exhibits absorption up to 860 nm (Figure 4-2b), which could explain the higher temperature compared to the other filters. As a general observation, it seems that the narrower the band gap, the higher temperature. The dashed line in Figure 4-7 displays this general trend.

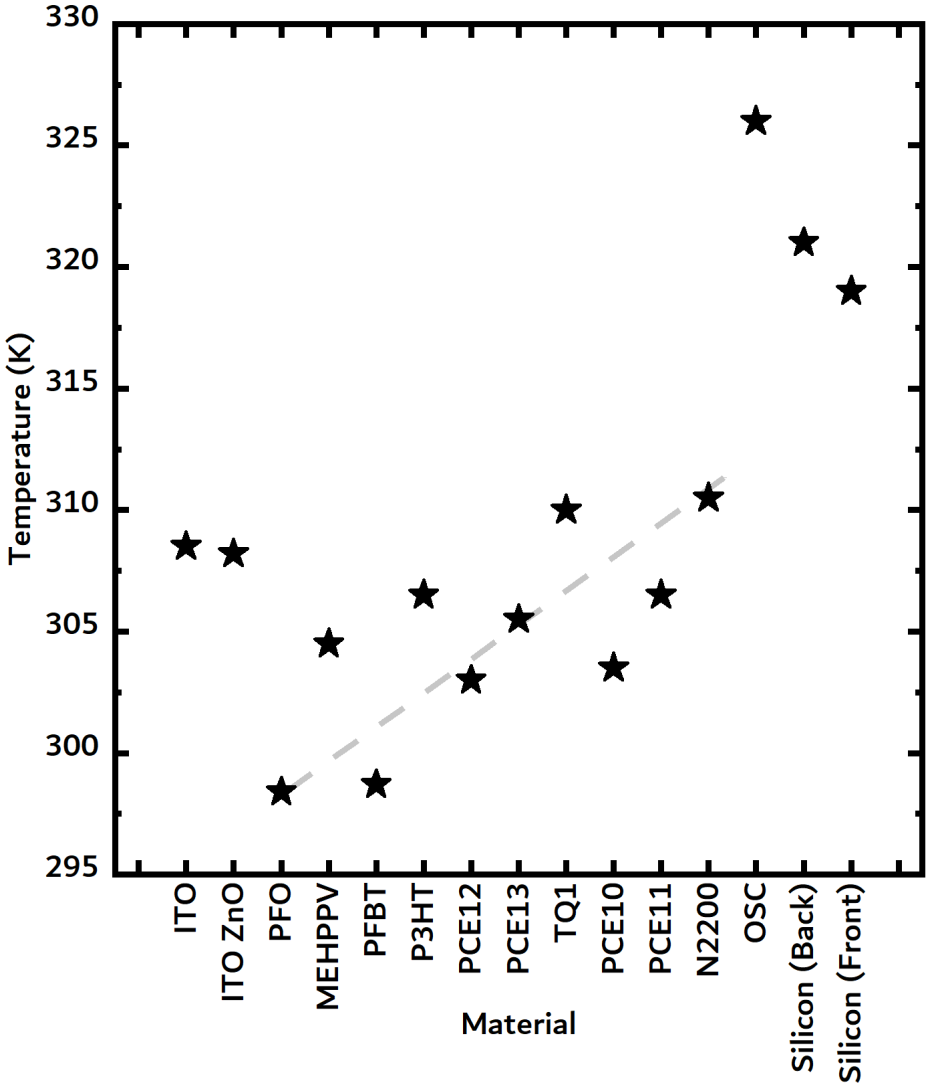

Figure 4-7. Steady-state temperatures achieved by the free-standing films used as "solar cell filters" under 1 sun illumination. The figure has been adapted from Jurado et al. [1].

To investigate the effect of contact material on temperature, the experiment was repeated placing different support materials in contact with the solar cell filters. Figure 4-8a shows the temperature evolution of the PCE 11 filter in contact with 3 different support materials, namely PET, glass, and black PLA. The achieved steady-state temperatures are shown in Figure 4-8b. Clearly, the presence of a support material helps enhance temperature. In the case of black PLA, the PCE 11 heated up an extra 10 K, likely due to absorption from the black PLA. From Figure 4-8c, the black PLA significantly enhanced temperature for the organic materials, achieving temperatures around 325 K.

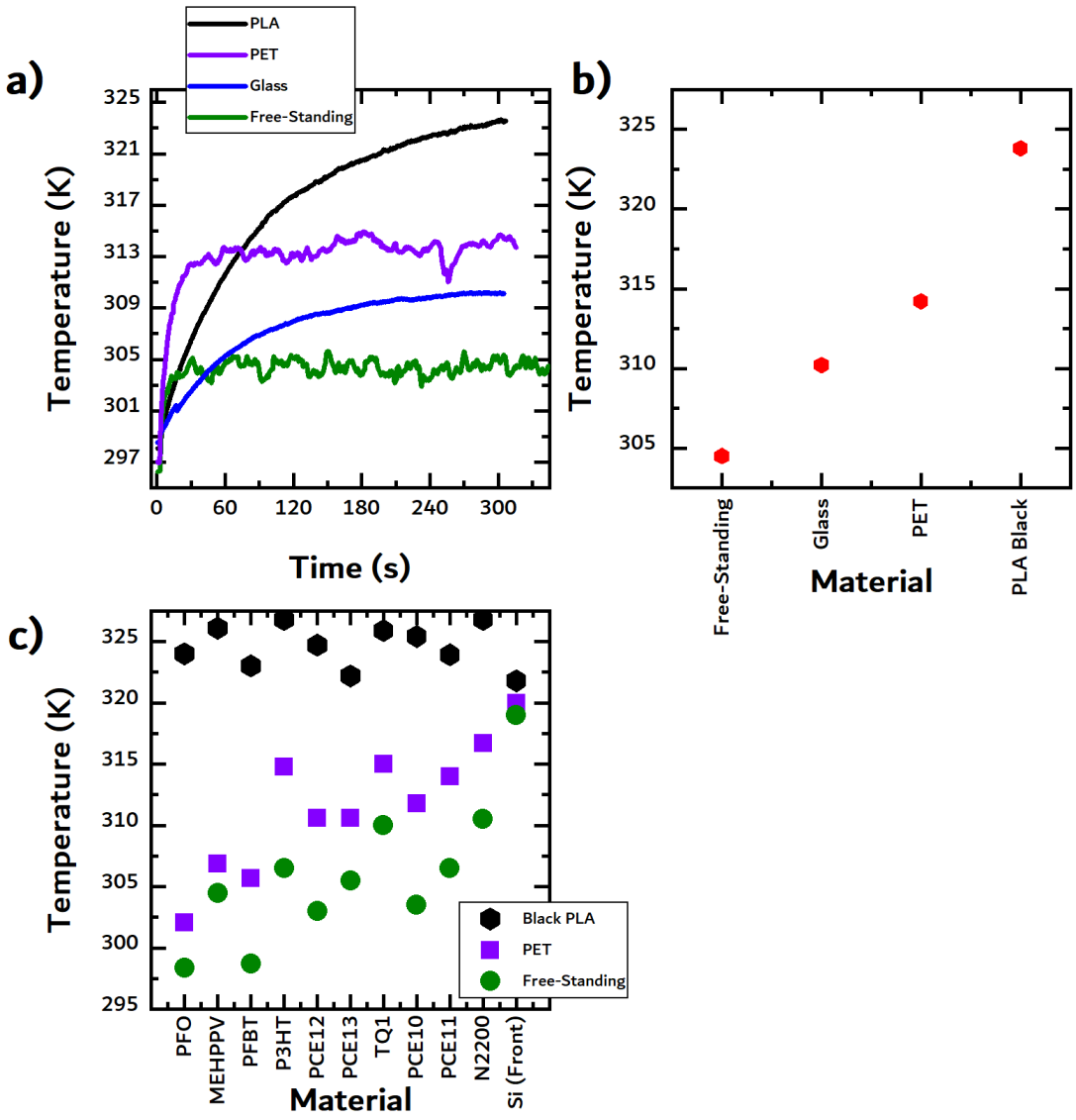

Figure 4-8. a) Temperature evolution of the PCE11 filter with different support materials; b) Steady-state temperature achieved by the PCE11 filter with different support materials and c) Temperatures of the OSC materials in contact with support materials. The figure has been adapted from Jurado et al. [1].

For the non-contact geometries, IR thermography was used to quantify the maximum temperatures acquired by the TE materials in the reflection and transmission geometries (see Figures 4-9a and 4-9b). In these experiments, the temperatures of the TE materials were measured as opposed to the temperatures of the solar cell filters. In a first step, the filters were placed at an angle of 45 degrees to reflect light towards the TE materials, emulating a device with a reflection geometry. In a second step, the filters were placed above the TE materials emulating a non-contact transmission geometry. A thermopile was used to measure the light reflected and transmitted by the filter, as can be seen in Table

4.3. As previously mentioned, a solar cell should reflect more than the filters do, because of reflection from the metallic back electrode and smoother surfaces. The results from the photothermal experiments are summarized in Figure 4-10. In Figure 4-10a, the DMSO-treated PEDOT:PSS reached the highest temperature of all the TE materials in reflection mode. The temperatures were very similar for all the filters, i.e. a ca. 10 K rise, with two exceptions in the case of the mirror and the white PLA. The mirror's reflectance is much higher than the rest of the materials, thus reflecting more light onto the TE materials. Conversely, the PLA's specular reflectance is much lower than the rest of the materials due to surface roughness. Temperature rise for the reflection geometry showed no clear dependence on the amount of power reflected by the filters, as seen in 3.10c.

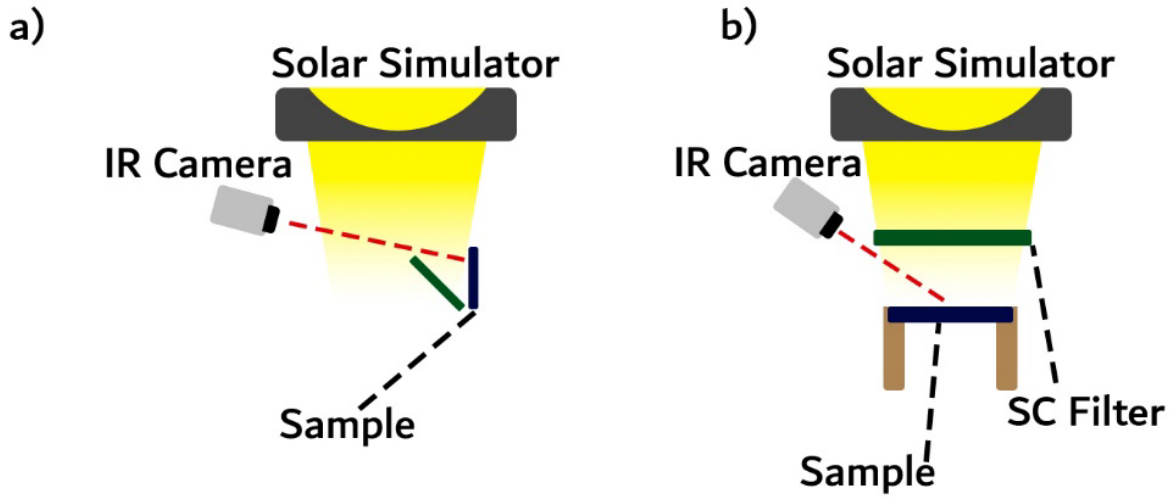

Figure 4-9. Schematic of the photothermal experiment for the a) non-contact reflection geometry and b) non-contact transmission geometry. The figure has been adapted from Jurado et al. [1].

Table 4.3. Light transmitted and reflected by the solar cell filters

Material	Transmitted Power Density	Reflected Power Density
	mW cm^{-2}	mW cm^{-2}
Air	90.00	-
Glass	80.90	20.24
ZnO	85.61	22.92
ITO	67.04	27.12
ITO ZnO	69.33	24.96
PFO	64.49	26.48
MEH-PPV	61.75	21.01
PFBT	35.66	21.90
P3HT	39.27	18.33
PCE12	43.00	23.81
PCE13	36.25	17.32
TQ1	36.15	15.02
PCE10	41.35	17.06
PCE11	27.07	18.59
N2200	32.01	21.14
OSC	6.96	14.64
PLA (White)	-	14.90
Si Cell	-	9.17
Mirror	-	69.14

*

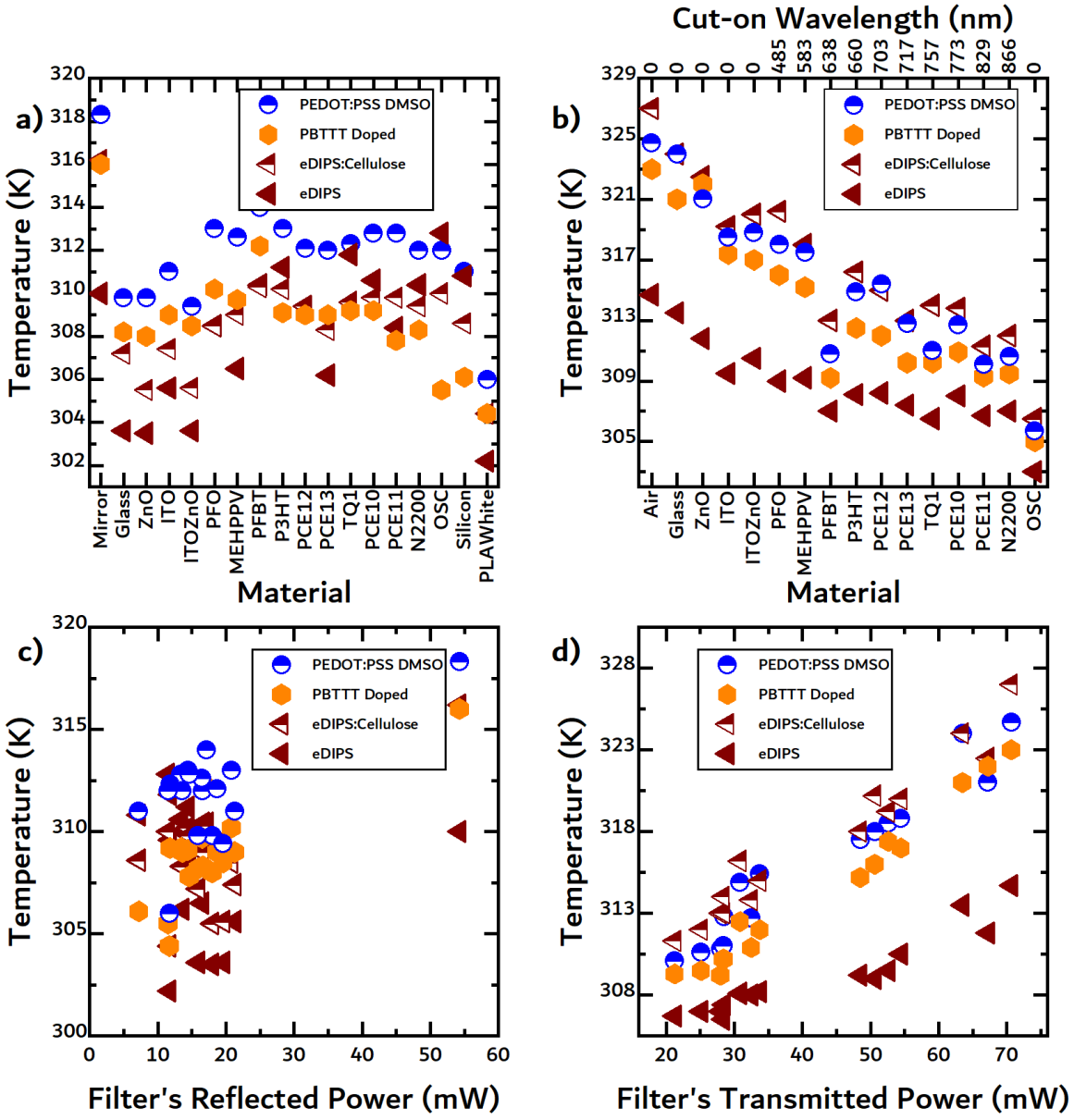

Figure 4-10. a) Steady-state temperatures achieved in reflection mode. b) Steady-state temperatures achieved in non-contact, transmission mode (under filtered illumination). c) Steady-state temperatures achieved in reflection mode replotted against the measured power reflected by the solar cell filters. d) Steady-state temperatures achieved in non-contact, transmission mode replotted against the measured power transmitted by the solar cell filters.

For the transmission geometry, the filters transmit light with energy below the bandgap to the TE materials, causing the TE materials to heat up. In Figure 4-10b, we observed that the eDIPS:cellulose composite heated up the most, which exhibits a thermal conductivity of ≈2.7 W m^{-1} K^{-1}. The pure eDIPS material exhibits a significantly higher thermal conductivity for comparison (≈27 W m^{-1} K^{-1}). The thermal conductivity of the composite sample is one order of magnitude different to that of the F_4TCNQ-doped PBTTT and DMSO-treated

PEDOT:PSS, which are reported to be 0.3 and 0.42 W m^{-1} K^{-1}, respectively [13], [14]. Recalling Figure 3-3, the composite sample absorbed strongly in the visible and up to 1200 nm, the F_4TCNQ-doped PBTTT sample absorbed strongly in the visible and up to 900 nm, while the DMSO-treated PEDOT:PSS sample absorbed weakly in the visible but strongly in the IR.

In Figure 4-10b, the measured cut-on wavelengths for each of the materials are seen in the upper x-axis. The temperature rise of the materials is strongly correlated with the bandgap of the filters in this geometry (and thus transmitted power as seen in Figure 4-10d), unlike in the non-contact reflection geometry. The temperature rises in the non-contact transmission geometry are much larger than those observed using a non-contact reflection geometry due to a larger percentage of light being transmitted than reflected, as seen in Figures 4-2 – 4-5.

4.5. Calculated Thermoelectric Geometries

In this section, the theoretical TEG efficiencies for the three geometries were calculated using equation 1.15 assuming two hypothetical thermoelectric materials with the optical and thermal properties of either eDIPS:cellulose, or DMSO-treated PEDOT:PSS, and a zT value of 0.5, corresponding to a state-of-the-art organic TE material [14]. It is important to note that the device efficiency of a working TEG depends on its geometry and the *zT*s of the n- and p-type materials. In general, n-type materials are less stable than p-type materials and exhibit lower *zT*s [15]–[17].

To investigate the relative benefit of coupling TEGs with OSCs, the best reported efficiencies for fullerene solar cells with the donors used as filters in this study are shown in Table 4.4. These reported OSC efficiencies were plotted against the calculated TEG efficiencies for eDIPS:cellulose and DMSO-treated PEDOT:PSS (Figures 4-11a and 4-11b, respectively), using the temperature data from the previous experiments for the hot side, and assuming room temperature for the cold side.

Table 4.4. Reported efficiencies for selected solar cell blends

Solar Cell	Efficiency	Reference
MEH-PPV:$PC_{61}BM$	2.9%	[18]
P3HT:$PC_{61}BM$	4.4%	[19]
PDBD-T(PCE12):$PC_{71}BM$	7.8%	[20]
TQ1:$PC_{71}BM$	7.08%	[21]
PCE10:$PC_{71}BM$	9.01%	[22]
PCE11:$PC_{71}BM$	10.5%	[23]
PCE13:$PC_{71}BM$	8.89%	[24]
PFBT:$PC_{61}BM$	<1	[25]
InfinityPV solar cell	1.4-1.6%	This work
Commercial Si Cell	7-9%	This work

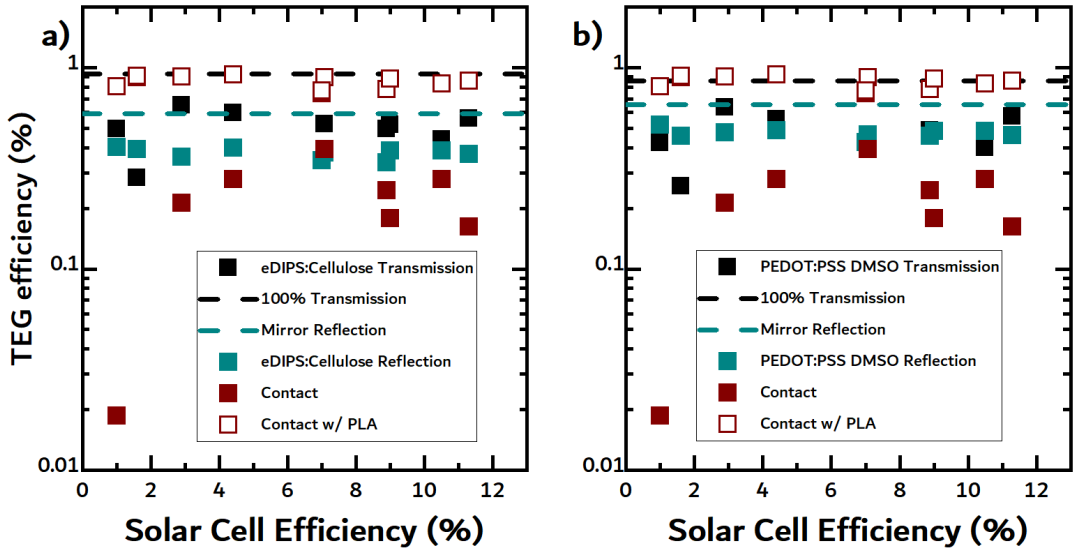

Figure 4-11. a) Calculated TEG efficiencies for the eDIPS:cellulose composite in the three different geometries: non-contact transmission mode (black squares), reflection mode (cyan squares), and contact mode (wine squares). The black dashed line assumes all light is transmitted – i.e. no filter- and represents the upper limit for TEG efficiency in non-contact transmission mode. The green dashed line assumes light is reflected off a realistic mirror – and represents the upper limit for reflection mode. The open wine squares represent the calculated TEG efficiencies when the filters are in contact with a slab of black PLA. b) Calculated TEG efficiencies for DMSO-treated PEDOT:PSS. The figure has been adapted from Jurado et al. [1].

In Figure 4-11, the black and cyan dashed lines represent the theoretical upper limits to efficiency in non-contact transmission mode and non-contact reflection mode, respectively. The upper limits for the non-contact transmission geometry were calculated using temperatures measured when no filter was placed above the TE material, i.e. 100% transmission. For the non-contact reflection geometry, the upper limits were calculated using temperatures when a mirror reflected light onto the TE materials. Recalling Figure 4-5f, the mirror does not reflect 100% of light; however, it is a reasonable approximation of ideal reflection under realistic conditions.

From Figure 4-11, it can be seen that independent of the geometry, for both material systems, the TEG efficiencies are much lower than the theoretical limits, as a result of strong absorption in the visible region by the solar cells. For the eDIPS:cellulose sample, the TEG efficiencies in non-contact transmission mode (black squares) are slightly higher than in non-contact reflection mode (cyan squares), as a result of the higher temperatures achieved in transmission mode. As previously discussed, TEGs convert heat into electricity more efficiently at higher temperatures, like all heat engines. Since a lesser amount of light is reflected than transmitted by the solar cells, the temperature rise in the eDIPS:cellulose sample is lower, and thus the TEG efficiency is lower.

The TEG efficiencies are spread over a larger range for the contact mode geometry (wine squares). The contact transmission geometry exhibits the highest theoretical efficiency, but for a large fraction of the OSC materials studied, the TEG efficiencies are slightly lower than in the other geometries. Likely the temperatures in a real device are being underestimated as only the temperature of the free-standing filter, i.e. the solar cell, is being measured, as opposed to the actual temperature of the TE material. As previously mentioned, it is difficult to measure the temperature of the TE material in contact geometry, so the TEG efficiencies were calculated using the temperature of the filters. As a result, the TEG efficiencies calculated here can be taken as the lower limit for this geometry. In a real device, there could be an additional gain in temperature as a result of absorption by the TE material and a reduction in convection through the presence of a support material, thus resulting in higher TEG efficiencies. Recalling Figure 4-8c, the support materials have a significant impact on temperature rise. In order to calculate an upper limit for this geometry, the temperatures from Figure 4-8c, i.e. those of the solar cell filters supported on PLA, were used to recalculate the thermoelectric efficiencies (open wine squares). It can be seen that the TEG efficiencies are higher in the contact geometry than in the other two geometries.

In the final step, the *zT* was varied and the TEG efficiencies recalculated for each geometry as can be seen in Figure 4-12. In all cases, the TEG efficiencies would be greatly increased by better TE materials. For the contact geometry, TEG efficiencies of 1% can be readily attained for materials with *zTs* higher than 0.5 (Figure 4-12a). For the non-contact transmission geometry (Figures 4-12b and c), *zTs* higher than 1 would be needed to achieve TEG efficiencies greater than 1%. For the non-contact reflection geometry (Figures 4-12d and e) eDIPS:cellulose and DMSO-treated PEDOT:PSS *zTs* higher than 2.5 would be needed to achieve TEG efficiencies greater than 1%.

Although the increase in device efficiency may appear modest, the advantage of coupling TEGs with OSCs is that device complexity is not increased. Compared to other strategies used to boost efficiency, such as light management using patterned active layers, or tandem cells, a hybrid PV-TE solid-state device is a simple connection of two separately fabricated devices. Tandem cells, on the other hand, are much more complex devices. The fabrication process of tandem cells is likely significantly longer than that for hybrid PV-TE devices because every step is dependent on preceding one. Hybrid PV-TE devices can be fabricated independently, and in parallel, likely reducing fabrication time and increasing yield. To justify the viability of hybrid PV-TE devices, the increased cost and lower device yield may need to be quantified rigorously. A promising preliminary conclusion is that the thermal insulating effect of the TEG boosts OSC conversion efficiency, and in the short term, this reason alone is encouraging to continue investigating thermal effects on OSC performance, the topic of the next chapter.

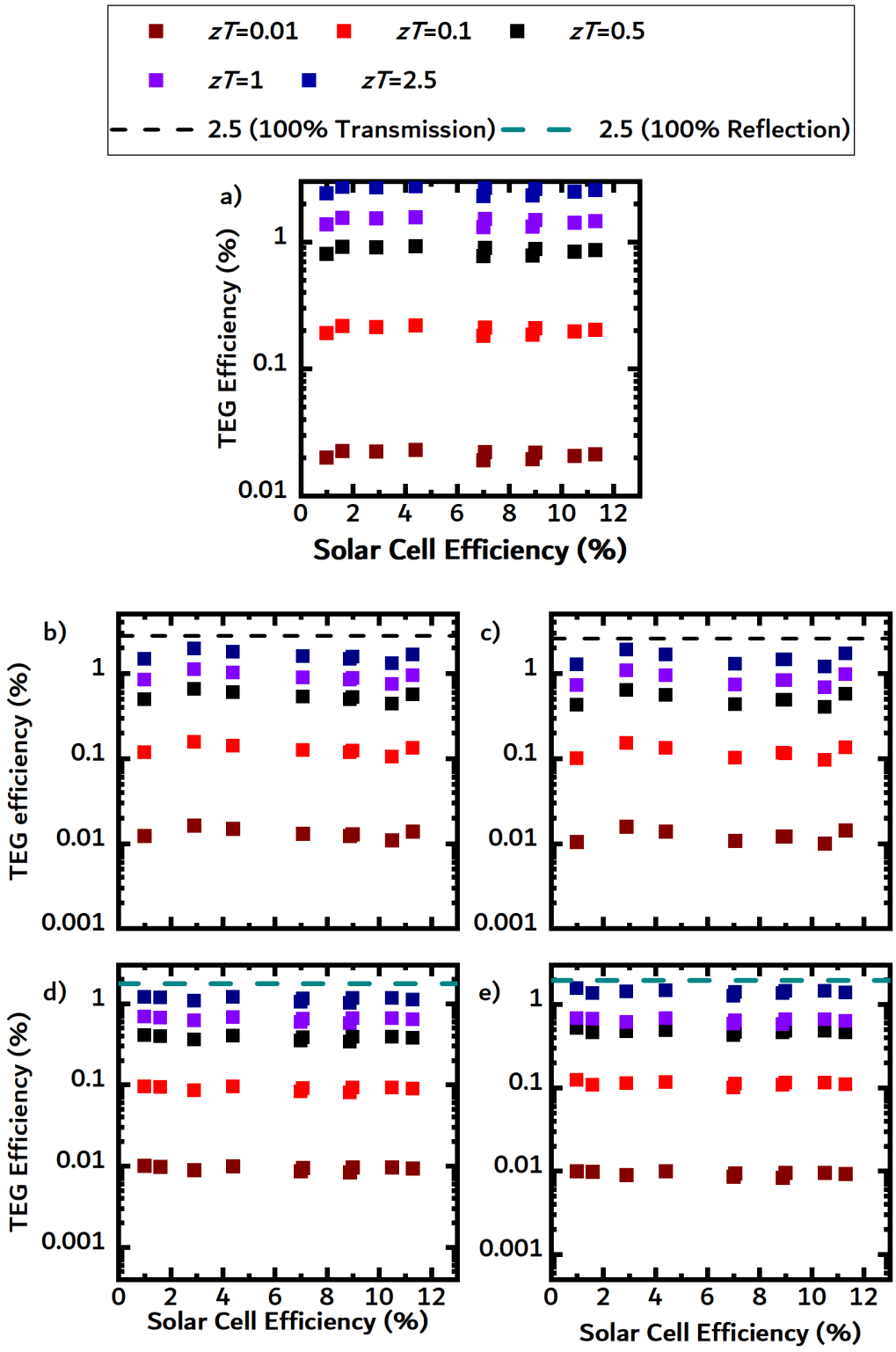

Figure 4-12. Calculated TEG efficiencies for various values of zT. a) Calculated TEG efficiencies in contact mode, for a zT of 0.01 (wine square), 0.1 (orange square), 0.5 (black square), 1 (purple square), and 2.5 (blue square). b) Calculated TEG efficiencies for eDIPS:Cellulose in transmission mode, where the dashed black line represents the TEG efficiency calculated assuming a zT of 2.5 with no filter above (100% transmission). c) Calculated TEG efficiencies for DMSO-treated PEDOT:PSS in non-contact transmission mode. d) Calculated TEG efficiencies for eDIPS:cellulose in non-contact reflection mode, where the dashed cyan line represents the TEG efficiency calculated assuming a zT of 2.5 with a commercial mirror (100% reflection). e) Calculated TEG efficiencies for DMSO-treated PEDOT:PSS in non-contact reflection mode. The figure has been adapted from Jurado et al. [1].

4.6. Chapter conclusions

Three geometries for organic-based solid-state hybrid PV-TE devices were evaluated: a non-contact reflection geometry, a non-contact transmission geometry, and a contact transmission geometry. In a first step, the transmittance and reflectance spectra of OSC materials were measured using FTIR spectroscopy. Next, the temperature rise of all OSC and TE materials was recorded in the three aforementioned geometries. In a last step, we calculated TEG efficiencies.

From the measured transmittance and reflectance spectra, a larger portion of solar radiation is transmitted than reflected by the OSC materials. Drawing upon the temperature data, three observations can be made. Firstly, the temperature available to SOTEGs appears to be higher in a transmission geometry than in a reflection geometry, corroborating the observation from the FTIR experiments. The higher temperatures would thus lead to higher TEG efficiencies. Secondly, the temperature rise of an OSC material can be enhanced by selecting the right support material, i.e. PLA with an extremely low thermal conductivity to reduce losses to convection. A reduction in convection losses would also result in higher TEG efficiencies. Thirdly, the temperature rise of the OSC materials appears to depend on the band gap of the material. The materials with narrower band gaps appeared to exhibit higher temperatures.

A SOTEG in a device with a contact transmission geometry makes use of the additional temperature gain from the solar cell, a characteristic unique to the contact geometry. Moreover, when a semi-transparent OSC is used, the SOTEG can absorb additional light transmitted by the solar cell, which should further increase temperature. In a hybrid device, apart from benefiting the SOTEG, the enhancement in temperature may help boost OSC efficiency. As seen in this chapter, temperature is detrimental to solar cell performance for traditional silicon solar cells. For a commercial OSC module on the other hand, temperature was shown to enhance efficiency, so higher temperatures in a hybrid device would be beneficial to OSCs.

4.7. References for Chapter 4

[1] J. P. Jurado, B. Dörling, O. Zapata-Arteaga, A. R. Goñi, and M. Campoy-Quiles, “Comparing different geometries for photovoltaic-thermoelectric hybrid devices based on organics,” *J. Mater. Chem. C*, vol. 9, no. 6, pp. 2123–2132, 2021, doi: 10.1039/D0TC05067A.

[2] W. Shockley and H. J. Queisser, “Detailed Balance Limit of Efficiency of p-n Junction Solar Cells,” *J. Appl. Phys.*, vol. 32, no. 3, p. 510, Jun. 1961, doi: 10.1063/1.1736034.

[3] Z. Tang, W. Tress, and O. Inganäs, “Light trapping in thin film organic solar cells,” *Materials Today*, vol. 17, no. 8. Elsevier, pp. 389–396, 01-Oct-2014, doi: 10.1016/j.mattod.2014.05.008.

[4] T. Tiedje, E. Yablonovitch, G. D. Cody, and B. G. Brooks, “Limiting Efficiency of Silicon Solar Cells,” *IEEE Trans. Electron Devices*, vol. 31, no. 5, pp. 711–716, 1984, doi: 10.1109/T-ED.1984.21594.

[5] S. M. Menke, N. A. Ran, G. C. Bazan, and R. H. Friend, “Understanding Energy Loss in Organic Solar Cells: Toward a New Efficiency Regime,” *Joule*, vol. 2, no. 1, pp. 25–35, Jan. 2018, doi: 10.1016/J.JOULE.2017.09.020.

[6] B. Lorenzi, P. Mariani, A. Reale, A. Di Carlo, G. Chen, and D. Narducci, “Practical development of efficient thermoelectric – Photovoltaic hybrid systems based on wide-gap solar cells,” *Appl. Energy*, vol. 300, p. 117343, Oct. 2021, doi: 10.1016/J.APENERGY.2021.117343.

[7] W. G. J. H. M. va. Sark, “Feasibility of photovoltaic – Thermoelectric hybrid modules,” *Appl. Energy*, vol. 88, no. 8, pp. 2785–2790, Aug. 2011, doi: 10.1016/J.APENERGY.2011.02.008.

[8] G. Li, S. Shittu, T. M. O. Diallo, M. Yu, X. Zhao, and J. Ji, “A review of solar photovoltaic-thermoelectric hybrid system for electricity generation,” *Energy*, vol. 158, pp. 41–58, Sep. 2018, doi: 10.1016/J.ENERGY.2018.06.021.

[9] K.-T. T. Park *et al.*, “Lossless hybridization between photovoltaic and thermoelectric devices,” *Sci. Rep.*, vol. 3, no. 1, p. 2123, Jul. 2013, doi: 10.1038/srep02123.

[10] J. Gasiorowski, R. Menon, K. Hingerl, M. Dachev, and N. S. Sariciftci, “Surface morphology, optical properties and conductivity changes of poly(3,4-ethylenedioxythiophene):poly(styrenesulfonate) by using additives,” *Thin Solid Films*, vol. 536, no. 100, pp. 211–215, Jun. 2013, doi: 10.1016/j.tsf.2013.03.124.

[11] D. J. Coutinho, G. C. Faria, D. T. Balogh, and R. M. Faria, “Influence of charge carriers mobility and lifetime on the performance of bulk heterojunction organic solar cells,” *Sol. Energy Mater. Sol. Cells*, vol. 143, pp. 503–509, Aug. 2015, doi: 10.1016/j.solmat.2015.07.047.

[12] B. Ebenhoch, S. A. J. Thomson, K. Genevičius, G. Juška, and I. D. W. Samuel, “Charge carrier mobility of the organic photovoltaic materials PTB7 and PC71BM and its influence on device performance,” *Org. Electron.*, vol. 22, pp. 62–68, Jul. 2015.

[13] O. Zapata-Arteaga, B. Dörling, A. Perevedentsev, J. Martín, J. S. Reparaz, and M. Campoy-Quiles, “Closing the Stability-Performance Gap in Organic Thermoelectrics by Adjusting the Partial to Integer Charge Transfer Ratio,” *Macromolecules*, vol. 53, no. 2, pp. 609–620, Jan. 2020, doi: 10.1021/acs.macromol.9b02263.

[14] G.-H. H. Kim, L. Shao, K. Zhang, and K. P. Pipe, “Engineered doping of organic semiconductors for enhanced thermoelectric efficiency,” *Nat. Mater.*, vol. 12, no. 8, p. 719, May 2013, doi: 10.1038/nmat3635.

[15] Y. Sun, C.-A. Di, W. Xu, and D. Zhu, “Advances in n-Type Organic Thermoelectric Materials and Devices,” *Adv. Electron. Mater.*, vol. 5, no. 11, p. 1800825, Nov. 2019, doi: 10.1002/AELM.201800825.

[16] J. Liu *et al.*, “Doping Engineering Enables Highly Conductive and Thermally Stable n-Type Organic Thermoelectrics with High Power Factor,” *ACS Appl. Energy Mater.*, vol. 2, no. 9, pp. 6664–6671, Sep. 2019, doi: 10.1021/ACSAEM.9B01179.

[17] Y. Nonoguchi *et al.*, “Simple Salt-Coordinated n-Type Nanocarbon Materials Stable in Air,” *Adv. Funct. Mater.*, vol. 26, no. 18, pp. 3021–3028, May 2016, doi: 10.1002/ADFM.201600179.

[18] S. Alem, R. de Bettignies, J.-M. M. Nunzi, and M. Cariou, “Efficient polymer-based interpenetrated network photovoltaic cells,” *Appl. Phys. Lett.*, vol. 84, no. 12, pp. 2178–2180, Mar. 2004, doi: 10.1063/1.1669065.

[19] W.-J. J. Yoon and P. R. Berger, “4.8% efficient poly(3-hexylthiophene)-fullerene derivative (1:0.8) bulk heterojunction photovoltaic devices with plasma treated AgOx/indium tin oxide anode modification,” *Appl. Phys. Lett.*, vol. 92, no. 1, p. 13306, Jan. 2008, doi: 10.1063/1.2830619.

[20] N. Y. Doumon *et al.*, “Photostability of Fullerene and Non-Fullerene Polymer Solar Cells: The Role of the Acceptor,” *ACS Appl. Mater. Interfaces*, vol. 11, no. 8, pp. 8310–8318, Feb. 2019, doi: 10.1021/acsami.8b20493.

[21] Y. Kim, H. R. Yeom, J. Y. Kim, and C. Yang, “High-efficiency polymer solar cells with a cost-effective quinoxaline polymer through nanoscale morphology control induced by practical processing additives,” *Energy Environ. Sci.*, vol. 6, no. 6, pp. 1909–1916, Jun. 2013, doi: 10.1039/c3ee00110e.

[22] “PTB7-Th (PCE10) | PBDTTT-EFT | 1469791-66-9 | Ossila.” [Online]. Available: https://www.ossila.com/products/pce10?_pos=2&_sid=1a5323ea4&_ss=r&variant=31832978391136. [Accessed: 18-Jun-2020].

[23] Y. Liu *et al.*, “Aggregation and morphology control enables multiple cases of high-efficiency polymer solar cells,” *Nat. Commun.*, vol. 5, no. 1, p. 5293, 2014, doi: 10.1038/ncomms6293.

[24] Y. Tamai *et al.*, “Ultrafast Long-Range Charge Separation in Nonfullerene Organic Solar Cells,” *ACS Nano*, vol. 11, no. 12, pp. 12473–12481, Dec. 2017, doi: 10.1021/ACSNANO.7B06575.

[25] Ł. Bernacki, Z. Lisik, and B. Łuszczyńska, “The evaluation of organic solar cell’s properties based on polymer F8BT and fullerene derivative C60PCBM,” *PRZEGLĄD ELEKTROTECHNICZNY*, vol. 1, no. 9, pp. 15–17, Sep. 2015, doi: 10.15199/48.2015.09.04.

Chapter 5. OSC Parameters

5.1. Temperature and OSC Performance

OSCs, apart from converting light to electricity, convert a significant, non-negligible amount of light to heat, as seen in chapter 4 (ca. 30 K temperature rise under 1 sun illumination). In the context of hybrid PV-TE devices, particularly those with a contact geometry, the heat generated by an OSCs is a critical design parameter that should be accounted for. As shown in chapter 4, the heat generated by an OSC can enhance TEG PCE, and depending on the blend of the photoactive layer (PAL) in the OSC, also enhance OSC efficiency.

In this chapter, the four OSC parameters, namely PCE, *FF*, V_{OC}, and J_{SC} are measured for a number of systems as a function of temperature. One representative system, PBDB-T:ITIC, was chosen to demonstrate that temperature can enhance OSC performance without provoking irreversible changes in the microstructure of the devices. Blade-coating, a method for high-throughput device fabrication, was used to fabricate solar cells with thickness gradients. For the PBDB-T:ITIC system, PCE, *FF*, and J_{SC} enhanced with temperature, while the V_{OC} reduced with temperature. The thicker pixels exhibited a larger enhancement in PCE, *FF*, and J_{SC} compared to the thinner pixels, originating from better charge carrier mobility. The increased charge carrier mobility allows for more efficient extraction of charge carriers in the device.

To highlight that the enhancement in PCE, *FF*, and J_{SC} originates from increased charge carrier mobility as opposed to changes in the microstructure, we carried out grazing-incidence small-angle X-ray scattering (GISAXS), grazing-incidence wide-angle X-ray scattering (GIWAXS), temperature-dependent external quantum efficiency (EQE), temperature-dependent space-charge limited current (SCLC), and light-intensity JV measurements. From the GISAXS profiles and GIWAXS patterns, no significant difference is observed between the pristine and annealed PBDB-T:ITIC samples, indicating no change in the morphology of the system. Next, the EQEs of the thick pixels significantly enhance with temperature, indicative of better charge transport in the devices with temperature. The extracted mobilities from the SCLC fits confirmed an enhancement in the charge transport with temperature.

The light-intensity experiments revealed that the recombination mechanism in the devices did not significantly change, further indicating that the origin of the enhancement in PCE,

FF, and J_{SC} lies in better charge transport in the device with temperature. Finally, drift-diffusion simulations were performed to investigate the impact of mobility and recombination on the device performance. The simulation results agreed well with experimental results, further confirming that temperature enhances charge transport, directly enhancing device performance.

5.1.1. Non-reversible reported Temperature Effects in OSCs

Annealing during the fabrication process has been widely employed as a strategy to enhance OSC performance [1]–[4]. Temperature treatments can help tune the microstructure in films, and thus impact absorption, charge transport, and recombination mechanisms. For instance, Chirvase et al. reported a change in the absorption spectrum of a P3HT:PC_{60}BM film and attributed the change to the molecular diffusion of the PCBM out of the polymer matrix [2]. The diffusion of the PCBM causes PCBM domains to be built up and allows for a better-ordered P3HT phase. As a result of the P3HT crystallization, the absorption of P3HT is enhanced. In addition, the electron transfer and transport improve, thus enhancing the J_{sc} and *FF* of the P3HT:PC_{61}BM device [2], [3].

Yi et al. reported a change in recombination mechanisms in a small molecule:PC_{71}BM device under different thermal annealing conditions [1]. They found that as the thermal annealing temperature increased, the crystal size and phase separation in the film became larger, causing two opposing effects: an increase in monomolecular recombination and a reduction in bimolecular recombination. The competing effects first caused the J_{sc}, *FF,* and PCE to increase before decreasing at higher annealing temperatures.

5.1.2. OSC Parameters and Temperature

Temperature can produce non-reversible and reversible effects on device performance. The non-reversible effects, such as those described in the previous section, are largely related to changes in the microstructure. The reversible effects associated with temperature, on the other hand, are related to the physics of absorption and the charge transport within an OSC. In general, the impact of temperature on J_{SC}, *FF,* and PCE are difficult to predict because the processes that take place in OSCs, i.e. charge carrier generation, transport, recombination and ultimately collection at the electrodes, are dependent on the materials in the PAL, its thickness, its morphology and light intensity [5]–[9]. The charge transport mechanism in OSCs can be described as thermally-activated hopping, and thus

temperature tends to enhance transport. Assuming no changes in the microstructure, charges are more likely to be extracted from the device as a result of the better charge transport, leading to an enhanced J_{SC} and PCE. The *FF*, determined by the competition between recombination and extraction of free charges, can also improve with temperature if the change in recombination of free charges does not outweigh the change in the extraction of free charges.

The V_{oc}, likewise, has also been reported to be temperature dependent [4], [10]–[12]. Different models are used to describe the temperature dependent behavior of the V_{OC}, attributing the origin of such behavior to a shift in the quasi-fermi levels, a reduction in the dark current, or a reduction of charge carrier density in the OSC [8], [13]–[15].

The temperature dependency of the V_{OC} can be derived by recalling Equation 1.3 and defining J_0, the reverse saturation current, as [11], [16]:

Equation 5.1. $$J_0 = qN_vN_c\left[\exp\left(\frac{-E_g}{k_BT}\right)\right]\left(\frac{L_n}{n_n\tau_n}+\frac{L_p}{n_p\tau_p}\right)$$

where N_v is the effective density of states in the valence band, N_c is the effective density of states in the conduction band, $E_g$is the bandgap, L_p is the mean-free path of the holes, L_n is the mean-free path of the electrons, n_p is the hole density, n_n is the electron density, τ_p is the hole lifetime, and τ_n is the electron lifetime. Combining Equations 1.3 and 5.1, and assuming $J_{SC} >> J_0$, V_{OC} can be written as

Equation 5.2. $$V_{OC} = \frac{nE_g}{q} - \frac{nkT}{q}\ln\left[\frac{1}{J_{SC}}qN_vN_c\left(\frac{L_n}{n_n\tau_n}+\frac{L_p}{n_p\tau_p}\right)\right]$$

From Equation 5.2, it can be seen that the V_{OC} is reduced with increasing temperature.

5.1.3. Reported Literature

In one work, Chirvase et al measured the temperature-dependent JV characteristics of a P3HT:$PC_{61}BM$ device in a temperature range of 100 K to 380 K [2], which exhibited a maximum in J_{SC} and PCE at 300 K. The enhancement in J_{SC} with temperature up to 300 K arises from the thermally-activated mobility. At temperatures higher than 300 K, the morphology of this PAL changes, and the change in morphology compensates the

thermally-activated mobility, thus leading to a lower J_{SC} and PCE. In a similar work, Lee measured a P3HT:$PC_{61}BM$ device in the temperature range of 300 K and 420 K [16]. Lee et al observed that the OSC parameters in the device decreased with temperature a similar trend reported by Chirvase et al.

In another work, Ebenoch et al measured the OSC parameters for a PBT7:$PC_{71}BM$ device in the temperature range of 77 K to 325 K, reporting the highest PCE for the device between 260 K and 295 K [17]. The J_{SC} and *FF* steadily increased up until 260 K, after which point the increase began to flatten out. The V_{OC} was reduced with temperature, and at temperatures above 290 K, the increase in J_{SC} and *FF* no longer overcame the drop in V_{OC}, so the PCE began to drop. Simarly to Chirvaste et al, Ebenoch et al attributed the increase in J_{SC} and *FF* to increased charge carrier mobility.

In the aforementioned works in literature, the OSCs have been based on fullerene acceptors, which exhibit poor thermal stability [18], [19]. Non-fullerene systems, on the other hand, show improved thermal stability compared to fullerene acceptors. [20]–[22]. Recently, temperature-dependent studies have been carried out on non-fullerene systems [23]–[25]. Chan et al. investigated the temperature-dependent charge separation and recombination dynamics in two non-fullerene systems, observing temperature-dependent charge separation in PBDB-T-2F:Y6 [24]. Brus et al. measured the light intensity- and temperature-dependent J-V characteristics of four non-fullerene systems to analyze the contribution of bimolecular, bulk, and trap-assisted recombination mechanisms in OSCs under open-circuit conditions [25].

The focus of this chapter is to investigate a number of systems incorporating NFAs and report their temperature-dependent OSC parameters. The reversible enhancement in PCE with temperature observed in a number of systems demonstrates their thermal stability while also elucidating the influence of thermally-activated charge carrier mobility on OSC performance.

5.2. Experimental Methods and Materials

In this chapter, the ten different, unoptimized, OSC systems that were investigated are shown in Table 5.1. The workhorse system in this chapter, PBDB-T:ITIC, was chosen because of its reported excellent thermal stability [26]. PBDB-T and two of its higher-performing derivatives were combined with other state-of-the-art NFAs to investigate if a

general trend with temperature existed among systems with NFAs. A custom sample holder capable of heating and cooling the OSCs was designed and built by Mr. Martí Gíbert and Dr. Nadia Vega. In this chapter, OSCs with inverted, ITO/ZnO/PAL/MoO_3 (10 or 40 nm)/Ag, and conventional, ITO/PEDOT:PSS (Ossila HTL Solar 3)/PAL/Ca(10 nm)/Al geometries were fabricated. The PAL of each sample was deposited using a linearly decreasing blade coating speed, resulting in a thickness gradient as seen in Figure 5-1. The JV-characteristics of the devices were taken between 293 K and 353 K. This temperature range covers a plausible operating range for OSCs, and the higher end of the temperature range provides insight on OSCs dispatched in places with extreme heat, such as the Sahara desert or Middle East, or the use of advanced geometries that convert the unused IR radiation into heat. To probe the thermal stability of the OSC device (inverted architecture), each JV measurement consisted of 1.5 heat cycles, meaning the OSC was measured as it was heated up and cooled down (1 full temperature cycle), and then heated up again (half cycle). After the initial JV characterization, the EQE of one of the best performing pixels of the inverted device was measured as a function of temperature to investigate changes in absorption. To probe changes in morphology, two experiments were performed by Dr. Jaime Martín and Dr. Edgar Gutiérrez Fernández at ALBA synchrotron: GIWAXS and GISAXS. Then, the JV characteristics of the inverted devices were taken as a function of intensity and temperature to probe recombination mechanisms. Finally, SCLC experiments were performed to probe the evolution of the hole and electron mobilities of the systems. For the hole-only devices, the device geometry was the following: ITO/PEDOT:PSS (Ossila HTL Solar 3)/PAL/MoO_3(40 nm)/Ag. For the electron-only devices, the device geometry used was the following: ITO/ZnO/PAL/Ca (10 nm)/Ag.

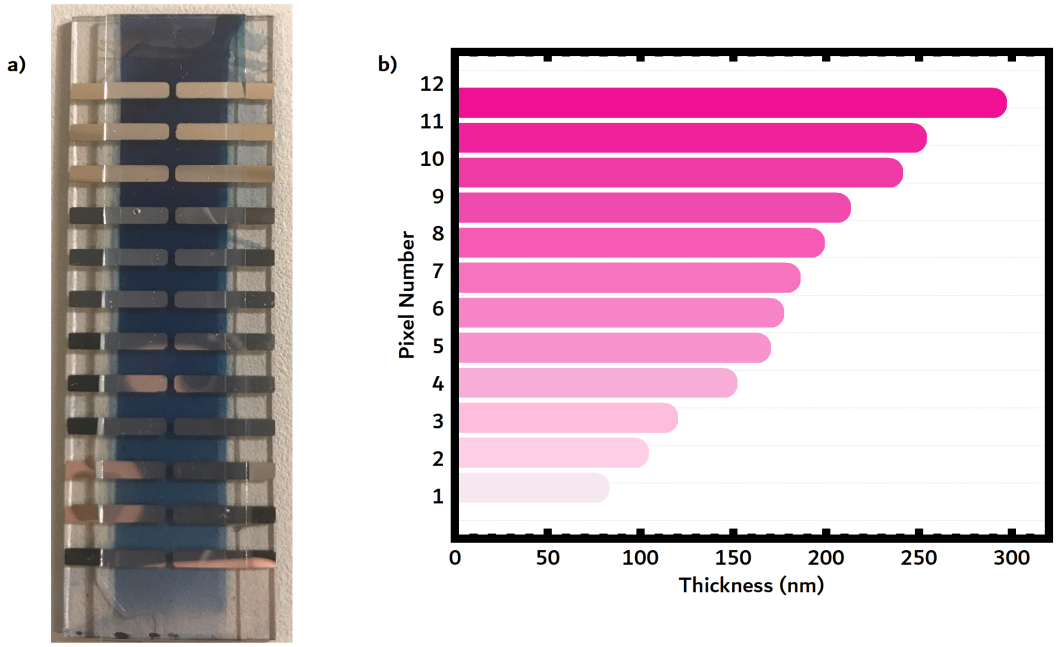

Figure 5-1. a) Image of a solar cell with thickness gradient. b) Plot of thickness versus pixel number

The work in this chapter was carried out in collaboration with Dr. Jenny Nelson's group at Imperial College London. Dr. Mohammed Azzouizi performed drift-diffusion simulations to investigate the effect of temperature, pixel thickness and light intensity on device performance. Dr. Jun Yan helped fit the SCLC curves to extract the charge carrier mobilities.

Table 5.1. OSC Systems investigated in this chapter

System	Solvent	Donor:Acceptor Ratio	Blade-coater speed (mm/s)
PBDB-T:O-IDFBR	o-Xylene	1:1	80-5
PBDB-T:ITIC	o-Xylene	1:1	80-5
PBDB-T:ITIC-4F	o-Xylene	1:1	80-5
PBDB-T:EH-IDTBR	o-Xylene	1:1	80-5
P3HT:$PC_{61}BM$	o-Xylene	1:1	80-5
PBDB-T-2-F:ITIC-4F	o-Xylene	1:1	80-5
P3HT:O-IDTBR	o-Xylene	1:1	80-5
PBDB-T:$PC_{71}BM$	o-Xylene	1:1	80-5
PBDB-T-2-Cl:ITIC-4F	o-Xylene	1:1	80-5
PBDB-T-2-Cl:Y6	o-Xylene	1:1	80-5

5.3. Results

Each device was fabricated with an inverted geometry and consisted of 24 pixels. For each device, the JV characteristics were measured as a function of at least 11 temperatures and 9 intensities, producing a considerable amount of data. A full temperature cycle for one device produced 4,752 individual JV curves. The quantity of data makes it unfeasible to discuss every system investigated, so in this thesis, PBDB-T:ITIC was chosen to be the representative system. As previously mentioned, PBDB-T:ITIC exhibits excellent thermal stability, thus making this system a suitable candidate to investigate reversible temperature-dependent effects. In the last section of this chapter, PBDB-T:ITIC will be compared with other systems to draw general conclusions.

5.3.1. The Effect of Temperature on the OSC Parameters

Figure 5-2 shows the four main solar cell parameters, namely PCE, V_{OC}, *FF,* and J_{SC}, measured as a function of temperature for a complete heating cycle. The four plots on the top (Figures a-d) correspond to the results when the device was heated from 298 K to 348 K, while the four plots on the bottom (Figures e-h) correspond to the results when the device was cooled from 348 K to 298 K. Upon heating the device, the PCE significantly improved

in almost every case. The apparent outlier in the data set is likely due to an extrinsic device factor, such as poor electrical contact with the sample holder. The thickest pixel, with a thickness of 290 nm, showed an 88% improvement in PCE, compared to the second thinnest pixel 97 nm, which showed an 8.8% improvement. At lower temperatures, the change in PCE is much quicker, than that at higher temperatures. For the thinner pixels, it appears that the enhancement in PCE begins to saturate above 333 K. The V_{OC} monolithically decreased with temperature in every case by approximately 0.04 V, a trend that agrees well with reported literature and explained by equation 5.2 [12], [17]. The origin of the reduction of the V_{OC} could be a shift in the quasi-Fermi levels [17].

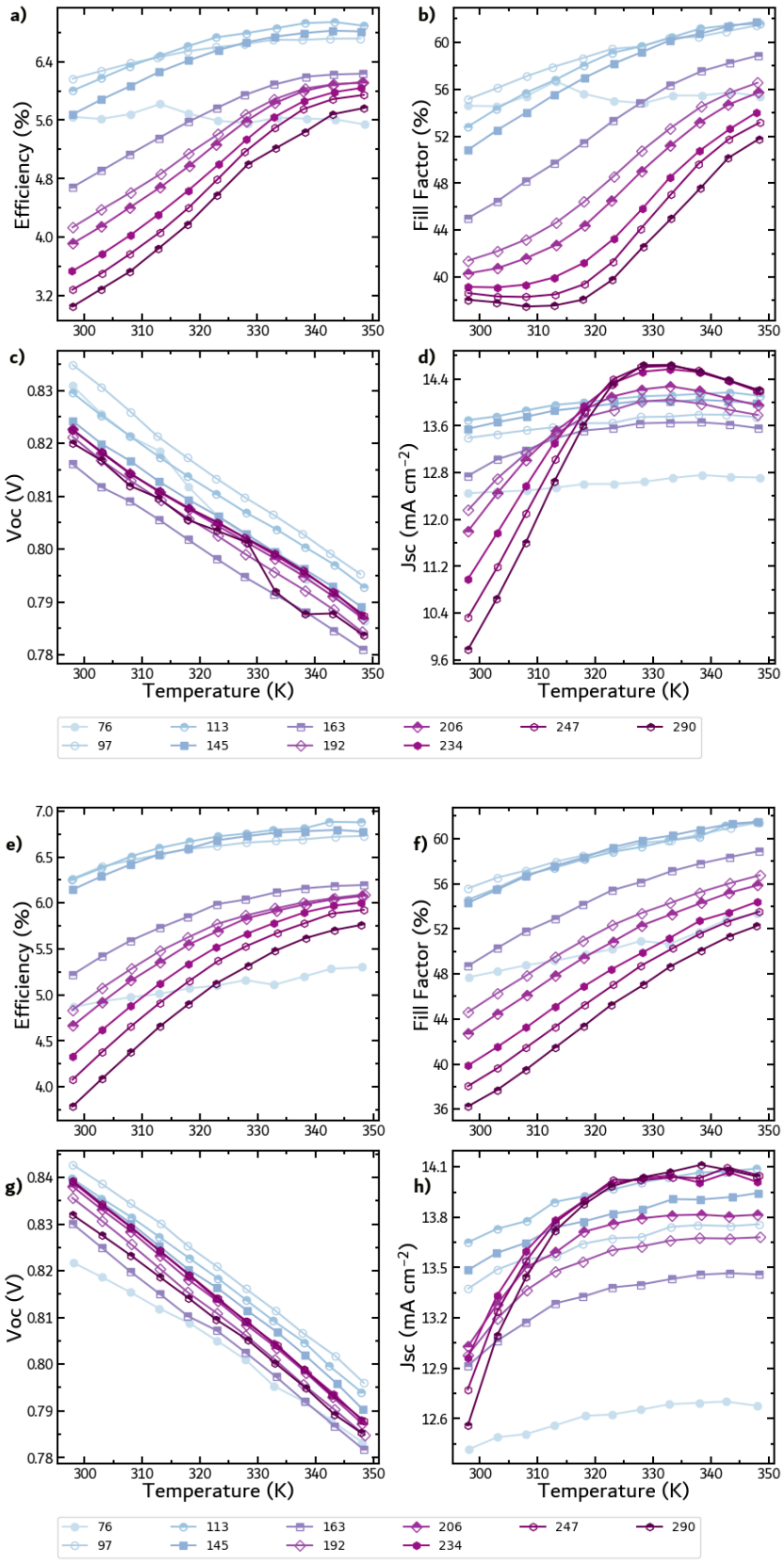

Figure 5-2. The OSC parameters as a function of temperature during the first heating cycle. Plots a-d correspond to the measurement when the device was heated from 298 K to 348 K: a) PCE, b) V_{OC}, c) *FF*, and d) J_{SC} against temperature. Figures e-h correspond to the measurement when the device was cooled down from 343 K to 298 K: e) PCE, f) V_{OC}, g) *FF*, and h) J_{SC}. Each line corresponds to a different pixel in nm.

The J_{SC} increased with temperature up to 328 K, before reducing or flattening out at higher temperatures, as seen in Figure 5.1d. For thinner pixels, the enhancement in J_{SC} is again much smaller than that observed in the thicker pixels, especially at lower temperatures. The J_{SC} is proportional to the number of charges generated, i.e. absorption coefficient, and their mobility. Since, in the absence of morphological changes, the absorption coefficient of the system does not improve with temperature, the apparent enhancement in J_{SC} must be related to the mobility of the charge carriers, which also improves with temperature.

The *FF* and J_{SC} displayed a slightly different trend than that of the PCE. For thinner pixels, the *FF* increased in a similar fashion to the PCE with temperature. For pixels with thicknesses greater than 234 nm, the *FF* appears to dip before increasing. Essentially, the *FF* is determined by the competition between recombination and charge extraction rates in an OSC, which are influenced by charge transport, the internal cell voltage, and charge generation [5]. The slight dip in *FF* could likely be explained by competing changes in the recombination and charge extraction rates. Temperature likely improves charge extraction at the electrodes because it enhances charge mobility. In organic semiconductors, the charge transport mechanism can be described as a thermally-activated hopping mechanism in highly-disordered systems, where temperature provides charge carriers sufficient energy to overcome barriers as a result of energetic disorder [27]. As the charge transport in the device improves, the dominant type of recombination could be shifting from monomolecular to bimolecular, similarly to what has been reported in literature [1]. In this case, the enhancement in charge transport outweighs any change in recombination mechanism.

From the data on the device when cooled, a reversible behavior is observed. The PCE at 298 K after the complete heating cycle either retained the same value before the heating cycle or slightly improved, especially for the thicker pixels. For example, the measured PCE of the thickest pixel 290 nm before the heating cycle and after the heating cycle were found to be 3.05%, and 3.79%, respectively. Likewise, there appears to be a slight enhancement of approximately 0.005 – 0.01 V in the V_{OC} in all cases after the heating cycle. Interestingly, the *FF* in the thicker films no longer shows the same behavior as it did upon heating. Rather, it decreased steadily upon cooling. The *FF* of some of the intermediate thickness exhibited a slight improvement after the heating cycle. Furthermore, an enhancement in the J_{SC} can be seen in the pixels with thickness greater than 192 nm. For the thinner pixels, the J_{SC} showed little to no enhancement.

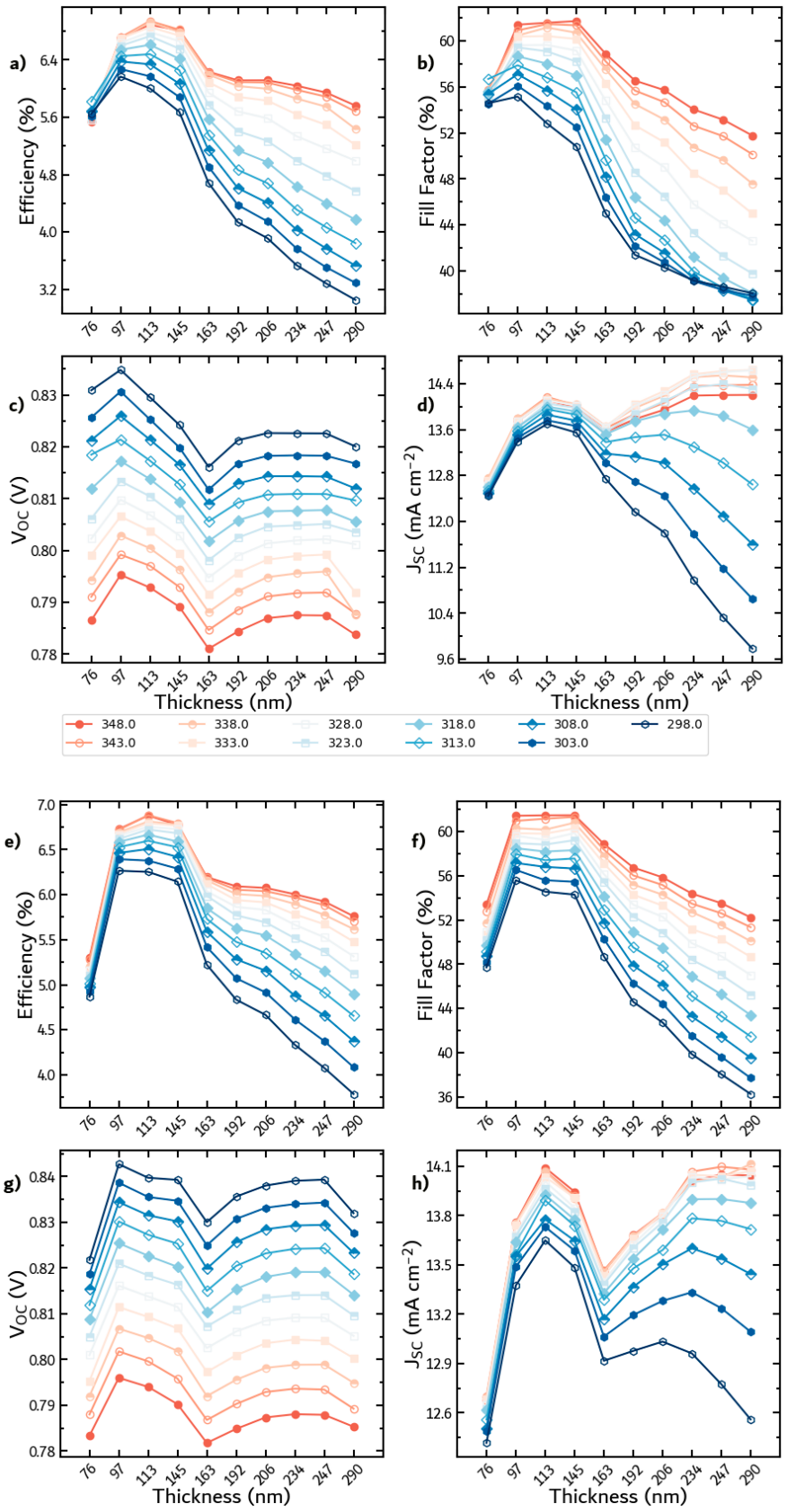

Figure 5-3. The OSC parameters as a function of pixel thickness during the first heating cycle. Plots a-d correspond to the measurement when the device was heated from 298 K to 348 K: a) PCE, b) V_{OC}, c) *FF*, and d) J_{SC} against temperature. Figures e-h correspond to the measurement when the device was cooled down from 343 K to 298 K: e) PCE, f) V_{OC}, g) *FF*, and h) J_{SC}. Each line corresponds to a different temperature in K.

The same data from Figure 5-2 is plotted in Figure 5-3 against film thickness. The enhancements in PCE (Figures 5-3a and e), *FF* (Figures 5-3c and g), and J_{SC} (Figures 5-3d and h) as a result of temperature are more pronounced in thicker pixels. Figure 5-4 plots the slope of PCE against temperature, highlighting the more pronounced effect in thicker pixels. At higher temperatures, the J_{SC} displays a thickness-dependent behavior that is consistent with interference effects. An OSC is composed of several layers with different indices of refraction, leading to significant reflection at each interface. Thus, light absorption in an OSC depends on the thickness of the PAL and optical interference ([28]–[32]). There appears to be relative maxima in J_{SC} when the pixel thickness is around 113 nm and greater than 234 nm, and relative minima in J_{SC} when pixel thickness is thinner than 97 nm or when pixel thickness is around 167 nm. Briefly, this thickness dependent behavior arises from the spatial distribution of the optical field in the OSC. Light is reflected at the interface between the bottom transport layer and back electrode. As PAL thickness is increased, the number of absorbed photons within the PAL increases. At lower temperatures, the thickness dependence of the J_{SC} is observed to a lesser extent, but the J_{SC} is likely limited due to the poor charge extraction originating from poor charge carrier mobilities [33].

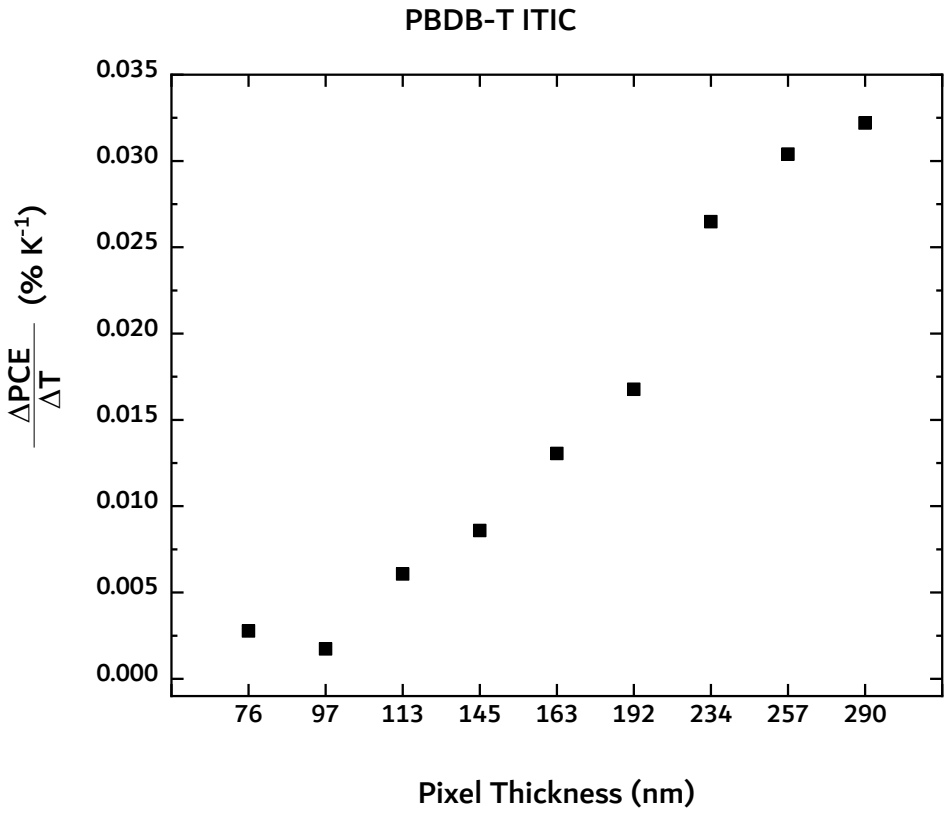

Figure 5-4. Change in PCE with Temperature as a function of pixel thickness.

From a technological perspective, temperature may be a strategy employed to make OSCs more thickness-independent. In the context of high-throughput manufacturing of large area OSCs, thicker films are more desirable. The state-of-the-art OSCs are made on a much smaller scale, involving non-scalable techniques such as spin-coating where thin films can be accurately obtained with relative ease. Thin films, however, cause many problems when high-throughput techniques, such as roll-to-roll, are used. Firstly, the flexible substrates used, such as PET, are rough, leading to spot defects such as pinholes in thinner devices [31]. Secondly, completely uniform films are difficult to attain using scalable techniques, and slight variations in thickness lead to significant differences in performance [34]. So, high-performing, thick OSCs displaying thickness-independent performance are critical to achieving OSC commercialization.

For hybrid PV-TE devices, these results provide insight on how an OSC will operate in a working device and motivate the use of a contact geometry. The thickness of the PAL will not only influence the performance of the OSC, but also the OSC device temperature. Additionally, the thickness of the PAL will influence the amount of light transmitted to the coupled SOTEG, and its performance. Thus, prudent hybrid device design should consider the thickness of the PAL in the OSC.

5.3.2. The Effect of Temperature on Morphology

The EQE of the PBDB-T:ITIC OSC as a function of temperature is shown in Figure 5-5. The shape of the EQEs with temperature are extremely similar, although a slight narrowing of the shoulder around 700 nm can be observed. Absorption changes with temperature, and typically results in a blueshifting of the absorption spectrum and a broadening of the absorption peaks [35]. The lack of significant differences in the EQE data with temperature likely indicate there is no change in morphology because the absorption doesn't change. The EQEs are slightly enhanced with temperature, agreeing well with the enhancement in J_{SC} seen in JV characterization. From the EQE spectra, the J_{SC} was calculated and is shown in Table 5.2.

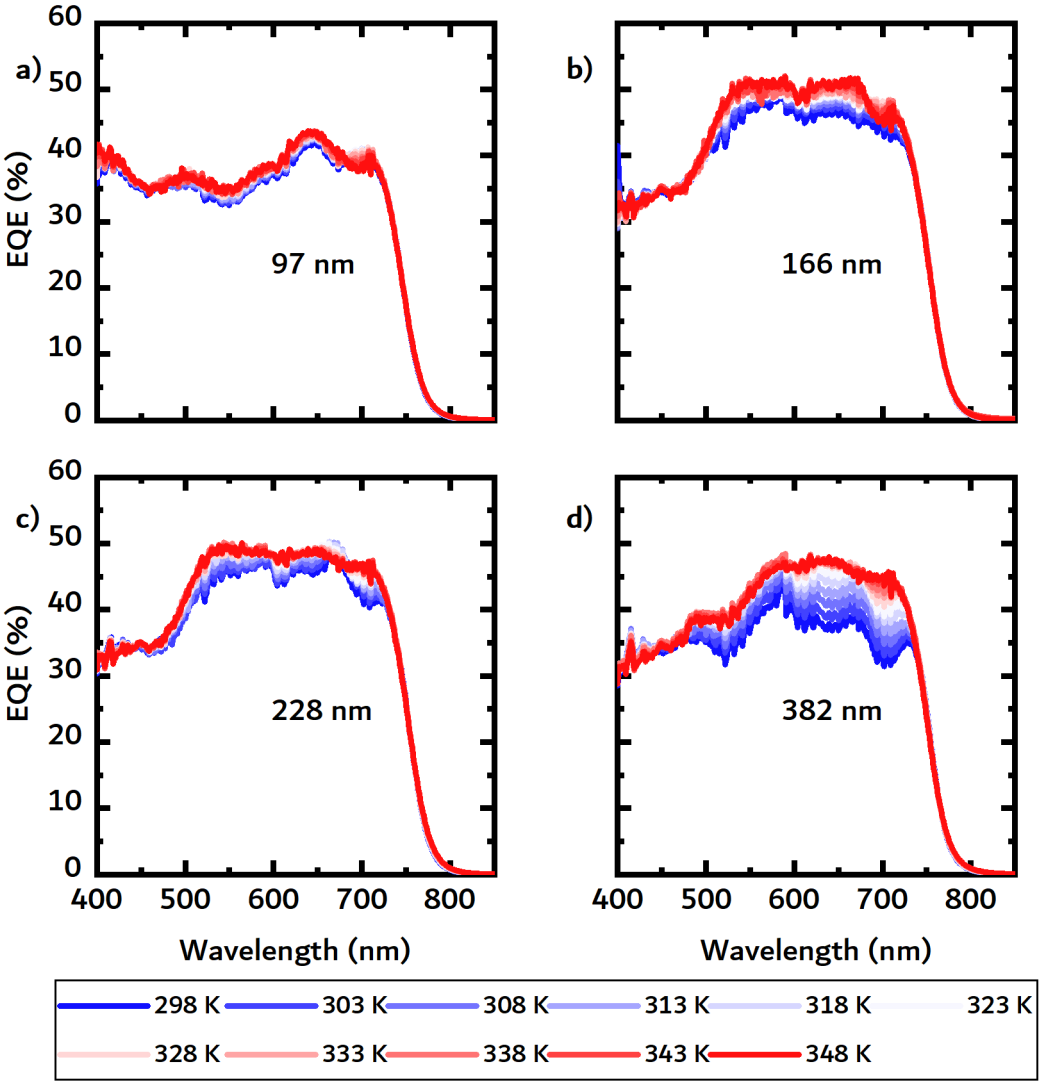

Figure 5-5. EQE measured as a function of temperature for pixels with a thickness of a) 97 nm, b) 166 nm, c) 228 nm, and d) 382 nm.

Table 5.2. Calculated J_{SC} from EQE spectra

	97 nm	166 nm	228 nm	382 nm
Temperature (K)	**J_{SC} (mA cm^{-2})**	**J_{SC} (mA cm^{-2})**	**J_{SC} (mA cm^{-2})**	**J_{SC} (mA cm^{-2})**
298	8.37	9.90	9.74	8.40
303	8.44	10.00	9.79	8.67
308	8.46	10.11	9.92	8.94
313	8.50	10.16	10.05	9.17
318	8.55	10.22	10.10	9.32
323	8.60	10.19	10.17	9.45
328	8.58	10.30	10.18	9.58
333	8.60	10.32	10.21	9.62
338	8.60	10.32	10.22	9.67
343	8.61	10.48	10.19	9.64
348	8.60	10.38	10.18	9.59

Thin films of PBDB-T:ITIC were deposited onto silicon substrates for GIWAXS and GISAXS. The GIWAXS patterns of an unannealed PBDB-T:ITIC sample and a PBDB-T:ITIC annealed at 348 K are shown in Figure 5-6 a and b, respectively. From the patterns, no significant difference is observed, so the structure of the PAL does not significantly change with temperatures up to 348 K. From the GISAXS intensity profiles shown in Figure 5-7, the annealed PBDB-T:ITIC sample showed a slightly higher scattering intensity, which indicated that annealing may provoke a slight separation of phases in the sample. In conclusion, the results from the section indicate that the morphology of the PBDB-T:ITIC PAL changes very little with temperature, so a change in morphology does not explain the enhancement in the OSC parameters with temperature.

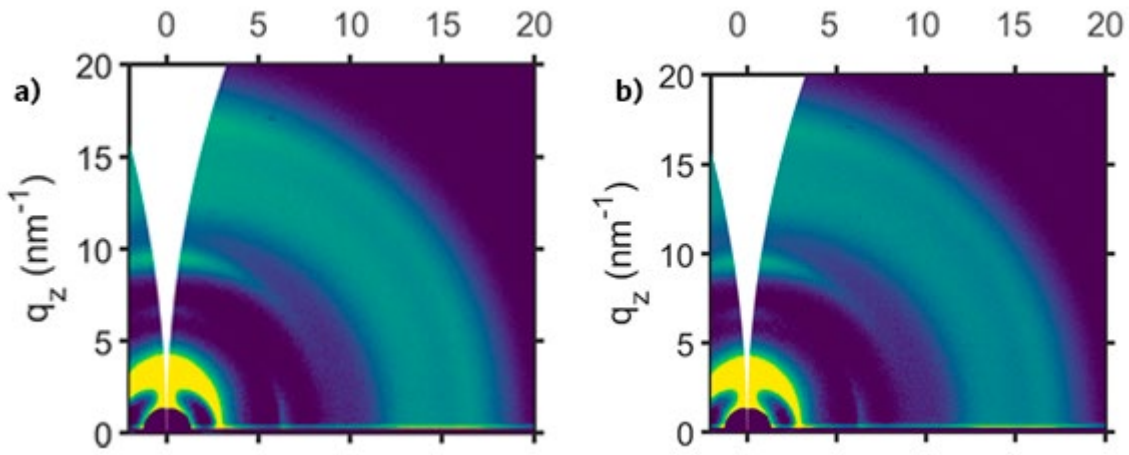

Figure 5-6. 2D GIWAXS patterns for PBDB-T:ITIC on a) an unannealed sample and b) a sample annealed at 348 K.

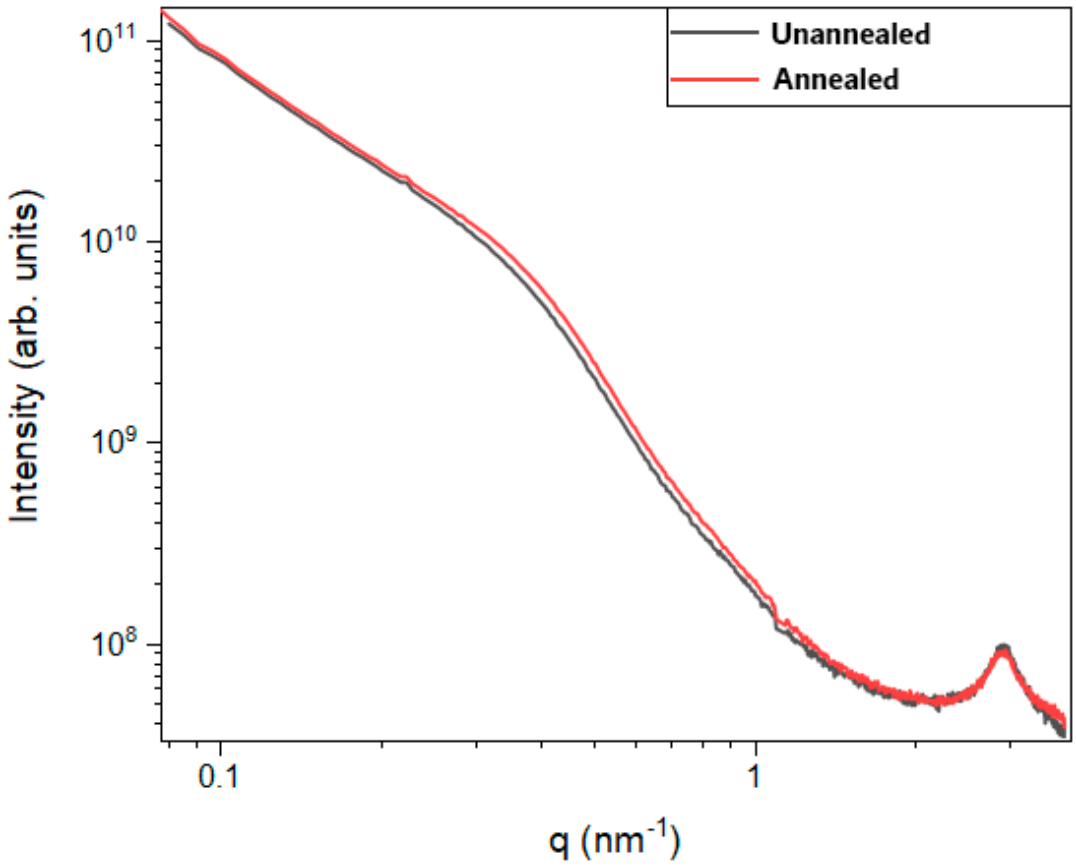

Figure 5-7. GISAXS profiles of the PBDB-T:ITIC sample before annealing (black line) and after annealing at 348 K (red line)

5.3.3. Drift Diffusion simulations

To investigate the influence of temperature on the OSC parameters, Dr. Mohammed Azzouzi at Imperial College London performed Drift Diffusion simulations on the PBDB-T:ITIC system. Briefly, a PIN structure was used to represent the device, where the p-layer was the HTL and the n-layer was the ETL. Series and shunt resistances were not considered, and the contacts are considered to be ideal (ohmic). The recombination mechanism considered in the simulation is of the second order. In other words, a charge transfer state from free charge carriers forms and then the charge transfer state recombines. The mobility of the free charge carriers was considered to be the same for both holes and electrons.

In the simulation, the charge carrier mobility, μ, and the recombination rate via the formation rate of free charge carriers to charge transfer states, k_{for}, are varied. Both are modeled to have a temperature dependence with an activation energy. The temperature-dependent charge carrier mobility is given by:

Equation 5.3. $$\mu(T) = \mu_{300\,K} \frac{\exp\left(-\frac{E_{a,\mu}}{k_B T}\right)}{\exp\left(-\frac{E_{a,\mu}}{k_B 300}\right)}$$

where $\mu_{300\,K}$ was set to 2x10^{-4} cm^2 V^{-1} s^{-1}, $E_{a,\mu}$ is the activation energy for charge carrier mobility, T is the device temperature, and k_B is the Boltzmann's constant. The temperature-dependent formation of charge transfer states from free charge carriers rate (recombination rate) is given by:

Equation 5.4. $$k_{for}(T) = k_{for,300\,K} \frac{\exp\left(-\frac{E_{a,k}}{k_B T}\right)}{\exp\left(-\frac{E_{a,k}}{k_B 300}\right)}$$

where $k_{for,300\,K}$ was set to 10^{-11} cm^3 s^{-1} and $E_{a,k}$ is the activation energy for the recombination rate.

The simulation shows four cases. In the first case, shown in Figure 5-8, mobility and recombination rate are temperature independent, i.e. $E_{a,\mu}$ and $E_{a,k}$ are set to 0. The V_{OC} reduces with temperature and thickness, similar to what was observed in the

experimental results. The J_{SC} appears to slightly decrease with temperature, while the *FF* appears to show a maximum with temperature between 300 K and 310 K, although the overall change is relatively small.

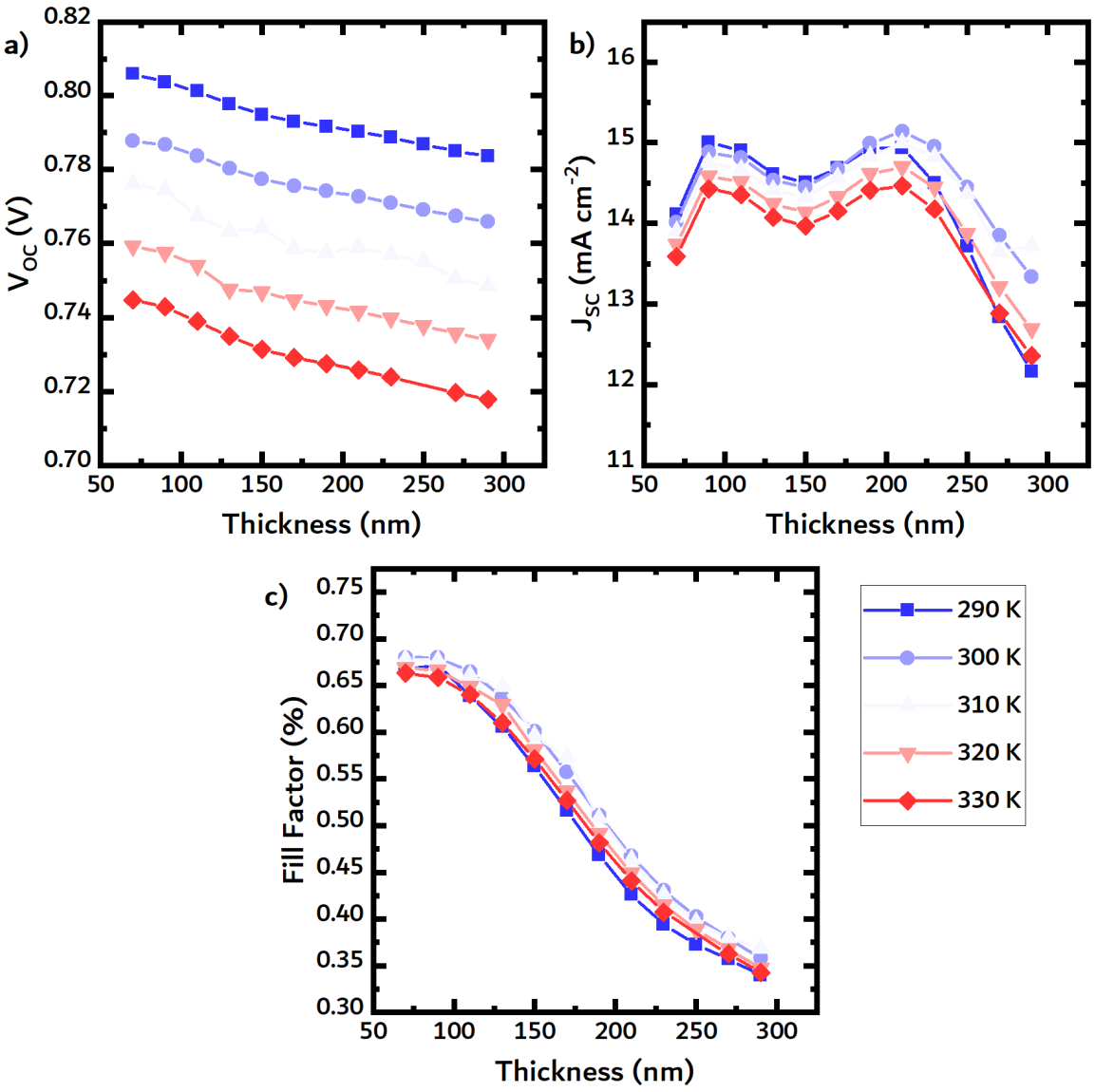

Figure 5-8. Results from the drift diffusion simulations. In this case, charge carrier mobility and recombination rate are simulated to be temperature independent. a) V_{OC}, b) J_{SC}, and c) *FF* plotted against temperature for various temperatures.

In the second case, shown in Figure 5-9, the recombination rate becomes increasingly more important with temperature ($E_{a,k}$ set to 0.4), while the charge carrier mobility does not change ($E_{a,\mu}$ set to 0). The V_{OC} reduces with temperature, similar to what was observed in the experimental results and in the first case. The J_{SC} and *FF* appear to decrease much more significantly with temperature compared to the first case.

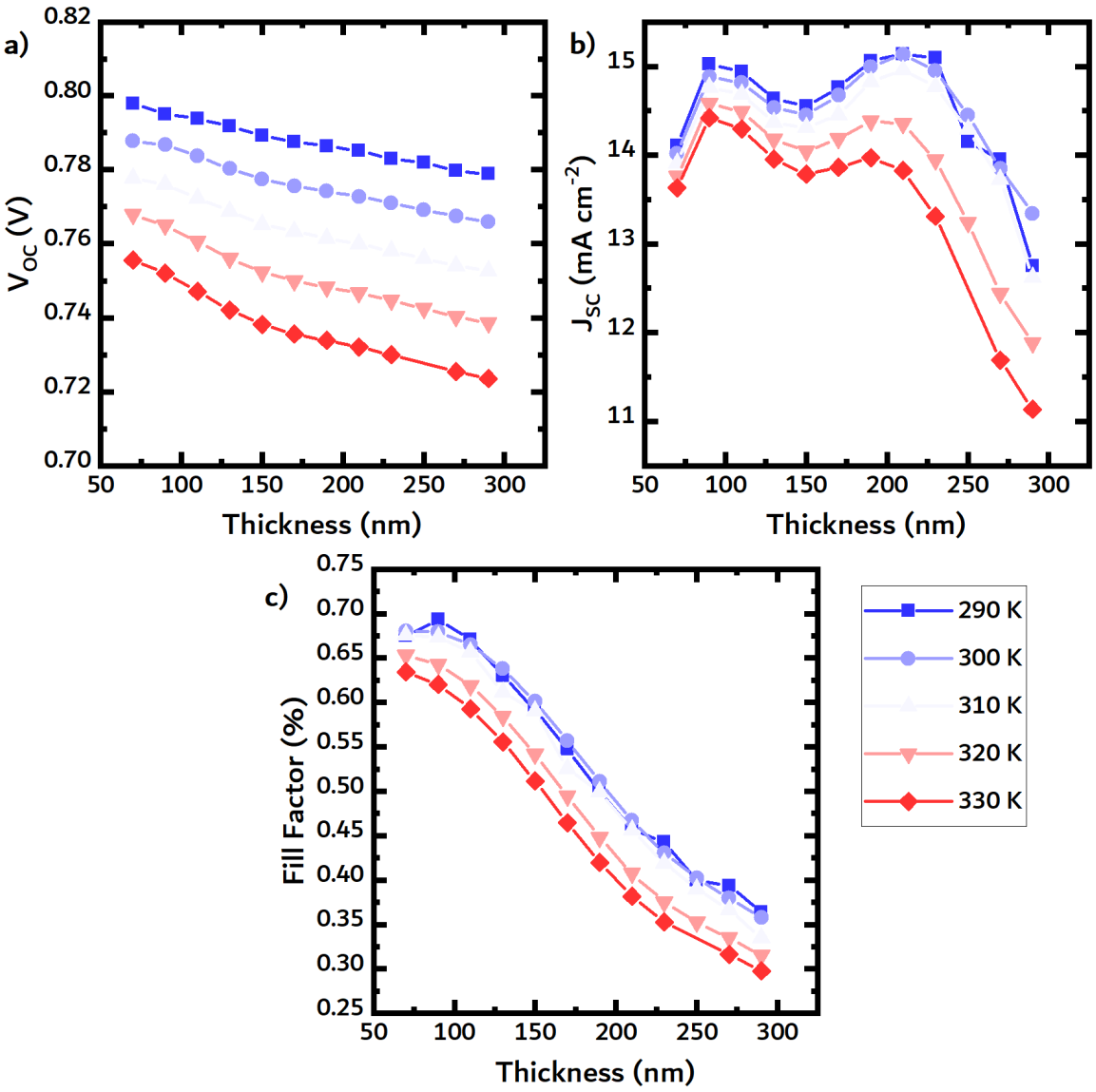

Figure 5-9. Results from the drift diffusion simulations. In this case, charge carrier mobility is temperature independent, while the recombination rate increases with temperature. a) V_{OC}, b) J_{SC}, and c) *FF* plotted against temperature for various temperatures.

In the third case, shown in Figure 5-10, the charge carrier mobility increases one order of magnitude (from 2x10^{-4} cm^2 V^{-1} s^{-1} to 2x10^{-3} cm^2 V^{-1} s^{-1}) across the temperature range of 300 K to 350 K ($E_{a,u}$ set to 0.4), while the recombination rate does not change ($E_{a,k}$ set to 0). The V_{OC} reduces with temperature, similar to what was observed in the experimental results and in the first two cases. The J_{SC} and *FF* increase with temperature, with a significant enhancement observed in the thicker pixels. The simulation results look very similar to the experimental results observed for the PBDB-T:ITIC device (see Figure 5-3).

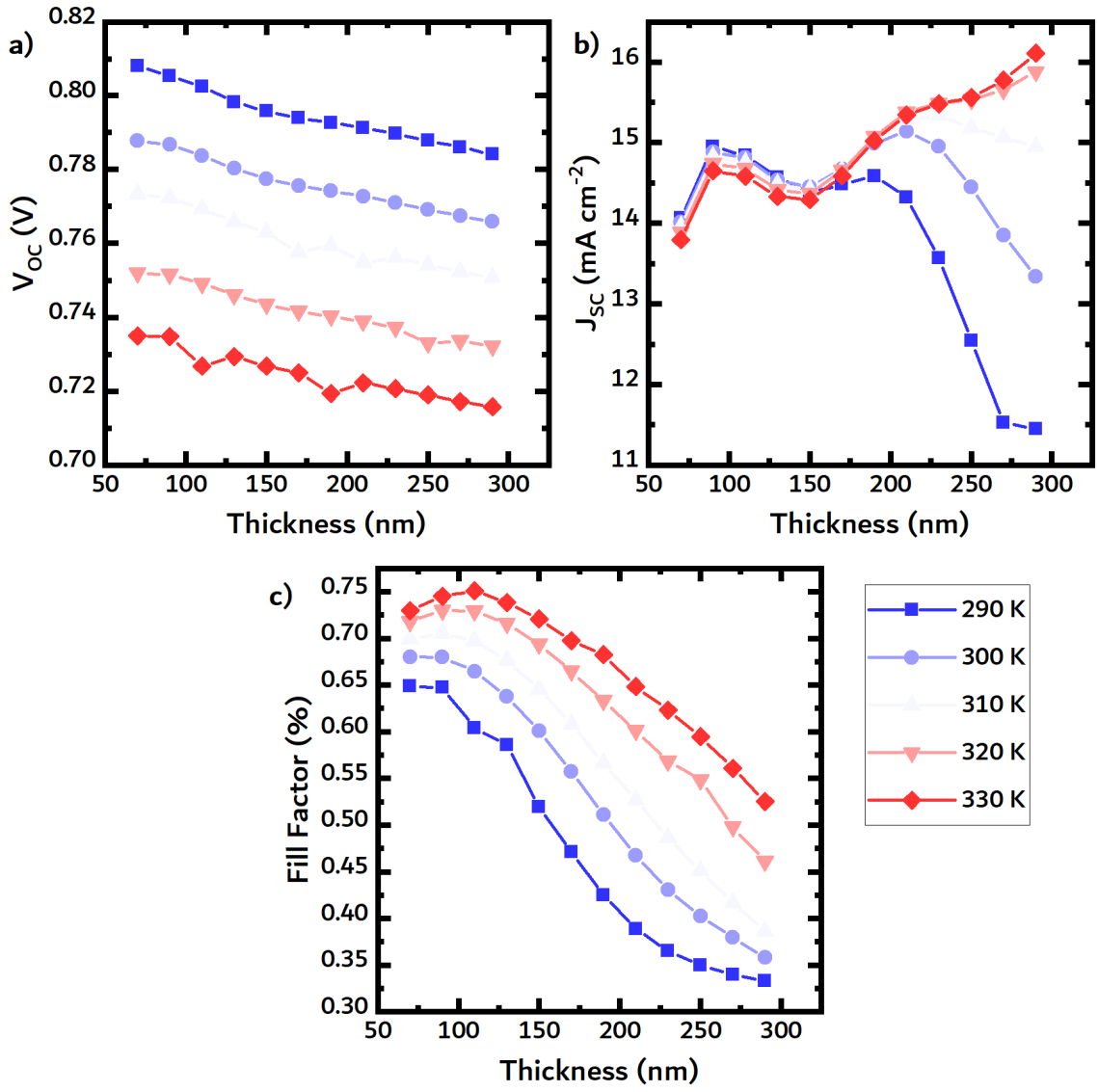

Figure 5-10. Results from the drift-diffusion simulations. In this case, charge carrier mobility increases with temperature, while the recombination rate is simulated to be temperature independent. a) V_{OC}, b) J_{SC}, and c) *FF* plotted against temperature for various temperatures.

In the last case, the charge carrier mobility increases one order of magnitude (2x10^{-4} cm^2 V^{-1} s^{-1} to 2x10^{-3} cm^2 V^{-1} s^{-1}) across the temperature range of 300 K to 350 K ($E_{a,u}$ set to 0.4), while the recombination rate also increases ($E_{a,k}$ set to 0.4). This case, shown in Figure 5-11, provides insight on two competing process, i.e. charge extraction rate and charge recombination rate, that influence both the J_{SC} and *FF*. The V_{OC} reduces with temperature, similar to what was observed in the experimental results and in the first three cases. Similar to what was observed in the third case, the J_{SC} and *FF* increase with temperature, with a significant enhancement observed in the thicker pixels. The enhancement in *FF* is slightly larger in this case compared to the third case, but this is expected since the *FF* is reduced as recombination losses become more important in devices.

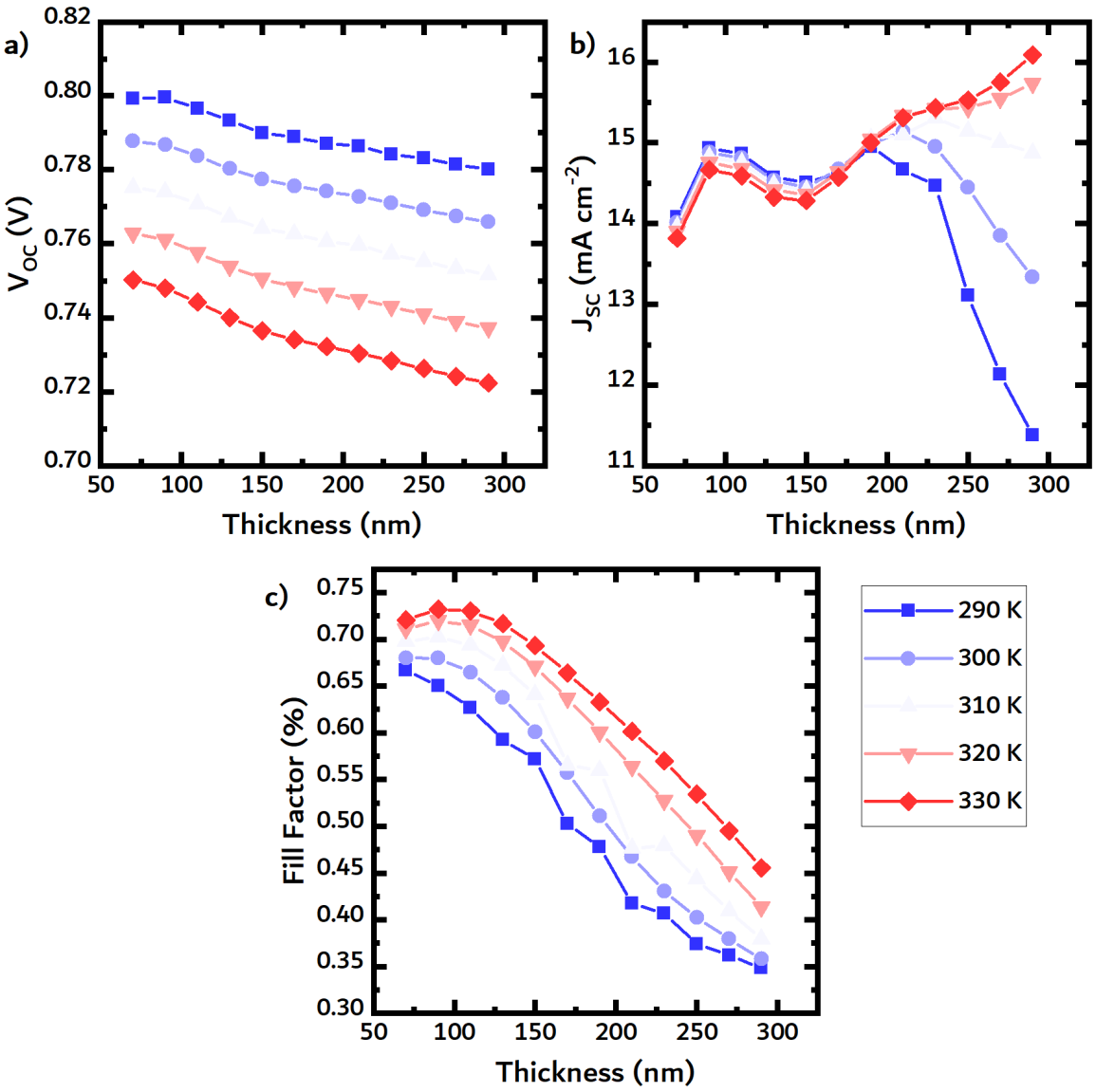

Figure 5-11. Results from the drift diffusion simulations. In this case, both charge carrier mobility and recombination rate increase with temperature. a) V_{OC}, b) J_{SC}, and c) *FF* plotted against temperature for various temperatures.

The results from the third and fourth cases agree remarkably well qualitatively with the experimental results shown in earlier sections of this chapter. The V_{OC} is reduced with temperature, and both J_{SC} and *FF* are enhanced with temperature, especially in the thicker pixels. The measured values for V_{OC} were slightly higher than the simulated values V_{OC} and reduced at a faster rate in comparison to the simulated values for V_{OC}. The measured values for J_{SC} were close with those obtained from the simulation, however, the measured values for J_{SC} increased with temperature for every thickness. In the simulation, the simulated values for J_{SC} decreased slightly with temperature in thinner pixels, while the J_{SC} increased significantly with temperature in thicker pixels.

The measured values for *FF* in thicker pixels agreed well those obtained from the simulation and enhanced with temperature at a similar rate as the simulated values. The measured values for *FF* for thinner pixels were smaller than those obtained from the simulation and did not enhance with temperature as the simulated values. Quantitatively, the simulated values for V_{OC} and *FF* obtained in the third case agreed the best with the experimental values. However, the simulated values for J_{SC} agreed better with those obtained in the fourth case. In conclusion, the simulation results show that the enhancement in charge carrier mobility with temperature can explain the improvement in device performance with temperature. Furthermore, the change in mobility outweighs any increase in recombination rate with temperature, as highlighted by the fourth case.

5.3.4. Mobility Results

Because of the reversible nature of the enhancement in the OSC parameters and the lack of changes in PAL morphology, the likely origin of temperature-dependent OSC behavior is temperature-dependent charge mobility. As previously mentioned, thermally-activated hopping is the dominant transport mechanism in highly disordered systems, such as bulk heterojunction PALs.

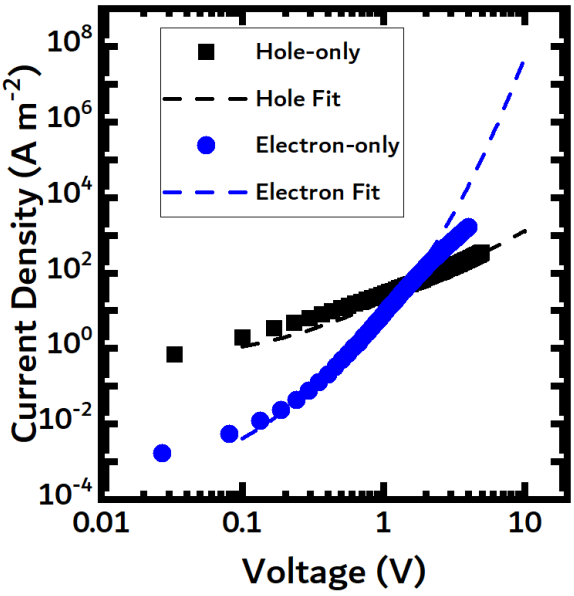

Figure 5-12. J-V curves of the hole-only (blue dots) and electron-only (black squares) device with a thickness of approximately 160 nm. The black and blue dashed lines are the fitted J-V curves extracted using the open source SCLC program by Felekidis et al [36].

In this thesis, SCLC was used to measure the mobility of the charge carriers. For a detailed explanation of SCLC and the models used to extract mobility parameters, the reader is referred to work done by Felekidis et al. [36] and Kim et al. [37]. Briefly, to perform the SCLC experiments, traps, series resistance and current leakage must be identified in the device and must have a negligible influence [37]. In order to correctly extract the mobilities, the models should be fitted to the voltage region where the trap states are completely filled by injected charge carriers, leading to a trap-free SCLC current [36]. For these experiments, a lower temperature range was chosen (278 to 313 K) because the voltage region where all the traps were filed was not easily identified at higher temperatures. Examples of the fitted J-V curves are shown in Figure 5-12.

In Figure 5-13, the measured electron and hole mobilities are shown. It can clearly be seen that with increasing temperature, the mobility of both the holes and the electrons increased, which could explain the enhancement in the OSC parameters with temperature. The results from the SCLC experiment support the simulation results, showing that charge carrier mobility for both the holes and the electrons increases with temperature. Recalling the simulation results in the previous section, an enhancement in charge mobility due to temperature was shown to greatly enhance the J_{SC}, especially in thicker pixels. The PCE and *FF* were also significantly enhanced by the improved charge carrier mobility.

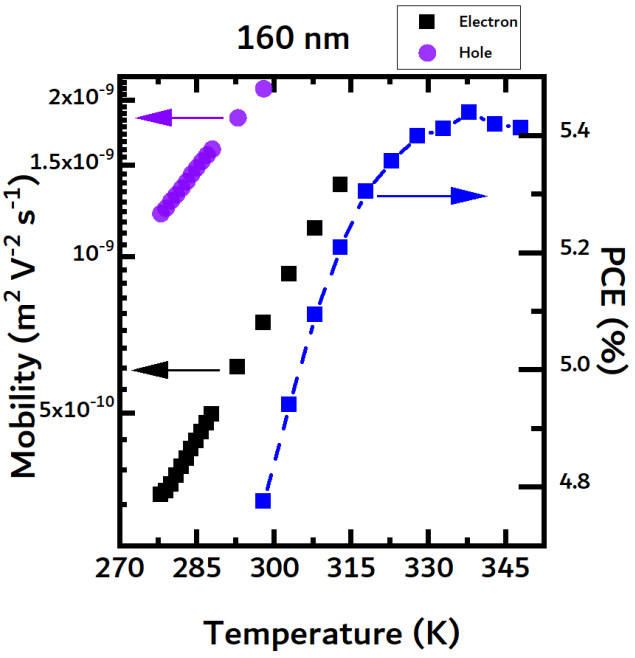

Figure 5-13. SCLC electron (purple circles) and hole (black squares) mobilities vs temperature (left axis) and PCE (blue squares) (right axis). Note that the range is different because at higher T we could not identify a voltage range for which the JV curves satisfied the SCLC equations

5.3.5. Light Intensity Studies

The drift-diffusion simulations showed that the temperature dependence in OSC performance arises from a trade-off between improved transport (as demonstrated in the previous section) and recombination. In this section, the OSC parameters were investigated as a function of light intensity to gain insight on the recombination mechanisms in the PBDB-T:ITIC device. In addition to temperature, both the J_{SC} and the V_{OC} are dependent on light intensity [38], [39]. Hartnagel et al. showed that J_{SC} is dependent on intensity according to the following equation [40]:

Equation 5.5. $$J_{SC} = qd\bar{G}$$

where d is the thickness of the PAL and $\bar{G}$ is the averaged generation rate over the thickness of the PAL. The generation rate is linearly correlated to light intensity, and thus to illumination intensity [40]. Since J_{SC} is dependent on intensity, V_{OC} is also dependent on light intensity, as shown in Equation 5.2. Recombination of free charge carriers reduces J_{SC}, and bimolecular recombination depends on light intensity.

The OSC parameters measured at 298 K are shown as a function of intensity in Figure 5-14. Interestingly, the pixels thicker than 113 nm showed a maximum in PCE when irradiance was less than 1 sun. The shape of the V_{OC} against intensity curve was found to be thickness dependent, and at low light intensities (0.1 sun), the V_{OC} drastically dropped. The behavior observed in the V_{OC} could likely be attributed to high leakage current, which is especially detrimental to solar cell performance at lower light intensities [41], [42]. Similar to the PCE, the *FF* displayed a maximum at light intensities less than 1 sun. The J_{SC} showed a linear dependence on intensity, agreeing well with the behavior reported in literature [17], [39].

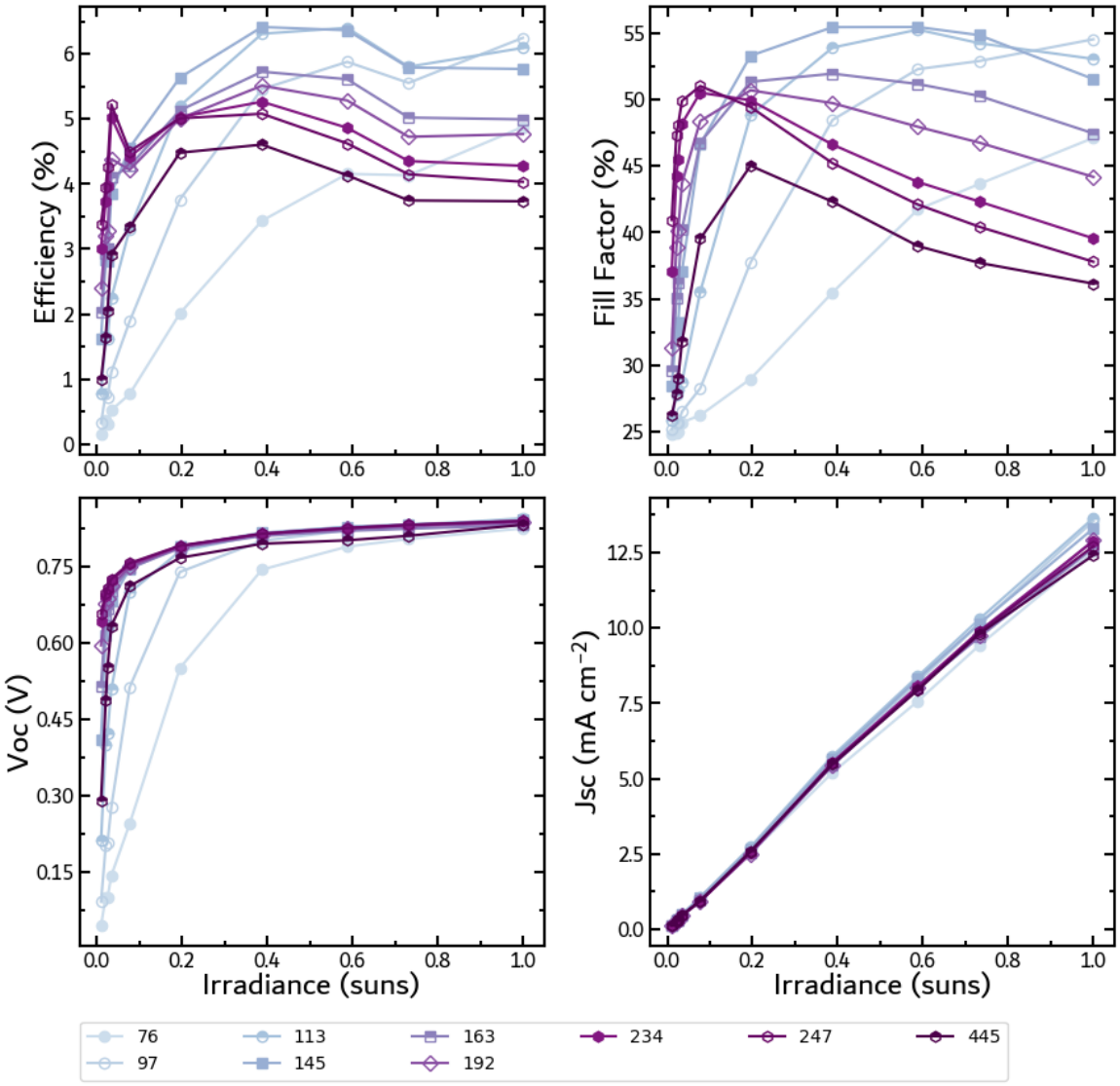

Figure 5-14. The OSC parameters as a function of light intensity at 298 K.
a) PCE, b) V_{OC}, c) *FF*, and d) J_{SC} against intensity. Each line corresponds to a different pixel in nm.

Because of the high leakage current in the device, especially in the thinner pixels, a new device with a slightly thicker HTL, MoO_3 (40 nm) in this case, was prepared. Although the PCEs of these devices were lower than the devices with a MoO_3 layer of 10 nm, the current leakage was significantly reduced, thus allowing for a more reliable analysis of the data from the light intensity experiments. Figure 5-15 shows the data from the devices with the thicker MoO_3 layer.

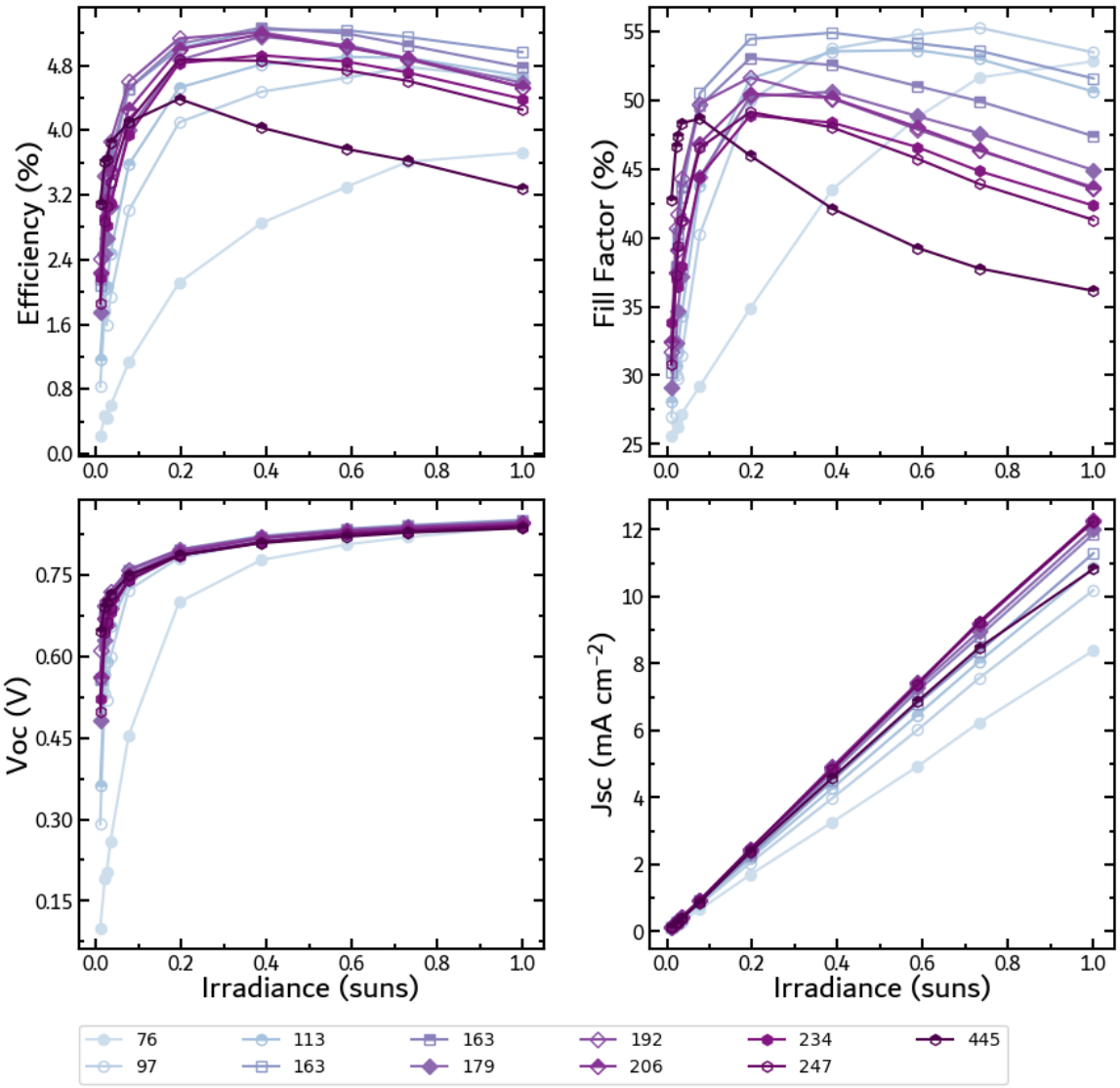

Figure 5-15. The OSC parameters as a function of light intensity at 298 K. a) PCE, b) V_{OC}, c) *FF*, and d) J_{SC} against intensity. The thickness of the MoO_3 layer in this PBDB-T:ITIC device was 40 nm. Each line corresponds to a different pixel in nm.

The plot of V_{OC} against the logarithm of light intensity can reveal insights on the amount of monomolecular recombination in a device [17], [43]. Recalling Equation 5.2, the V_{OC} should scale logarithmically with intensity, resulting in a straight line on a semi-log plot. The V_{OC} should scale linearly with $\frac{nkT}{q} ln(intensity)$, where the ideality factor, n, should lie between 1 and 2. When the ideality factor is equal to 1, bimolecular recombination dominates. When equal to 2, monomolecular or trap-assisted recombination dominates [13], [17], [43]–[45].

The plot of J_{SC} against light intensity on a log-log plot gives insight into bimolecular recombination at short-circuit conditions [38], [39], [46]. The J_{SC} has been observed to follow a power law dependence on light intensity:

Equation 5.6. $$J_{SC} = Intensity^{\alpha}$$

where the value of α, the fitting coefficient, should lie between 0.5 and 1. If bimolecular recombination is significant under short-circuit conditions, the J_{SC} will follow a square-root dependence on light intensity [39]. If α is close to unity, bimolecular recombination is not significant under short-circuit conditions.

The semi-log plot of V_{OC} and the log-log plot of J_{SC} against light intensity at 298 K of one pixel (247 nm) are shown in Figures 5-16a and b, respectively. In Figure 5-16a, the slopes are not linear, and the V_{OC} seems to rapidly diminish at low light intensities. The diminishing V_{OC} effect is more prevalent in thinner pixels and is attributed to current leakage, likely from the presence of pinholes in the devices. Recalling Figure 1.10, the parasitic leakage current corresponds to the current that travels through the parallel shunt resistance, thus reducing the photocurrent. Devices with higher shunt resistances will suffer less parasitic leakage current.

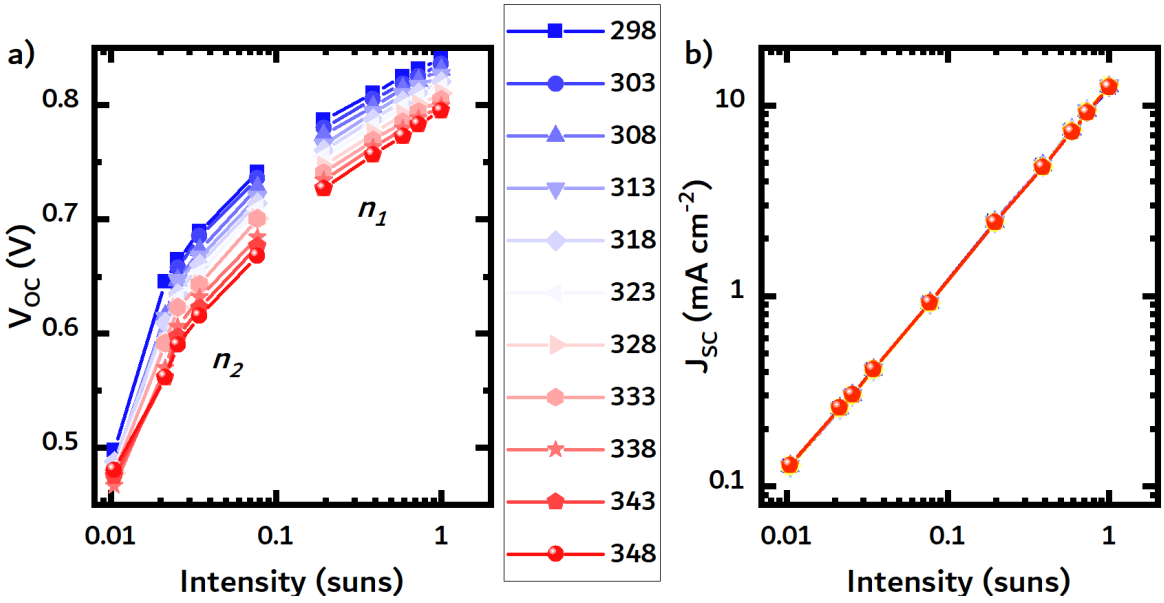

Figure 5-16. a) Semi-log plot of V_{OC} against light intensity. b) Log-log plot of J_{SC} against light intensity. The thickness of the PBDB-T:ITIC pixel was 247 nm. Each line corresponds to a different temperature in K.

Because the influence of current leakage is smaller in thicker pixels, the V_{OC} of a thick pixel (247 nm) was investigated as a function of intensity and temperature. The current leakage has less of an effect on the V_{OC} at higher light intensities, but there still appears to be a small deviation at intensities lower than 0.08 sun. Thus, the ideality factor, n_1, was calculated only using the data from the higher intensities (greater than 0.08 sun), and then again for the data at intensities lower than 0.08 sun, n_2. The calculated ideality factors are shown in Table 5.3. Comparing the two calculated ideality factors, there is a significant difference depending on the fitted intensity range, so the values in Table 5.3 serve a qualitative purpose. Ideality factors between 1 and 2 indicate that bimolecular and monomolecular recombination coexist in the OSC device. The ideality factor, n_1, slightly increases, which could indicate that monomolecular recombination becomes more prevalent with temperature. The ideality factors calculated using the lower intensities, n_2, are unreliable, but included for reference purposes. It should be emphasized that these light-intensity voltage measurements are still likely skewed by the leakage current. In conclusion, ensuring leakage current is minimized in OSC is critical to achieving accurate values for the ideality factor.

Dela Peña et al used light intensity studies as a means to probe the influence of changes in OSC morphology on solar cell performance, reporting a significant change in ideality factors for thermally degraded PBDB-T-2F:Y7 and PBDB-T-2F:ITIC-4Cl OSCs compared to non-degraded devices [47]. They found that monomolecular recombination sites increased as the solar cell degraded, and thus limiting performance of the devices. In the device investigated in this chapter, the change in ideality factor is much smaller than the ones reported by Dela Peña et al, and more importantly, the change in ideality factor with temperature is reversible, consistent with the findings from GISAXS and GIWAXS, that morphology does not change with temperature.

From Figure 5-16b, the calculated coefficient, α, exhibited only small deviation from 1. This means that bimolecular recombination is not significant at short-circuit conditions. Unlike the V_{OC}, the J_{SC} is not affected by current leakage [41]. The lack of change in α with temperature is also consistent with the measured J_{SC} and EQE data. If bimolecular recombination losses were to increase with temperature, the EQE signal and J_{SC} would likely be reduced [48].

Table 5.3. Calculated ideality factors.

Temperature (K)	n_1	n_2
298	1.294	4.593
303	1.310	4.852
308	1.333	4.498
313	1.381	4.373
318	1.354	4.059
323	1.351	4.040
328	1.389	3.880
333	1.378	3.832
338	1.380	3.724
343	1.408	3.420
348	1.430	3.127

5.4. Temperature Effects in Other Systems

The temperature-dependent PCE behavior for the other 9 OSC systems are shown in Figure 5-17. The systems were divided into three classes: systems with a reversible enhancement in PCE, systems with no apparent change in PCE, and systems with an irreversible change in PCE. Besides PBDB-T:ITIC, three other systems exhibited a similar enhancement in PCE, *FF*, and J_{SC} and a decrease in V_{OC} with temperature (Figure 5-13a): PBDB-T:O-IDFBR, PBDB-T:ITIC-4F, and PBDB-T:EH-IDTBR. In a second class of systems, Three systems displayed no obvious enhancement in PCE with temperature: P3HT:$PC_{61}BM$, PBDB-T-2F:ITIC-4F, and P3HT:O-IDTBR. To understand the different behaviors, the slopes of J_{SC}, *FF,* and V_{OC} against temperature are plotted in Figure 5-18.In the first class of systems, the change in J_{SC} and *FF* with temperature is much more significant than the change in J_{SC} and *FF* with temperature for the second class of systems. However, the V_{OC} reduced at a similar rate in the two classes. Therefore, it can be concluded that no enhancement in PCE is observed because the decrease in V_{OC} compensates the relatively modest increase in J_{SC} and *FF* in the second class of systems.

In the final class, the last three systems appeared to degrade irreversibly with temperature: PBDB-T:$PC_{71}BM$, PBDB-T-2Cl:ITIC-4F, and PBDB-T-2CL:Y6. This class of systems displayed a “zig-zag” behavior, where device performance continually degraded. The degradation of these systems could be due to changes in morphology, for example.

The fact that for the cases in which reversible behavior is observed, the different OSC parameters always go in the same direction suggest that the behavior is universal, but the final outcome is governed by the compromise between thermally induce transport improvements and recombination.

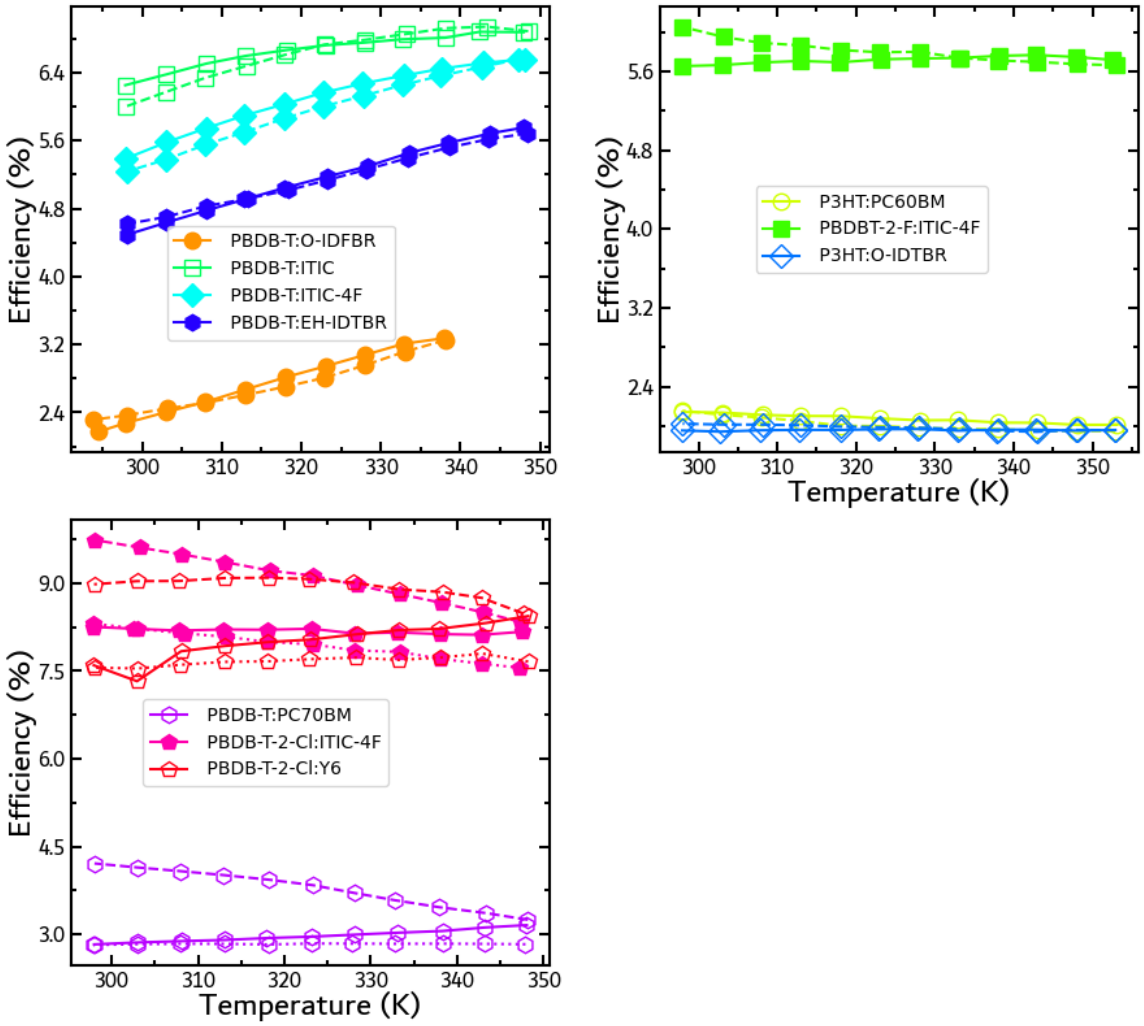

Figure 5-17. The measured PCE as a function of temperature for 3 classes of systems: a) systems that display a strong, reversible temperature dependence; b) systems where no obvious temperature dependence was observed; c) systems with an irreversible temperature difference. The dashed lines represent the PCE measured as the temperature was raised, while the solid lines represent the PCE measured as the temperature was lowered. In plot c, the dotted lines represent an additional PCE measurement performed after the initial heating cycle to highlight the irreversibility of the PCE behavior.

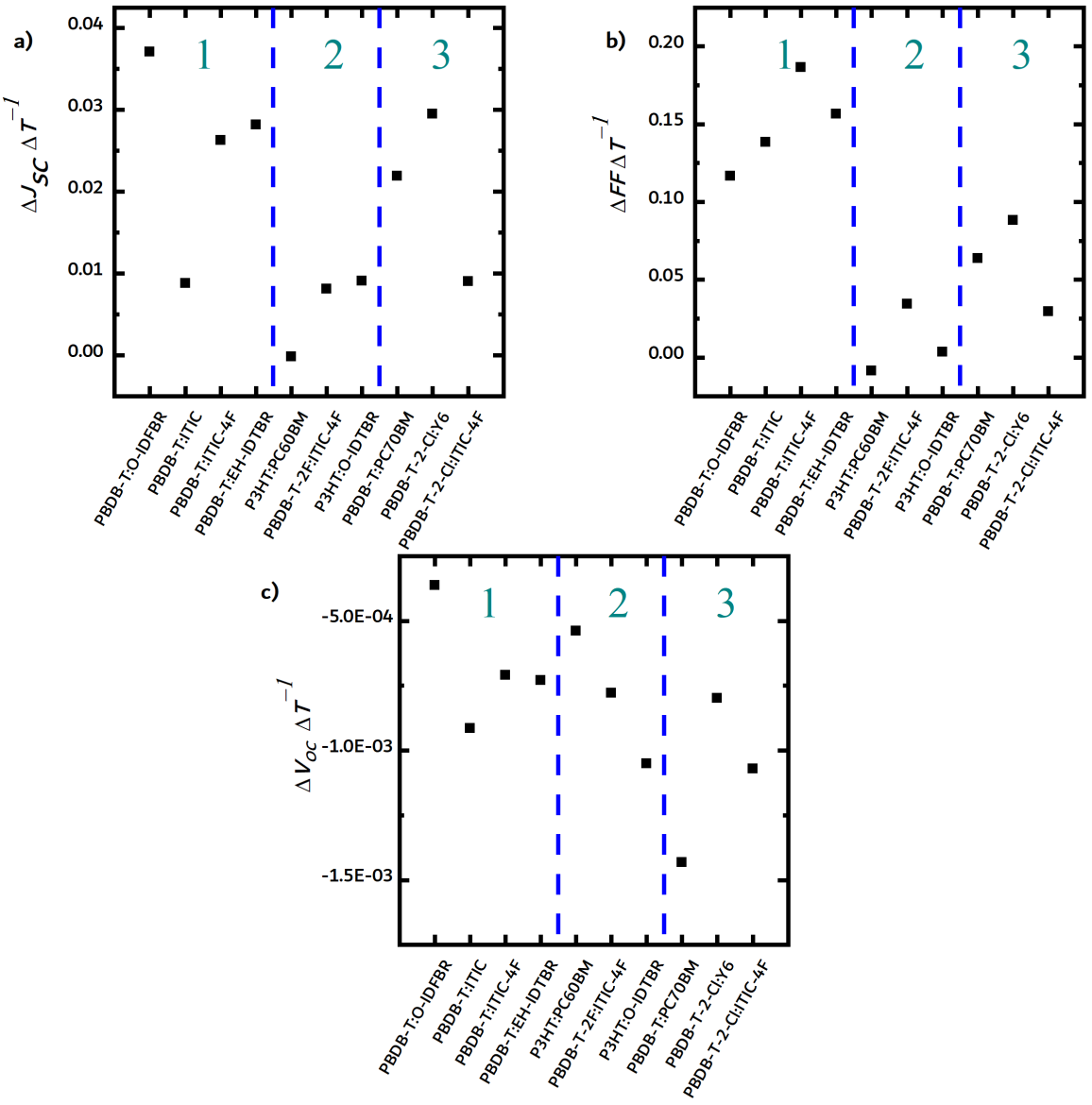

Figure 5-18. Plots of a) $\frac{\Delta J_{SC}}{\Delta T}$, b) $\frac{\Delta FF}{\Delta T}$, and c) $\frac{\Delta V_{OC}}{\Delta T}$. The values used were those obtained while cooling down the devices. The blue dashed lines separate the systems into the 3 separate classes as illustrated in Figure 5-13.

5.5. Conclusions

In this chapter, temperature has been shown to enhance the PCE, *FF*, and J_{SC} in four systems: PBDB-T:ITIC, PBDB-T:O-IDFBR, PBDB-T:ITIC-4F, and PBDB-T:EH-IDTBR. This behavior is highly reversible for all four of these systems, and its origin lies in the thermally-activated charge carrier mobilities, as indicated by the drift-diffusion calculations performed by collaborators at Imperial College London. The EQEs measured as a function of temperature revealed no significant changes in absorption, likely indicating no morphological changes with temperature. GISAXS and GIWAXS experiments also

confirmed that temperature did not provoke any significant changes in morphology, thus discarding morphological changes as an explanation to the observed behavior in the aforementioned systems. SCLC experiments were performed to measure the hole and electron mobilities. Finally, the OSC parameters were measured as a function of light intensity. From the log-log plot, bimolecular recombination was found to be insignificant under short-circuit conditions. Unfortunately, the devices fabricated in this chapter suffered from high leakage currents, so no conclusions were able to be made on the dominant recombination mechanisms.

5.6. References for Chapter 5

[1] Z. Yi *et al.*, “Effect of thermal annealing on active layer morphology and performance for small molecule bulk heterojunction organic solar cells,” *J. Mater. Chem. C*, vol. 2, no. 35, pp. 7247–7255, Aug. 2014, doi: 10.1039/C4TC00994K.

[2] D. Chirvase, J. Parisi, J. C. Hummelen, and V. Dyakonov, “Influence of nanomorphology on the photovoltaic action of polymer–fullerenecomposites,” *Nanotechnology*, vol. 15, no. 9, p. 1317, Aug. 2004, doi: 10.1088/0957-4484/15/9/035.

[3] M. Al-Ibrahim, O. Ambacher, S. Sensfuss, and G. Gobsch, “Effects of solvent and annealing on the improved performance of solar cells based on poly(3-hexylthiophene): Fullerene,” *Appl. Phys. Lett.*, vol. 86, no. 20, p. 201120, May 2005, doi: 10.1063/1.1929875.

[4] A. K. Thakur, G. Wantz, G. Garcia-Belmonte, J. Bisquert, and L. Hirsch, “Temperature dependence of open-circuit voltage and recombination processes in polymer–fullerene based solar cells,” *Sol. Energy Mater. Sol. Cells*, vol. 95, no. 8, pp. 2131–2135, Aug. 2011, doi: 10.1016/J.SOLMAT.2011.03.012.

[5] D. Bartesaghi *et al.*, “Competition between recombination and extraction of free charges determines the fill factor of organic solar cells,” *Nat. Commun. 2015 61*, vol. 6, no. 1, pp. 1–10, May 2015, doi: 10.1038/ncomms8083.

[6] T. Kirchartz, T. Agostinelli, M. Campoy-Quiles, W. Gong, and J. Nelson, “Understanding the Thickness-Dependent Performance of Organic Bulk Heterojunction Solar Cells: The Influence of Mobility, Lifetime, and Space Charge,” *J. Phys. Chem. Lett.*, vol. 3, no. 23, pp. 3470–3475, Dec. 2012, doi: 10.1021/JZ301639Y.

[7] C. M. Proctor, C. Kim, D. Neher, and T.-Q. Nguyen, “Nongeminate Recombination and Charge Transport Limitations in Diketopyrrolopyrrole-Based Solution-Processed Small Molecule Solar Cells,” *Adv. Funct. Mater.*, vol. 23, no. 28, pp. 3584–3594, Jul. 2013, doi: 10.1002/ADFM.201202643.

[8] R. Mauer, I. A. Howard, and F. Laquai, “Effect of Nongeminate Recombination on Fill Factor in Polythiophene/Methanofullerene Organic Solar Cells,” *J. Phys. Chem. Lett.*, vol. 1, no. 24, pp. 3500–3505, Dec. 2010, doi: 10.1021/JZ101458Y.

[9] L. Wu, H. Zang, Y.-C. Hsiao, X. Zhang, and B. Hu, “Origin of the fill factor loss in bulk-heterojunction organic solar cells,” *Appl. Phys. Lett.*, vol. 104, no. 15, p. 153903, Apr. 2014, doi: 10.1063/1.4871582.

[10] I. Riedel and V. Dyakonov, “Influence of electronic transport properties of polymer-fullerene blends on the performance of bulk heterojunction photovoltaic devices,” *Phys. status solidi*, vol. 201, no. 6, pp. 1332–1341, May 2004, doi: 10.1002/PSSA.200404333.

[11] V. Dyakonov, “Mechanisms controlling the efficiency of polymer solar cells,” *Appl. Phys. A 2004 791*, vol. 79, no. 1, pp. 21–25, Jun. 2004, doi: 10.1007/S00339-003-2496-7.

[12] G. Bardizza, E. Salis, C. Toledo, and E. D. Dunlop, “Power performance and thermal operation of organic photovoltaic modules in real operating conditions,” *Prog. Photovoltaics Res. Appl.*, vol. 28, no. 6, pp. 593–600, Jun. 2020, doi: 10.1002/pip.3234.

[13] L. J. A. Koster, V. D. Mihailetchi, R. Ramaker, and P. W. M. Blom, “Light intensity dependence of open-circuit voltage of polymer:fullerene solar cells,” *Appl. Phys. Lett.*, vol. 86, no. 12, p. 123509, Mar. 2005, doi: 10.1063/1.1889240.

[14] D. Credgington and J. R. Durrant, “Insights from Transient Optoelectronic Analyses on the Open-Circuit Voltage of Organic Solar Cells,” *J. Phys. Chem. Lett.*, vol. 3, no. 11, pp. 1465–1478, Jun. 2012, doi: 10.1021/JZ300293Q.

[15] M. M. Mandoc, L. J. A. Koster, and P. W. M. Blom, “Optimum charge carrier mobility in organic solar cells,” *Appl. Phys. Lett.*, vol. 90, no. 13, p. 133504, Mar. 2007, doi: 10.1063/1.2711534.

[16] D. Lee, J. Y. Kim, G. Park, H. W. Bae, M. An, and J. Y. Kim, “Enhanced Operating Temperature Stability of Organic Solar Cells with Metal Oxide Hole Extraction Layer,” *Polym. 2020, Vol. 12, Page 992*, vol. 12, no. 4, p. 992, Apr. 2020, doi: 10.3390/POLYM12040992.

[17] B. Ebenhoch, S. A. J. Thomson, K. Genevičius, G. Juška, and I. D. W. Samuel, “Charge carrier mobility of the organic photovoltaic materials PTB7 and PC71BM and its influence on device performance,” *Org. Electron.*, vol. 22, pp. 62–68, Jul. 2015.

[18] F. C. Jamieson, E. B. Domingo, T. McCarthy-Ward, M. Heeney, N. Stingelin, and J. R. Durrant, “Fullerene crystallisation as a key driver of charge separation in polymer/fullerene bulk heterojunction solar cells,” *Chem. Sci.*, vol. 3, no. 2, pp. 485–492, Jan. 2012, doi: 10.1039/C1SC00674F.

[19] M. Campoy-Quiles *et al.*, “Morphology evolution via self-organization and lateral and vertical diffusion in polymer:fullerene solar cell blends,” *Nat. Mater. 2008 72*, vol. 7, no. 2, pp. 158–164, Jan. 2008, doi: 10.1038/nmat2102.

[20] W. Zhao *et al.*, “Fullerene-Free Polymer Solar Cells with over 11% Efficiency and Excellent Thermal Stability,” *Adv. Mater.*, vol. 28, no. 23, pp. 4734–4739, Jun. 2016, doi: 10.1002/ADMA.201600281.

[21] W. Li, D. Liu, and T. Wang, “Stability Of Non-Fullerene Electron Acceptors and Their Photovoltaic Devices,” *Adv. Funct. Mater.*, p. 2104552, 2021, doi: 10.1002/ADFM.202104552.

[22] E. M. Speller *et al.*, “From fullerene acceptors to non-fullerene acceptors: prospects and challenges in the stability of organic solar cells,” *J. Mater. Chem. A*, vol. 7, no. 41, pp. 23361–23377, Oct. 2019, doi: 10.1039/C9TA05235F.

[23] C. Ma *et al.*, “Unraveling the Temperature Dependence of Exciton Dissociation and Free Charge Generation in Nonfullerene Organic Solar Cells,” *Sol. RRL*, vol. 5, no. 4, p. 2000789, Apr. 2021, doi: 10.1002/SOLR.202000789.

[24] C. C. S. Chan *et al.*, “Quantification of Temperature-Dependent Charge Separation and Recombination Dynamics in Non-Fullerene Organic Photovoltaics,” *Adv. Funct. Mater.*, p. 2107157, Aug. 2021, doi: 10.1002/ADFM.202107157.

[25] V. V. Brus *et al.*, “Temperature and Light Modulated Open-Circuit Voltage in Nonfullerene Organic Solar Cells with Different Effective Bandgaps,” *Adv. Energy Mater.*, vol. 11, no. 4, p. 2003091, Jan. 2021, doi: 10.1002/AENM.202003091.

[26] Y. Zhang *et al.*, “Thermally Stable All-Polymer Solar Cells with High Tolerance on Blend Ratios,” *Adv. Energy Mater.*, vol. 8, no. 18, p. 1800029, Jun. 2018, doi: 10.1002/AENM.201800029.

[27] V. Coropceanu, J. Cornil, D. A. da S. Filho, Y. Olivier, A. Robert Silbey, and Jean-Luc Brédas, “Charge Transport in Organic Semiconductors,” *Chem. Rev.*, vol. 107, no. 4, pp. 926–952, Apr. 2007, doi: 10.1021/CR050140X.

[28] F. Nickel *et al.*, “Spatial mapping of photocurrents in organic solar cells comprising wedge-shaped absorber layers for an efficient material screening,” *Sol. Energy Mater. Sol. Cells*, vol. 104, pp. 18–22, Sep. 2012, doi: 10.1016/J.SOLMAT.2012.04.026.

[29] R. Betancur *et al.*, “Optical interference for the matching of the external and internal quantum efficiencies in organic photovoltaic cells,” *Sol. Energy Mater. Sol. Cells*, vol. 104, pp. 87–91, Sep. 2012, doi: 10.1016/J.SOLMAT.2012.04.047.

[30] J. Mescher, A. Mertens, A. Egel, S. W. Kettlitz, U. Lemmer, and A. Colsmann, “Illumination angle and layer thickness influence on the photo current generation in organic solar cells: A combined simulative and experimental study,” *AIP Adv.*, vol. 5, no. 7, p. 077188, Jul. 2015, doi: 10.1063/1.4928074.

[31] Y. Chang, X. Zhu, K. Lu, and Z. Wei, “Progress and prospects of thick-film organic solar cells,” *J. Mater. Chem. A*, vol. 9, no. 6, pp. 3125–3150, Feb. 2021, doi: 10.1039/D0TA10594E.

[32] L. A. A. Pettersson, L. S. Roman, and O. Inganäs, “Modeling photocurrent action spectra of photovoltaic devices based on organic thin films,” *J. Appl. Phys.*, vol. 86, no. 1, p. 487, Jun. 1999, doi: 10.1063/1.370757.

[33] F. Deledalle *et al.*, “Understanding the Effect of Unintentional Doping on Transport Optimization and Analysis in Efficient Organic Bulk-Heterojunction Solar Cells,” *Phys. Rev. X*, vol. 5, no. 1, p. 011032, Mar. 2015, doi: 10.1103/PhysRevX.5.011032.

[34] C. Duan, F. Huang, and Y. Cao, “Solution processed thick film organic solar cells,” *Polym. Chem.*, vol. 6, no. 47, pp. 8081–8098, Nov. 2015, doi: 10.1039/C5PY01340B.

[35] J.-Y. Yang and M. Hu, “Temperature-Induced Large Broadening and Blue Shift in the Electronic Band Structure and Optical Absorption of Methylammonium Lead Iodide Perovskite,” *J. Phys. Chem. Lett.*, vol. 8, no. 16, pp. 3720–3725, Aug. 2017, doi: 10.1021/ACS.JPCLETT.7B01719.

[36] N. Felekidis, A. Melianas, and M. Kemerink, “Automated open-source software for charge transport analysis in single-carrier organic semiconductor diodes,” *Org. Electron.*, vol. 61, pp. 318–328, Oct. 2018, doi: 10.1016/J.ORGEL.2018.06.010.

[37] J. C. Blakesley *et al.*, “Towards reliable charge-mobility benchmark measurements for organic semiconductors,” *Org. Electron.*, vol. 15, no. 6, pp. 1263–1272, Jun. 2014, doi: 10.1016/J.ORGEL.2014.02.008.

[38] P. Schilinsky, C. Waldauf, and C. J. Brabec, “Recombination and loss analysis in polythiophene based bulk heterojunction photodetectors,” *Appl. Phys. Lett.*, vol. 81, no. 20, p. 3885, Nov. 2002, doi: 10.1063/1.1521244.

[39] I. Riedel, J. Parisi, V. Dyakonov, L. Lutsen, D. Vanderzande, and J. C. Hummelen, “Effect of temperature and illumination on the electrical characteristics of polymer-fullerene bulk-heterojunction solar cells,” *Adv. Funct. Mater.*, vol. 14, no. 1, pp. 38–44, 2004, doi: 10.1002/ADFM.200304399.

[40] P. Hartnagel and T. Kirchartz, “Understanding the Light-Intensity Dependence of the Short-Circuit Current of Organic Solar Cells,” *Adv. Theory Simulations*, vol. 3, no. 10, p. 2000116, Oct. 2020, doi: 10.1002/ADTS.202000116.

[41] C. M. Proctor and T.-Q. Nguyen, “Effect of leakage current and shunt resistance on the light intensity dependence of organic solar cells,” *Appl. Phys. Lett.*, vol. 106, no. 8, p. 083301, Feb. 2015, doi: 10.1063/1.4913589.

[42] B. Xiao, P. Calado, R. C. I. MacKenzie, T. Kirchartz, J. Yan, and J. Nelson, “Relationship between Fill Factor and Light Intensity in Solar Cells Based on Organic Disordered Semiconductors: The Role of Tail States,” *Phys. Rev. Appl.*, vol. 14, no. 2, p. 024034, Aug. 2020, doi: 10.1103/PhysRevApplied.14.024034.

[43] F. Gao *et al.*, “Trap-Induced Losses in Hybrid Photovoltaics,” *ACS Nano*, vol. 8, no. 4, pp. 3213–3221, Apr. 2014, doi: 10.1021/NN501185H.

[44] T. Kirchartz and J. Nelson, “Meaning of reaction orders in polymer:fullerene solar cells,” *Phys. Rev. B*, vol. 86, p. 165201, 2012, doi: 10.1103/PhysRevB.86.165201.

[45] L. K. Ma *et al.*, “High-Efficiency Indoor Organic Photovoltaics with a Band-Aligned Interlayer,” *Joule*, vol. 4, no. 7, pp. 1486–1500, Jul. 2020, doi: 10.1016/J.JOULE.2020.05.010.

[46] A. K. K. Kyaw *et al.*, “Intensity Dependence of Current–Voltage Characteristics and Recombination in High-Efficiency Solution-Processed Small-Molecule Solar Cells,” *ACS Nano*, vol. 7, no. 5, pp. 4569–4577, May 2013, doi: 10.1021/NN401267S.

[47] T. A. Dela Peña *et al.*, “Understanding the Charge Transfer State and Energy Loss Trade-offs in Non-fullerene-Based Organic Solar Cells,” *ACS Energy Lett.*, pp. 3408–3416, Sep. 2021, doi: 10.1021/ACSENERGYLETT.1C01574.

[48] S. R. Cowan, J. Wang, J. Yi, Y.-J. Lee, D. C. Olson, and J. W. P. Hsu, “Intensity and wavelength dependence of bimolecular recombination in P3HT:PCBM solar cells: A white-light biased external quantum efficiency study,” *J. Appl. Phys.*, vol. 113, no. 15, p. 154504, Apr. 2013, doi: 10.1063/1.4801920.

Chapter 6. Conclusions and Perspectives

6.1. Conclusions

This thesis compiles results of work on solar organic thermoelectrics, geometries for hybrid PV-TE devices, and temperature-dependent OSC behavior.

In the first part of this thesis, we demonstrated that organic thermoelectrics can harvest solar energy. Firstly, we characterized organic TE materials spanning 4 material classes as solar absorbers using FTIR spectroscopy and IR thermography. Organic TE materials can absorb across the solar spectrum, and their temperature can rise more than 50 K under 2 sun illumination. The temperature rise was demonstrated to be dependent on film thickness and the material's thermal conductivity.

Next, we investigated the effect of light on the TE parameters, observing small photoconductivity effects in a mat of CoMoCAT CNTs and a free-standing PEDOT:PSS film but no noticeable change in the Seebeck coefficient. Furthermore, we investigated the influence of critical design parameters, namely leg length and illuminated area, on SOTEG power output. We showed that there is a trade-off in leg length and electrical resistance. Shorter leg lengths reduce electrical resistances, however, this decrease is compensated for by a reduction in thermovoltage at very short leg lengths. We also demonstrated that there is an optimum illuminated area. Illuminating too much of the SOTEG legs causes both sides of the device to thermalize, while too little limits the thermovoltage.

After investigating device parameters, we presented several device architectures for SOTEGs, and briefly compared planar and vertical devices. We fabricated a proof-of-concept SOTEG device with 6 legs. The proof-of-concept device, although its output of 180 nW under 2 sun illumination is relatively modest, still highlights the ability of organic materials to make low-complexity devices.

In the second part of this thesis, we investigated possible geometries for hybrid PV-TE devices. We used FTIR spectroscopy to characterize the transmittance and reflectance spectra of several OSC materials and IR thermography to characterize temperature rise of the OSC and TE materials. The recorded temperature rises were used as a proxy for TEG efficiencies, also calculated in chapter 4.

Comparing the transmittance and reflection spectra, a large portion of solar radiation is transmitted by the OSC materials than reflected. From the temperature data, we are able to make three observations. Firstly, the temperature rises in a transmission geometry are higher than those observed in a reflection geometry, resulting in higher TEG efficiencies.

Secondly, the support material greatly influences the temperature rise of the OSC and TE materials by reducing heat losses, especially convection, and prudent design should adequately choose support material. In this thesis, we examined support materials with low-thermal conductivities, including PET and PLA, but a future study could involve investigating other possible support materials.

Thirdly, the temperature rise of the OSC materials in a transmission geometry was observed to depend on the band gap of the material, with the highest temperatures attained by the materials with the narrower band gaps.

We highlight that placing a SOTEG in a device with a contact transmission geometry allows the SOTEG to make use of waste heat generated by the solar cell. If a semi-transparent OSC is used, the SOTEG can also make use of the transmitted light by the OSC, leading to higher device temperatures, and therefore, higher TEG efficiencies.

In the third part of this thesis, we detailed the effect of temperature on the OSC parameters, namely PCE, *FF*, J_{SC}, and V_{OC}. In a commercial OSC module, we observed an enhancement in PCE with temperature, which motivated us to investigate the light intensity- and temperature-dependent OSC parameters of ten different organic systems. A high through put processing method, namely blade-coating, was used to fabricate OSCs with a variable PAL thickness, producing a considerable amount of data.

For one representative system, PBDB-T:ITIC, we observed a reversible temperature-dependent enhancement in PCE, *FF*, and J_{SC}, and a reversible temperature-dependent reduction in V_{OC}. The temperature-dependent enhancement in PCE, *FF*, and J_{SC} was also observed to be thickness-dependent, with the enhancement more pronounced in thicker pixels. The temperature-dependent EQEs corroborated the temperature-dependent J-V characteristics, again showing a more pronounced enhancement in J_{SC} with temperature in thicker pixels.

We used GISAXS and GIWAXS to confirm that the enhancement in OSC performance for PBDB-T:ITIC was not due to changes in the microstructure. Drift-diffusion simulations performed by an external collaborator agreed well with the experimental results, showing that the origin of the enhancement in OSC performance instead lies in the thermally-activated charge transport. We performed SCLC experiments to measure the temperature-dependent hole and electron mobility, observing an enhancement in mobility for both types of charge carriers with temperature.

Light-intensity experiments were performed to characterize the recombination mechanisms. Although the fabricated OSCs suffer from leakage current at low intensities (intensities less than 0.1 sun), the calculated ideality factors revealed a mix of monomolecular and bimolecular recombination in the PBDB-T:ITIC system that did not significantly change with temperature.

We did a global comparison of the ten different systems, dividing them into one of three classes: systems with a reversible enhancement in PCE, systems with no apparent change in PCE, and systems with an irreversible change in PCE. The first class of systems – to which PBDB-T:ITIC, PBDB-T:O-IDFBR, PBDB-T:ITIC-4F, and PBDB-T:EH-IDTBR belong – showed an enhancement in PCE, *FF*, and J_{SC} and a reduction in V_{OC}. The second class of systems, comprised of P3HT:$PC_{61}BM$, PBDB-T-2F:ITIC-4F, and P3HT:O-IDTBR, showed no obvious enhancement in PCE. The third class of systems, composed of PBDB-T:$PC_{71}BM$, PBDB-T-2Cl:ITIC-4F, and PBDB-T-2CL:Y6, appeared to degrade irreversibly with temperature.

In this thesis, three different types of devices were explored to harvest solar radiation: SOTEGs, hybrid PV-TE devices, and OSCs. OSCs convert sunlight into electricity much more efficiently than SOTEGs. The highest reported PCE for an OSC is over 19% under 1 sun illumination, while the theoretical efficiency for an ideal SOTEG with a ZT of 0.5 being just 1% under 1 sun illumination [1], [2]. It is clear that better TE materials are need to obtain devices with higher SOTEG efficiencies, but ultimately, like all heat engines, higher temperatures are needed to achieve higher STEG efficiencies [3].

Combining OSCs with SOTEGs in a hybrid device offers one key advantage over other approaches to boost efficiency, such as tandem cells. Device complexity is not increased with hybrid PV-TE devices, as both individual devices can be fabricated individually and in parallel. Compared to single-junction solar cells, hybrid PV-TE devices with a contact

transmission geometry could still be interesting because of the thermal insulating effect of the SOTEG. In the case PCE is enhanced with temperature, a SOTEG can help increase device temperature and lead to higher device efficiencies.

6.2. Perspectives and future work

The work carried out gives perspectives on a new application for organic thermoelectrics: solar harvesting. The unique properties of organic TE materials allow for low-complexity SOTEG devices, as demonstrated in the first part of the thesis. The bulk of the thesis consisted on exploring thin-film organic TE materials, but thick, porous organic TE materials, such as porous polymer matrices or CNT sponges, are also interesting for SOTEGs. In the first two chapters related to SOTEGs, we showed that a desirable solar TE material is thick, possesses a low thermal conductivity and exhibits broadband absorption across the solar spectrum. CNT sponges, for example, are black, meaning they exhibit absorption in the solar spectrum, and have extremely low thermal conductivities [4]. Therefore, future work could involve fabricating porous materials for SOTEGs.

In the context of OSCs, the light intensity- and temperature-dependent J-V characteristics provide insight on the importance of the thermally-activated charge transport on the OSC parameters. Some systems incorporating NFAs exhibited excellent thermally-stability. Additionally, applying temperature to some OSC systems could be seen as an approach to achieve thickness-independent PCEs. In the commonly used large-area deposition techniques, such as roll-to-roll, thicker PALs are needed to prevent pinholes. The thicker PALs often exhibit lower PCEs compared to those from thinner PALs, but applying temperature may help to improve OSC performance of thicker OSCs.

The focus of future work on temperature-dependent OSC behavior could go into two directions. One direction could be finding ways to enhance further temperature of the OSC. A simple possibility would be to explore different electrodes, substrates, or encapsulation materials to reduce thermal losses via convection or conduction. Another approach could be incorporating photonics or plasmonics structures to help increase the temperature of the OSC by using the unused part of the solar spectrum.

Although temperature enhances OSC performance in some systems, other systems thermally degrade, so the second direction for future work could be stability. More work on understanding the degradation mechanisms in the thermally degraded systems is needed.

For the systems that do work, especially the systems exhibiting high PCEs, it would be interesting to conduct longer term stability studies and explore the use of different solvents in order to investigate films with different microstructures.

6.3. References for Chapter 6

[1] Y. Cui *et al.*, “Single-Junction Organic Photovoltaic Cell with 19% Efficiency,” *Adv. Mater.*, p. 2102420, Aug. 2021, doi: 10.1002/ADMA.202102420.

[2] J. P. Jurado, B. Dörling, O. Zapata-Arteaga, A. Roig, A. Mihi, and M. Campoy-Quiles, “Solar Harvesting: a Unique Opportunity for Organic Thermoelectrics?,” *Adv. Energy Mater.*, vol. 9, no. 45, p. 1902385, Dec. 2019, doi: 10.1002/aenm.201902385.

[3] M. A. Green and S. P. Bremner, “Energy conversion approaches and materials for high-efficiency photovoltaics,” *Nat. Mater.*, vol. 16, no. 1, p. 23, Dec. 2016, doi: 10.1038/nmat4676.

[4] X. Yang, J. Cui, K. Xue, Y. Fu, H. Li, and H. Yang, “Thermal conductivity and thermoelectric properties in 3D macroscopic pure carbon nanotube materials,” *Nanotechnol. Rev.*, vol. 10, no. 1, pp. 178–186, Jan. 2021, doi: 10.1515/NTREV-2021-0013.

Appendix A. Witec Data

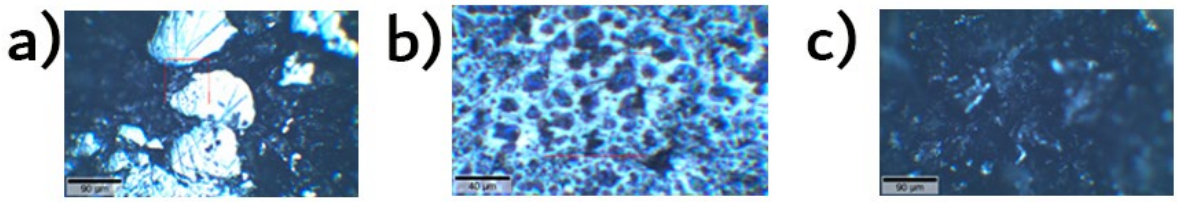

Figure A.1. Optical images of a) Ni-ett, b) Ni-diett, and c) Ni-btt. The red boxes represent the Raman scan area

A cluster analysis (Figure A.2) was performed on the Raman data using a WITec alpha 300 RA+ confocal Raman setup, coupled to an Olympus objective with 10× magnification to provide further insight on the origin of the differences in thermal conductivity. A 633 nm centered laser was used to perform the Raman experiments. The Ni-ett and Ni-diett samples exhibited a uniform chemical composition, but there were minor differences in the surface structure. For the Ni-ett sample, there was a higher Raman intensity in the smoother domains. For the Ni-diett sample, there were two distinct Raman spectra present, one associated with the porous “holes” (blue) and the second spectrum associated with the surrounding “scaffolding” (red). The Ni-btt sample, on the other hand, revealed a much more complex picture compared to the other two OCMPs. The surface of the Ni-btt sample was much rougher, and the composition appeared to be inhomogeneous. The cluster analysis identified three different Raman spectra. One spectrum was identified as noise (purple), and the other two were identified as distinct Raman signals (green and orange). The peak positions and shapes are slightly different, possibly indicating a slightly different chemical composition. These slight differences could account for the larger standard deviation measured in the thermal conductivity of the Ni-btt sample.

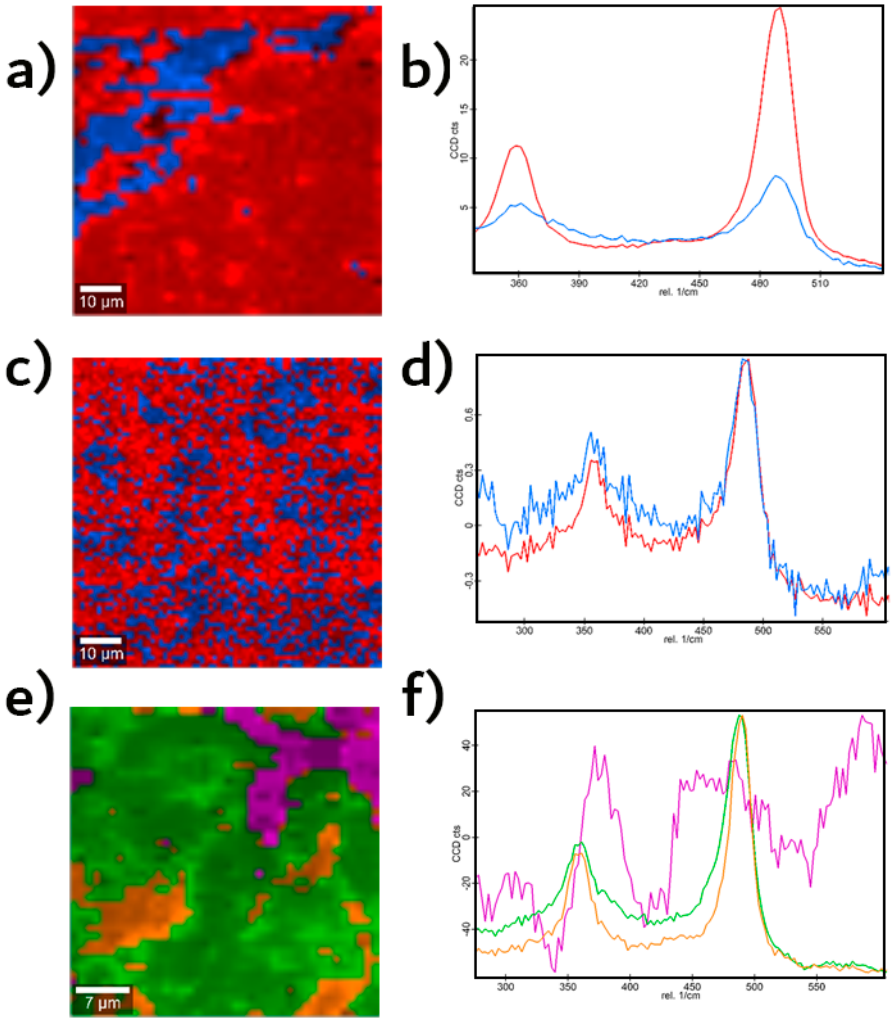

Figure A. 2. Cluster analysis performed on the Raman data. Cluster analysis on the optical images of a) Ni-ett, c) Ni-diett, and e) Ni-btt. The Raman spectra of the clusters in the b) Ni-ett, d) Ni-diett, and Ni-btt samples.

The spectral range of the Raman scans was extended up to 2000 cm^{-1} to probe the surface composition (Figure A.3). The broad band in the range of 1200–1600 cm^{-1} is associated with vibrations in the organic ligands (carbon bonds) and indicates the presence of amorphous carbon, or carbon with very different environments. The bands in the lower wavenumber region (between 300 and 500 cm^{-1}) are associated with vibrations involving heavy atoms. The change in the ratio between the intensities of the inorganic and organic vibrations suggests there are differences in stoichiometry in the different regions, which may explain the variations in thermal conductivity.

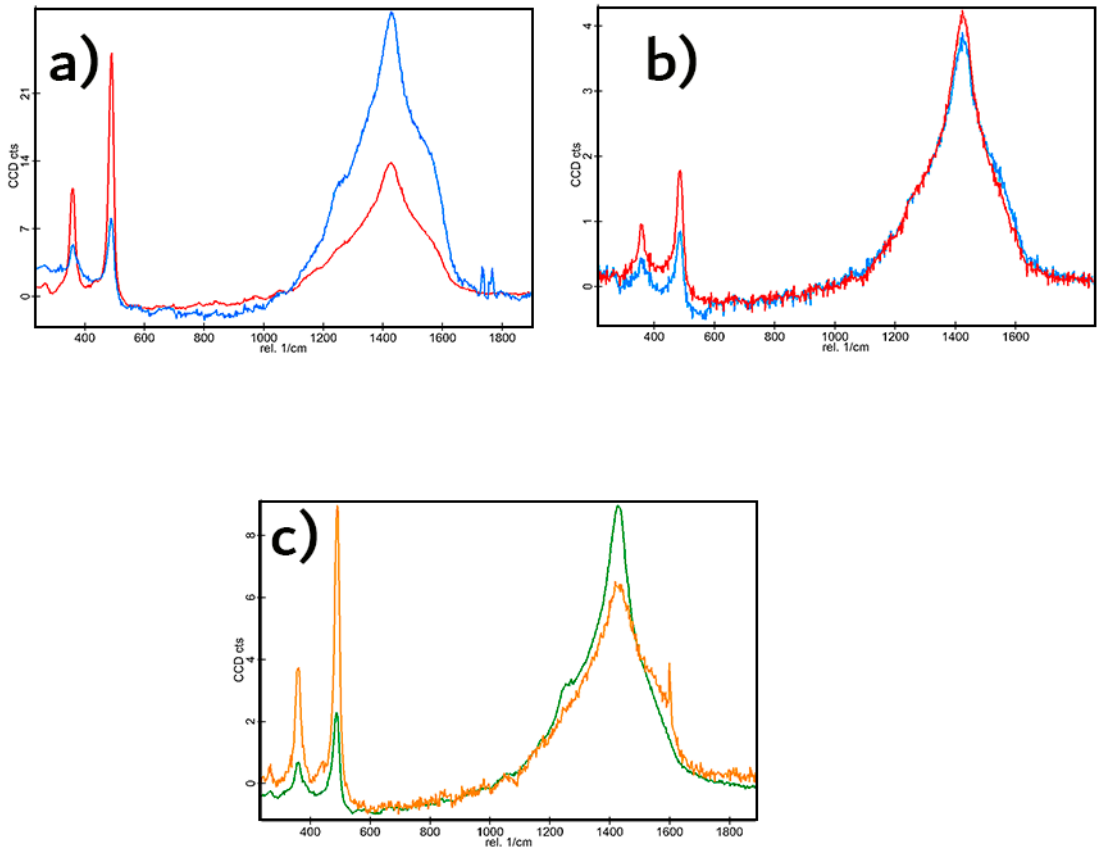

Figure A.3. Cluster analysis on the extended Raman data for the b) Ni-ett, d) Ni-diett, and Ni-btt samples.

To quantify the potential differences in thermal conductivity, the spectra were fitted at the peak around 360 cm^{-1}, and the histogram for each sample was calculated (Figure A.4). For Ni-ett, the distribution of the spectral position of the Raman peak was relatively narrow (about ± 5 cm^{-1}) while the distribution was much broader for Ni-diett and Ni-btt (about ± 25 cm^{-1}). These deviations are entirely consistent with the increase in the standard deviation observed between the three independent points for each sample.

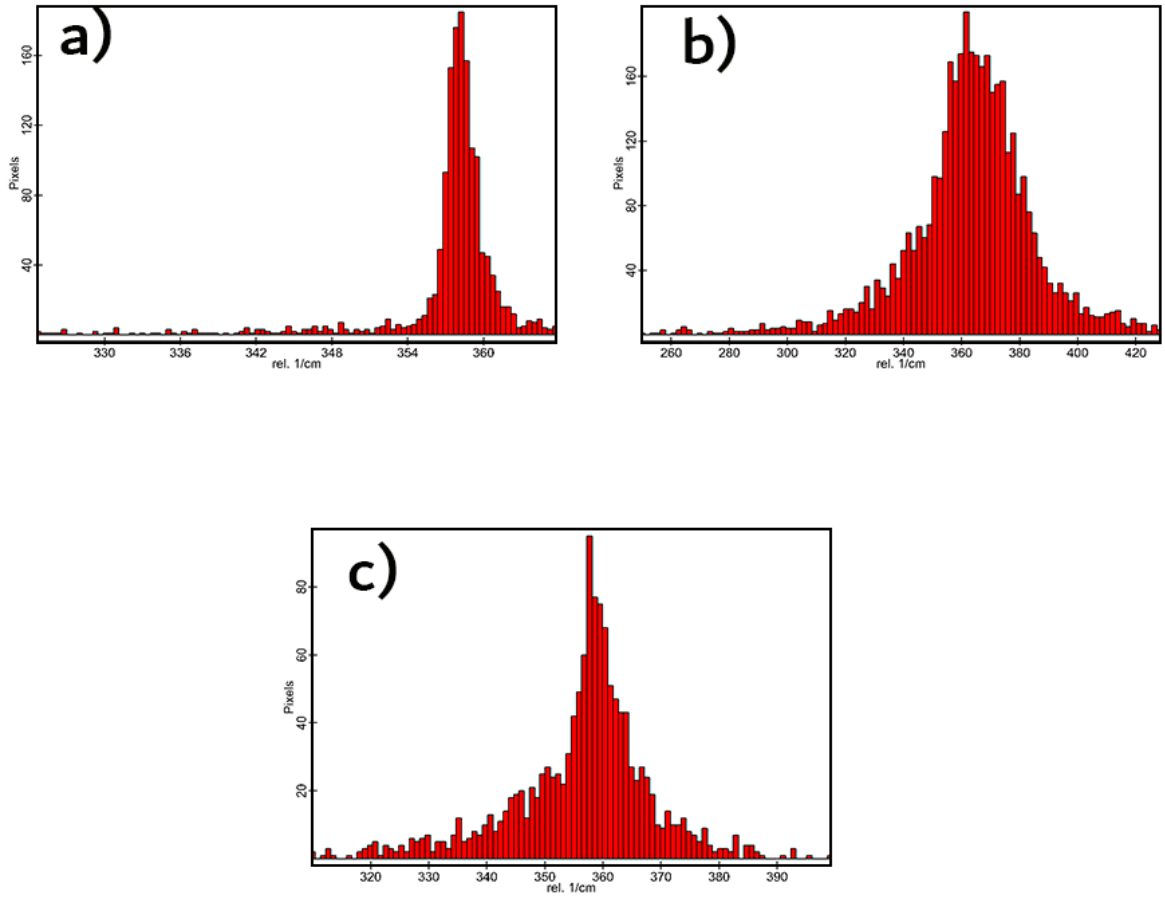

Figure A.4. Histograms of first Raman peak (around 360 cm-1) positions for the a) Ni-ett, b) Ni-diett and c) Ni-btt samples.